Radio-Frequency Spectroscopy on the Mass-Imbalanced ^{6}Li-^{40}K Fermi-Fermi Mixture

DISSERTATION

by

Dipl.-Phys. Michael Jag

submitted to the Faculty of Mathematics, Computer Science,
and Physics of the University of Innsbruck

in partial fulfillment of the requirements
for the degree of Doctor of Philosophy (PhD)

Advisors:
Univ.-Prof. Dr. Rudolf Grimm,
Institute for Experimental Physics, University of Innsbruck
Institute for Quantum Optics and Quantum Information of the
Austrian Academy of Sciences

Univ.-Prof. Dr. Francesca Ferlaino,
Institute for Experimental Physics, University of Innsbruck
Institute for Quantum Optics and Quantum Information of the
Austrian Academy of Sciences

Innsbruck, July 2016

Summary

Ultracold quantum gases are ideal systems to experimentally tackle fundamental problems in both many- and few-body physics. The parameters characterizing such systems can be controlled and readout to an unprecedentedly high degree of precision. In this thesis, we discuss our experimental investigations of mixtures of two ultracold gases of different fermionic atom species, ^{6}Li and ^{40}K. The studies can be assigned to two main research themes. These are the fundamental many-body system consisting of an impurity in a Fermi sea on the one hand, and Li-K few-body physics on the other hand.

To address the many-body physics of an impurity in a Fermi sea experimentally, we realize a mixture of a few K atoms and a large, dense cloud of fermionic Li atoms. The interaction between the impurity atoms and the atoms of the Fermi sea can be tuned by means of a magnetic Feshbach resonance. We then employ radio-frequency spectroscopy of the K atoms in various interaction regimes, ranging from strongly repulsive to strongly attractive, to reveal the energy landscape of the impurities in the Fermi sea. In the regime of strong interactions, where the scattering length exceeds the inter-particle separation, the impurity together with the excitation of the Fermi sea are described as a quasiparticle termed polaron, following Fermi liquid theory. We determine the energy, the residue, and the lifetime of such polarons in our system. Then, by applying a spin-echo technique, we investigate the decoherence of impurities in a Fermi sea as a function of the interaction strength. For moderate interaction strengths, our measurements provide a determination of the quasiparticle scattering rate. For near-resonant interactions, the decoherence rates are almost an order of magnitude larger.

In another series of experiments, we probe the response of a Fermi sea to a rapidly introduced impurity on timescales much shorter than the Fermi time. Employing a Ramsey-type interferometry technique, we track the formation dynamics of repulsive and attractive polaron in real time. For resonant interactions, we observe the quantum interference arising from the simultaneous excitation of the corresponding repulsive and attractive many-body branches.

To investigate the physics of Li-K few-body systems, we create dense samples of Li-K dimers from almost balanced mixtures of Li and K atoms. We then perform radio-frequency spectroscopy to investigate the elastic interactions of heavy K atoms with light-heavy Li-K dimers. Contrary to the atom-dimer interactions in a mass-balanced Fermi-Fermi mixture, our measurements reveal a strong K-LiK attraction in a regime of Li-K repulsion. This atom-dimer attraction is speculated to facilitate the access to the realization of exotic many-body states and phases.

Whether it is possible to experimentally realize such phases, strongly depends on the lifetime of the atom-dimer mixture, which is typically limited by the lifetime of the dimer cloud. Therefore, we also investigate the lifetimes of dimer clouds as a function of the magnetic detuning from a Feshbach resonance. Our measurements allow us to discriminate between different contributions to the decay of our dimer sample and to determine accurate rates for the spontaneous decay as well as for the decay arising from collisions between two dimers or between one dimer and one atom.

Zusammenfassung

Ultrakalte Quantengase sind ideale Systeme, um fundamentale Probleme sowohl der Vielteilchen- als auch der Mehrteilchen-Physik experimentell in Angriff zu nehmen. Die Parameter, die solche Systeme charakterisieren, können zu einem beispiellos hohen Grad an Präzision kontrolliert und ausgelesen werden. In dieser Arbeit werden Experimente mit Gemischen zweier Gase verschiedener fermionischer Atom-Spezies, ^{6}Li und ^{40}K, diskutiert. Unsere Untersuchungen können zwei größeren Forschungsthemen zugeordnet werden. Diese sind zum einen das grundlegende Vielteilchen-System, bestehend aus einem Fremdatom und einem Fermi-See, und zum anderen die Li-K Mehrteilchen-Physik.

Um uns der Vielteilchen-Physik eines Fremdatoms im Fermi-See zu widmen, erzeugen wir ein Gemisch von wenigen K-Atomen und einer großen, dichten Wolke von Li-Atomen. Wir können die Wechselwirkung zwischen den Fremdatomen und den Atomen des Fermi-Sees mittels einer magnetischen Feshbach-Resonanz variieren. Wir führen dann Radiofrequenz-Spektroskopie an den Kalium-Atomen in mehreren Wechselwirkungsregimes, von stark repulsiv bis stark attraktiv, durch und legen so das Energiespektrum des Kalium-Atoms im Lithium-Fermi-See offen. Im stark wechselwirkenden Regime, wo die Streulänge größer ist als der Teilchenabstand, wird das Fremdatom, zusammen mit der Anregung des Fermi-Sees, Landaus Theorie der Fermi-Flüssigkeiten folgend, als Quasiteilchen beschrieben, das Polaron genannt wird. Wir bestimmen die Energie, das Residuum und die Lebensdauer der Polaronen in unserem System. Des Weiteren untersuchen wir die Dekohärenz der Fremdatome im Fermi-See als Funktion der Wechselwirkungsstärke, unter Verwendung einer Spin-Echo-Technik. Für mäßige Wechselwirkungsstärke stellen unsere Messungen eine Bestimmung der Quasiteilchen-Streurate dar. Bei nahresonanter Wechselwirkung bestimmen wir nahezu eine Größenordnung höhere Dekohärenzraten.

In einer weiteren Messreihe untersuchen wir, auf Zeitskalen viel kürzer als die Fermi-Zeit, wie unser System auf ein rasch eingeführtes Fremdatom reagiert. Unter Verwendung einer Ramsey-Interferometrie-Technik verfolgen wir die Entstehung von repulsivem und attraktivem Polaron in Echtzeit. Bei resonanter Wechselwirkung beobachten wir die Quanteninterferenz, die durch gleichzeitiges Anregen des repulsiven und attraktiven Vielteilchen-Zweiges zustande kommt.

Für die Untersuchungen der Physik in Li-K Mehrteilchen-Systemen erzeugen wir dichte Li-K-Dimerproben aus einem beinahe ausgewogenen Gemisch von Li- und K-Atomen. Wir führen dann Radiofrequenz-Spektroskopie durch, um die elastische Wechselwirkung zwischen K-Atomen und Li-K-Dimeren zu untersuchen. Im Gegensatz zur Atom-Dimer-Wechselwirkung in einem Gemisch zweier Gase gleichschwerer fermionischer Atome, zeigen unsere Messungen eine starke K-LiK-Anziehung in einem Regime, wo sich Li- und K-Atome gegenseitig abstoßen. Die beobachtete Atom-Dimer-Anziehung in unserem Gemisch soll es vereinfachen, exotische Vielteilchenzustände und -phasen experimentell zu realisieren.

Ob es möglich ist, solche Phasen experimentell zu realisieren, hängt stark von der Lebensdauer des Atom-Dimer-Gemischs ab, die typischer Weise durch die Dimer-Lebensdauer begrenzt ist. Daher untersuchen wir die Lebensdauer von Dimer-Wolken als Funktion der

magnetischen Verstimmung von einer Feshbach-Resonanz. In unseren Messungen können wir zwischen verschiedenen Beiträgen zum Zerfall einer Dimerprobe unterscheiden und wir erhalten die Raten für den spontanen Zerfall sowie für den Zerfall durch Stöße zwischen zwei Dimeren oder zwischen einem Dimer und einem Atom.

Contents

Chapter 1

Introduction

1.1 The interest in ultracold Fermi gases

Ultracold Fermi gases are pristine many-body systems. Realized under certain conditions, these systems can show aspects of behavior that find their direct counterpart in condensed-matter systems of tremendous interest [Ben14]. These condensed-matter systems include, e.g., high-temperature superconductors (high-T_c SC), the so-called quark-gluon plasma, a state our universe is assumed to be gone through shortly after the big bang, or neutron stars.

The reason for the enormous interest in these condensed matter systems is rooted in their importance. Gaining knowledge about the early stage and the evolution of the universe or, in the case of high-T_c SCs, being able to build wires that can conduct current at room temperature without losses, are strong driving forces to do research. The discovery of the latter would, for example, be an amazing scientific achievement with huge potential application on the energy market. However, all of the mentioned condensed-matter systems have in common that essential features of them are not understood. Huge efforts are made to obtain theoretical descriptions reproducing such features, and rather frequently new proposals emerge. For the theorists it is crucial to have their proposals experimentally tested.

Due to the astonishing analogies between the condensed-matter systems mentioned above and ultracold Fermi gases (though they have very different densities and temperatures) the latter offer an ideal testbed to benchmark potential theoretical descriptions or trigger their development. This process is referred to as quantum simulation: One can realize ultracold Fermi gases, offering excellent control of almost all relevant system parameters, under well defined conditions and use them to simulate a condensed-matter system [Blo12]. The ultracold Fermi gas is then typically investigated under variation of a system parameter and its behavior can be checked against the theoretical prediction. As a result, one can give crucial input for the theorist, i.e. in an ideal case one can falsify or verify a theoretical approach.

Usually such testing procedures require continuous control of the system's parameters: the interactions between fermions, the temperature, the density of fermions, the dimensionality

of the confinement (1D, 2D, 3D), the mass ratio of different fermions, and the population of various states of the fermions. We will discuss in the course of this thesis, how we can experimentally access and tune these parameters of ultracold, trapped Fermi-Fermi mixtures.

1.2 Short history of ultracold Fermi gases

At the time when the work presented in this thesis was started, there was already a large variety of groups working on ultracold Fermi gases. Here, we give a short summary of the achievements with ultracold atomic Fermi gases prior to the thesis.

It was a few years after the first realization of a Bose-Einstein condensate (BEC) of ultracold ^{87}Rb and ^{23}Na in 1995 [Dav95, And95] that a degenerate gas of fermionic atoms was experimentally realized [DeM99]. Initially, the experiments used stable fermionic alkali isotopes, which are ^{40}K [DeM99, Roa02] on the one hand, and ^{6}Li [Tru01, Sch01, Gra02, Had02, Joc03b] on the other hand. In the mean time, the list of elements of which ultracold degenerate Fermi gases were realized was extended by ^{3}He* [McN06], ^{171}Yb [Fuk07a], ^{173}Yb [Fuk07b], ^{87}Sr [DeS10, Tey10], ^{161}Dy [Lu12], ^{167}Er [Aik14], and ^{53}Cr [Nay15].

New fields of research were opened up by establishing mixtures of fermions in two different spin states of the same atomic species where interactions can be tuned utilizing Feshbach resonances [Chi10]. With such systems, Fermi gases under strongly interacting conditions [O'H02, Bou03] and, in particular, under the strongest possible, resonant interactions, the so-called unitary Fermi gas, could be investigated as prominently demonstrated by the measurement of the heat capacity of the unitary Fermi gas [Kin05]. Moreover, Feshbach resonances were utilized to create dense samples of diatomic Fermi-Fermi molecules [Reg03, Str03, Cub03, Joc03a]. Such molecules, made up of two fermionic constituents, are in fact bosons and follow bosonic quantum statistics. Soon after the first production of dense molecule samples, this was spectacularly demonstrated by experimentally realizing a BEC of Fermi-Fermi molecules [Joc03b, Gre03, Zwi03, Bou04]. These studies sparked experimental efforts on investigating the pairing properties in the crossover from the BEC (bosonic) to a weakly attractive two-component Fermi gas, described by Bardeen-Cooper-Schrieffer (BCS) theory (fermionic). Experimentally, the first BEC-BCS crossover studies were reported in Refs. [Bar04b, Reg04b]. Already shortly after, measurements of the collective modes [Kin04, Bar04a] showed evidence for superfluidity. Vivid proof for superfluidity in the crossover regime was then delivered by the observation of vortices in a strongly interacting Fermi gas [Zwi05]. Later, numerous experiments addressed the investigation of superfluid properties in Fermi gases and, to list some of the prominent examples, yielded the observation of critical velocities [Mil07], a quenched moment of inertia [Rie11], and second sound [Sid13].

Fermi gases consisting of spin-state mixtures with an imbalanced population were started to be explored only a few years later by the Hulet (Rice) and the Ketterle (MIT) groups. They addressed the question of survival of superfluidity in these mixture versus interaction strength [Zwi06] and demonstrated the phase separation of such mixtures into a superfluid core surrounded by remnant majority atoms [Par06, Shi06]. These observations triggered

further investigations of the phase diagram of the unitary Fermi gas [Shi08] as well as the measurements of the equation of state, describing its thermodynamic properties both in the unitarity regime (Ref. [Nas10] and references therein) and in the BEC-BCS crossover [Nav10]. Experiments addressing the physics in the almost fully population-imbalanced Fermi mixture - few impurities in a Fermi sea - were carried out only a few years prior to this thesis work [Sch09]. For strong interactions, the impurities and the excitations it causes to the fermionic environment form a quasiparticle termed polaron [Lan56]. This system is one of the simplest and most basic ones in condensed-matter theory, where it finds its analog in polarons formed by electrons exciting the crystal lattice the electrons are traveling through.

The list of spectacular results obtained using ultracold Fermi gases is by far not exhausted. Already the ones mentioned above, however, expose a wealth of physics that can be addressed with them. These experiments were using homo-nuclear mixtures of fermionic gases, i.e. mixtures of either ^{6}Li or ^{40}K atoms in two different spin-states, where the components necessarily have equal mass.

Mass-imbalanced Fermi-Fermi mixtures
A very important and experimentally vastly untackled question is the effect of a mass imbalance between the components on the physics of a Fermi-Fermi mixture. There are many theoretical proposals to investigate its effect both in the many- and in the few-body regime, see e.g. Ref. [Gio08] and references therein for an overview. Exotic phenomena and superfluid phases are predicted to exist, which gives rise to more complex and interesting phase diagrams compared to mass-balanced systems [Isk06, Par07, Bar08]. Such phases include the Fulde–Ferrell–Larkin–Ovchinnikov (FFLO) phase [Ful64, Lar65, Mat11], the Sarma [Sar63], and the breached-pair phase [Gub03, For05] or a stable crystalline phase [Pet07]. In the few-body regime, novel long-lived trimer and few-body cluster states are predicted to exist [Kar07, Lev09, SN13, Blu12].

Experimentally, this intriguing new physics can be addressed with a mixture of two gases of different fermionic atom species. Furthermore, such mixtures add another tuning knob to the toolbox to investigate Fermi gases. By adding species-selective optical lattice potentials, such systems allow for the investigation of Fermi-Fermi mixtures in mixed dimensions [Nis08]. Similarly, employing an optical lattice potential of unequal depth for the two species, one can tune the imbalance of the species' effective masses simply by varying the intensity of the lattice laser beam.

To our knowledge, currently there are only two combinations of different fermionic species that experimental groups are working on. These are the combinations of ^{6}Li with $^{171/173}$Yb [1] in the Gupta group at the University of Washington [Han13] and in the Takahashi group at Kyoto University [Har11] and of ^{6}Li with ^{40}K in four groups worldwide, including the Dieckmann group in Singapore (formerly Munich) [Cos10], the Zwierlein group at MIT [Wu11], the Salomon group in Paris [Sie15], and us.

[1] The applicability of interaction tuning by means of a magnetic Feshbach resonance in this mixture, however, is questionable: The resonances are predicted to be narrow, with a width $\Delta < 3\,\mathrm{mG}$, and to appear at high magnetic fields, $> 1000\,\mathrm{G}$, due to the missing hyper-fine structure of ground-state Yb [Bru12]. The demanded magnetic field stability to exploit such resonances for interaction tuning is far beyond what has been realized in experiments and, well possible, out of reach.

Status of the Li-K mixture and the FeLiKx lab in 2011
When the author of the present thesis joined the team of the FeLiKx lab, situated at the Institute for Quantum Optics and Quantum Information (IQOQI), to start my PhD work in 2011, the toolbox to investigate strongly interacting ^{6}Li-^{40}K Fermi-Fermi mixtures was just filled. Cooling and preparation procedures were developed [Tag08, Wil09, Spi10b, Spi10a, Wu11], as well as the stability of the mixture and possibilities to tune the inter-species interactions were characterized [Wil08, Spi09, Tie10, Cos10, Spi10a, Nai11]. Furthermore, there were first results on the creation of bosonic molecules from the Fermi-Fermi mixture by means of Feshbach association [Voi09, Spi10a]. And in 2010, the first measurements on a strongly interacting mass-imbalanced mixture were performed by our group [Tre11a, Tre11b], revealing a hydrodynamic behavior of the mixture during time-of-flight expansion. In early 2011, the team had just started to perform first radio-frequency spectroscopic measurements on a few fermionic ^{40}K atoms immersed in a Fermi sea of ^{6}Li atoms across an inter-species Li-K Feshbach resonance [Koh12a]. This developed into one of the two main subjects of the present thesis, the investigation of the many-body system composed of an impurity interacting with a Fermi sea.

1.3 Thesis overview

In this thesis, we discuss the experiments that we carried out since the author of the present thesis joined the team in the laboratory. These experiments followed two lines of research: the many-body system of a K impurity in a Li Fermi sea (*Chapter 3*, *4*, and *5*), and Li-K few-body physics (*Chapter 6* and *7*), which we investigate in experiments with mixtures of fermionic atoms and dimers.

Chapter 2 gives a basic introduction to important theoretical ingredients of the experimentalist's toolbox, which one needs to perform measurements such as the ones presented in this thesis.

In *Chapter 3* we report on the observation of repulsive and attractive polarons in our Li-K experiment. Such quasiparticles are the main building blocks of Fermi-liquid theory. We identify these quasiparticles by recording the energy spectrum of K impurities in a Li Fermi sea using radio-frequency spectroscopy near the 155-G Li-K Feshbach resonance. Additionally, we determine the lifetime of the repulsive polarons in our system. We find the quasiparticles to be remarkably long-lived, with a lifetime exceeding 200 μs even deep in the strongly interacting regime. Driving Rabi oscillations between the strongly interacting and a non-interacting state of the K atom, we determine the residue of the quasiparticles across the resonance.
The results are published in *Nature* **485**, 615 (2012).

In *Chapter 4* we outline our results on the investigations of the coherence of K impurities in a Li Fermi sea across an interspecies Feshbach resonance. We use a spin-echo sequence to determine the decoherence rate of the impurities from the decay of the contrast of interference fringes. Combining the spin-echo sequence with an ultrafast interaction-switching technique, using laser light, empowers us to measure decoherence deep in the strongly interacting regime:

while executing the time consuming spin rotations away from resonance (where decoherence mechanisms are slow) we switch the interactions to the desired strength of the interactions only for the time between the radio-frequency pulses. On resonance, these measurements reveal decoherence rates comparable to the inverse of the fastest timescale (the Fermi time $\tau_F = \hbar/\epsilon_F$) in our experiment.
The results are published in *Phys. Rev. Lett.* **115**, 135302 (2015).

In *Chapter 5* we report on our experiments where we probe the coherence of K impurities in the Li Fermi sea on ultrafast timescales, faster than τ_F. Our method is a combination of Ramsey interferometry with the ultrafast interaction switching technique similar to the one of the previous chapter. In the strongly interacting regime, these measurements allow us to track the dynamics of the coherence of the impurity in the Fermi sea in real time. On the repulsive/attractive side of the resonance, our measurements reveal the formation of quantum many-body states, i.e. the build-up of repulsive/attractive polarons. For resonant interactions we observe revivals of the Ramsey contrast, after a fast initial contrast decrease. The results will be published soon; A preprint is available at arXiv:1604.07423.

In *Chapter 6* we discuss our results on the investigation of the interactions of K atoms with LiK dimers in the vicinity of our Li-K Feshbach resonance. We apply radio-frequency spectroscopy to measure transition-peak shifts of K atoms when immersed in the dimer cloud. We interpret the peak-shifts as a mean-field energy shift of the K atoms in the LiK-dimer environment. We find that the interactions change their character as the resonance is being approached from weakly repulsive, far from resonance, to strongly attractive, close to resonance. This is in strong contrast to the mass-balanced case, where the atom-dimer interactions are on the same order as the atom-atom interactions and are therefore expected to remain repulsive across the entire range investigated. Furthermore, we determine the scattering rate from the widths of the transition peaks, and find a remarkable agreement with the prediction from our mean-field approach.
The results are published in *Phys. Rev. Lett.* **112**, 075302 (2014).

In *Chapter 7* we report on the investigation of the lifetime of bosonic dimers formed in our ^{6}Li-^{40}K Fermi-Fermi mixture near a Feshbach resonance. We perform lifetime measurements using both trapped, high-density as well as expanded, low-density samples after release from the trap. The combination of these measurements allows us to discriminate between the spontaneous and the collisional dimer decay. Furthermore, we determine the dimer decay due to Li-LiK collisions in a trapped atom-dimer mixture. Our measurements reveal a more than three-fold (five-fold) decrease in decay due to dimer-dimer (atom-dimer) collisions as the Feshbach resonance is approached. This observation can largely be explained by the increased fermionic character of the halo-dimers together with Pauli blocking.
This chapter contains the experimental part of a manuscript in preparation.

Finally, in *Chapter 8* the thesis concludes with an short- to medium-term outlook on research topics that will be addressed with the FeLiKx machine.

Chapter 2

Introduction to the Experimentalist's Toolbox

2.1 Scattering-formalism basics

In this section, we first summarize the basic concepts of elastic scattering of neutral atoms as it can be found in many textbooks, e.g. in Ref. [Lan81]. Staying close to Ref. [Wal10], we then consider a very simple case of scattering in a square-well potential, which we then extend in order to prepare for the discussion of scattering near a so-called narrow Feshbach resonance, as laid-out in more detail in Ref. [Pet13].

2.1.1 Scattering amplitude and cross section

The Hamiltonian of the relative motion of two particles (1 and 2) with momentum $\mathbf{p}_{1,2}$, mass $m_{1,2}$, and at location $\mathbf{r}_{1,2}$ interacting via a potential $V(\mathbf{r}_1 - \mathbf{r}_2)$ is given by

$$\mathcal{H} = \frac{\mathbf{p}^2}{2\mu} + V(\mathbf{r}). \tag{2.1}$$

Here, we used the relative momentum $\mathbf{p} = (\frac{\mu}{m_1}\mathbf{p}_1 - \frac{\mu}{m_2}\mathbf{p}_2)$, the reduced mass $\mu = m_1 m_2/(m_1 + m_2)$, the relative coordinate $\mathbf{r} = \mathbf{r}_1 - \mathbf{r}_2$, and the interaction potential $V(\mathbf{r})$ with $\lim_{\mathbf{r}\to\infty} V(\mathbf{r}) = 0$.

The Schrödinger equation for the relative motion of the particles is

$$\left(\frac{\mathbf{p}^2}{2\mu} + V(\mathbf{r})\right)\psi_k(\mathbf{r}) = E_k\psi_k(\mathbf{r}), \tag{2.2}$$

and we are now looking for solutions (eigenfunctions) with (eigen)energies $E_k = \hbar^2 k^2/(2\mu)$ that have the following form

$$\psi_k(\mathbf{r}) \propto e^{ikz} + f(k,\theta,\phi)\frac{e^{ikr}}{r} \tag{2.3}$$

far away from the scattering event (i.e. for large $|\mathbf{r}|$, where $V(\mathbf{r}) \to 0$). Such a collisional state is a superposition of two waves: The first part is the incoming plane wave, which, for simplicity, we assume to be propagating along the z axis. The second part, including the so-called scattering amplitude $f(k,\theta,\phi)$, is the scattered wave. The scattering amplitude $f(k,\theta,\phi)$ generally depends on the energy of the collision $\propto k^2$ and the polar (θ) and the azimuthal (ϕ) angles between incoming and outgoing wave.

Considering only spherically symmetric potentials, $V(\mathbf{r}) = V(r)$, the problem is simplified significantly. Expanding $\psi_k(\mathbf{r})$ in terms of its radial and angular parts $R_l(k,r)$ and $Y_{lm}(\theta,\phi)$ (the spherical harmonic functions), respectively, we obtain

$$\psi_k(\mathbf{r}) = \sum_{l=0}^{\infty} \sum_{m=-l}^{l} R_l(k,r) Y_{lm}(\theta,\phi). \tag{2.4}$$

Then, we separate $\mathbf{p}^2$ in Eq. (2.2) into a radial and angular part, $\mathbf{p}^2 \to \left(p_r^2 + \frac{\mathbf{L}^2}{r^2}\right)$ with the radial and angular momentum operator $p_r = -i\hbar\left(\frac{\partial}{\partial r} + \frac{1}{r}\right)$ and $\mathbf{L}$, respectively. Exploiting $\mathbf{L}^2 Y_{lm}(\theta,\phi) = \hbar^2 l(l+1) Y_{lm}(\theta,\phi)$ we obtain the equation for the radial part of the wavefunction

$$\left[\frac{\hbar^2}{2\mu}\left(-\frac{d^2}{dr^2} - \frac{2}{r}\frac{d}{dr} + \frac{l(l+1)}{r^2}\right) + V(r)\right] R_l(k,r) = E R_l(k,r). \tag{2.5}$$

Furthermore, for $V(\mathbf{r}) = V(r)$, the scattering problem becomes invariant under rotation around the z axis, which means that the scattering amplitude in Eq. (2.3) becomes independent of ϕ, i.e. $f(k,\theta,\phi) \to f(k,\theta)$ and $\psi_k(\mathbf{r}) = \psi_k(r,\theta,\phi) \to \psi_k(r,\theta)$. Applying these substitutions together with the partial-wave expansion of the plane wave e^{ikz} to Eq. (2.3) yields the so-called partial-wave expansion of the scattering amplitude. The details of the derivation are outlined (e.g.) in reference [Dal98] and here we only give the result,

$$f(k,\theta) = \frac{1}{2ik}\sum_{l=0}^{\infty}(2l+1)(e^{2i\delta_l} - 1)P_l(\cos\theta), \tag{2.6}$$

where δ_l denotes the scattering phase shift and P_l are the Lengendre polynomials. This expression holds for scattering of distinguishable atoms. For identical fermions or bosons the summation is only over all odd, $l = 1,3,5,\ldots$ ($p,f,h,\ldots$ waves), or even, $l = 0,2,4,\ldots$ ($s,d,g,\ldots$ waves), respectively.

In ultracold atomic gases, at ultra-low temperatures T, typically atoms can not overcome the potential barrier $E_{\mathrm{cb}} = \hbar^2 l(l+1)/[2\mu r^2] \gg k_{\mathrm{B}}T$ (k_{B} is the Boltzmann constant) in a collision and will just be reflected by it. It is often said that higher partial-wave interactions are "frozen out". Therefore, the scattering in the potential $V(r)$ will go to zero for $l > 0$ and Eq. (2.6), in this case, reduces to the s-wave ($l = 0$) scattering amplitude [Lan81]

$$f(k,\theta) = f_0(k) = \frac{e^{2i\delta(k)} - 1}{2ik} = \frac{1}{k\cot\delta(k) - ik}, \tag{2.7}$$

where $\delta(k)$ is the momentum-dependent s-wave scattering phase shift, which fully describes the scattering process.

From the scattering amplitude one can derive the (differential) cross section σ ($\frac{d\sigma}{d\Omega}$)

$$\frac{d\sigma}{d\Omega} = |f|^2 \quad \text{and} \quad \sigma = \oint_{4\pi} \frac{d\sigma}{d\Omega} d\Omega, \tag{2.8}$$

where $d\Omega$ is the infinitesimal solid angle. For the case of pure s-wave scattering of two distinguishable atoms, the cross section is given by

$$\sigma_{l=0} = 4\pi |f_0(k)|^2.$$

Another very useful expression for the cross section is provided by the optical theorem [Lan81], which relates σ to the imaginary part of the forward scattering amplitude $\mathrm{Im} f(k,0)$:

$$\sigma = \frac{4\pi}{k} \mathrm{Im} f(k,0). \tag{2.9}$$

2.1.2 Scattering in a spherical square-well potential

In this section we investigate the scattering of two particles in a spherical square-well potential at low energy ($k \to 0$). Staying close to the description in Ref. [Wal10], we give an intuition for the tuning of the interaction strength (rather s-wave scattering length a) by varying the depth of a square-well potential and, thereby, the energetic detuning of a bound state from the collisional threshold of the two colliding particles.

We can simplify Eq. (2.5) to a 1D Schrödinger equation if we substitute $R_l(r)$ by $\chi(r)/r$

$$-\chi''(r) + V(r)\chi(r) = E\chi(r). \tag{2.10}$$

Let us now assume $V(r)$ to be the following square-well potential of range r_0

$$V(r) = \begin{cases} U_{\min} = -\frac{\hbar^2 \kappa_0^2}{2\mu} & \text{for } r < r_0 \\ 0 & \text{for } r > r_0 \end{cases}, \tag{2.11}$$

where $U_{\min} = -\hbar\kappa_0^2/[2\mu]$ is the depth of the well. Outside and inside the potential well, the solution of Eq. (2.10) is $\chi_{\text{out}} \propto \sin(kr + \delta)$ and $\chi_{\text{in}} \propto \sin(\sqrt{\kappa_0^2 + k^2} r)$, respectively. The phase shift δ is obtained from the boundary condition to the solutions, continuity of the wavefunction and its derivative at $r = r_0$,

$$\chi'_{\text{out}}(r_0)/\chi_{\text{out}}(r_0) = \chi'_{\text{in}}(r_0)/\chi_{\text{in}}(r_0) \to k\cot(kr_0 + \delta) = \sqrt{\kappa_0^2 + k^2}\cot(\sqrt{\kappa_0^2 + k^2} r_0). \tag{2.12}$$

Because it is somewhat instructive, we solve Eq. (2.12) for the scattering phase shift δ and get

$$\delta = -kr_0 + \arctan\left(\frac{kr_0}{\sqrt{k^2 + \kappa_0^2}\, r_0 \cot\left(\sqrt{k^2 + \kappa_0^2}\, r_0\right)} \right).$$

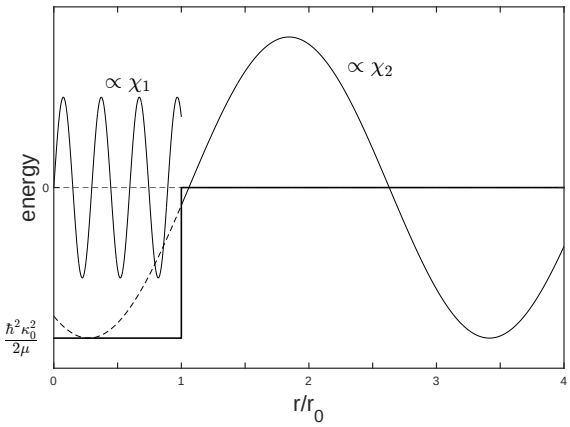

Figure 2.1: Radial wavefunction χ_1 and χ_2 within and outside the range r_0 of the potential of depth $\frac{\hbar^2\kappa_0^2}{2\mu}$. The collision energy $\frac{\hbar^2k^2}{2\mu}$ is near zero and shown as the horizontal dashed line.

The first term $-kr_0$ is just a background contribution to the phase shift, linear in k. The second term, however, shows the tunability of the phase shift by varying the potential depth $\propto \kappa_0^2$: While the collision energy at ultralow temperatures is typically small compared to the depth of the potential wells hosting many bound states, $k^2 \ll \kappa_0^2$, the contribution of the second term to δ is small. However, increasing the potential depth such that $\sqrt{\kappa_0^2+k^2}r_0 \approx (n+\frac{1}{2})\pi$, i.e. the potential turns deep enough to host another bound state, the second term can become infinitely large.

Doing some calculus we obtain the cotangent of the scattering phase shift δ

$$\cot\delta = \frac{k\tan(kr_0)\tan\left(\sqrt{\kappa_0^2+k^2}r_0\right)+\sqrt{\kappa_0^2+k^2}}{k\tan\left(\sqrt{\kappa_0^2+k^2}r_0\right)-\sqrt{\kappa_0^2+k^2}\tan(kr)}.$$

To obtain information about the momentum dependence of scattering in our model potential, we Taylor expand $k\cot\delta(k)$ for low momenta $k\to 0$ up to second order in k. This procedure is called the *effective-range expansion*. Its details, for this simple potential, are presented in Ref. [Wal10] and here we just give the result:

$$k\cot\delta = -\frac{1}{r_0-\frac{\tan(\kappa_0 r_0)}{\kappa_0}}+\frac{1}{2}k^2r_0\left(1-\frac{3\left(r_0-\frac{\tan(\kappa_0r_0)}{\kappa_0}\right)+\kappa_0^2r_0^3}{3\kappa_0^2r_0\left(r_0-\frac{\tan(\kappa_0r_0)}{\kappa_0}\right)^2}\right), \tag{2.13}$$

or, equivalently,

$$k\cot\delta(k) = -\frac{1}{a}+\frac{1}{2}k^2r_{\text{eff}}, \tag{2.14}$$

where we used the definition of the s-wave scattering length a

$$a \equiv -\lim_{k\to0}\frac{1}{k\cot\delta(k)} = r_0-\frac{\tan(\kappa_0r_0)}{\kappa_0}, \tag{2.15}$$

and introduced the effective range as

$$r_{\text{eff}} = r_0 \times \left(1 - \frac{3a + \kappa_0^2 r_0^3}{3\kappa_0^2 r_0 a^2}\right) \tag{2.16}$$

for the square-well potential.
Let us discuss Eq. (2.14) by rewriting it using $a(k) = -[k \cot \delta(k)]^{-1}$,

$$a(k) = \frac{a}{1 - \frac{1}{2} r_{\text{eff}} k^2 a}. \tag{2.17}$$

From this equation we see, that the correction of the second term in the denominator to the momentum-dependent scattering length $a(k)$ becomes important only for $k^2 \gtrsim 1/|r_{\text{eff}} a|$. Hence, the effective range r_{eff} can be viewed as a measure for the momentum dependence of scattering in a given scattering potential. Also we see from the effective range expansion, that the effect of momentum dependence on the scattering length gets stronger for larger a.

However, for large $a \gg r_0$, the effective range of the square-well potential (Eq. (2.16)) always yields

$$r_{\text{eff}} \overset{a \gg r_0}{\to} r_0.$$

That means, the model does not allow an effective range different than r_0 for diverging a. This important fact disqualifies the square-well potential as a model potential to catch the scattering physics in the vicinity of a so-called *narrow* Feshbach resonance giving rise to a strong momentum dependence of the scattering amplitude, where typically $r_{\text{eff}} \gg r_0$. To properly simulate the latter, one can extend the simple square-well potential by a delta-function barrier at $r = r_0$, as we will see in the next section.

2.1.3 Scattering in a spherical square-well potential with a delta-function barrier

Staying close to the description of Dmitry Petrov in Ref. [Pet13], we extend our previous square-well model potential by a delta-function barrier to mimic a weak coupling between the short-range and long-range parts of the wavefunction

$$V(r) = g\delta(r - r_0) + \begin{cases} U_{\text{min}} = -\frac{\hbar^2 \kappa_0^2}{2\mu} & \text{for } r < r_0 \\ 0 & \text{for } r > r_0 \end{cases}. \tag{2.18}$$

This potential is shown in Fig. 2.2. We now proceed analogously to the preceding section to extract the s-wave scattering length a and the effective range r_{eff} from the effective range expansion.

The boundary condition for the solution of the 1D Schrödinger equation, Eq. (2.10), for a square-well potential with a delta-function barrier is given by

$$k \cot(kr_0 + \delta) - \sqrt{\kappa_0^2 + k^2} \cot(\sqrt{\kappa_0^2 + k^2} r_0) = g, \tag{2.19}$$

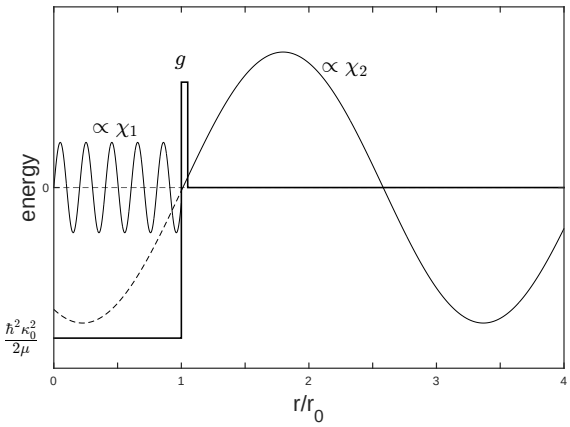

Figure 2.2: Radial wavefunctions χ_1 and χ_2 and the potential $V(r)$ with the delta-function barrier of height g. The collision energy $\frac{\hbar^2 k^2}{2\mu}$ is shown as the horizontal dashed line.

and we obtain in analogy to the previous section

$$\cot\delta(k) = \frac{\sqrt{k^2+\kappa_0^2} + \tan\left(\sqrt{k^2+\kappa_0^2}r_0\right)\left[g + k\tan\left(kr_0\right)\right]}{k\tan\left(\sqrt{k^2+\kappa_0^2}r_0\right) - \tan\left(kr_0\right)\left[g\tan\left(\sqrt{k^2+\kappa_0^2}r_0\right) + \sqrt{k^2+\kappa_0^2}\right]}. \tag{2.20}$$

The Taylor expansion of $k\cot\delta$ for small momenta k up to second order only has terms of order 0 and 2. As we compare to Eq. (2.15), the 0th-order term can be identified as $-1/a$, yielding

$$a = r_0 - \frac{1}{g + \kappa_0\cot\left(\kappa_0 r_0\right)}. \tag{2.21}$$

In Figure 2.3 we show the dependence of the scattering length a on the depth of the potential well. By varying the depth of the well we can tune the scattering length to a resonance, whenever a bound state crosses zero energy. Weakening the coupling between the short-range and the long-range part of the wavefunction by introducing the delta-function barrier $g > 0$, we narrow down the resonance. To illustrate this effect, we compare the case of scattering in a potential without barrier ($g = 0$) to the case of scattering in a potential with a barrier of height $gr_0 = 10$.

From the 2nd-order term of the expansion of Eq. (2.20) we obtain the effective range

$$r_{\text{eff}} = r_0\left(1 - \frac{3r_0\left(a\left(1+ag+ag^2r_0\right) - gr_0^2\left(1+2ag-gr_0\right)\right) + r_0^4\kappa_0^2}{3a^2\kappa_0^2 r_0^2}\right). \tag{2.22}$$

Eq. (2.21) and (2.22) agree with Eq. (2.15) and (2.16), respectively, for $g \to 0$, as to be expected.

As stated in the previous section, the effect of r_{eff} on the scattering amplitude is important when $|k^2| \geq 1/|r_{\text{eff}}a|$. For these large values of a the effective range (Eq. (2.22)) can be well

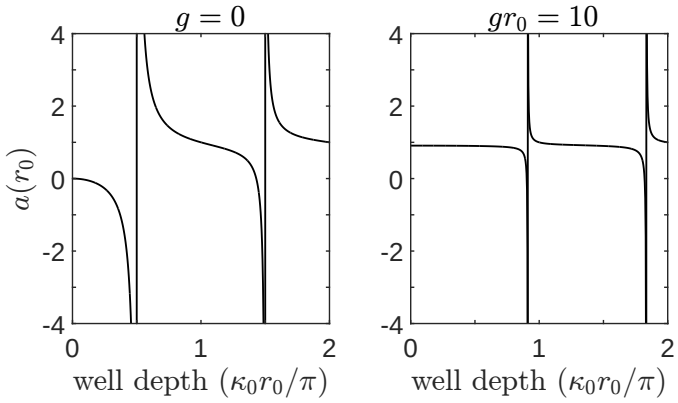

Figure 2.3: Scattering length versus depth of the scattering potential. Left: Scattering in a potential without a delta-function barrier. Right: Scattering in a potential with a delta-function barrier decoupling the short- and the long-range solutions for $r < r_0$ and $r \gg r_0$, respectively. The figure is reproduced from Ref. [Pet13].

approximated by its value for $a \to \infty$ [Pet04a]

$$r_{\text{eff}} \overset{a\to\infty}{\to} -2R^* = r_0 \times \left(1 - \frac{g\,(1+gr_0)}{\kappa_0^2 r_0}\right),$$

where we introduced the positive length parameter R^* [Pet04a]. With this, the effective-range expansion, Eq. (2.14), can be written in another common form,

$$k \cot \delta(k) = -\frac{1}{a} - R^* k^2 + \ldots.$$

2.2 Tuning interactions near a Feshbach resonance

In the field of ultracold quantum gases, Feshbach resonances [Fes58, Fes62, Fan61] are a commonly used tool to tune interactions between atoms. The concept of Feshbach resonances is discussed in detail in the review [Chi10]. Here, we only provide an intuitive picture, which is then used to introduce the quantities relevant for interaction tuning near a magnetic Feshbach resonance.

A magnetic s-wave Feshbach resonance is a resonance of the s-wave scattering length a in a collision of two atoms. This resonance appears when a magnetic field B is tuned across a resonance value B_0, where the the scattering state is strongly affected due to the presence of a bound state the colliding atoms couple to. Figure 2.4 illustrates the scenario using two molecular potential curves. Consider two atoms with a small relative momentum $k \to 0$ colliding in the energetically *open* channel $V_{\text{bg}}(r)$, $V_{\text{bg}}(r \to \infty) < E = \frac{\hbar^2 k^2}{2\mu} \to 0$. As

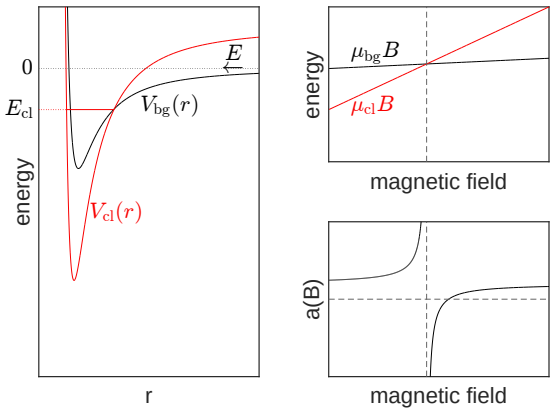

Figure 2.4: Simplified illustration of interaction tuning close to a Feshbach resonance. The left panel shows the open and the close channel as well as a bound state detuned by an energy E_{cl} far away from the collisional energy threshold at zero energy $E = 0$. The top right panel shows the shift of the collisional threshold and of the bound state in the presence of a magnetic field B. At $B = B_0$ the bound state reaches the threshold and a Feshbach resonance occurs. The lower right panel shows the behavior of the s-wave scattering a length around the Feshbach resonance at B_0 (dashed vertical line) given by Eq. (2.23).

discussed in the preceding section, V_{bg} will impose a phase shift to the solution for the scattering wavefunction, giving rise to the background scattering length a_{bg}. Varying the magnetic field B, shifts V_{bg} along the energy axis by $\mu_{bg}B$, where μ_{bg} is the magnetic moment of the atoms. The background scattering length a_{bg} remains essentially constant, as the shape of V_{bg} is hardly affected by the magnetic field.

The potential curve V_{cl} ($V_{cl}(r \to \infty) > E$) in Fig. 2.4 may correspond to the molecular potential of the two atoms in a different (spin) state representing the *closed* channel. This potential hosts a bound state at energy $E_{cl}(B) < 0$ and shifts in presence of a magnetic field B by $\mu_{cl}B$, where μ_{cl} is the magnetic moment of the closed channel. Typically μ_{cl} and μ_{bg} are not identical, instead one can define the differential magnetic moment $\delta\mu = \mu_{cl} - \mu_{bg}$. Therefore, assuming $\delta\mu > 0$, the bound state at $E_{cl}(B) < 0$ shifts towards the threshold for the two atoms with zero kinetic energy at $E = 0$ in the presence of a magnetic field B. Then, a finite coupling between the open and the closed channel will strongly affect the solution for the scattering wavefunction and, especially, it will cause a resonance for the scattering length a at $B = B_0$, where the bound state reaches the threshold (cf. Sec. 2.1). Around such a Feshbach resonance the dependence of the scattering length a on magnetic field B, as derived by Moerdijk et al. [Moe95], is given by the simple expression

$$a(B) = a_{bg}\left(1 - \frac{\Delta B}{B - B_0}\right), \tag{2.23}$$

where ΔB and B_0 are the width and the center of the Feshbach resonance.

A coupling between the open and the closed channel will, indeed, as well affect the solution of the bound-state's wavefunction and therefore its energy $E_b(B) \neq E_{cl}$ around the Feshbach

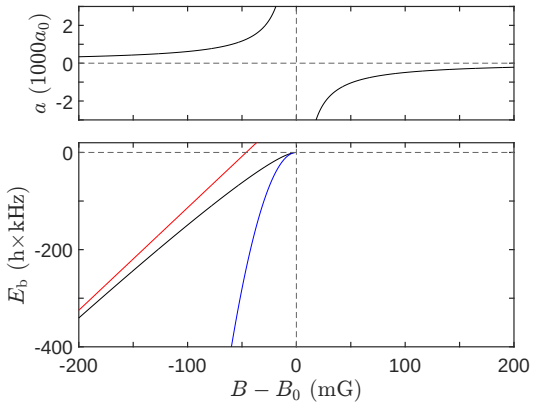

Figure 2.5: Scattering length and dimer binding energy around a Feshbach resonance with $R^* = 2650\,a_0$, $\Delta B = 0.88\,\mathrm{G}$ and $a_{\mathrm{bg}} = 63.0\,a_0$ corresponding to the parameters of the 155-G Feshbach resonance between Li$|1\rangle$ and K$|3\rangle$. The upper graph shows the scattering length according to Eq. (2.23). The lower graph shows the molecular binding energy E_b from Eq. (2.25) as the solid black line. The solid red line corresponds to the linear extrapolation of the binding energy $\propto \delta\mu$ at large detunings $R^* \gg a$. The solid blue line shows the universal binding energy $\propto a^{-2}$.

resonance. The binding energy $E_b(B)$ can be derived from the poles of the scattering amplitude, as pointed out, for example, in Ref. [Pet04a]. Let us first express the binding energy in terms of κ, such that $E_b(B) = \frac{\hbar^2\kappa^2}{2\mu}$, where μ is the reduced mass of the two colliding atoms. We then apply the expansion in Eq. (2.14) to Eq. (2.7), set $k \to i\kappa$ and require

$$\frac{1}{a} - R^*\kappa^2 - \kappa = 0, \tag{2.24}$$

with the range parameter $R^* = \hbar^2(2\mu\delta\mu a_{\mathrm{bg}}\Delta B)^{-1}$ [Pet04a]. Solving the quadratic equation, Eq. (2.24), for κ, we obtain the binding energy

$$E_b(B) = -\frac{\hbar^2}{8\mu R^{*2}}\left(\sqrt{1 + \frac{4R^*}{a(B)}} - 1\right)^2. \tag{2.25}$$

Note that in the model of Ref. [Pet04a] the two free atoms are assumed to be non-interacting other than through the short-range coupling to the closed channel and the magnetic-field dependence of the scattering length a in the above equation follows $a(B) \to a_{\mathrm{bg}}\frac{\Delta}{B-B_0}$.

In Fig. 2.5 we plot the scattering length and the binding energy of the Feshbach molecule in the vicinity of the Li$|1\rangle$-K$|3\rangle$ Feshbach resonance at $B_0 \approx 155\,\mathrm{G}$, respectively. The latter is fully characterized by $a_{\mathrm{bg}} = 63.0\,a_0$, $\Delta B = 0.88\,\mathrm{G}$, and $R^* = 2650\,a_0$ ($a_0 = 5.29 \times 10^{-11}\,\mathrm{m}$ is the Bohr radius). For small detunings $B - B_0$ from the resonance, where $a \gg R^*$, the binding energy is quadratic in $1/a$, $E_b(B) = -\frac{\hbar^2}{2\mu a(B)^2}$, shown as the blue line in the Fig. 2.5. Here, the radial wavefunction of the molecule is $\propto \exp(-\kappa r) = \exp(-r/a)$ and the mean inter-atomic separation is hence also order a, largely exceeding the range of the molecular potential [Kö06]. Due to this fact, these dimers are also called halo dimers or universal dimers and their wavefunction is essentially independent of the molecular potential details.

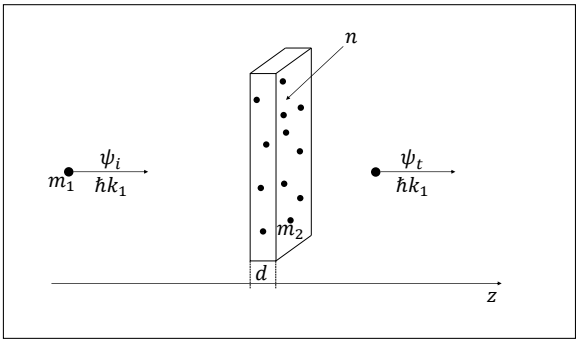

Figure 2.6: A particle of mass m_1 crosses a thin slice filled with scatterers of mass m_2. The initial plane wave ψ_i propagates along the z-axis. It crosses a slice filled with homogeneously distributed scatterers with a number density n. The transmitted wave ψ_t. The figure is adopted and modified from Ref. [Dal98].

The magnetic field region, where E_b is well approximated by $-\frac{\hbar^2}{2\mu a(B)^2}$ is called the universal region.

At large detunings, where $|R^*| \gg a(B)$, the dependence of the binding energy of the scattering length changes to $E_b(B) \approx \frac{\hbar^2}{2\mu a(B) R^*}$ and becomes linear, with a slope given by the differential magnetic moment $\delta\mu = \mu_{\mathrm{cl}} - \mu_{\mathrm{bg}}$ between the uncoupled closed channel and the background channel. This linear extrapolation of the binding energy is shown as the red solid line in Fig. 2.5. Such dimers are called closed-channel dimers. As we see from the discussion, Eq. (2.25) nicely interpolates between these two regimes.

2.3 Description of the mean-field energy

In general, the interactions of a particle with a cloud of distinguishable particles, which we will call scatterers in the following, is a many-body problem. The idea of the mean-field theory is, to reduce this many-body to a one-body problem, by treating all interactions of the particle with the scatterers as an effective interaction, or a *field* the particle is traveling through. In a regime of weak particle-scatterer interactions, i.e. for $n|a|^3 \ll 1$, where n is the density of the scatterers and a the particle-scatterer scattering length, this can be done. We want to follow the refractive-index approach of Ref. [Dal98] to derive the (mean-field) energy of a particle scattering in a dilute cloud of scatterers. This approach is based on the analogy of this physics to scattering of long-wavelength light in a dilute medium and is strongly leaned on the corresponding description in Ref. [Jac99].

Let us consider a particle of mass m_1 traveling along the z-axis with momentum $\hbar k_1$ through a thin slice of thickness d filled with scatterers. This scenario is illustrated in Fig. 2.6. The scatterers of mass m_2 shall be homogeneously distributed, described by the constant number density n. Furthermore the scatterers are distinguishable from the incident particle. For simplicity, we will assume that the scatterers remain at rest ($\hbar k_2 = 0$) and that they are sufficiently dilute, such that one can treat each collision between incident particle and any one

scatterer independently. For low momenta $\hbar k_1 \to 0$, this is usually written as the condition $n|a|^3 \ll 1$.

The incident state is a plane wave $\psi_i(z) \propto e^{ik_1 z}$. The transmitted wave is a superposition of the incident wave and of all the scattered waves (similar to Eq. (2.3)) resulting from collisions.

$$\psi_t(z) = e^{ik_1 z} + n \int_{\text{slice}} \frac{f(k)}{|\mathbf{r} - \mathbf{r}_s|} e^{ik|\mathbf{r}-\mathbf{r}_s|} e^{ik_1 \frac{(z+z_s)}{2}} d^3 r_s \tag{2.26}$$

The integration is done over the entire slice $\mathbf{r}_s = [x_s, y_s, z_s]$ and we used the relative momentum $\hbar k = \hbar \frac{\mu}{m_1} k_1$, where $\mu = m_1 m_2/(m_1 + m_2)$ is the reduced mass. This exactly solves to $\psi_t(z) = A \exp(ik_1 z)$ [Dal98], with

$$A = 1 + i\frac{2\pi n d}{k} f(k,0) \approx e^{i\frac{2\pi n d}{k} f(k,0)}, \tag{2.27}$$

where $f(k,0)$ is the forward-scattering amplitude (Eq. (2.6)) and where the latter is correct to first order in d.

It is very insightful to separate the forward-scattering amplitude into its real part, $\mathrm{Re} f(k,0)$, and imaginary part, $\mathrm{Im} f(k,0)$. Furthermore using the optical theorem (Eq. (2.9)), $\sigma = [4\pi/k]\mathrm{Im} f(k,0)$, we obtain for the transmitted wave

$$\psi_t(z) = e^{-\frac{1}{2} n d \sigma} e^{i\frac{2\pi n d}{k} \mathrm{Re} f(k,0)} \psi_i(z). \tag{2.28}$$

Hence, the transmitted wave $\psi_t(z)$ has a decreased amplitude and a shifted phase with respect to the incident wave $\psi_i(z)$, described by the imaginary and the real part of the forward-scattering amplitude, respectively.

We can interpret these observations in a rather straight-forward way. The forward-propagating wave amplitude is attenuated by elastic collisions with cross section σ causing the incident wave to be scattered out of the forward direction. The phase shift, on the other hand, arises from the momentum of the particle being changed by $\delta k_1 = \frac{2\pi n}{k} \mathrm{Re} f(k,0)$ inside the slice. And the change of kinetic energy $\frac{2\pi\hbar^2 n}{\mu} \mathrm{Re} f(k,0)$ of the particle inside the slice can then be related to a mean-field potential

$$U = -\frac{2\pi\hbar^2 n}{\mu} \mathrm{Re} f(k,0), \tag{2.29}$$

that the scatterers pose for the particle. To summarize, while the particle is in the slice filled with scatterers, its energy is changed $\propto n \mathrm{Re} f(k,0)$ and its amplitude of forward propagation is diminished $\propto \exp(n\sigma)$ after it passed the slice. In *Chapter* 6, we use these findings to interpret our experimental results on the atom-dimer interactions obtained by radio-frequency spectroscopy. Since these atom-dimer interactions have strong contributions from higher partial waves, $l > 0$, we stress explicitly the dependence of the mean-field energy and elastic scattering cross section on the forward-scattering amplitude including all partial waves.

However, let us reduce these findings to the $\hbar k \to 0$-regime of pure s-wave scattering to simplify the following discussion. Here, the s-wave scattering amplitude is $f(k,0) \to (-a^{-1} -$

$ik)^{-1}$, and Eq. (2.29) reduces to the well-known expression $U_s = \frac{2\pi\hbar^2 n}{\mu}a$. In the following we discuss two interesting limits within the regime, where $n|a|^3 \ll 1$ is fulfilled: strong ($ka \approx 1$) scattering in a dilute gas ($n^{1/3} \ll k$) and weak ($ka \ll 1$) scattering in a dense gas ($n^{1/3} \gg k$).

Particles traversing a dilute gas ($n^{1/3} \ll k$) impinge one scatterer at a time. If one was to calculate a macroscopic cross section of the entire medium it was just the single-scatterer cross section times the number of scatterers. In such media, under strong-scattering conditions, i.e. $ka \approx 1$, the total amount of wave amplitude scattered sideways can be large. The described situation is similar to visible light entering the atmosphere, which is described by Rayleigh scattering [Jac99]. Here, electromagnetic waves scatter from the electric dipoles of molecules in the atmosphere and the scattering cross section is $\propto k^4$. Therefore, short-wavelength light is scattered most and the sky appears blue.

Considering weak scattering ($ka \ll 1$) in a dense medium, where $n^{1/3} \gg k$, the scattering is collective. To describe this our approach from above would need to be adapted by allowing the incident particle to scatter from several scatterers and essentially simultaneously. But, we can learn already from the analog of light scattering in a dense medium, such as visible light scattering in a dense gas or in water. Here, the light dominantly propagates into the forward direction, which can be understood from the interference of scattered waves originating from nearby scatterers, which is dominantly destructive (constructive) into the sideways (forward) direction [Hec02]. Interestingly, a higher density of the medium increases the suppression of side-ways scattering in the regime of a long-wavelength particle probing a dense medium.

We have now discussed a few examples of a particle scattering in a medium in the weakly interacting regime, where the mean-field approach is valid. In several Chapters of this thesis we go beyond this mean-field regime. In *Chapter* 3 we present measurements of the interaction energy of particles in a dense Fermi gas in the strongly interacting regime. In the strongly interacting regime the particle essentially interacts with the entire Fermi sea at once and the Fermi sea can be excited in terms of particle-hole excitations. The particle including the excitations propagates as a quasiparticle termed polaron through the Fermi sea, dramatically different from the physics described in this chapter. The coherence of these quasiparticles is discussed in *Chapter* 4 where we also identify its collisional properties.

2.4 Elastic atom-dimer interactions near a Feshbach resonance

In the previous sections we have introduced the formalism of ultracold scattering of atoms as well as the tunability of the interactions between atoms in trapped atomic clouds by means of a magnetic Feshbach resonance. We have shown that, on the repulsive side of a Feshbach resonance, there always exists an energetically lower-lying dimer state, into which an interacting atom-atom mixture can decay. This decay, which will be discussed in *Chapter* 3 for the case of a Li-K mixture, limits the lifetime of the mixture. Experimenting with an repulsively interacting Fermi-Fermi mixture on timescales on the order of or larger than this lifetime, knowledge of the interactions of the dimers, i.e. the decay products, with the atoms as well as between the dimers is crucial. While the inelastic processes will be discussed in

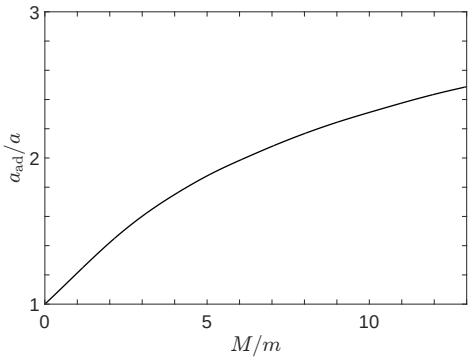

Figure 2.7: Atom-dimer s-wave scattering length a_{ad} versus mass imbalance of the dimer components for $a \gg r_0$. Replotted data from Ref. [Pet03].

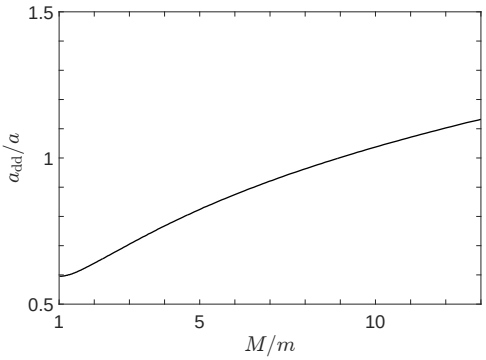

Figure 2.8: Dimer-dimer s-wave scattering length a_{dd} versus mass imbalance of the dimer components for $a \gg r_0$. Replotted data from Ref. [Pet05].

detail in *Chapter* 7, the purpose of this section is to summarize the elastic interactions for the case of a Fermi-Fermi mixture, which are partially also discussed in *Chapter* 6.

For a theoretical description of atom-dimer (dimer-dimer) scattering in fermionic mixtures, one has to solve a three-body (four-body) problem. This can be rather easily done for the case of a scattering length a largely exceeding the range of the interatomic potential, $a \gg r_0$. Here, the radial wavefunction of the weakly bound, open-channel (Feshbach) dimer state is given by [KÖ06]

$$\phi(r) = \frac{1}{\sqrt{2\pi a}} \exp\left(-\frac{r}{a}\right) \quad \text{for} \quad r \gg r_0. \tag{2.30}$$

This is the so-called "halo-dimer" state, where the wavefunction of the dimer is characterized purely by the atom-atom s-wave scattering length a. The spatial extend of the halo-dimer is extremely large, on the order of a. In this regime, the three- and four-body problems of elastic atom-dimer and dimer-dimer collisions, respectively, are exactly solvable [Pet04b] and the amplitudes of elastic s-wave interactions between atoms and dimers and among dimers depend solely on a.

The elastic atom-dimer interactions in the s-wave channel are characterized by an atom-dimer scattering length a_{ad}. The details of its calculation are presented in Ref. [Pet03]. In Figure 2.7, we show the behavior of a_{ad} as a function of the mass imbalance M/m for $M > m$, re-plotted from Ref. [Pet03]. The s-wave atom-dimer interactions are always repulsive and become stronger for an increasing mass imbalance. Whereas in homo-nuclear Fermi mixtures $a_{\mathrm{ad}} \approx 1.2\,a$, it reaches approximately $2\,a$ for $m_{\mathrm{K}}/m_{\mathrm{Li}}$.

Analogously, the elastic s-wave dimer-dimer interaction are characterized by the dimer-dimer scattering length a_{dd}. The details of its derivation are given in Refs. [Pet04b] and [Pet05]. In Figure 2.8 we re-plot the results from these calculations published in Ref. [Pet05]. Similarly to atom-dimer scattering, the s-wave interaction is always repulsive and strengthens with mass imbalance, being $a_{\mathrm{dd}} = 0.6\,a$ for dimers composed of equal mass fermions and $0.9\,a$ for the case of the Li-K mixture. Without going into detail, we mention, that the presented

theoretical results for a_{ad}, and a_{dd} were all obtained in the $a/R^* = 0$ limit, i.e. for the wide-resonance case. The effect of a finite R^* on the atom-dimer and dimer scattering process is discussed in Ref. [Lev11]. A considerable value for R^* decreases the open-channel fraction of the dimer wave function and effectively weakens the atom-dimer and dimer-dimer interactions, yielding lower values for a_{ad}, and a_{dd}, respectively.

The discussed $l = 0$ contribution to the atom-dimer interaction is, however, not at all sufficient to describe the scattering process. Under typical experimental conditions, also when atom-atom scattering for $l > 0$ is suppressed, higher partial-wave contributions to atom-dimer scattering can be strong and even dominate the interactions. This important fact is the subject of the publication presented in *Chapter* 6. A very complete summary for atom-dimer interactions, especially for our Li-K Fermi-Fermi mixture, is given in reference [Lev11]. Here, we recall its most important findings, and to prepare the ground for *Chapter* 6, we give an intuition for the angular-momentum dependence in atom-dimer collisions.

Let us consider a heavy-heavy-light three-fermion system. While for large separations r, atom and dimer can be described by separate wavefunctions, in an atom-dimer collision (i.e. for $r \to 0$) we have to solve the three-body Schrödinger equation to retrieve the (three-body) wavefunction describing the system. A good qualitative understanding, however, can already be gained from considering the problem in the Born-Oppenheimer approximation. Applying the latter, we can write the wavefunction as the product of a wavefunction $\phi(r)$ describing the two heavy fermions of mass M separated by r and a light-atom (mass m) wavefunction ψ, and assume that the latter adiabatically adjusts itself to the distance r between the heavy fermions. The light-fermion wavefunction ψ is a superposition of the wavefunction of the light fermion bound to either of the heavy ones, ψ_1 and ψ_2, respectively. This superposition can be symmetric or antisymmetric, $\psi = \psi_1 \pm \psi_2$, as depicted in Fig. 2.9. For $r \to 0$, the curvature of the anti-symmetric light atom wavefunction $\psi_1 - \psi_2$ ($\psi_1 + \psi_2$) is increased (decreased) with respect to the far separated system, giving rise to an increased (decreased) energy of the respective state. In this picture, the symmetry of the collision of the atom with the dimer (say $l = 0$ or 1, i.e. s or p wave) is projected onto the two-heavy-atom wavefunction.

Finally, the total wavefunction $\propto \psi\phi(r)$ must be restricted to be antisymmetric with respect to the permutation of the two heavy fermions. This gives rise to an angular-momentum dependent interaction: If the atom-dimer collision occurs in an even (odd) partial wave, i.e. $s, d, \dots$ ($p, f, \dots$), the heavy-fermion wavefunction is symmetric (anti-symmetric) and the light-atom is forced into the anti-symmetric (symmetric) state. In the symmetric (anti-symmetric) state the potential U_+ (U_-) arising from the light-fermion exchange is positive (negative), giving rise to a repulsive (an attractive) interaction.

The exact quantitative analysis [Lev11] shows that $U_+ \propto -1/[mr^2]$. For $l > 0$, this attractive exchange potential competes with the centrifugal barrier $U_{\mathrm{cb}} \propto l(l+1)\hbar^2/Mr^2$. With increasing mass imbalance M/m the net attraction U_-/U_{cb} increases and is strongest in the partial wave $l = 1$. In Fig. 2.10 we show the p-wave atom-dimer potentials $V_{l=1} = U_- + U_{\mathrm{cb}}$ for the mass imbalance of the Li-K system ($M/m = 6.7$) as well as for larger mass imbalances. For a mass ratio $M/m \to 8.2$ the potential $V_{l=1}$ develops a well deep enough to host a three-body bound state [Kar07], and when $M/m \geq 13.6$, the potential becomes overall

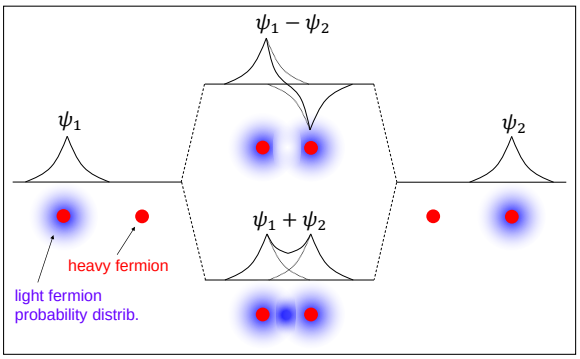

Figure 2.9: Scenario of an atom-dimer collision. When atom and dimer are separated, $r \to \infty$, the light-atom wavefunction is ψ_1 or ψ_2, respectively, corresponding to the light atom being bound to either of the heavy ones. As atom and dimer approach each other, the wavefunction is the superposition $\psi = \psi_1 \pm \psi_2$, that can be symmetric or anti-symmetric. Depending on the symmetry of the collision, the light atom is forced in either of the states at lowered $(\psi_1 + \psi_2)$ or increased $(\psi_1 - \psi_2)$ energy, respectively.

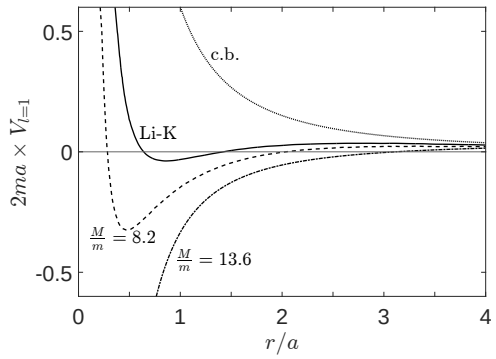

Figure 2.10: Atom-dimer p-wave potentials for various mass imbalances and for $R^* \ll a$. The dotted line is the p-wave centrifugal barrier $\propto m^{-2}$. The solid, dashed, and dashed-dotted lines correspond to the p-wave potentials for the Li-K system ($M/m = 6.7$), $M/m = 8.2$, and $M/m = 13.6$, respectively. The data is collected and replotted from Ref. [Lev11].

attractive $\propto -r^{-2}$, giving rise to an infinite number of bound states leading to the Efimov effect [Efi70]. All the curves shown correspond to $R^* = 0$. A large R^* effectively weakens the atom-dimer exchange interactions and, therefore, has a similar effect as a decreased mass ratio [Lev11].

In Fig. 2.11 we show the phase shifts as a function of collision energy in units of dimer binding energy $E_{\rm coll}/E_{\rm b}$ in the three lowest partial waves for the Li-K system, where $M/m \approx 6.7$, as the solid lines. For collision energies $E_{\rm coll} \approx 0.2E_{\rm b}$ the p-wave attraction dominates the scattering process, such that summing over all partial waves the net interactions are attractive. Also for mass-balanced systems, $M = m$, the contribution of p-wave interaction to the total scattering cross section is not negligible, as the phase shifts for the mass-balanced case show (dashed lines in Fig. 2.11). The collisional phase shifts acquired in the p-wave channel are still on the order of $\sim 10\%$ of the s-wave phase shift in the vicinity of a Feshbach

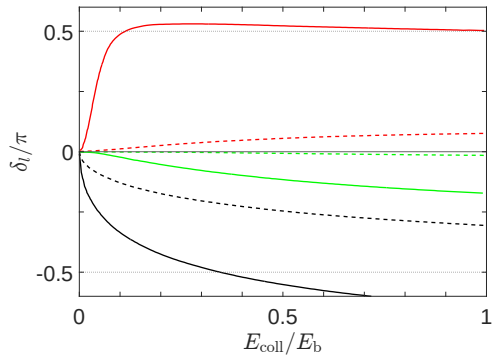

Figure 2.11: The phase shifts acquired in an atom-dimer collision in the three lowest partial waves for $R^* = 0$. The black, red, and green lines correspond to the phase shift in an s-, p-, and d-wave collision, respectively. Solid lines are for the Li-K mass imbalance, whereas the dashed lines are for the mass-balanced case. The data is replotted from Ref. [Lev11].

resonance, where the collision energy E_{coll} can become a significant fraction of the dimer binding energy E_{b}.

2.5 Basics of radio-frequency spectroscopy in our Li-K system

In every publication presented in this thesis we use radio-frequency (rf) pulses to manipulate the hyper-fine states of either the lithium-6 or potassium-40 atoms, respectively. We will therefore use this section to review the most essential findings from treating the problem of a two-level system coupling to an rf photon. This will allow us to introduce the method of rf spectroscopy, a tool used every day in our lab to, e.g., determine magnetic fields or interaction shifts of transition lines. We will conclude this section giving an example for a measurement of a mean-field energy shift of K atoms immersed in a Li cloud.

In Figures 2.12 and 2.13 we show the hyper-fine manifolds of the ground states of ^{6}Li and ^{40}K, respectively, for magnetic fields B up to 200 G. We label these states counting them with rising energy. The Feshbach resonance we exploit for interaction tuning is located at $B_0 \approx 155$ G and occurs between potassium in the third-to-lowest state K$|3\rangle$ and lithium in its lowest hyper-fine state Li$|1\rangle$ (red in Fig. 2.13 and 2.12, respectively). The neighboring hyper-fine states, i.e. Li$|2\rangle$ and K$|2\rangle$ and K$|4\rangle$ (blue in Fig. 2.13 and 2.12, respectively) are separated by $E/h \approx 68$ MHz from Li$|1\rangle$ and $E/h \approx 39$ MHz and $E/h \approx 41$ MHz from K$|3\rangle$, respectively. Note that these radio frequencies correspond to wavelength of a few meters and the momentum transferred to an atom in a absorption process is negligible. Thus, these rf transitions can be interpreted as pure spin-flip operations.

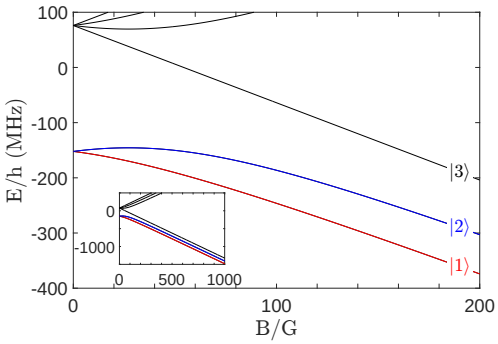

Figure 2.12: Hyper-fine structure of the ground-state manifolds of Li versus magnetic field B. The inset shows the hyperfine structure of the ^{6}Li over a larger magnetic field range.

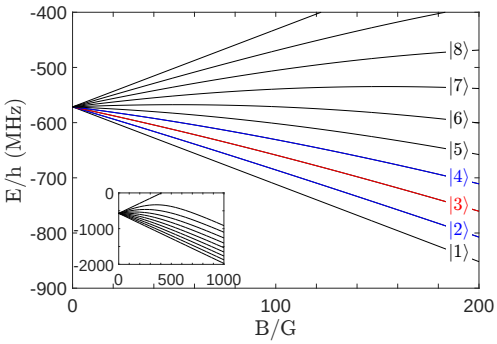

Figure 2.13: Hyper-fine structure of the $F = 9/2$ manifold of the ^{40}K ground-state versus magnetic field B. The inset extends over a larger magnetic field range.

2.5.1 Rabi-flopping: two-level system without interactions

The setup to discuss the so-called *Rabi problem* is illustrated in Figure 2.14(a). In our Li-K system, such a two-level system is realized, e.g., by identifying the "ground state" $|0\rangle$ as the K atom residing in state K$|2\rangle$, and the "excited state" $|1\rangle$ as the K atom residing in K$|3\rangle$. We can couple these states by rf photons of a frequency $\nu \approx \nu_0$, near-resonant to the hyper-fine splitting $h\nu_0$ between the states K$|2\rangle$ and K$|3\rangle$ at a magnetic field B, and off-resonant to all other neighboring hyper-fine states.

Measuring all energies relative to the energy of the $|0\rangle$ state, the Hamiltonian, describing the system, is given by

$$H = H_0 + V_{\mathrm{rf}} = \begin{pmatrix} h\nu_0 & 0 \\ 0 & 0 \end{pmatrix} + \frac{\hbar\Omega}{2} \begin{pmatrix} 0 & e^{-i2\pi\nu t} \\ e^{i2\pi\nu t} & 0 \end{pmatrix}, \tag{2.31}$$

where H_0 describes the unperturbed atom, V_{rf} is the atom-light interaction term. Furthermore, $\Omega = \frac{\mathbf{d}_{01}\cdot\mathbf{E}}{\hbar}$ is the Rabi frequency, where $\mathbf{d}_{01}$ is the magnetic dipole matrix element and $\mathbf{E}$ is the electric field vector. Then we look for the solution of the Schrödinger equation $i\hbar\frac{d}{dt}\psi = H\psi$ that has the form $\psi(t) = c_0(t)|0\rangle + c_1(t)e^{i2\pi\nu t}|1\rangle$. Using the rotating-wave approximation (assuming $\delta = \nu - \nu_0 \ll \nu$ and $\Omega \ll \nu$) we end up with

$$i\hbar\frac{d}{dt}\begin{pmatrix} c_1 \\ c_0 \end{pmatrix} = \hbar \begin{pmatrix} 2\pi\delta & \frac{\Omega}{2}e^{-i2\pi\delta t} \\ \frac{\Omega}{2}e^{i2\pi\delta t} & 0 \end{pmatrix} \begin{pmatrix} c_1 \\ c_0 \end{pmatrix}. \tag{2.32}$$

It is very interesting to discuss the solution of these coupled equations for the case, where one state is initially unoccupied. The occupation probabilities of the states $|1\rangle$ and $|0\rangle$ are given by $|c_1(t)|^2$ and $|c_0(t)|^2$, respectively. Assuming that an atomic sample was initially, at $t = 0$, prepared in the $|0\rangle$ state, we can derive the occupation of the $|1\rangle$ state versus time t,

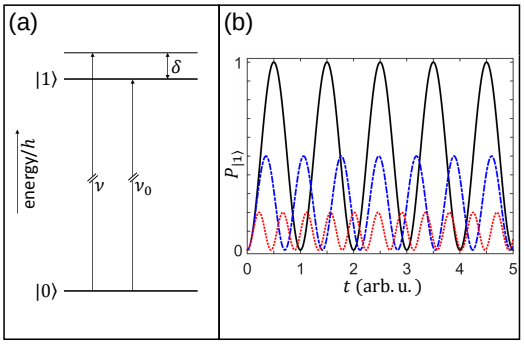

Figure 2.14: Two-level system coupling to radio-frequency photons of frequency ν. (a) Illustration of the ground and excited states $|0\rangle$ and $|1\rangle$, respectively, separated by an energy $h\nu_0$ that are coupled by radio-frequency photons of frequency ν with a detuning $\delta = \nu - \nu_0$. (b) Oscillations of the excited-state population in the presence of coupling of the $|0\rangle$ and $|1\rangle$ by a radio-frequency $\nu = \nu_0 + \delta$ for $\delta = 0$, $\Omega/[2\pi]$, and $2\Omega/[2\pi]$ represented by the solid black, dashed blue, and dotted red line, respectively.

during which the sample is in a field of radio-frequency photons,

$$P_{|1\rangle}(t) = |c_1(t)|^2 = \frac{\Omega^2}{\Omega_{\text{eff}}^2} \times \sin^2\left(\frac{\Omega_{\text{eff}}}{2}t\right), \tag{2.33}$$

where $\Omega_{\text{eff}} = \sqrt{\Omega^2 + (2\pi\delta)^2}$.

In Figure 2.14(b) we show examples of these oscillations of the excited-state population $P_{|1\rangle}(t)$ for three different detunings δ, as described by Eq. (2.33). These oscillations occur at a frequency, the effective Rabi frequency Ω_{eff}, which has the lowest value for $\delta = 0$, where $\Omega_{\text{eff}} = \Omega$. A full population transfer from the $|0\rangle$ to the $|1\rangle$ state can only be accomplished for $\delta = 0$. The shortest possible resonant, $\delta = 0$, pulse flipping the entire (half of the) population of the atoms from one state to the other has a duration of π/Ω ($\pi/[2\Omega]$) and is called a π ($\pi/2$) pulse.

We typically determine our magnetic field by measuring the Zeeman energy $\hbar\omega$ between two hyperfine states at a high magnetic field by rf spectroscopy and using the Breit-Rabi formula [Bre31]. We prepare a sample of several thousand K$|2\rangle$ atoms at a magnetic field B and apply an rf pulse with a given intensity and a duration corresponding to less or equal than the π-pulse duration. We perform this experiment for several radio frequencies ν around the hyper-fine transition frequency ν_0 to the state K$|3\rangle$ to determine the frequency of maximum transfer. Applying the Breit-Rabi formula [Bre31] we then determine the magnetic field corresponding to the measured hyper-fine splitting $h\nu_0$ between the states K$|2\rangle$ and K$|3\rangle$.

2.5.2 Two-level system with one (weakly) interacting state - measuring the mean-field energy

In this subsection, we extend the two-level system of the previous subsection by allowing the state $|1\rangle$ to be an interacting state. We consider only interactions between K$|3\rangle$ atoms and

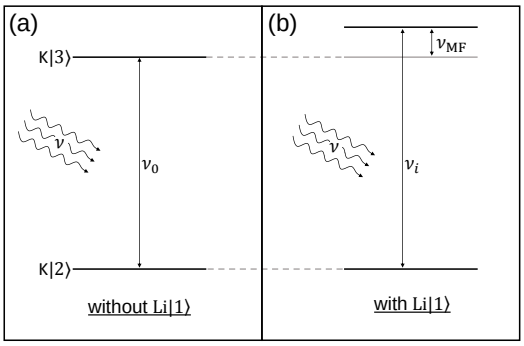

Figure 2.15: Sketch of the interaction-shift of the excited state $|1\rangle$. (a) In the absence of interactions, with zero population of the Li$|1\rangle$ state, the K$|2\rangle$ and K$|3\rangle$ levels are separated by an energy $h\nu_0$ corresponding to the Zeeman splitting between these two states. (b) When the K atoms reside in a Li$|1\rangle$ environment, which causes a mean field for the interacting K$|3\rangle$ atoms, the excited state energy shifts. Comparing the transition frequencies ν_i to ν_0, we can determine the mean-field energy $E_\mathrm{MF} = h\nu_\mathrm{MF} = h(\nu_\mathrm{i} - \nu_0)$

co-trapped Li$|1\rangle$ atoms. The Li$|1\rangle$-K$|3\rangle$ interactions can be tuned by means of the Feshbach resonance at a magnetic field of about 155 G, as introduced earlier.

In the magnetic field region of at least ± 2 G around the center of this Feshbach resonance, interactions in all neighboring spins-state combinations are very weak, described by respective small background scattering lengths. For the combinations of Li$|1\rangle$-K$|2\rangle$, Li$|1\rangle$-K$|4\rangle$, and Li$|2\rangle$-K$|3\rangle$ these background scattering lengths a_bg are all around $65\,a_0$ [Nai11]. This property of the Li-K system is turns out to be extremely valuable, as it is one of these states that we use as the initial (final) state from (to) which we transfer, when performing spectroscopy, and it allows us to interpret any changes in the spectral response, as we tune the magnetic field near the Li$|1\rangle$-K$|3\rangle$ Feshbach resonance, to arise from Li$|1\rangle$-K$|3\rangle$ interactions. This is in strong contrast to, e.g., the widely used Li spin-state mixture, where the high-field Feshbach resonances between any combination of the lowest three spin states strongly overlap and interactions are generally strong ($> 1000\,a_0$) [Zür13, Chi10].

In our lab, we frequently use rf spectroscopy to measure interaction shifts of hyperfine transitions. Therefore, we give a few more details about how we perform such measurements and what needs to be considered, when analyzing and interpreting spectroscopy data. We do this by considering an example under typical experimental conditions. To simplify the discussion, we assume a very low temperature and a rather large detuning from resonance. Here, the forward scattering amplitude $\mathrm{Re}\,f(k)$ is well approximated by $-a$ and the interactions are treated within mean-field theory.

For the case of a weakly interacting Li$|1\rangle$-K$|3\rangle$ mixture ($|a^3 n_\mathrm{Li}| \ll 1$), the energy of a K$|3\rangle$ atom propagating through a Li$|1\rangle$ atom cloud shifts by $E_\mathrm{MF} = \frac{2\pi\hbar^2 n_\mathrm{Li}}{\mu} a$ (cf. Eq. (2.29)). Here, n_Li is the Li number density and $\mu = m_\mathrm{Li} m_\mathrm{K}/[m_\mathrm{Li} + m_\mathrm{K}]$ is the reduced mass. The radio frequency for driving transitions from K$|2\rangle$ to K$|3\rangle$ (or vice versa) will then be shifted by E_MF/h (h is Planck's constant). This is illustrated in Figure 2.15. Generally, comparing the transition frequencies in the absence (e.g. when Li is in the state Li$|2\rangle$), Fig. 2.15(a), and presence, Fig. 2.15(b) of interactions, ν_0 and ν_i, respectively, one directly retrieves the

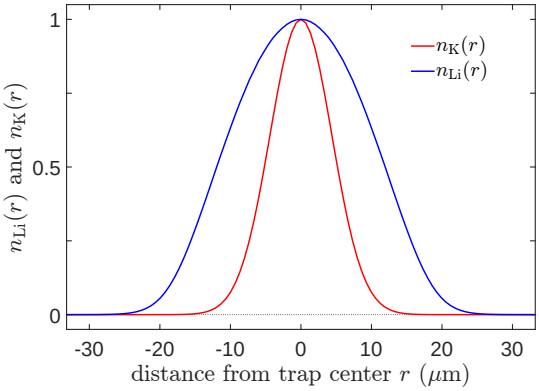

Figure 2.16: Normalized lithium and potassium in-trap number densities as a function of the radial distance r from the trap center. We show the number densities of a central cut, perpendicular to the axial direction of our cigar-shaped atom clouds. To obtain the data, we assumed 10^4 K atoms in thermal equilibrium with a degenerate gas of $3 \cdot 10^5$ Li atoms at a temperature $T = 400\,\mathrm{nK}$ in an optical dipole trap. The optical confinement is characterized by the radial (r) and axial (a) trap frequencies of Li and K, $\nu_{\mathrm{Li},r} = 600\,\mathrm{Hz}$, $\nu_{\mathrm{Li},a} = 75\,\mathrm{Hz}$, $\nu_{\mathrm{K},r} = 330\,\mathrm{Hz}$, and $\nu_{\mathrm{K},a} = 42\,\mathrm{Hz}$, respectively.

mean-field energy shift as $E_{\mathrm{MF}} = h\nu_{\mathrm{MF}} = h(\nu_i - \nu_0)$.

In the experiment, we perform rf spectroscopy of an ensemble of K atoms, whose number-density distribution in the trap is described by $n_{\mathrm{K}}(\mathbf{r})$. These K atoms are trapped together with a Li cloud (number-density distribution $n_{\mathrm{Li}}(\mathbf{r})$) in an optical dipole trap. This means that the K atoms experience an inhomogeneous Li number distribution, $n_{\mathrm{Li}} \to n_{\mathrm{Li}}(\mathbf{r})$ depending on their position $\mathbf{r}$ in the trap. In Figure 2.16 we show the K (red solid line) and Li (blue solid line) number densities of a central cut, perpendicular to the axial direction of a cigar-shaped cloud, as a function of the distance r from the trap center and for typical experimental conditions[1].

Applying a hypothetical rf π pulse of infinite duration at a frequency ν, the rf response, i.e. the fraction of K atoms transferred into the K$|3\rangle$ state, is given by

$$A(\nu) \propto \int_{\mathrm{trap}} n_{\mathrm{K}}(\mathbf{r})\delta\left(\nu - \nu_0 - \nu_{\mathrm{MF}}\right) d^3r = \int_{\mathrm{trap}} n_{\mathrm{K}}(\mathbf{r})\delta\left(\nu - \nu_0 - \frac{\hbar n_{\mathrm{Li}}(\mathbf{r})}{\mu}a\right) d^3r. \qquad 2.34$$

This response is shown as the red crosses in Figure 2.17 for the same conditions as in Fig. 2.16 and for $a \approx -1000\,a_0$. The low-frequency onset at approximately $-2.3\,\mathrm{kHz}$ originates from atoms in the trap center at high Li density. The spectral tail reaches up to $\nu - \nu_0 = 0$ and stems from atoms in the wings of the thermal distribution of the K atoms. From the spectral response we can derive the average mean-field shift $\bar{\nu}_{\mathrm{MF}} = \int n_{\mathrm{K}}(\mathbf{r})\frac{\hbar n_{\mathrm{Li}}(\mathbf{r})}{\mu}a\,d^3r$, which corresponds to the first moment of $A(\nu)$. For our example the average mean-field shift is $\bar{\nu}_{\mathrm{MF}} = 1.79\,\mathrm{kHz}$, shown as the vertical black dashed line in Fig. 2.17.

[1] We assumed a thermal distribution of 10^4 K atoms at a temperature $T = 400\,\mathrm{nK}$ mixed and thermalized with a degenerate Li gas of $3 \cdot 10^5$ atoms confined in an optical trap, characterized by radial (r) and axial (a) trap frequencies of $\nu_{\mathrm{Li},r} = 600\,\mathrm{Hz}$, $\nu_{\mathrm{Li},a} = 75\,\mathrm{Hz}$, $\nu_{\mathrm{K},r} = 330\,\mathrm{Hz}$, and $\nu_{\mathrm{K},a} = 42\,\mathrm{Hz}$, respectively.

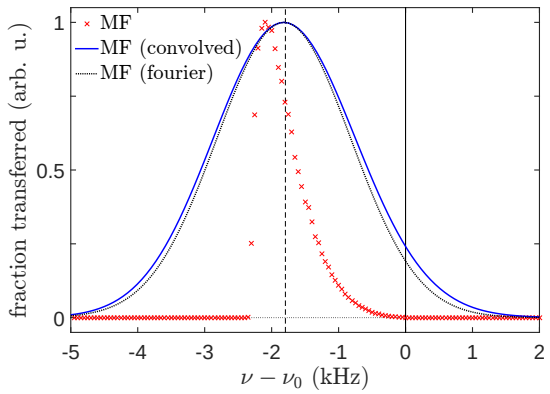

Figure 2.17: Calculated spectral response in our system in a regime, where the mean-field approximation is valid. The red crosses correspond to the spectral response of our system to the application of an infinitely long rf pulse, whereas the blue solid line is obtained using an rf pulse of 1 kHz Gaussian width. Both spectra have the same first moment of about $\bar{\nu}_{\mathrm{MF}} = \nu - \nu_0 = 1.79\,\mathrm{kHz}$ (black dashed vertical line). The black dotted line corresponds to a Gaussian (1 kHz width) centered at $\bar{\nu}_{\mathrm{MF}}$.

In a real experiment, the rf-pulse duration is finite. This causes a Fourier broadening of the spectral response, which is inversely proportional to the duration. Indeed, an rf pulse with a Gaussian intensity envelope of $1/\sqrt{e}$ duration τ (full-width-half-maximum (FWHM) duration $\tau_{1/2}$) translates into a Gaussian shaped response with a width of $\Delta\nu = \frac{1}{2\pi\tau}$ (FWHM of $\Delta\nu_{1/2} = \frac{2\ln 2}{\pi\tau_{1/2}}$) in the frequency domain. Applying an rf pulse of a finite duration, we therefore retrieve a spectrum $A_{\mathrm{G}}(\nu)$ that is the convolution of the spectral response $A(\nu)$ (Eq. (2.34)) with such a Gaussian,

$$A_{\mathrm{G}}(\nu) \propto \int A(\nu') e^{-\frac{1}{2}\frac{(\nu-\nu')^2}{\Delta\nu^2}} d\nu'. \tag{2.35}$$

The spectrum $A_{\mathrm{G}}(\nu)$ obtained with an rf pulse of duration $\tau = 160\,\mu\mathrm{s}$ is plotted in Figure 2.17 as the blue solid line. It is centered at the frequency $\bar{\nu}_{\mathrm{MF}}$ and has a width only slightly larger than the Fourier width, in this case 1 kHz. This can be seen by comparing $A_{\mathrm{G}}(\nu)$ to the spectral shape of the 160-μs rf pulse centered at $\bar{\nu}_{\mathrm{MF}}$, shown as the black dotted line in Fig. 2.17. Only for the case that the Fourier width of the rf pulse, $\Delta\nu$, is much larger than the width of the spectral response $A(\nu)$, one can determine the average mean-field energy shift in our inhomogeneous Li-K system by observing the shift of the peak-transfer frequency.

Without getting into detail, we mention, that there are further effects leading to broadening of spectral lines, besides broadening due to inhomogeneity and Fourier broadening arising from the finite-length of the rf-pulse. The interacting state can have a finite lifetime causing Lorentzian broadening of the transition line due to several processes: Most prominently, these are decay of the interactring state into a third (other hyper-fine or molecular) state at a rate $1/\tau_{\mathrm{d}}$ or momentum-changing scattering of K atoms with the Li environment at a rate $1/\tau_{\mathrm{s}}$. These processes essentially gives rise to an "effective lifetime" $\tau = (1/\tau_{\mathrm{s}} + 1/\tau_{\mathrm{d}})^{-1}$ of the interacting state, causing Lorentzian broadening of the line with a FWHM of $(2\pi\tau)^{-1}$.

Chapter 3

Publication: Metastability and Coherence of Repulsive Polarons in a Strongly Interacting Fermi Mixture[1]

Nature **485**, 615 (2012)
submitted 26 November 2011, accepted 9 March 2012
DOI: 10.1038/nature11065

C. Kohstall[1,2], M. Zaccanti[1], M. Jag[1,2], A. Trenkwalder[1], P. Massignan[3], G. M. Bruun[4], F. Schreck[1], and R. Grimm[1,2]

[1] *Institut für Quantenoptik und Quanteninformation (IQOQI), Österreichische Akademie der Wissenschaften, 6020 Innsbruck, Austria*
[2] *Institut für Experimentalphysik und Zentrum für Quantenphysik, Universität Innsbruck, 6020 Innsbruck, Austria*
[3] *ICFO - Institut de Ciències Fotòniques, Mediterranean Technology Park, 08860 Castelldefels (Barcelona), Spain*
[4] *Department of Physics and Astronomy, University of Aarhus, 8000 Aarhus C, Denmark*

[1] The author of the present thesis performed the measurements and analyzed the data together with C.K., M.Z., and A.T. under the supervision of F.S. and R.G. and contributed to writing the manuscript.

3.1 Abstract

Ultracold Fermi gases with tunable interactions provide a test bed for exploring the many-body physics of strongly interacting quantum systems [Blo08, Gio08, Rad10, Che10]. Over the past decade, experiments have investigated many intriguing phenomena, and precise measurements of groundstate properties have provided benchmarks for the development of theoretical descriptions. Metastable states in Fermi gases with strong repulsive interactions [Dui05, LeB09, Con09, Jo09, Pil10, Cha11, San12] represent an exciting area of development. The realization of such systems is challenging, because a strong repulsive interaction in an atomic quantum gas implies the existence of a weakly bound molecular state, which makes the system intrinsically unstable against decay. Here we use radio-frequency spectroscopy to measure the complete excitation spectrum of fermionic ^{40}K impurities resonantly interacting with a Fermi sea of ^{6}Li atoms. In particular, we show that a well-defined quasiparticle exists for strongly repulsive interactions. We measure the energy and the lifetime of this 'repulsive polaron' [Pil10, Mas11, Sch11], and probe its coherence properties by measuring the quasiparticle residue. The results are well described by a theoretical approach that takes into account the finite effective range of the interaction in our system. We find that when the effective range is of the order of the interparticle spacing, there is a substantial increase in the lifetime of the quasiparticles. The existence of such a long-lived, metastable many-body state offers intriguing prospects for the creation of exotic quantum phases in ultracold, repulsively interacting Fermi gases.

3.2 Introduction

Landau's theory of Fermi liquids [Lan56], and the underlying concept of quasiparticles, is central to our understanding of interacting Fermi systems over a wide range of energy scales, including liquid helium-3, electrons in metals, atomic nuclei and quark–gluon plasma. In the field of ultracold Fermi gases, the normal (non-superfluid) phase of a strongly interacting system can be interpreted in terms of a Fermi liquid [Lob06, Sch09, Nav10, Nas11]. In the population-imbalanced case, quasiparticles known as Fermi polarons are the essential building blocks and have been studied in detail experimentally [Sch09] for attractive interactions. Recent theoretical work [Pil10, Mas11, Sch11] has suggested a novel quasiparticle associated with repulsive interactions. The properties of this repulsive polaron are of fundamental importance to the prospects of repulsive many-body states. A crucial question for the feasibility of future experiments is the stability against decay into molecular excitations [Pek11, Mas11, San12]. Indeed, whenever a strongly repulsive interaction is realized by means of a magnetically tuned Feshbach resonance [Chi10] (FR), a weakly bound molecular state is present into which the system may rapidly decay.

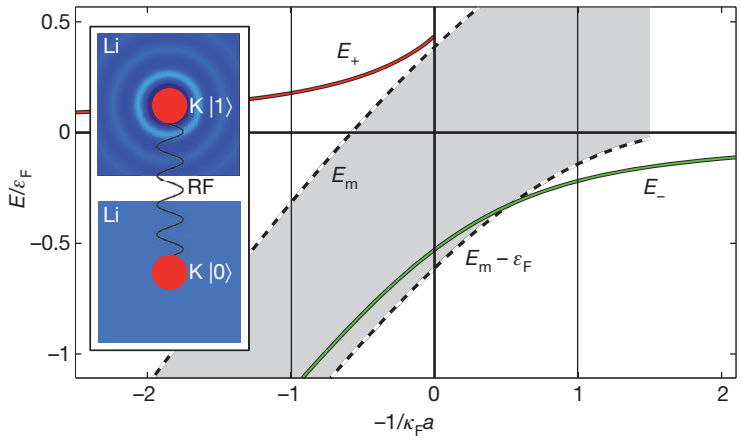

Figure 3.1: Energy spectrum of an impurity in the Fermi sea. The energies, E_+ (red line) and E_- (green line), of the two polaronic branches are plotted as functions of the interaction parameter, $-1/\kappa_F a$. The shaded area between the dashed lines representing E_m and $E_m - \epsilon_F$ (see text) shows the continuum of molecular excitations. The vertical lines at $1/\kappa_F a = \pm 1$ indicate the width of the strongly interacting regime. The inset illustrates our radio-frequency (RF) spectroscopic scheme whereby the impurity is transferred from a noninteracting spin state, $|0\rangle$, to the interacting state, $|1\rangle$.

3.3 Main results

Our system consists of impurities of fermionic ^{40}K atoms immersed in a large Fermi sea of ^{6}Li atoms, which is characterized by an effective Fermi energy of $\epsilon_F = h \times 37\,\mathrm{kHz}$ and a temperature of $T = 0.16\,\epsilon_F/k_B$ (Methods), where h and k_B respectively denote the Planck and the Boltzmann constants. For a particular combination of spin states [Nai11] (quantum numbers $F = 9/2, m_F = -5/2$ for ^{40}K and $F = 1/2, m_F = +1/2$ for ^{6}Li), the mixture has a FR centred at $B_0 = 154.719\,\mathrm{G}$ (Methods). The FR enables us to tune widely the s-wave interaction, parameterized by the scattering length, a, using a magnetic field, B. The interaction strength is described by the dimensionless parameter $-1/\kappa_F a$, where $\kappa_F = \hbar^{-1}\sqrt{2m_{Li}\epsilon_F} = 1/2,850a_0$ is the Fermi wavenumber. Here $\hbar = h/2\pi$, a_0 is the Bohr radius and m_{Li} is the mass of a ^{6}Li atom. Near the centre of the FR, the linear approximation $-1/\kappa_F a \approx (B - B_0)/20\,\mathrm{mG}$ holds. The momentum dependence of the interaction is characterized by the effective range, which we express in terms of the parameter R^* as defined in Ref. [Pet04a] (Methods and Supplementary Information). For our relatively narrow FR, $R^* = 2,700a_0$ and the corresponding value of $\kappa_F R^* = 0.95$ indicates that the finite effective range will have an important influence on the interaction with the Fermi sea.

In Fig. 3.1, we illustrate the basic physics of our impurity problem in the $T = 0$ limit, showing the energies of different states as functions of the interaction parameter. The situation is generic for any impurity in a Fermi sea, but quantitative details depend on both the mass ratio of the two atomic species and the width of the FR. The theoretical curves are based

on a generalization of an approach presented in Refs. [Pun09, Mas11] to our case of a finite effective range.

The spectrum has two quasiparticle branches, which do not adiabatically connect when the FR is crossed, and a molecule–hole continuum (MHC), indicated by the shaded area in Fig. 3.1. The interaction-induced energy shifts of the two branches ($E_+ > 0$ and $E_- < 0$) are generally described in a many-body picture by dressing the impurities with particle–hole excitations. Far away from the FR centre, this simplifies to a mean-field shift proportional to a. The lower branch of the system (E_-; green line) corresponds to the attractive polaron, which has recently received a great deal of attention theoretically [Che10, Lob06, Com07, Pun09, Sad11] as well as experimentally [Nas09, Sch09, Nav10]. This polaronic branch remains the ground state of the system until a critical interaction strength is reached, where the system energetically prefers to form a bosonic ^{6}Li^{40}K molecule by binding the ^{40}K impurity to a ^{6}Li atom from the Fermi sea [Pro08, Pun09, Sad11]. The MHC arises from the fact that an atom with an energy between 0 and ϵ_F can be removed from the Fermi sea to form the molecule. This continuum thus exists in an energy range between E_m and $E_\mathrm{m} - \epsilon_\mathrm{F}$ (Fig. 3.1, dashed lines), where E_m is the energy of a dressed molecule including the binding energy of a bare molecule in vacuum and a positive interaction shift. The attractive polaron can decay into a molecular excitation if this channel opens up energetically ($E_- \geq E_\mathrm{m} - \epsilon_\mathrm{F}$).

The upper branch (Fig. 3.1, red line) corresponds to the repulsive polaron [Pil10, Mas11, Sch11] with an energy $E_+ > 0$. Approaching the FR from the $a > 0$ side, E_+ gradually increases and reaches a sizeable fraction of ϵ_F. However, the polaronic state becomes increasingly unstable as it decays to the lower-lying states (attractive polaron and MHC). Close to the FR centre, the repulsive polaronic state becomes ill-defined as the decay rate approaches $E_+/\hbar$.

To investigate the excitation spectrum of the impurities, we use radio-frequency spectroscopy [Chi04, Shi07, Ste08]. We initially prepare the ^{40}K atoms in a non-interacting spin state, $|0\rangle \equiv |F = 9/2, m_F = -7/2\rangle$ and then, with a variable frequency, ν_rf, drive radio-frequency transitions into the resonantly interacting state $|1\rangle \equiv |F = 9/2, m_F = -5/2\rangle$. Our signal is the fraction of atoms transferred, measured as a function of the radio-frequency detuning, $\nu_\mathrm{rf} - \nu_0$, with respect to the unperturbed transition frequency, ν_0, between the two spin states. This excitation scheme provides access to the full energy spectrum of the system. In particular, it allows us to probe the metastable repulsive polaron as well as all states in the MHC. We furthermore take advantage of the coherence of the excitation process by driving Rabi oscillations. This is an important practical advantage, because it allows very fast and efficient transfer of population into a short-lived quasiparticle state by application of π-pulses. Moreover, we find that measurements of the Rabi frequency directly reveal quasiparticle properties (see below).

In Fig. 3.2, we show false-colour plots of our signal as detected for different values of the detuning parameter, $\Delta = h(\nu_\mathrm{rf} - \nu_0)$, and for variable interaction strength, $-1/\kappa_\mathrm{F} a$. Figure 3.2a displays a set of measurements that we optimized for the signal strength and spectral resolution of the polaronic excitations by using moderate radio-frequency power. The two insets show the polaron peaks on top of a background due to additional excitations in the Fermi sea (Supplementary Information). The spectrum in Fig. 3.2b was optimized for detec-

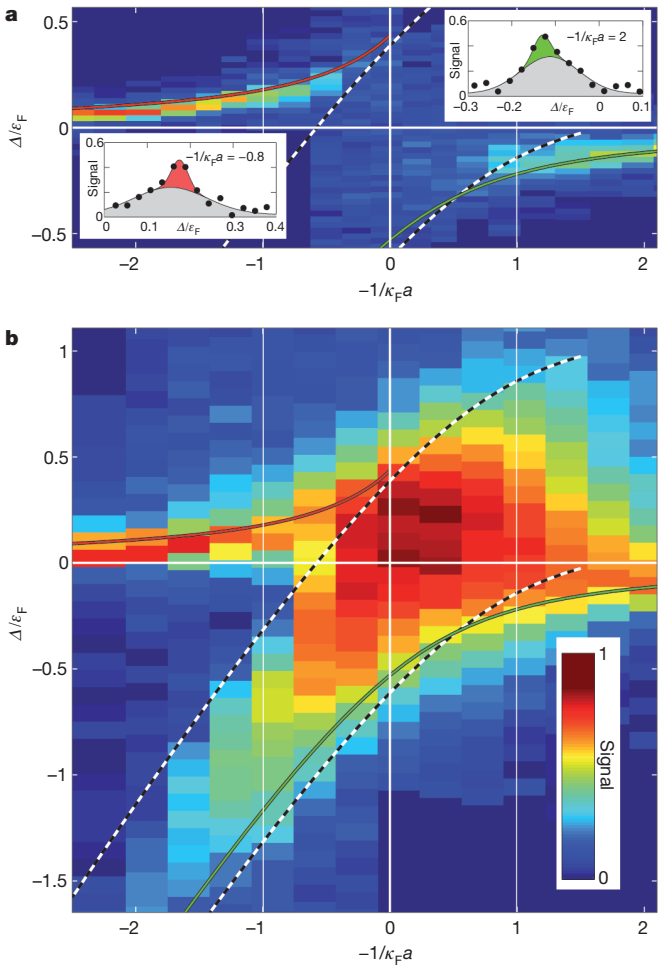

Figure 3.2: Spectral response of ^{40}K impurities in a ^{6}Li Fermi sea. The false-colour plots show the fraction of ^{40}K atoms transferred from the noninteracting spin state, $|0\rangle$, to the interacting state, $|1\rangle$, for different values of the radio-frequency detuning parameter, $\Delta = h(\nu_{\rm rf} - \nu_0)$, and for variable interaction strength, $-1/\kappa_{\rm F}a$: low radio-frequency power (**a**); high radio-frequency power (**b**). For comparison, the lines correspond to the theoretical predictions for E_+, E_-, $E_{\rm m}$, and $E_{\rm m} - \epsilon_{\rm F}$ as shown in Fig. 3.1. In **a**, the two insets show the signals for $-1/\kappa_{\rm F}a = -0.8$ and 2, respectively, corresponding to vertical cuts through the signal data.

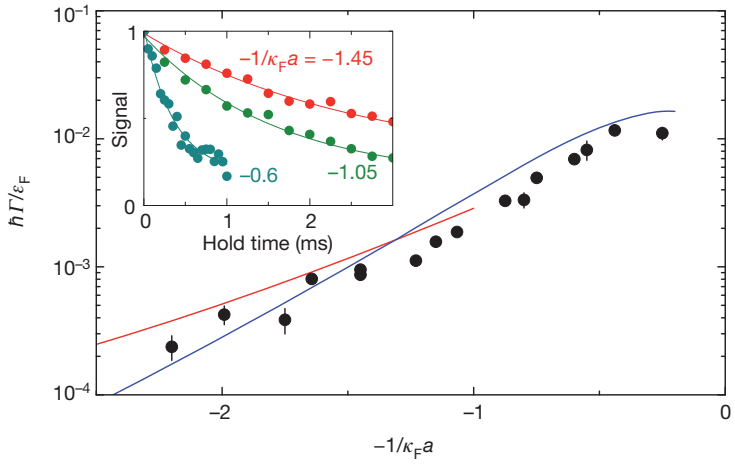

Figure 3.3: Decay rate of the repulsive polaron. The data points display the measured decay rates, Γ, as extracted by exponential fits to decay curves; the error bars indicate the fit uncertainties. Sample decay curves are shown in the inset. The solid lines represent theoretical calculations of the two-body decay into the attractive polaron (blue line) and the three-body decay into the MHC (red line).

tion of the molecular excitations. Here we had to use a much higher radio-frequency power (greater than that in Fig. 3.2a by a factor of 100) because of the reduced Franck–Condon wavefunction overlap. For the polaronic branches, the high radio-frequency power leads to highly nonlinear saturation behaviour.

Our data show both polaronic branches, and the measured energies of the branches are in excellent agreement with theory. The attractive polaron is found to disappear in the strongly interacting regime. This behaviour, which is different from that observed in ^{6}Li spin mixtures [Sch09], is consistent with the crossing of E_- and $E_m - \epsilon_F$ at $-1/\kappa_F a \approx +0.6$ as we expect for our system. By contrast, the repulsive polaron extends far into the strongly interacting regime. The spectrum has a sharp peak that fades out near $-1/\kappa_F a \simeq -0.3$ (Supplementary Information). The low radio-frequency power produces only a weak MHC signal (Fig. 3.2a), whereas for high radio-frequency power the MHC signal is strong (Fig. 3.2b). For weaker interactions on the $a > 0$ side of the FR ($-1/\kappa_F a < -1$), the molecular signal decreases because of the reduced Franck–Condon overlap. Outside the strongly interacting regime, the situation corresponds to the radio-frequency association of bare molecules (Supplementary Information).

To investigate the decay of the repulsive branch, we apply a radio frequency pulse sequence to convert repulsive polarons in state $|1\rangle$ back into non-interacting impurities in state $|0\rangle$ after a variable hold time (Methods). This back-conversion depends sensitively on the radio-frequency resonance condition and thus allows us to discriminate ^{40}K atoms in the polaronic state from those forming molecules. In Fig. 3.3, we present the experimental results. The

inset shows three sample curves taken for different values of the interaction parameter. The main panel displays the values extracted for the decay rate, Γ, from the decay curves using exponential fits. The data reveal a pronounced increase in decay as the FR centre is approached, which is in good agreement with theoretical model calculations [Mas11] (Fig. 3.3, solid lines; Supplementary Information). The decay populates the MHC and may occur in a two-step process whereby the repulsive polaron decays via a two-body process into an attractive polaron (Fig. 3.3, blue line) that in turn decays into a molecular excitation. Alternatively, the repulsive polaron may decay directly into the MHC in a three-body process (Fig. 3.3, red line). Very close to the FR centre, for $-1/\kappa_{\mathrm{F}}a = -0.25$, we find that $\hbar\Gamma/\epsilon_{\mathrm{F}} \approx 0.01$, which corresponds to a $1/e$ lifetime of about $400\,\mu$s. By comparing this decay rate with the corresponding energy shift, $E_+ = 0.30\,\epsilon_{\mathrm{F}}$, we obtain $\hbar\Gamma/E_+ \approx 0.03 \ll 1$, which demonstrates that the repulsive polaron exists as a well-resolved, metastable quasiparticle even deep in the strongly interacting regime.

The lifetime observed for the repulsive branch is remarkably long, when compared with findings in recent experiments on ^{6}Li spin mixtures[San12]. The latter mass-balanced system features a broad FR with a negligible effective range ($R^* \to 0$). Our theoretical approach allows us to give a general answer to the question of how mass imbalance and the width of the FR influence the lifetime. We find that the mass imbalance has only a minor role [Mas11] and that the dominant effect results from the finite effective range. In the strongly repulsive regime, our system allows us to obtain the same amount of repulsive interaction energy as would a hypothetical system with a broad FR ($R^* \to 0$), but with an almost ten-fold increased lifetime (Supplementary Information).

Apart from energy and lifetime, the polaron is characterized by its effective mass, m^*, and its quasiparticle residue, Z ($0 \leq Z \leq 1$). The difference between m^* and the bare mass [Mas11] does not produce any significant features in our radio-frequency spectra. The residue quantifies how much of the non-interacting particle is contained in the polaron's wavefunction, which can be written as $\sqrt{Z}\,|1\rangle$ plus terms describing excitations in the Fermi sea. The pre-factor $\sqrt{Z}$ directly manifests itself in the Rabi frequency, Ω, that describes the coherent radio-frequency coupling between the non-interacting state and the polaronic state (Supplementary Information).

In Fig. 3.4, we show the experimental data on Rabi oscillations for variable interaction strength. The sample curves in Fig. 3.4a demonstrate both the interaction-induced change in the frequency and a damping effect. We apply a simple harmonic oscillator model (including a small increasing background) to analyse the curves, which yields the damping rate, γ, and the frequency, Ω. The damping strongly increases close to the FR centre, but does not show any significant dependence on the unperturbed Rabi frequency,Ω_0 (Fig. 3.4b). We note that the population decay rates, Γ, measured for the repulsive branch (Fig. 3.3) stay well below the values of γ, which suggests that collision-induced decoherence is the main damping mechanism.

Figure 3.4c shows the measured values for the Rabi frequency normalized to Ω_0. The interaction-induced reduction of Ω/Ω_0 is found to be independent of the particular value of Ω_0 (comparison of blue squares and red dots; see also Supplementary Information). The solid lines show $\sqrt{Z}$ as calculated within our theoretical approach for both the repulsive po-

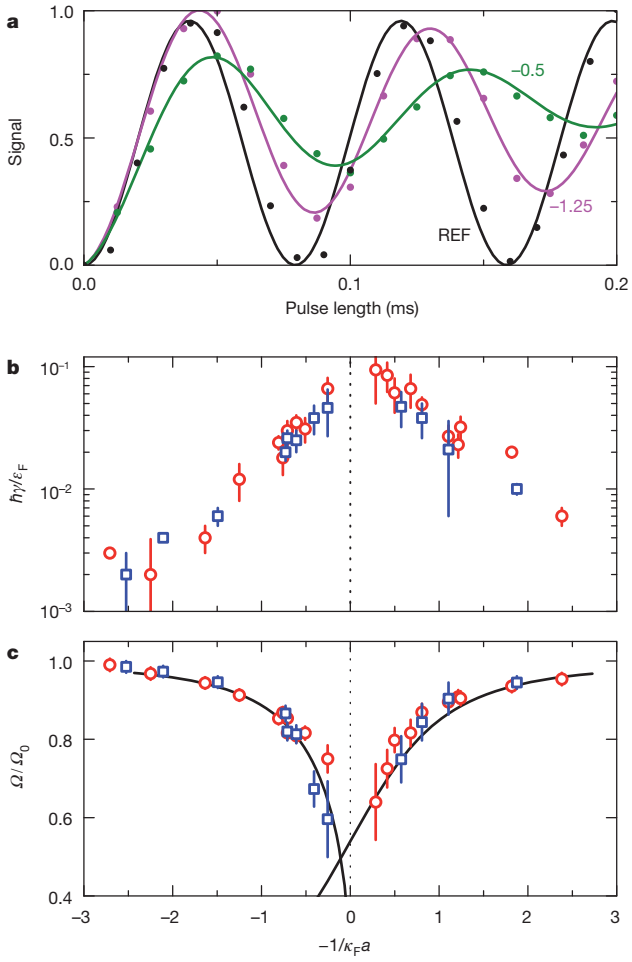

Figure 3.4: Rabi oscillations and the quasiparticle residue. **a**, Sample Rabi oscillations (for $-1/\kappa_F a = -1.25$ (magenta points) and $-1/\kappa_F a = -0.5$ (green points)) with harmonic oscillator fits (solid lines) demonstrate the two effects of the interaction with the Fermi sea: damping and a reduction of the Rabi frequency. The black curve (REF) is a reference curve recorded without ^{6}Li. **b**, **c**, Damping rates, γ (b), and the normalized Rabi frequencies, Ω/Ω_0 (**c**), as measured for two different values of the radio-frequency power: $\Omega_0 = 2\pi \times 6.5\,\mathrm{kHz}$ (blue) and $2\pi \times 12.6\,\mathrm{kHz}$ (red). The error bars indicate the fit uncertainties. The solid lines represent the theoretical behaviour of $\sqrt{Z}$ for the repulsive polaron (left) and the attractive polaron (right).

laron and the attractive polaron. The comparison with the experimental data demonstrates a remarkable agreement with the relation $\sqrt{Z} = \Omega/\Omega_0$. Our results therefore suggest that measuring the Rabi frequency is a precise and robust way to determine the quasiparticle residue, Z, and thus provides a powerful alternative to methods based on the detection of the narrow quasiparticle peak in the spectral response [Sch09, Pun09].

In general, our set of spectroscopic methods applies to any resonantly interacting spin or species mixture that can be efficiently radio-frequency-coupled to a weakly interacting one. Such a situation is the rule rather than the exception in ultracold atomic systems [Chi10]. In mixtures of different species, we anticipate a large variety of suitable systems. For the mass-balanced case of a spin mixture, the well-established ^{40}K system [Ste08] would be an obvious choice. We also point out that narrow FRs are more common in the field than broad ones [Chi10]. Therefore, effects of the finite effective range similar to those described in our work will govern the behaviour of most systems that can be realized in the laboratory. The benefit of an increased lifetime could help overcome the problem of decay into molecular excitations [Pek11, San12] in the experimental investigation of metastable many-body states that rely on repulsive interactions, such as phase-separated states of two fermionic components [Dui05, LeB09, Con09, Jo09, Cha11, San12].

Methods summary

A cloud of 2×10^4 ^{40}K atoms is confined in an optical dipole trap together with a ^{6}Li Fermi sea of 3.5×10^5 atoms, at a temperature of $T \approx 290\,\mathrm{nK}$. The K atoms reside in the centre of the much larger Li cloud and thus sample a nearly homogeneous Li environment. The relevant energy scale is given by the Li Fermi energy averaged over the K density distribution, $\epsilon_F = h \times 37\,\mathrm{kHz} = 1.8\,\mu\mathrm{K}$.

The FR is fully characterized by the parameters [Nai11] $B_0 = 154.719\,\mathrm{G}$ (centre), $\Delta B = 0.88\,\mathrm{G}$ (width), $a_{\mathrm{bg}} = 63.0\,a_0$ (background scattering length), and $\delta\mu/h = 2.3\,\mathrm{MHz/G}$ (differential magnetic moment). The scattering length can be calculated from the standard expression [Chi10] $a(B) = a_{\mathrm{bg}}(1 - \Delta B/(B - B_0))$, and the range parameter [Pet04a] is obtained as $R^* = \hbar^2/(2m_{\mathrm{r}}a_{\mathrm{bg}}\,\delta\mu\,\Delta B) = 2700\,a_0$, where m_{r} is the reduced mass of the K–Li pair. We note that the common textbook definition of the effective range corresponds to $r_{\mathrm{e}} = -2R^*$, for $a \to \pm\infty$.

The radio-frequency pulses used in measuring the data in Figs 3.2 and 3.3 were Blackman-shaped to avoid side lobes in the spectrum. The pulses were 1 ms (Fig. 3.2a) or 0.5 ms (Fig. 3.2b) long, and the radio-frequency power was adjusted such that π-pulses (Fig. 3.2a) or 5π-pulses (Fig. 3.2b) were realized in the absence of interactions with the Fermi sea. For the measurements in Fig. 3.3, a first π-pulse (duration between 150 and 500 μs) was used to drive the impurity from state $|0\rangle$ into state $|1\rangle$, selectively creating repulsive polarons. A second, 60-μs, π-pulse transferred the population remaining in state $|0\rangle$ into a third state. A third pulse, equal to the first one, transferred the state-$|1\rangle$ polarons back into state $|0\rangle$, where they were finally measured using spin-state-selective absorption imaging. The measurements shown in Fig. 3.4 were performed with simple square pulses.

Acknowledgements

We thank A. Sidorov for contributions in the early stage of the experiments, and T. Enss, S. Giorgini, W. Ketterle, J. Levinsen, C. Lobo, D. Petrov, A. Recati, R. Schmidt, J. Song, C. Trefzger, P. Zoller, W. Zwerger, M. Zwierlein, and in particular M. Baranov for many stimulating discussions. We acknowledge support by the Austrian Science Fund FWF through the SFB FoQuS. M.Z. is supported within the Lise Meitner program of the FWF. P.M. is indebted to M. Lewenstein for support through the ERC Advanced Grant QUAGATUA.

3.4 Methods

Experimental conditions

Our system consists of 2×10^4 ^{40}K atoms and 3.5×10^5 ^{6}Li atoms confined in an optical dipole trap. The trap is realized with two crossed beams derived from a 1,064-nm single-mode laser source. The measured trap frequencies for Li and K are respectively $\nu_r = 690$ and 425 Hz radially and $\nu_z = 86$ and 52 Hz axially; this corresponds to a cigar-shaped sample with an aspect ratio of about eight. The preparation procedure is described in detail in Ref. [Spi10a]. The Fermi energies, according to the common definition for harmonic traps, $E_\mathrm{F} = h\sqrt[3]{6N\nu_r^2\nu_z}$, are $E_\mathrm{F}^\mathrm{Li} = h \times 44\,\mathrm{kHz} = k_\mathrm{B} \times 2.1\,\mu\mathrm{K}$ and $E_\mathrm{F}^\mathrm{K} = h \times 10.4\,\mathrm{kHz} = k_\mathrm{B} \times 500\,\mathrm{nK}$. At a temperature of $T \approx 290\,\mathrm{nK}$, the ^{6}Li component forms a deeply degenerate Fermi sea ($k_\mathrm{B}T/E_\mathbf{F}^\mathrm{Li} \approx 0.14$) whereas the ^{40}K component is moderately degenerate ($k_\mathrm{B}T/E_\mathrm{F}^\mathrm{K} \approx 0.6$).

Effective Fermi energy

The ^{40}K atoms sample a nearly homogeneous ^{6}Li environment. This is because the optical trapping potential for ^{40}K is about twice as deep as for ^{6}Li and the ^{40}K cloud is confined to the centre of the much larger ^{6}Li Fermi sea [Tre11a]. This allows us to describe the system in terms of the effective Fermi energy, ϵ_F, defined as the mean Fermi energy experienced by the ^{40}K atoms. We find that $\epsilon_\mathrm{F} = h \times 37\,\mathrm{kHz}$, with two effects contributing to the fact that this value is about 15% less than $E_\mathrm{F}^{\mathrm{L}i}$. The finite temperature reduces the Li density in the trap centre, leading to a peak local Fermi energy of $h \times 40\,\mathrm{kHz}$. Moreover, the ^{40}K atoms sample a small region around the trap centre, where the density and local Fermi energy are somewhat lower than in the centre. The distribution of Fermi energies experienced by the ^{40}K cloud, that is, the residual inhomogeneity of our system, can be quantified in terms of a standard deviation of $h \times 1.9\,\mathrm{kHz}$.

Concentration

The mean impurity concentration (mean number density ratio, n_K/n_{Li}) is about 0.4, if both spin states of the population of K atoms are considered. This may be too large a-priori to justify the interpretation of our data in terms of the low-concentration limit. We find that this interpretation is nevertheless valid, as we take advantage of several facts. Under strongly interacting conditions, only a fraction of the K atoms are transferred into spin state $|1\rangle$ (Fig. 3.2), which reduces the concentration of interacting impurities. A recent quantum Monte Carlo calculation of the equation of state of a zero-temperature ^{6}Li–^{40}K Fermi–Fermi mixture [Gez09] further supports our interpretation in the low-concentration limit: the strongest interaction in the mass-imbalanced system is expected when there are about 4 times more ^{40}K atoms than ^{6}Li atoms, and for concentrations up to a value of 1 the interaction energy per ^{40}K atom is expected to remain essentially constant. To support our basic assumption with experimental data, we also measured radio-frequency spectra for variable numbers of ^{40}K atoms, confirming that finite concentration effects remained negligibly small in the relevant parameter range.

Interaction control through Feshbach resonance

The FR used for interaction tuning is discussed in detail in Refs. [Nai11, Tre11a]. It is present for ^{6}Li in the lowest spin state ($F = 1/2, m_F = +1/2$) and for ^{40}K in the third-to-lowest spin state ($F = 9/2, m_F = -5/2$). The latter represents our interacting state, $|1\rangle$. The neighbouring state with $m_F = -7/2$ serves as state $|0\rangle$; here the interspecies scattering length ($+65\,a_0$) is so small that any interaction can be neglected to a good approximation. The tunable scattering length for state $|1\rangle$ in the Fermi sea is well described by the standard formula, $a = a_{bg}(1 - \Delta B/(B - B_0))$, with $a_{bg} = 63.0\,a_0$, $\Delta B = 0.88\,\mathrm{G}$, and $B_0 = 154.719(2)\,\mathrm{G}$. The value given for B_0 refers to the particular optical trap used in the present experiments, as it includes a small shift induced by the trapping light. The value therefore deviates somewhat from the one given in Refs. [Nai11, Tre11a]. In free space, without the light shift, the resonance centre is located at 154.698(5) G. The uncertainties given for the resonance centre, B_0 (2 mG in the trapped case and 5 mG for free space), correspond to standard deviations, obtained from analysing molecule association spectra for various trap settings.

The character of the resonance is closed-channel dominated [Chi10]. Following the definition [Pet04a] of a range parameter, $R^* = \hbar^2/(2m_r a_{bg}\,\delta\mu\,\Delta B)$, where $m_r = m_{Li}m_K/(m_{Li} + m_K)$ is the reduced mass and $\delta\mu/h = 2.3\,\mathrm{MHz/G}$ is the differential magnetic moment, the resonance is characterized by $R^* = 2,700\,a_0$. For $a \to \pm\infty$, this parameter corresponds to the common textbook definition [Chi10] of the effective range, $r_e = -2R^*$. Our value for R^* coincidentally lies very close to $1/\kappa_F = 2,850\,a_0$, which means that the strongly interacting regime corresponds roughly to the universal range of the resonance. Our system therefore represents an intermediate case ($\kappa_F R^* = 0.95$), where the behaviour is near universal, but with significant effects arising from the finite effective range.

Details on radio-frequency pulses

To measure the data in Fig. 3.2, we used Blackman pulses [Kas92] to avoid side lobes in the spectrum. For Fig. 3.2a, the pulses were 1-ms long (spectral width, $0.7\,\mathrm{k}Hz \simeq 0.02\,\epsilon_F/h$) and the radio-frequency power was adjusted such that π-pulses would be realized in the absence of interactions with the Fermi sea. For the data in Fig. 3.2b, the radio-frequency power was increased by a factor of 100 and the pulse duration was set to 0.5 ms. This resulted in pulses with an area of 5π without the Fermi sea. For the lifetime measurements in Fig. 3.3, we used a sequence of three Blackman pulses. The first pulse (duration between 150 and 500 ms) was set to drive the non-interacting impurity from spin state $|0\rangle$ ($m_F = -7/2$) into state $|1\rangle$ ($m_F = -5/2$); here the frequency was carefully set to resonantly create repulsive polarons and the pulse area was set to fulfill the π-pulse condition. The second pulse was a short (60-ms) cleaning pulse, which removed the population remaining in $|0\rangle$ by transferring it to another, empty, spin state ($m_F = -9/2$). The third pulse had the same parameters as the first one and resonantly transferred the population of the polaronic state in $|1\rangle$ back to the non-interacting state, $|0\rangle$, where it was finally measured by spin-state-selective absorption imaging. The measurements of Rabi oscillations in Fig. 3.4 were performed with simple square pulses.

3.5 Supplementary information

3.5.1 Theoretical framework

The theoretical results presented in the main text and in this Supplementary Information are obtained from a model that describes the behaviour of a single impurity embedded in a Fermi sea with tuneable s-wave interaction near a Feshbach resonance with arbitrary effective range. Two different wavefunctions are needed, depending on whether one is interested in the polaron [Che06, Com07] or molecule [Mor09, Pun09, Com09] properties. The quasiparticle parameters for the polaron (energy E_+ and E_-, residue Z, effective mass) and the molecule properties can be found either variationally, or diagrammatically using the ladder approximation. Both approaches yield identical results, which closely match independent Monte-Carlo calculations [Pro08]. The properties of the repulsive polaron, which is intrinsically unstable due to the presence of the molecule-hole continuum (MHC) and of the attractive polaron, are obtained from the self energy. In particular, the interaction induced energy shift and the decay rate are given by the real part and twice the imaginary part of the self energy, respectively [Mas11].

Previous treatments [Che06, Com07, Mor09, Pun09, Com09, Pro08, Mas11] were based on a universal scattering amplitude, describing broad Feshbach resonances. To include effects of the finite effective range we employ a many-body T-matrix given by [Bru05a, Mas08b]

$$T(\mathbf{K},\omega) = \left[\frac{m_r}{2\pi\hbar^2\tilde{a}(\mathbf{K},\omega)} - \Pi(\mathbf{K},\omega)\right]^{-1}. \tag{3.1}$$

Here $\hbar\mathbf{K} = \mathbf{p}_\mathrm{K} + \mathbf{p}_{\mathrm{L}i}$ is the total momentum with $\mathbf{p}_{\mathrm{L}i}$ and $\mathbf{p}_\mathrm{K}$ the momenta of Li and K,

$m_r = m_{\mathrm{Li}} m_{\mathrm{K}}/(m_{\mathrm{Li}} + m_{\mathrm{K}})$ the reduced mass, $\Pi(K,\omega)$ the Li-K pair propagator in the presence of the Fermi sea, and $\tilde{a}(\mathbf{K},\omega) \equiv a_{\mathrm{bg}}\left(1 - \frac{\Delta B}{B - B_0 - E_{CM}/\delta\mu}\right)$ an energy-dependent length parameter, with a_{bg}, ΔB, B_0, and $\delta\mu$ being the background scattering length, the width, the center, and the relative magnetic moment of the Feshbach resonance. $E_{CM}(\mathbf{K},\omega) = \hbar\omega - \hbar^2\mathbf{K}^2/(2M) + \epsilon_F$, with $M = m_{\mathrm{Li}} + m_{\mathrm{K}}$, is the energy in the center of mass reference frame of the colliding pair. In vacuum and close to resonance, the scattering amplitude of our model has the usual low energy expansion

$$-f_k^{-1} = a^{-1} + ik - r_e k^2/2 + \ldots, \tag{3.2}$$

with the relative momentum $\hbar\mathbf{k} = (m_{\mathrm{Li}}\mathbf{p}_{\mathrm{K}} - m_{\mathrm{K}}\mathbf{p}_{\mathrm{Li}})/M$. The effective range is approximated by $r_e \approx -2R^*(1 - a_{\mathrm{bg}}/a)^2$, where we introduce the range parameter $R^* = \hbar^2/(2m_r a_{\mathrm{bg}}\Delta B\delta\mu)$, see Ref. [Pet04a].

Within the one particle-hole approximation, the energies $E_\pm$ of the repulsive and attractive polarons at zero temperature are given by the two solutions of the implicit equation

$$E_\pm = \frac{\mathbf{p}_{\mathrm{K}}^2}{2m_K} + \mathrm{Re}[\Sigma(\mathbf{p}_{\mathrm{K}}, E_\pm)], \tag{3.3}$$

where the self-energy describing the interactions of the impurity with the bath reads [Com07]

$$\Sigma(\mathbf{p}_{\mathrm{K}},\omega) = \sum_{\mathbf{p}_{\mathrm{Li}} < k_F} T\left(\mathbf{p}_{\mathrm{K}} + \mathbf{p}_{\mathrm{Li}}, \omega + \frac{\mathbf{p}_{\mathrm{Li}}^2}{2m_{\mathrm{Li}}} - \epsilon_F\right). \tag{3.4}$$

The residue of polarons with vanishing momentum, which we plot in Fig. 3.4c of the main paper, are given by

$$Z_\pm = \left[1 - \mathrm{Re}\left[\frac{\partial\Sigma(\mathbf{p}_{\mathrm{K}} = 0,\omega)}{\partial\omega}\right]_{E_\pm}\right]^{-1}. \tag{3.5}$$

A more detailed theoretical analysis of this model is given in Ref. [Mas12].

3.5.2 Polaron peak in the spectral response

The spectra in Fig. 3.2a of the main text show a narrow, *coherent* peak on top of a spectrally broad, *incoherent* background. Here, we investigate these two spectral parts in more detail. Note that the background is actually better visible in Fig. 3.2b, but these spectra do not allow for a quantitative comparison of the two parts because of the strong saturation of the narrow polaron peaks.

The narrow peak stems from the attractive or repulsive polarons, which correspond to well defined energy levels, provided that the lifetime of the quasiparticle exceeds the pulse duration. As a consequence, the lineshape is expected to be Fourier limited except for the rapidly decaying repulsive polarons very close to resonance. In contrast, the background is spectrally wide, on the order of ε_F. The main contribution to the background stems from the MHC. Another contribution may arise from the excitation of additional particle-hole pairs in the

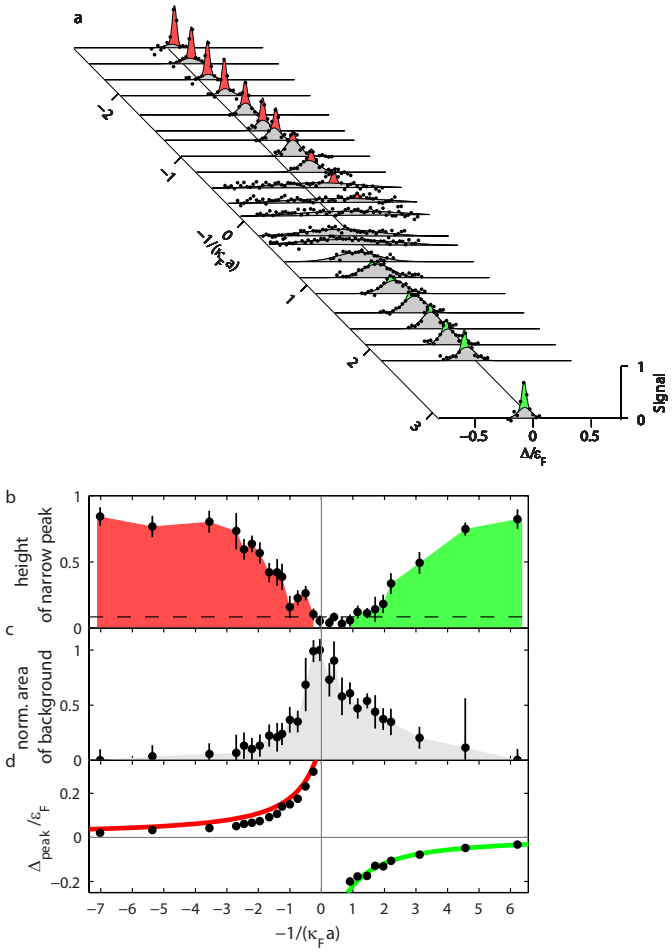

Figure 3.5: Double Gauss analysis of the low-power spectra. The data are the same as presented in Fig. 3.2a plus additional data in an extended range of $1/(\kappa_F a)$. (a) The Gauss function fitting the wide background is shaded grey. The Fourier-limited Gauss function, fitting the narrow peak, is coloured red (green) along the repulsive (attractive) polaron branch. We identify the narrow peak with one of the polaron branches only if its maximum signal exceeds a threshold value of 0.085, corresponding to two times the standard deviation of the noise in our data. Any smaller peak may be caused by fitting to a noise component. The lower panels show (b) the maximum signal of the narrow peak with the dashed line indicating the threshold, (c) the area under the wide Gauss function normalized to its maximum value, and (d) the detuning at the center of the narrow peak, provided that the peak signal exceeds the threshold, compared to the theoretical calculation of E_+ and E_- (red and green line). The error bars indicate the fit uncertainties.

Fermi sea when transferring to a quasiparticle with a momentum that is different from the momentum of the impurity in the initial state.

We distinguish between the narrow peak and the wide background by means of a double Gauss fit. Vertical cuts through Fig. 3.2a are presented in Fig. 3.5a together with the fit curves. The width σ_p of the Gauss function fitting the narrow peak is fixed to the one associated with the Gaussian fit of the Blackman pulse line shape used in the experiment, $\sigma_p = 0.7\,\mathrm{kHz} = 0.019\,\varepsilon_F/h$. We constrain the width σ_b of the Gauss function reproducing the

background to $3\times0.019\,\varepsilon_F/h < \sigma_b < 0.5\,\varepsilon_F/h$. The lower bound avoids the misinterpretation of the narrow peak as background and the upper bound, corresponding to the maximal width of the continuum as obtained from the spectra in Fig. 3.2b, avoids unphysically large values of σ_b when the background signal is weak. We find that the narrow peak dominates for weak positive and negative interaction strength while the wide background dominates in the strongly interacting regime. This trend is shown in Fig. 3.5b and Fig. 3.5c, where we present the maximum signal of the narrow peak and the area of the background, respectively. Note, that the signal in Fig. 3.5b is proportional to the area of the narrow peak since σ_p is kept constant. Figure 3.5d shows the detuning at the center of the narrow peak, which corresponds to the energy of the quasiparticles. The measured energies agree remarkably well with the calculation. The slight mismatch between theory and experiment may be attributed to systematic errors in the determination of ε_F and B_0.

The area of the wide background exhibits a maximum close to $-1/(\kappa_F a) = 0$, but it shows an asymmetry as it falls off significantly slower on the attractive ($a < 0$) side, see Fig. 3.5c. We attribute this asymmetry to the narrow character of the Feshbach resonance. The interaction becomes resonant when the real part of the inverse scattering amplitude, given in Eq. (3.2), is zero. This leads to the resonance condition $a_{res}^{-1} = r_e k^2/2$, where a_{res} is the value of the scattering length at which the interaction becomes resonant. In the limit of a broad resonance with $r_e = 0$, this condition is fulfilled for any k at the center of the resonance, where the scattering length diverges. However, at a narrow resonance with $r_e < 0$ the condition requires a negative a_{res} for $k > 0$. The mean square momentum in the Fermi sea is $3/5 \times \kappa_F^2$, leading to a mean square relative momentum of $3/5 \times (40/46 \times \kappa_F)^2$. Using this value for k^2, and inserting $r_e \approx -2R^*$ in the above resonance condition, we obtain $-1/(\kappa_F a) = 0.43$. This represents an effective shift of the Feshbach resonance center, as we average over all momenta of the Fermi sea [Ho12]. The magnitude of this shift agrees well with the observed asymmetry. Moreover, we find that many features at our narrow resonance appear to be shifted, e.g. the polaron-to-molecule crossing. However, the narrowness has many more implications and cannot simply be reduced to this shift. We will come back to this point in the context of the lifetime of the repulsive polaron, see Sec. 3.5.4.

The repulsive polaron peak is clearly visible up to $-1/(\kappa_F a) \approx -0.3$ while the attractive polaron peak vanishes already at $-1/(\kappa_F a) \approx 0.9$, see Fig. 3.5b. The fading out of the quasiparticle peak towards the strongly interacting regime approximately coincides with the position where the quasiparticle branches merge into the MHC. This shows that the polaron state is hardly observable as soon as it becomes degenerate with molecule-hole excitations. The MHC is not strictly limited to the range from E_m to $E_m - \varepsilon_F$, as discussed in more detail in Sec. 3.5.3. It extends below $E_m - \varepsilon_F$ because of finite temperature effects. It also extends slightly above E_m because of additional excitations in the spectral function of the molecules [Sch11]. As a consequence, for finite temperature, the attractive polaron can become degenerate with molecule-hole excitations for values of the interaction parameter above the calculated polaron-to-molecule crossing. This explains that the observed sharp peak is observed to disappear already at $-1/(\kappa_F a) \approx 0.9$, which lies somewhat above the zero-temperature polaron-to-molecule crossing predicted at 0.6.

It is interesting to consider the data analysis presented in Fig. 3.5b and c in relation to the common method of extracting the quasiparticle residue Z from the spectral weight of the

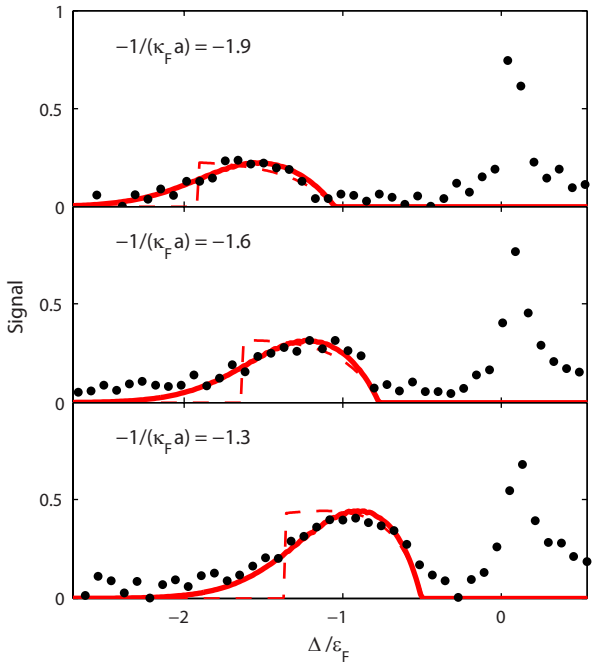

Figure 3.6: Molecule association spectra for different values of the interaction parameter. The signal is the fraction of transferred atoms as a function of the rf detuning. The data correspond to vertical cuts through Fig. 3.2b. The dashed line is the line shape model for zero temperature and the solid line for finite temperature. The upper threshold of the theoretical spectra corresponds to E_m.

narrow peak [Din01]. Close to resonance, we are in the linear response regime and our data can be interpreted in terms of this method. Our data suggests that this method leads to a significant underestimation of Z. For example at $-1/(\kappa_F a) \approx 0.9$, where the narrow peak of the attractive polaron vanishes, our theory still predicts $Z \approx 0.7$. This underestimation is consistent with the one reported in Ref. [Sch09], see also related discussion in Ref. [Pun09]. A plausible explanation may be that such a method does not probe the polaron states alone, but also the molecule-hole excitations, which are degenerate with the polaron state. Our alternative method of measuring the residue via the Rabi frequency, as presented in the main paper, offers the advantage of being much less affected by the molecule-hole contribution. In fact, only the coherent part of the quasiparticle is expected to produce Rabi oscillations, see Sec. 3.5.6.

3.5.3 Molecule-hole continuum

The spectra presented in Fig. 3.2b of the main text reveal the MHC. This continuum arises from processes where the rf field associates a K impurity and a Li atom out of the Fermi sea to a molecule. Here we present a simple model for the spectral line shape, which allows us to interpret the data up to $-1/(\kappa_F a) \approx -1$, see Fig 3.6.

For modeling the line shape, we consider two-body processes in which the rf field associates one K and one Li atom to a molecule. Higher-order processes, involving more than two particles, are neglected in this model but are briefly discussed at the end of this section. Let us first consider the association of Li and K with momenta $p_{\mathrm{L}i} = p_{\mathrm{K}} = 0$. This results in a molecule at rest plus a Fermi sea with a hole in the center. The energy of this state is determined by the binding energy of the molecule and by the interaction of the molecule with the Fermi sea. It is given by E_m and sets the onset of the MHC from the right (the top) in Fig. 3.6 (Fig. 3.2b). In general, Li and K have finite initial relative momentum $\hbar k$, leading to an initial relative kinetic energy in the center of mass frame $E_r = \hbar^2 k^2/2m_r$. The energy conservation of the association process is expressed in the Dirac δ function in Eq. (3.6). As a consequence, the molecule spectrum extends downwards to energies below E_m. We now consider an ensemble of K and Li atoms. Our experimental conditions are well approximated by a thermal cloud of K in a homogeneous Fermi sea of Li (see Methods). The momentum distribution of Li is given by the Fermi-Dirac distribution $f_{\mathrm{L}i}^{\mathrm{F}D}(E_{\mathrm{L}i})$, with $E_{\mathrm{L}i} = p_{\mathrm{L}i}^2/2m_{\mathrm{L}i}$. The one of K is approximated by the Maxwell-Boltzmann distribution $f_{\mathrm{K}}^{MB}(E_{\mathrm{K}})$, with $E_{\mathrm{K}} = p_{\mathrm{K}}^2/2m_{\mathrm{K}}$. The latter distribution does not change its momentum dependence with position, thus, no integration over space is needed to obtain the spectral response

$$\mathcal{S}(\Delta) \propto \int\int d^3p_{\mathrm{L}i}\ \ d^3p_{\mathrm{K}}\ \ f_{\mathrm{L}i}^{\mathrm{F}D}(E_{\mathrm{L}i})\ \ f_{\mathrm{K}}^{MB}(E_{\mathrm{K}})\ \ \mathcal{F}(k)\ \ \delta(-E_m + E_r + \Delta), \tag{3.6}$$

where $\mathcal{F}(k)$ is the Franck Condon overlap of the initial wavefunction with the molecule wavefunction. In our case the interaction in the initial state is negligible and $\mathcal{F}(k)$, as given in Ref. [Chi05], reduces to $\mathcal{F}(k) \propto (E_r/E_b^3)^{1/2}(1 + E_r/E_b)^{-2}$. The parameter E_b is the binding energy of a molecule in vacuum at a resonance with finite effective range and reads $E_b = \hbar^2/(2m_r a^{*2})$ with the parameter [Pet04a] $a^* = -r_e/(\sqrt{1 - 2r_e/a} - 1)$. In the calculation of $\mathcal{F}(k)$, we do not account for interactions with the Fermi sea. Because of this approximation, we apply the model only for $-1/(\kappa_F a) < -1$. For fitting the model line shapes to the experimental data, adjustable parameters are the individual heights of the spectra and the center of the Feshbach resonance. The latter parameter is required to be the same for all data sets in Fig 3.6. Independently determined parameters are $k_B T/\varepsilon_F = 0.16$ and $\varepsilon_F = h \times 37\,\mathrm{kHz}$. The model (solid lines) reproduces our data remarkably well. It allows us to pinpoint the resonance position to $B_0 = 154.719(2)\,\mathrm{G}$. This determination of B_0 relies on our theoretical model to calculate E_m. To test this model dependence, we replace E_m simply by the binding energy of the molecule in vacuum plus the mean field energy, considering the corresponding atom-dimer scattering length [Lev11]. Using this simple model, the fit yields a resonance position that is 1 mG higher, which shows that the model dependence causes only a small systematic uncertainty. Moreover, the statistical fit uncertainty and the field calibration uncertainty are about 1 mG each.

For $T = 0$ and all other parameters unchanged, the model provides the dashed lines in Fig 3.6. The spectra show a sharp drop at $\Delta = E_m - (40/46)\,\varepsilon_F$, which corresponds to the association of an impurity at rest and a majority atom at the Fermi edge. In an equal-mass mixture this process would occur at $\Delta = E_m - (1/2)\,\varepsilon_F$. Thus, the width of the MHC in the two-body approximation is much larger for a heavy impurity than it is for an equal-mass impurity and it is even narrower for a light impurity.

The true zero temperature ground state is actually at the energy $E_m - \varepsilon_F$, a molecule at

rest formed from a K atom at rest and a Li atom at the Fermi edge. However, to reach this state, momentum conservation requires a higher-order process, i.e. the scattering of at least one additional Li atom from and to the Fermi surface. Such processes are not included in the model presented here, which only considers the direct association of two atoms by an rf photon.

In the strongly interacting regime the spectral function of the molecule shows additional excitations above the molecular ground state [Sch11]. This leads to an extension of the MHC spectral response above E_m, of which we find clear indications in our data. The lower panel in Fig 3.6 shows finite signal above E_m and the extension above E_m is very evident in the strongly interacting regime, see Fig. 3.2b.

3.5.4 Decay rate of the repulsive polarons

We analyze the decay of the repulsive polarons by assuming that they decay into well defined attractive polarons or well-defined molecules. In this quasiparticle picture, the decay is associated with the formation of a particle-hole pair in the Fermi sea to take up the released energy. In this sense, the decay into the attractive polaron is a 2-body process and the decay into the molecule is a 3-body process. We calculate the decay rate for these two channels by including them into the polaron self energy using a pole expansion of the K propagator writing $G(\mathbf{k},\omega) \simeq Z_+/(\hbar\omega - E_+ - \hbar^2k^2/(2m_\mathrm{K})) + Z_-/(\hbar\omega - E_- - \hbar^2k^2/(2m_\mathrm{K}))$ and a pole expansion of the T-matrix writing $T(\mathbf{k},\omega) \simeq Z_m g^2/(\hbar\omega - (E_m - \varepsilon_F) - \hbar^2k^2/(2M))$. Here, $Z_\pm$ is the quasiparticle residue of the repulsive and attractive polaron respectively and Z_m the quasiparticle residue of the molecule. The factor $g^2 = 2\pi\hbar^4/(m_r^2 a^*\sqrt{1-2r_e/a})$ is the residue of the vacuum T-matrix for a general resonance. The details of this approach are given in Refs. [Mas11, Bru10], the only difference being that here we include the effects of the finite effective range. The imaginary part of the self energy gives the decay rate of the wavefunction and we thus take twice the imaginary part to calculate the population decay. The 2-body decay into the attractive polaron and an additional particle-hole pair is calculated numerically to all orders in the T-matrix by inserting the pole expansion for the K propagator in the self energy in the ladder approximation. For the 3-body decay into a molecule and an additional particle-hole pair, we include terms containing two Li holes in the K self energy [Bru10], and an expansion to second order in the T-matrix relevant for $-1/(\kappa_F a) \ll -1$ yields

$$\Gamma_{PM} \simeq \frac{64\kappa_F a}{45\pi^3}\frac{Z_+^3}{m_\mathrm{K}^2\sqrt{m_{Li}}}\left(1+\frac{m_{Li}}{M}\right)^{3/2}\left(\frac{\hbar\kappa_F}{\sqrt{2(E_+ - E_m + \epsilon_F)}}\right)^5 \frac{a}{a^*\sqrt{1-2r_e/a^*}}\frac{\epsilon_F}{\hbar}. \quad 3.7$$

For simplicity, we have taken $Z_m = 1$, which is an appropriate assumption for $-1/(\kappa_F a) \ll -1$. The effect of the narrow resonance on the decay rate enters through the quasiparticle residue Z_+, the energies E_+, E_-, E_m and directly through the effective range r_e. This decay rate has the same a^6 dependence as the three-body decay in vacuum in the limit of a broad resonance derived in Ref. [Pet03]. The numerical prefactor however differs since we have included the effects of the Fermi sea in a perturbative calculation.

The results for the decay rates of repulsive polarons are shown in Fig. 3.7. The experimental

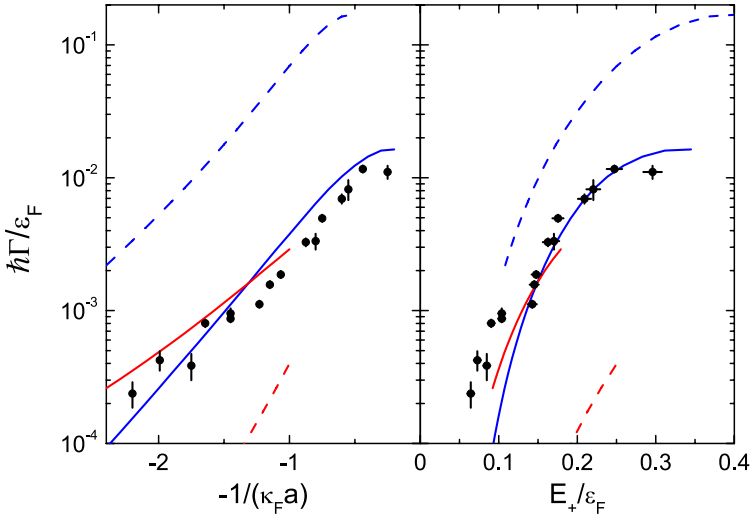

Figure 3.7: Decay rates of repulsive K polarons in a Fermi sea of Li atoms, shown as a function of interaction strength (left) and of the energy of the repulsive polaron (right). Blue and red lines represent the two- and three-body contributions, respectively, while data points are the experimental findings as also shown in Fig. 3.3 of the main text. The results for the moderately narrow resonance under study here (solid lines) is compared with the theoretical results obtained for the universal limit of a very broad resonance (dashed lines). The experimental values of E_+ are obtained by interpolation of the narrow peak position data Δ_{peak}, see Fig. 3.5d.

data agree well with the theoretical results obtained for our narrow resonance (continuous lines) as already shown in Fig. 3.3 in the main text. For comparison, we also show the decay rates one would obtain in the limit of a broad resonance (dashed lines). We find that as magnitude of the effective range increases with respect to the interparticle spacing, the dominant two-body decay is strongly suppressed. This suppression is mainly due to a large reduction of the attractive polaron residue Z_-. Instead, the weaker three-body decay increases, which we attribute to the reduction of the polaron-molecule energy difference $E_+ - E_m + \epsilon_F$. Taking both decay rates together, the decay rate is at least an order of magnitude smaller at our narrow resonance as compared to the case of a broad resonance. It is important to note that this strong suppression of the decay at a given $-1/(\kappa_F a)$ cannot be simply attributed to the effective resonance shift at our narrow Feshbach resonance as discussed in Sec. 3.5.2. When taking this shift into account, a suppression factor of five to ten remains. To highlight this point, we choose a representation that is independent of the interaction parameter and that gives the dependence on the polaron energy, a direct manifestation of strong interactions. The right panel shows the same data and calculations as a function of E_+. Also for a given E_+, the repulsive polaron at our narrow resonance turns out to be much more stable than the repulsive polaron at a broad resonance.

3.5.5 Decay of repulsive polarons to molecules

The decay of the repulsive polarons, shown in Fig. 3.3 of the main text, is measured by applying a special three-pulse scheme (see Methods). In this section we exploit the flexibility

of this scheme to study the decay to lower-lying energy states in more detail. At a given interaction strength $-1/(\kappa_F a) = -0.9$, we demonstrate that the repulsive polarons decay to molecules by showing that an rf spectrum taken after decay perfectly matches a reference spectrum of molecules.

To populate the repulsive polaron branch, as done for the measurements of the decay rate, we tune the energy of the first pulse to E_+, corresponding to $\Delta = 0.16\,\varepsilon_F$ at $-1/(\kappa_F a) = -0.9$. The pulse duration ($t_p = 0.06\,\mathrm{ms}$) and the intensity are set to correspond to a π-pulse in the noninteracting system. The second pulse removes the remaining non-transferred atoms by transferring them to a third spin state. In contrast to the decay measurement presented in the main text, we here use much more rf power for the third pulse to be able to efficiently dissociate molecules. For this purpose, we set $t_p = 0.3\,\mathrm{ms}$ and the pulse area corresponds to a 3π-pulse in the noninteracting system. By varying the rf detuning, we record spectra for zero hold time (black squares) and for a hold time of 2 ms (red dots), see Fig. 3.8a. The peak at small positive detuning shows the back-transfer of repulsive polarons. The corresponding signal decreases with hold time, signalling the decay of the repulsive polaron. In addition, a wide continuum in a range of negative detunings rises with increasing hold time. Such a wide continuum involves coupling to high momentum states, signaling a short distance between K and ^{6}Li. To confirm that this continuum stems from molecules, we compare it to a reference spectrum of the dissociation of molecules (blue diamonds). We find a perfect match. To take such a reference spectrum, only the detuning of the first rf pulse is changed to directly associate molecules in the MHC instead of populating the repulsive polaron branch. We achieve a good association efficiency with $\Delta = -0.54\,\varepsilon_F$ and $t_p = 0.5\,\mathrm{ms}$.

To study the evolution of the molecule population, which is fed by the decay of the repulsive polarons, we set the detuning of the third pulse to the peak of the molecule signal at $\Delta = -1.3\,\varepsilon_F$ and record the signal as a function of the hold time, see Fig. 3.8b. A simple exponential fit yields a rate of about $1\,\mathrm{ms}^{-1} = 0.0043\,\varepsilon_F/\hbar$, which is in good agreement with the measured decay rate of the repulsive polaron at $-1/(\kappa_F a) = -0.9$. The finite signal at zero hold time may have two origins. One contribution is some decay during the finite pulse durations of the three pulses, which are not included in the hold time. Another contribution may be the high momentum tail of the repulsive polarons as discussed in Ref. [Sch09].

Note that we do not find any second sharp peak at negative detuning, which would indicate the population of the attractive polaron branch. In case the repulsive polaron decays to the attractive polaron, the absence of the attractive polaron peak implies a very rapid subsequent decay of the attractive polaron to the MHC. Such a fast decay of the attractive polaron to the MHC is consistent with the very small signal of the attractive polaron peak throughout the regime of strong interaction as discussed in Sec. 3.5.2.

Let us briefly discuss the possible role of inelastic two-body relaxation in the Li-K mixture, which is energetically possible as K is not in the lowest spin state. This process was identified in Ref. [Nai11] as a source of losses. However, this relaxation is about an order of magnitude slower than the measured decay rate of the repulsive polaron and thus does not affect our measurements.

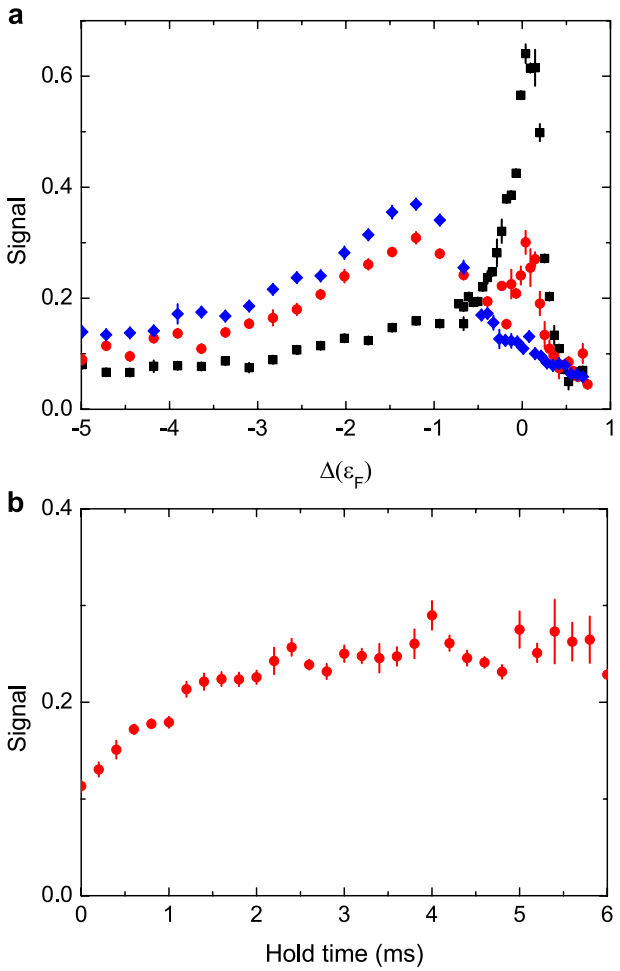

Figure 3.8: Decay of repulsive polarons to molecules at $-1/(\kappa_F a) = -0.9$. (a) The black squares (red dots) show the spectrum right after (2 ms after) the repulsive polaron has been populated. The blue diamonds show the dissociation spectrum of molecules for reference. The signal is the fraction of atoms transferred from the interacting spin state $|1\rangle$ to the noninteracting spin state $|0\rangle$. Note that the polaron peak at positive detuning is highly saturated and thus its signal is not proportional to the number of polarons. (b) The rf energy detuning is fixed to $\Delta = -1.3\,\varepsilon_F$ and the signal is recorded versus hold time. The error bars indicate the statistical uncertainties derived from at least three individual measurements.

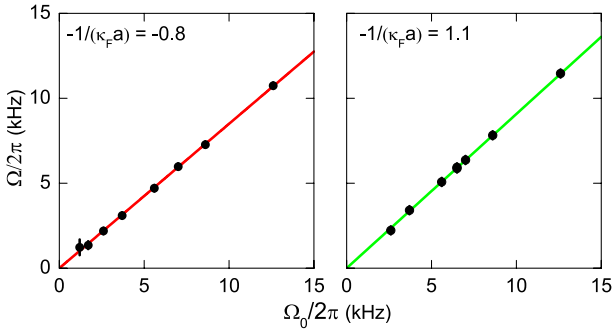

Figure 3.9: Linear increase of the Rabi frequency Ω with the unperturbed Rabi frequency Ω_0. The left (right) panel shows the driving to the repulsive (attractive) polaron. The solid lines are linear fits without offset and demonstrate the proportionality $\Omega \propto \Omega_0$.

3.5.6 Rabi oscillations and polaron quasiparticle residue

For high rf power, the signal is well beyond linear response and the K atoms exhibit coherent Rabi oscillations between the spin states $|0\rangle$ and $|1\rangle$. In this regime the oscillations are so fast, that the polaron decay plays a minor role and can be ignored to a first approximation. The Rabi frequency depends on the matrix element of the rf probe between the initial state $|0\rangle$ and the final state $|1\rangle$. Since the probe is homogenous in space, it does not change the spatial part of the atomic wavefunction and it can be described by the operator [Mas08a] $\hat{R} \propto \Omega_0 \sum_{\mathbf{q}} (\hat{a}^\dagger_{1\mathbf{q}} \hat{a}_{0\mathbf{q}} + h.c.)$ where $\hat{a}^\dagger_{i\mathbf{q}}$ ($\hat{a}_{i\mathbf{q}}$) creates (annihilates) a K atom with momentum $\mathbf{q}$ in spin state i and Ω_0 is the unperturbed Rabi frequency of the $|0\rangle$ to $|1\rangle$ transition in the non-interacting case. Considering for simplicity an impurity at rest, the initial non-interacting state is given by $|I\rangle = \hat{a}^\dagger_{0\mathbf{q}=0}|\mathrm{F}S\rangle$ where $|\mathrm{F}S\rangle$ is the Li Fermi sea. The final polaronic state at zero momentum can be written as [Che06]

$$|F\rangle = \sqrt{Z}\hat{a}^\dagger_{1\mathbf{q}=0}|\mathrm{F}S\rangle + \sum_{q<\hbar\kappa_F<p} \phi_{\mathbf{p},\mathbf{q}} \hat{a}^\dagger_{1\mathbf{q}-\mathbf{p}} \hat{b}^\dagger_{\mathbf{p}} \hat{b}_{\mathbf{q}} |\mathrm{F}S\rangle + \ldots \tag{3.8}$$

where $\hat{b}^\dagger_{\mathbf{q}}$ ($\hat{b}_{\mathbf{q}}$) creates (annihilates) a Li atom with momentum $\mathbf{q}$. The second term contains a Fermi sea with at least one particle-hole excitation and thus is orthogonal to an unperturbed Fermi sea. Therefore the matrix element reduces to $\langle F|\hat{R}|I\rangle = \sqrt{Z}\,\Omega_0$ and we obtain the Rabi frequency

$$\Omega = \sqrt{Z}\,\Omega_0. \tag{3.9}$$

We neglect the momentum dependence of the quasiparticle residue and do not perform a thermal average over the initial states, which we expect to be a good approximation since $T \ll \epsilon_F/k_B$.

In Fig. 3.9 we plot the observed Rabi frequency Ω as a function of the unperturbed Rabi frequency Ω_0. We find that the proportionality $\Omega \propto \Omega_0$ holds over a wide range of rf power. The measurements presented in the main text, taken at $\Omega_0 = 2\pi \times 6.5\,\mathrm{kHz}$ and $12.6\,\mathrm{kHz}$, are safely within this range.

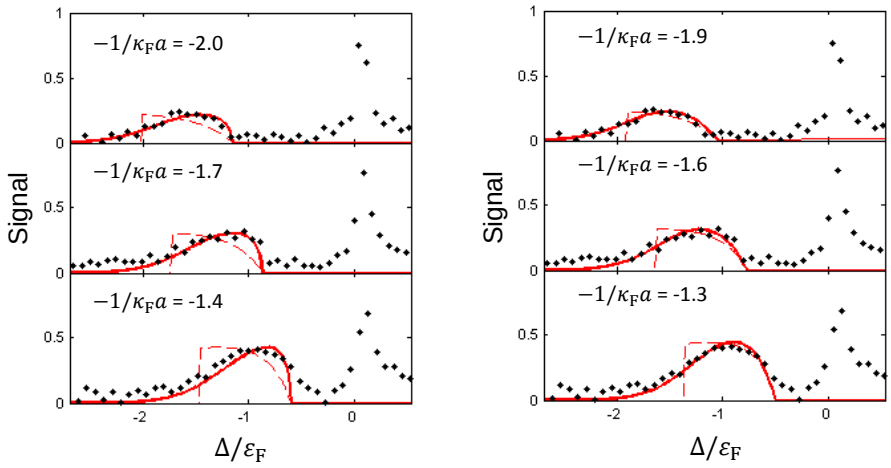

Figure 3.10: Molecule association spectra for different values of the interaction parameter. The signal is the fraction of transferred atoms as a function of the rf detuning. The black diamonds correspond to the experimental data. Left: The solid (dashed) lines correspond to the corrected line-shape model for finite (zero) temperature, where the Feshbach resonance center is shifted to a 1.5 mG higher field. Right: Replotted from Fig. 3.6 with an error in the line-shape model, see text.

3.6 Correction: Molecule-hole continuum

Our attention was called to an error in the line-shape model (Eq. (3.6)), after publication of the work presented in this section. As the factor $\mathcal{F}(k)$, we inserted the energy-normalized Franck-Condon factor from Ref. [Chi05] fulfilling $\int dE\mathcal{F}(E) = 1$. This factor includes an additional density-of-state $\rho(E_r) \propto \sqrt{E_r}$, that must be divided out, in the integration over momentum in Eq. (3.6). Hence, the Franck-Condon factor used in this equation should read $\mathcal{F}(k) \propto (1/E_b^3)^{1/2}(1 + E_r/E_b)^{-2}$.

Revisiting our data analysis we find only a minor effect on the results presented in this section. The result of our reanalysis of the data shown in Fig. 3.6, i.e. fitting the corrected line-shape model to the molecule-association data, is shown in the left column of Fig. 3.10. From this reanalysis, we determine the center of the Feshbach resonance to be at $B_0 = 154.7205(20)$ mG, a slightly larger magnetic-field value compared to our previous erroneous analysis, which yielded 154.719(2) mG. To take this correction of the Feshbach resonance center into account, all experimental data should be shifted to about 0.08 lower values of the interaction parameter $-1/(\kappa_F a)$, i.e. $-1/(\kappa_F a) \to -1/(\kappa_F a) - 0.08$.

Chapter 4

Publication: Decoherence of Impurities in a Fermi Sea of Ultracold Atoms[1]

Physical Review Letters **115**, 135302 (2015)
submitted 10 June 2015, published 22 September 2015
DOI: 10.1103/PhysRevLett.115.135302
Editor's suggestion

M. Cetina[1,2], M. Jag[1,2], R. S. Lous[1,2], J. T. M. Walraven[1,3], R. Grimm[1,2], R. S. Christensen[4], and G. M. Bruun[4]

[1] *Institut für Quantenoptik und Quanteninformation (IQOQI), Österreichische Akademie der Wissenschaften, 6020 Innsbruck, Austria*
[2] *Institut für Experimentalphysik, Universität Innsbruck, 6020 Innsbruck, Austria*
[3] *Van der Waals-Zeeman Institute, Institute of Physics, University of Amsterdam, Science Park 904, 1098 XH Amsterdam, The Netherlands*
[4] *Department of Physics and Astronomy, Aarhus University, DK-8000 Aarhus C, Denmark*

[1] The author of the present thesis contributed to developing the experimental procedures together with M.C., performed the measurements with M.C. and R.S.L., and analyzed the data together with M.C., and R.S.L. under the supervision of R.G. All authors contributed to writing the manuscript.

4.1 Abstract

We investigate the decoherence of ^{40}K impurities interacting with a three-dimensional Fermi sea of ^{6}Li across an interspecies Feshbach resonance. The decoherence is measured as a function of the interaction strength and temperature using a spin-echo atom interferometry method. For weak to moderate interaction strengths, we interpret our measurements in terms of scattering of K quasiparticles by the Fermi sea and find very good agreement with a Fermi liquid calculation. For strong interactions, we observe significant enhancement of the decoherence rate, which is largely independent of temperature, pointing to behavior that is beyond the scattering of quasiparticles in the Fermi liquid picture.

4.2 Introduction

Many-body fermionic systems with strong interactions play a central role in condensed-matter, nuclear, and high-energy physics. The intricate quantum correlations between fermions challenge our understanding of these systems. Mixtures of ultracold fermionic gases offer outstanding opportunities to study strongly interacting fermions experimentally. Since the turn of the century, the excellent control over the strength of the interaction and the composition of these mixtures has allowed investigations addressing the broad spectrum from few-body to many-body phenomena [Blo08, Gio08]. Tuning of the interaction is achieved using Feshbach resonances [Chi10]. The composition is varied by selecting internal states or by mixing different atomic species. This development has led to many exciting results concerning the quantum phases of fermionic mixtures, their excitations, superfluid behavior, and the equation of state [Zwi15].

In two-component fermionic systems with a large population imbalance, the minority atoms have been shown to form quasiparticles termed Fermi polarons, even for surprisingly large coupling strengths [Sch09, Koh12b, Kos12, Mas14]. These are long-lived states described by Fermi liquid theory [Bay04]. Their lifetime is limited by scattering against the majority atoms, which is suppressed by Pauli blocking as the temperature approaches zero [Lan57, Lan56]. Although the quasiparticle scattering rate has been determined in two-dimensional electron gases [Ber95, Mur95, Slu96], measurements in well-defined three-dimensional (3D) fermionic systems have remained an experimental challenge.

Intriguing questions are related to the behavior of impurities and, more generally, Fermi mixtures in the strongly interacting regime [Mas14, Nas11, Sag15]. For investigating an impurity in a Fermi sea, Refs. [Goo11, Kna12] suggested a time-domain method that is applicable for a wide range of interaction strengths. This approach can be regarded as a measurement of the coherence of a superposition of internal states of the impurity atoms using interferometery [Cro09]. Atom coherence has previously been used to probe many-body demagnetization in fermionic systems [Bar14] and impurity scattering in bosonic systems [Sce13].

In this Letter, we report on measurements of decoherence of K atoms immersed in a Fermi

sea of Li using the method proposed in Ref. [Kna12], in the regime of strong population imbalance. We tune the interaction between the Li and K atoms using an interspecies Feshbach resonance (FR). For weak to moderately strong interactions, we interpret the measured decoherence in terms of scattering of K quasiparticles by the Li Fermi sea. We find very good agreement with a Fermi liquid calculation. This provides a determination of the quasiparticle scattering rate in a clean 3D fermionic system. We extend our measurements to strong Li-K interactions and find decoherence rates that are comparable to the fastest dynamics available in our system. These rates do not increase with temperature, which is an indication of zero-temperature quantum dynamics in a fermionic many-body system.

4.3 Main results

The starting point of our experiments is an evaporatively cooled, thermally equilibrated mixture of typically 3×10^5 ^{6}Li atoms and 1.5×10^4 ^{40}K atoms, trapped in a crossed-beam 1064-nm optical dipole trap under conditions similar to those in Ref. [Koh12b]. The Li cloud is degenerate, with $k_B T/\epsilon_F$ as low as 0.15, where T is the temperature and $\epsilon_F \approx h \times 35\,\mathrm{kHz}$ is the average Li Fermi energy sampled by the K atoms. Because of the Li Fermi pressure and the more than two times stronger optical potential for K, the K cloud is much smaller than the Li cloud [Tre11a], and therefore samples a nearly homogenous Li environment, with a standard deviation in the local Li Fermi energy of less than $0.1\,\epsilon_F$. In spite of the smaller size of the K cloud, the concentration of K in the Li sea remains low, with $\bar{n}_\mathrm{K}/\bar{n}_{\mathrm{Li}} \approx 0.3$, where $\bar{n}_\mathrm{K}$ ($\bar{n}_{\mathrm{Li}}$) is the average K (Li) number density sampled by the K atoms. The K ensemble is correspondingly non-degenerate, with $k_B T/E_F^\mathrm{K} > 0.9$, where E_F^K is the peak K Fermi energy.

We tune the interaction between the K and Li atoms using an interspecies FR between the Li atoms in the lowest Zeeman sub-level Li$|1\rangle$ and K atoms in the third-lowest sub-level K$|3\rangle$ [Nai11]. We quantify the interactions between Li and K by the dimensionless interaction parameter $-1/\kappa_F a$, where $\kappa_F = \hbar^{-1}\sqrt{2 m_{\mathrm{Li}} \epsilon_F}$ is the Li Fermi wavenumber with m_{Li} the Li mass, and a is the s-wave interspecies scattering length. The latter can be tuned as $a = a_{bg}[1 - \Delta/(B - B_0)]$ by applying a magnetic field B, where $B_0 \approx 154.7\,\mathrm{G}$ is the resonance center, $a_{bg} = 63.0\,a_0$ (a_0 is Bohr's radius) and Δ=880 mG [Nai11]. The relatively narrow nature of our FR causes significant momentum dependence of the interspecies interaction. We characterize this effect by the length parameter R^* [Pet04a, Koh12b]. In our experiments $\kappa_F R^*$ is approximately 0.9, corresponding to an intermediate regime where the interaction is near-universal with substantial effective-range effects.

We probe the decoherence of the K atoms using a radio-frequency (rf) interferometric technique, as illustrated in Fig. 4.1. The K atoms are initially prepared in the second-lowest Zeeman sub-level K$|2\rangle$ while the Li atoms remain in the Li$|1\rangle$ state throughout the experiment. On the time scale of our measurements, the interactions between these atoms, characterized by the s-wave scattering length $a_{12} \approx a_{bg}$, can be neglected. We apply a $\pi/2$ rf-pulse (typically 10 μs-long) to prepare the K atoms in an equal superposition of the K$|3\rangle$ and K$|2\rangle$ states. After a variable interaction time τ, we apply a second $\pi/2$ rf-pulse before determining the numbers N_2 and N_3 of atoms in the K$|2\rangle$ and K$|3\rangle$ states using absorption

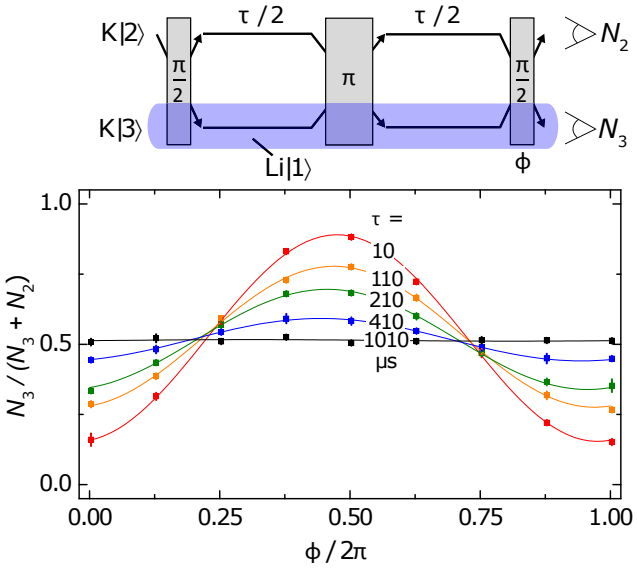

Figure 4.1: Interferometeric method for measuring the decoherence of K in a Li Fermi sea. The upper illustration shows a schematic of the rf pulse sequence. The atoms in the K$|3\rangle$ state interact with a Fermi sea of Li$|1\rangle$ atoms, as indicated by the shaded region. The graph shows the fraction of the K atoms transferred to the K$|3\rangle$ state as a function of the relative phase of the final $\pi/2$ rf pulse for various interaction times τ and for $-1/\kappa_F a$=2.1, $T = 0.16\epsilon_F/k_B$.

imaging (see Supplemental Material). To decrease the sensitivity to the magnetic field noise and to the inhomogeneities in the atom densities, we perform a spin echo by splitting the interaction time into two equal halves separated by a π rf-pulse.

Shifting the phase of the rf oscillator by ϕ between the π and the second $\pi/2$ pulses causes a sinusoidal variation in the fraction $f = N_3/(N_2 + N_3)$ of the K atoms transferred to K$|3\rangle$, as shown in Fig. 4.1. We quantify the coherence of the state of the K atoms by the contrast $C = (f_{max} - f_{min})/(f_{max} + f_{min})$ of these oscillations. The interaction of the K atoms with the Li cloud causes an exponential decrease in the observed contrast with increasing interaction time τ, as shown in Fig. 4.2(a). The interaction also shifts the rf transition frequency and decreases the rf coupling between the K$|2\rangle$ and K$|3\rangle$ states [Koh12b], which we account for by adjusting the rf frequency and the duration of our rf pulses. In this way, we measure the decoherence of K atoms for $-1/\kappa_F a < -0.8$ and $-1/\kappa_F a > 1.4$. Near the center of the resonance, the fast loss of contrast during the rf pulses limits the applicability of this method.

To measure the decoherence of K in the strongly interacting regime, we use laser light to rapidly displace our magnetic FR [Bau09b, Bau09a, Cla15]. Optical control of our FR allows us to apply the rf pulses away from the FR and then rapidly bring the atoms into resonance for the duration of the interaction time[2] τ. This method circumvents the loss of contrast during the rf pulses and allows us to probe the K decoherence across the full range of interaction parameters. The displacement of our FR arises from the laser-induced differential AC Stark shift between the free-atom level and the molecular state involved in the FR. The

[2] For measurements on the attractive (repulsive) side of the FR, we shift B_0 upwards (downwards). For measurements near the resonance, we verify that the direction of the shift of B_0 does not affect the result.

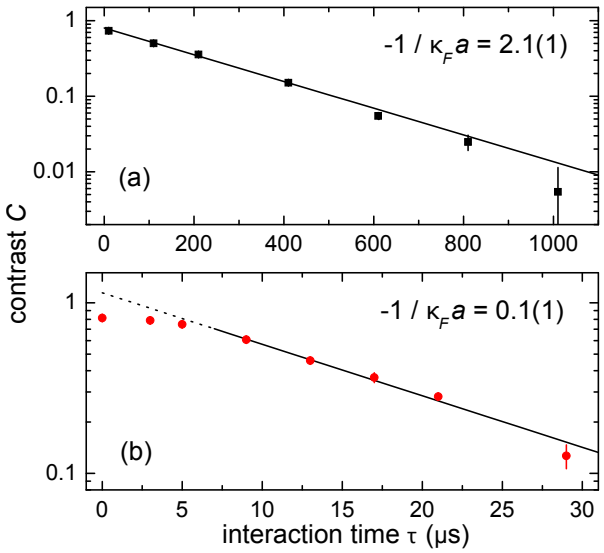

Figure 4.2: Contrast C as a function of interaction time τ. In (a), we show results for moderately attractive interspecies interactions ($-1/\kappa_F a$=2.1), corresponding to Fig. 4.1. In (b), we probe the system in the strongly interacting regime ($-1/\kappa_F a$=0.15) for $T = 0.20\,\epsilon_F/k_B$ by rapidly shifting the interaction parameter from 2.2 to 0.15 during the interaction time. The solid lines are exponential fits to the points with $\tau > 7\,\mu$s. The dotted line is an extrapolation to τ=0.

AC Stark shift is induced by the 1064-nm trapping light, as we investigated in Ref. [Jag14]. Although the differential shift here amounts to only 10% of the total trapping potential, using a high-intensity beam with up to 65 kW/cm^2, we can displace B_0 by up to 40 mG in less than 200 ns – all while preserving the harmonic trapping potential (see Supplemental Material). This displacement corresponds to a change in the interaction parameter of up to $\pm$2.1 on a timescale of 0.05 τ_F, where $\tau_F = \hbar/\epsilon_F \approx 4.5\,\mu$s is the Fermi time.

In Fig. 4.2(b), we show the dependence of the contrast C on the interaction time τ near the center of our FR. The contrast starts to decay after an initial delay of approximately τ_F. This delay can be explained in terms of quantum evolution of the system with an interaction energy bounded from above by ϵ_F [Kna12]. For $\tau > 1.6\tau_F \approx 7\,\mu$s, the decrease in contrast is well-described by an exponential decay. The fitted rate γ_{coh}=0.28(2)τ_F^{-1} is comparable to the inverse Fermi time, indicating that our experiment cannot be fully described by the scattering of quasiparticles in the Fermi liquid picture, which assumes long-lived quasiparticles [Bay04].

In Fig. 4.3 we show the dependence of the fitted rate γ_{coh} on the interaction parameter. We present data with two decades of dynamic range and demonstrate a dramatic resonant enhancement of the decoherence rate, reaching values up to $0.4\,\tau_F^{-1}$. The data do not exhibit any clear dependence on $\bar{n}_\mathrm{K}/\bar{n}_{\mathrm{Li}}$ across the full range $0.17 \leq \bar{n}_\mathrm{K}/\bar{n}_{\mathrm{Li}} \leq 0.43$. In addition to the statistical errors indicated by the error bars, the data are subject to variations of k_BT/ϵ_F, $\kappa_F R^*$ and $\bar{n}_\mathrm{K}/\bar{n}_{\mathrm{Li}}$ with standard deviations of 0.01, 0.02 and 0.07 about their mean values of 0.16, 0.93 and 0.27, respectively. The calibration of the Li atom number introduces a 6% systematic uncertainty in ϵ_F and τ_F, as well as a corresponding 3% uncertainty in κ_F. Our total error budget includes further 3% systematic errors in a and R^* arising from

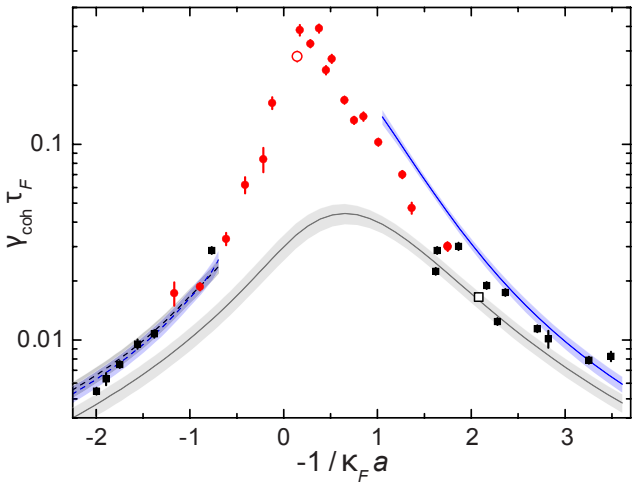

Figure 4.3: Decoherence rate of K in a Li Fermi sea as a function of the interaction parameter for an average temperature T=0.16 ϵ_F/k_B (see text). The measurements with (without) rapid shifting of the FR are shown as the red circles (black squares). The measurements from Fig. 4.2 are indicated by open symbols. The solid upper (blue) and lower (black) lines correspond to the prediction of the Fermi liquid theory with and without medium corrections, respectively. The dashed lines incorporate corrections due to decay to Feshbach molecules. The shaded areas show the 1σ effect of the experimental uncertainties on the theoretical predictions.

the uncertainty in ΔB, and a ± 0.05 error in $1/\kappa_F a$ resulting from an uncertainty in the determination of B_0 of ± 1 mG (see Supplemental Material).

For weak to moderate interactions, there are well-defined K quasiparticles, and we now show that the evolution of the contrast C on timescales much longer than τ_F can be related to the mean quasiparticle scattering rate γ_s. Each scattering event provides which-way information that distinguishes between the two paths in the interferometer in Fig. 4.1 and thus erases the interference effect. At any given time, the interaction affects only one of the two paths, decreasing the probability for the system to stay in this path at the rate γ_s. Since our signal arises from the interference of the amplitudes in the two interferometer paths, we expect the interaction to lead to a decrease of the observed contrast at the rate $\gamma_s/2$.

From Fermi liquid theory, the scattering rate γ_{p_1} of a K quasiparticle with momentum $\mathbf{p}_1$ is given by [Bay04]

$$\gamma_{p_1} = \iint d\check{p}_2 d\Omega \frac{m_r p_r}{4\pi^2} |\mathcal{T}|^2 [f^{\mathrm{Li}}_{p_2}(1 - f^{\mathrm{K}}_{p_3} - f^{\mathrm{Li}}_{p_4}) + f^{\mathrm{K}}_{p_3} f^{\mathrm{Li}}_{p_4}]. \tag{4.1}$$

Here $\mathcal{T}$ is the scattering matrix for the scattering of K atoms with Li atoms with momenta $\mathbf{p}_1$ and $\mathbf{p}_2$ respectively to momenta $\mathbf{p}_3$ and $\mathbf{p}_4$. We have defined $d\check{p}_2 = d^3p_2/(2\pi)^3$, and Ω is the solid angle for the direction of the outgoing relative momentum. The distribution functions are $f_p^{\mathrm{Li/K}} = [e^{\beta(E_p^{\mathrm{Li/K}} - \mu_{\mathrm{Li/K}})} + 1]^{-1}$ with the chemical potentials $\mu_{\mathrm{Li/K}}$ for the Li /K atoms respectively. The dominant medium effects can be shown to enter in the scattering matrix $\mathcal{T}$ via ladder diagrams, whereas the quasiparticles can be assumed to have the ideal gas energy dispersion $E_p^{\mathrm{K/Li}} = p^2/2m_{\mathrm{K/Li}}$ [Bru05b, Ens12]. The details of the calculation of γ_{p_1} are described in [Chr15]. In addition, we account for the reduced quasiparticles residue

Z by multiplying the collision rate by Z calculated from the ladder approximation [Mas14]. To obtain the mean scattering rate γ_s, we calculate the thermal average $\gamma_s = \int d\check{p} f_p^{\mathrm{K}} \gamma_p$. To include the effects of the trap, we use effective Fermi energies, which are obtained by averaging the local Fermi energy over the density of the K atoms in the trap. This approach is justified since the K atoms only probe a small region of the Li gas, and because the momentum distribution of the K atoms is nearly classical.

On the repulsive side of the FR, we need to consider additional effects arising from the decay of the atoms into the molecular state that underlies our FR. The rate Γ of this process was calculated and confirmed by measurements in Ref. [Koh12b], reaching values as high as 0.02 τ_F^{-1} close to resonance. Since the decay to molecules provides which-way information, it will contribute at least $\Gamma/2$ to the measured decoherence rate. The decay also releases energy and creates holes in the Li Fermi sea, increasing the value of $k_B T/\epsilon_F$ during our measurement to 0.20 (1) (see Supplemental Material).

In Fig. 4.3, we plot the calculated decoherence rate $\gamma_s/2$ as a function of the interaction parameter. The lower solid line is obtained by using the vacuum scattering matrix $\mathcal{T}_{\mathrm{vac}}$ [Chr15] in (4.1), whereas the upper solid line is obtained by using a $\mathcal{T}$ matrix which includes medium effects using the ladder approximation. The dashed lines include the effects of decay into the molecular state. The calculated decoherence rate agrees with the experimental values very well for $-1/k_F a \gtrsim 1.5$ and for $-1/k_F a \lesssim -1$. This gives strong evidence that the observed decoherence indeed is due to quasiparticle collisions. The significant asymmetry of the decoherence rate around $1/k_F a = 0$ arises from the narrow nature of the FR [Chr15]. The calculated decoherence rate is larger when medium effects are included in the $\mathcal{T}$ matrix. This is due to pair correlations, which can increase the collisional cross section significantly [Chr15]. We see that the inclusion of these medium effects on the scattering matrix improves the agreement with the experimental data. For stronger interactions, the calculation does not fit the experiment, which is expected since there are no well-defined quasiparticles in the unitarity regime [Koh12b]. Our model agrees with the observed absence of a dependence of γ_{coh} on $\bar{n}_{\mathrm{K}}/\bar{n}_{\mathrm{Li}}$ since the K cloud is close to the classical regime where $f_{p_3}^{\mathrm{K}} \ll 1$ and the momentum distribution of the K atoms is solely determined by the temperature.

Further insight into the nature of the observed decoherence can be gained by varying the temperature of our atom mixture, which we accomplish by changing the endpoint of our evaporative cooling. We show the dependence of the measured decoherence rate on temperature in Fig. 4.4. In addition to the statistical errors shown by the error bars, the data are subject to small variations of $-1/\kappa_F a$, $\kappa_F R^*$ and $\bar{n}_{\mathrm{K}}/\bar{n}_{\mathrm{Li}}$ with standard deviations of 0.05, 0.03 and 0.1, respectively. Our total error budget also includes the above-mentioned systematic uncertainties in ϵ_F, κ_F, a and R^*.

Away from the FR, the measured decoherence rates are in very good agreement with the predictions of the Fermi liquid theory. The linear dependence of γ_{coh} on temperature in this regime arises from the high relative mass of the K atoms, causing the Li-K scattering to resemble scattering by fixed impurities. This is similar to the situation in metals where the scattering of electrons by fixed nuclei gives rise to the well-known linear dependence of the nuclear decoherence rates on temperature [Kor50]. The red circles in Fig. 4.4 represent the measurements for resonant interactions. The rates obtained in this regime are more

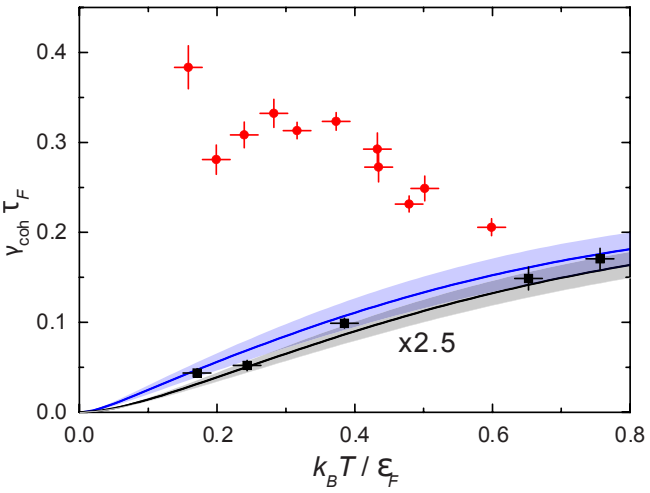

Figure 4.4: Decoherence rate of K in a fermionic Li cloud as a function of temperature. The data for $-1/\kappa_F a$=0.2, $\kappa_F R^*$=0.94, $\bar{n}_K/\bar{n}_{Li}$=0.2 ($-1/\kappa_F a$=2.4, $\kappa_F R^*$=0.89, $\bar{n}_K/\bar{n}_{Li}$=0.3) measured with (without) rapid shifting of the FR is shown as red circles (black squares). The solid blue and black lines correspond to the predictions of the Fermi liquid theory for $-1/\kappa_F a$=2.4 with and without medium corrections, respectively. The shaded areas show the 1σ effect of the experimental uncertainties on the theoretical predictions.

than an order of magnitude higher than the off-resonant rates, and do not increase with temperature.

4.4 Conclusion

In conclusion, we established that for weak to moderate interaction strengths, the decoherence of K in a Li Fermi sea is dominated by quasiparticle scattering. Our observations for strong interactions cannot be explained solely by quasiparticle scattering and indicate decoherence processes which persist at zero temperature. This offers an exciting opportunity to explore the many-body quantum dynamics of an impurity submerged in a Fermi sea.

Acknowledgements

We thank F. Schreck, C. Kohstall, I. Fritsche, P. Jeglič, Y. Ohashi, R. Schmidt, E. Demler, and, especially, M. Parish, J. Levinsen and M. Baranov for helpful discussions. We thank P. Massignan for sending us data for the quasiparticle residue and decay. We acknowledge funding by the Austrian Science Fund FWF within the SFB FoQuS (F40-P04) and support of the Villum Foundation via Grant No. VKR023163.

4.5 Supplemental material

4.5.1 Optical trap setup

We perform our measurements in dipole traps formed by two single-frequency, 1064-nm laser beams produced by a solid-state laser system (Innolight Mephisto 42NE MOPA). The beams intersect at an angle of 16°. To avoid standing wave effects, the beams are offset in frequency by 5 to 10 MHz. To shift the Feshbach resonance (FR), we keep one of the two beams ("D") static and use acousto-optic modulators (AOMs) to rapidly change the other beam. Changing only the intensity of this latter beam would excite strong oscillations of the atomic cloud. We counter this by switching from a beam with a low peak intensity and small size ("S") to a beam with a large intensity and large size ("V") propagating in the same direction. The waists, positions and intensities of the "S" and "V" beams are adjusted so as to match the centers and curvatures of the resulting optical potentials, preventing collective excitations of the atomic cloud.

This method for shifting the FR poses two technical challenges. First, the overlap between the optical axes of the "S" and "V" beams needs to be maintained with an accuracy that is much better than the smallest extent of the atomic clouds (about 5 μm). Second, to maximize the shift of the resonance, the curvature of the optical potential due to the larger beam needs to be minimized relative to its intensity. We address both of these challenges using the optical system shown in Fig. 4.5.

To ensure beam pointing stability, we couple the laser light into Panda polarization-maintaining fiber patchcords (Thorlabs P3-980PM-FC) with 6 μm core diameter. For the "S" and "D" beams, we use 5-m long fibers. When using a 5-m long fiber for the "V"-beam, we observed a saturation of the fiber output power at 1.1 W, together with a sharp increase of the reflected power from the fiber. These effects were not observed with up to 10 W of output power from the fiber when a 2-m long fiber was used. We interpret these observations in terms of stimulated Brillouin scattering [Ruf04], whose threshold power is inversely proportional to the fiber length.

To prevent the degradation of the fiber ends, the "V" beam is operated with brief (< 0.3 ms) and infrequent (< 1/min) pulses. Although, in the P3-980PM-FC patchcords, the fiber is attached to the ferrule using an epoxy adhesive, we did not observe any degradation of the fiber transmission after one year of operation with peak powers up to 10 W.

To maintain relative pointing stability of the "S" and "V" beams, the outputs of the "S" and "V" fibers (e^{-2} divergence half-angle = 74(3) mrad) are combined on a polarizing beamsplitter. At this location, the "S" and "V" beams have waists of 0.31(1) mm and 0.75(1) mm, respectively. In the same plane, "S" and "V" beams are converging with radii of curvature of 370(20) mm and 390(20) mm, respectively. The output of the beamsplitter is projected with 7.6× demagnification onto the atoms using a telescope composed of the lenses labeled as L1, L2, L3 and L4 in Fig. 4.5. The distance between the lenses L2 and L3 is adjusted so as to obtain a nearly collimated "S" beam after the lens L3 with a 1.2(1)-mm waist.

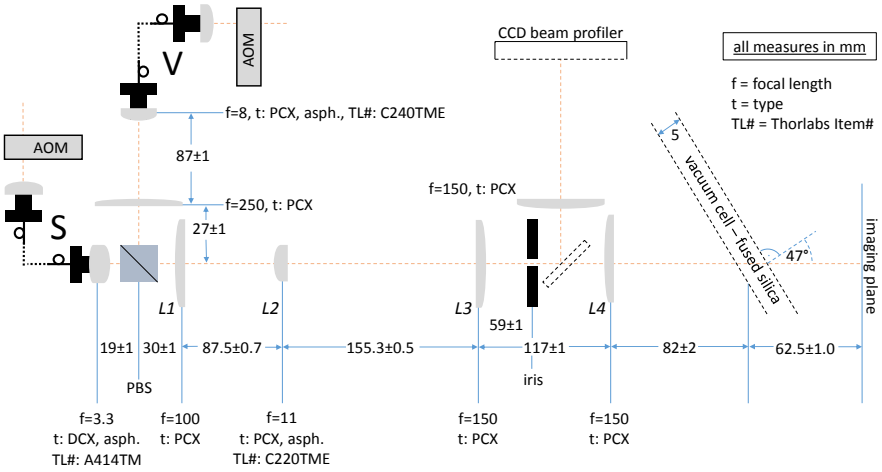

Figure 4.5: Illustration of the optical setup for producing and switching optical dipole traps of different sizes with highly stable relative position.

Higher spatial frequency components in the beams (arising e.g. from stray reflections) increase the curvature of the optical potential relative to its depth. To mitigate this problem, we spatially filter the "S" and "V" beams by passing them through a 5.3-mm diameter graphite aperture in a plane that is Fourier-conjugate to the location of the atoms (Fig. 4.5).

We measured the sizes of the "S" and "V" beams at the location of the atoms by deflecting the beams using an auxiliary mirror and then focusing them onto a CCD beam profiler, as shown in Fig. 4.5. The $1/e^2$ radii of the "S" and "V" beams were determined to be 38(2) μm, and 91(3) μm, respectively. The size of the "D" beam at the location of the atoms was determined to be 48(2) μm.

4.5.2 Parameters of the 154.7 G Feshbach resonance

The FR that we employ for tuning the interactions in our system occurs between ^{6}Li atoms in their lowest internal state, denoted Li$|1\rangle$ ($F = 1/2$, $m_F = +1/2$), and ^{40}K atoms in their third-to-lowest state K$|3\rangle$ ($F = 9/2, m_F = -5/2$). We parametrize the Li$|1\rangle$-K$|3\rangle$ scattering length near the 154.7 G FR by the usual expression [Chi10]

$$a\,(B) = a_{bg}\left(1 - \frac{\Delta}{B - B_0}\right). \tag{4.2}$$

For the background scattering length $a_{\rm bg}$ and the resonance width Δ, we use the values $a_{\rm bg} = 63.0\ a_0$ and $\Delta = 0.880$ G from the coupled-channel calculation in [Nai11].

The narrow nature of the Li$|1\rangle$-K$|3\rangle$ FR causes a significant variation of Li-K scattering across the range of the collision energies encountered in our experiment [Chi10]. We obtain quantitative information on this effect from measurements of the molecular binding energy. We measure the binding energy using two methods: radio-frequency (rf) association

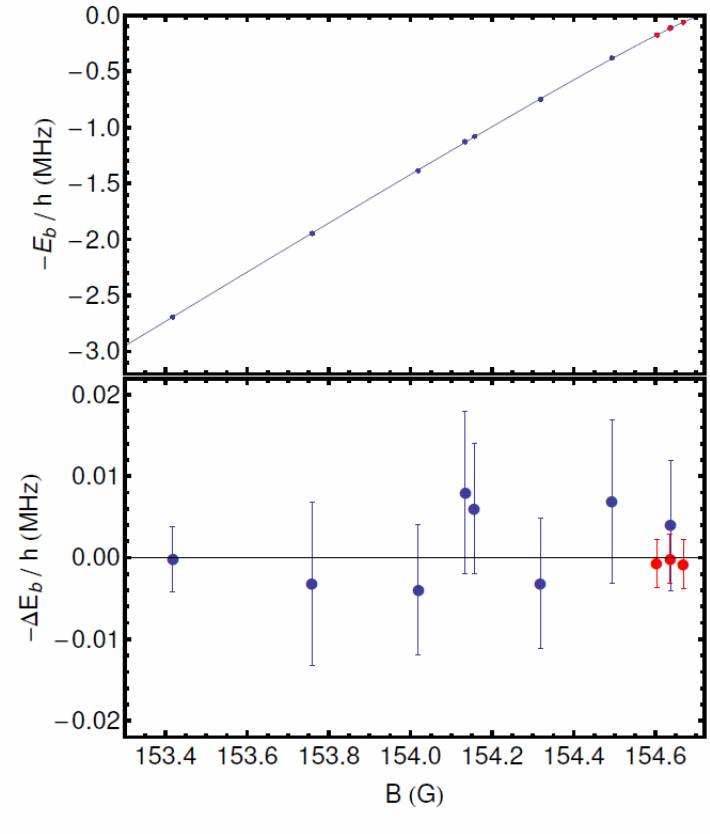

Figure 4.6: Molecular binding energy near the 154.7 G Li|1⟩-K|3⟩ Feshbach resonance measured using rf association (red points) and magnetic field modulation spectroscopy (blue points). The lower panel shows the residuals of a fit to the data with the model based on Eq. (4.3) with $\delta\mu$ and B_0 as free parameters.

[Jag14] and magnetic field modulation spectroscopy [Lan09]. The combined results of these measurements are shown in Fig. 4.6.

In order to parametrize the dependence of the molecular binding energy E_b on the magnetic detuning $B - B_0$ near the dissociation threshold, we first introduce the wavenumber κ, in terms of which $E_\mathrm{b} = \hbar^2\kappa^2/2\mu$, where $\mu = m_\mathrm{Li}m_\mathrm{K}/(m_\mathrm{Li} + m_\mathrm{K})$ is the reduced mass. We then express the magnetic detuning $B - B_0$ as a function of κ by a Taylor expansion up to second order of the form

$$B - B_0 \quad = \quad -a_\mathrm{bg}\Delta\kappa - \frac{\hbar^2\kappa^2}{2\mu\delta\mu} \; . \tag{4.3}$$

The coefficient $a_\mathrm{bg}\Delta$ in front of the linear term is determined by the well-known universal relation between κ and a near the resonance. We fit Eq. (4.3) to the data from Fig. 4.6 with $\delta\mu$ and B_0 as free parameters, while fixing a_bg and Δ to the values from Ref. [Nai11]. From this fit, we obtain $\delta\mu/h = 2.35\,(2)$ MHz/G. Our fitting model is equivalent to the prediction of the two-channel model from [Pet04a] with $R^* = \hbar^2/(2\mu a_\mathrm{bg}\delta\mu\Delta)$. We note that this model neglects the background scattering term in Eq. (4.2).

Our measurements of the binding energy allow us to determine the momentum dependence

of Li-K collisions near the resonance. For small values of the collision momentum $\hbar k$, we can use the well-known effective range expansion to write the inverse scattering amplitude as

$$f(k)^{-1} = -\frac{1}{a} + \frac{1}{2} r_{\text{eff}} k^2 - ik \ .$$

Since the existence of the bound state implies that the scattering amplitude has a pole at $k = i\kappa$, we obtain

$$0 = \frac{1}{a} - \frac{1}{2} r_{\text{eff}} (i\kappa)^2 + i(i\kappa) \ .$$

Substituting the expression (4.2) for $a(B)$, we can then write

$$a_{\text{bg}}^{-1} \left(1 - \frac{\Delta}{B - B_0}\right)^{-1} + \frac{1}{2} r_{\text{eff}} \kappa - \kappa = 0 \ .$$

Then, substituting the expression (4.3) for the detuning $B - B_0$, we obtain

$$a_{\text{bg}}^{-1} \left(1 - \frac{\Delta}{-a_{\text{bg}} \Delta \kappa - \frac{\hbar^2 \kappa^2}{2\mu \delta\mu}}\right)^{-1} + \frac{1}{2} r_{\text{eff}} \kappa - \kappa = 0 \ .$$

Taylor-expanding this near $\kappa = 0$, we get

$$\left(-a_{\text{bg}} + \frac{r_{\text{eff}}}{2} + \frac{\hbar^2}{2 a_{\text{bg}} \mu \delta\mu \Delta}\right) \kappa^2 + O\left(\kappa^3\right) = 0 \ ,$$

whence we obtain

$$r_{\text{eff}} = 2 a_{\text{bg}} - \frac{\hbar^2}{a_{\text{bg}} \mu \delta\mu \Delta} \ . \tag{4.4}$$

We can summarize the parameters of the Li$|1\rangle$-K$|3\rangle$ FR with three independent parameters:

$$\begin{aligned} a_{\text{bg}} &= 63.0\, a_0 \ , \\ \Delta &= 0.880\, \text{G} \ , \\ \delta\mu/h &= 2.35\,(2)\ \text{M}Hz/G \ . \end{aligned}$$

From this, we can derive the values

$$\begin{aligned} R^* &= 2650\,(25)\ a_0 \ , \\ r_{\text{eff}} &= -5175\,(50)\ a_0 \ . \end{aligned}$$

4.5.3 Light shift of the Feshbach resonance

As we pointed out in the main text, as well as in Refs. [Koh12b, Jag14], the optical trap induces a differential light shift between the atom pair state and the molecular state giving rise to the FR near 154.7 G. This leads to a light-induced shift of the FR. To produce these

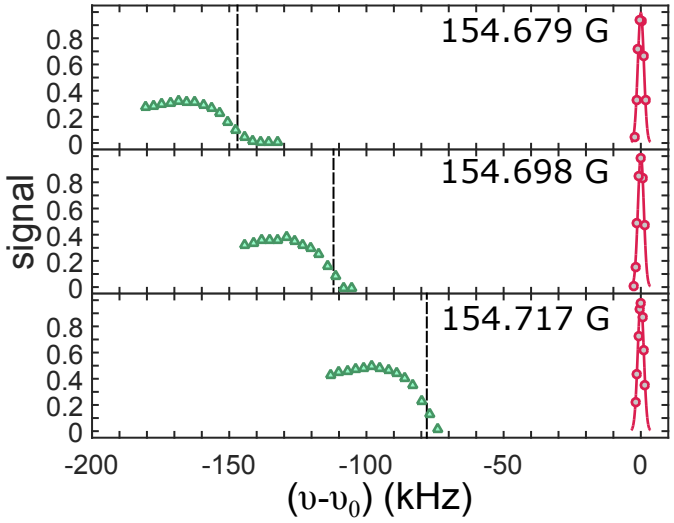

Figure 4.7: Data from the molecular rf-association spectroscopy for trap 3. The red points were taken with a 0.5-ms rf pulse with an intensity set to the value matching the π-pulse condition in the absence of interactions (no Li$|1\rangle$ present). The green points were recorded with more than 30$\times$ increased rf intensity. The dashed lines indicate the binding energy $E_\mathrm{b}(B)$ as determined with the 20% criterion (see text).

shifts in the experiments presented in the main text, we use a near-infrared laser as discussed in Section 4.5.1 in four different trap settings (see Table 4.1).

To determine the resonance center B_0 for a given trap setting, we follow the experimental procedure outlined in the Supplemental Material of Ref. [Jag14]. For the data analysis, we use the updated binding energy model presented in the preceeding Section. For each trap setting, we perform rf association spectroscopy of the Feshbach molecules. We start by preparing a nonresonant mixture of Li atoms in the state Li$|1\rangle$ and K atoms in their second-to-lowest state K$|2\rangle$ several tens of mG below B_0. At this field, we apply an rf pulse (duration of a few 100 μs) at a variable frequency ν, several kHz below the unperturbed K$|2\rangle\rightarrow$K$|3\rangle$ transition frequency ν_0. This pulse drives Li$|1\rangle$-K$|2\rangle$ atom pairs into the Li$|1\rangle$K$|3\rangle$ dimer state. To determine the number of dimers associated, we subsequently dissociate the dimers into pairs of Li$|1\rangle$ and K$|3\rangle$ atoms by a magnetic field ramp (duration of a few 100 μs) to a magnetic field above 154.8 G. By recording absorption images we then determine the populations N_2 and N_3 of the K spin states K$|2\rangle$ and K$|3\rangle$, respectively.

Plotting the signal, given by $N_3/(N_3+N_2)$, against the rf detuning $\nu-\nu_0$, we resolve the molecule association spectrum. In Fig. 4.7 we show sample spectra recorded for one of the trap settings used in the experiments. We determine the energy of the molecules relative to the energy of noninteracting K$|3\rangle$ atoms from the onset frequency of the molecular association spectra. As the onset frequency, we use the upper rf frequency at which the fraction of atoms transferred is roughly 20% of its peak height. We have checked that, within the errors of our measurements, this criterion agrees with the result obtained by fitting the line-shape model of Ref. [Chi05] to the spectra, as was done in Ref. [Koh12b]. This procedure is applied at various magnetic fields for each trap setting used in the experiments.

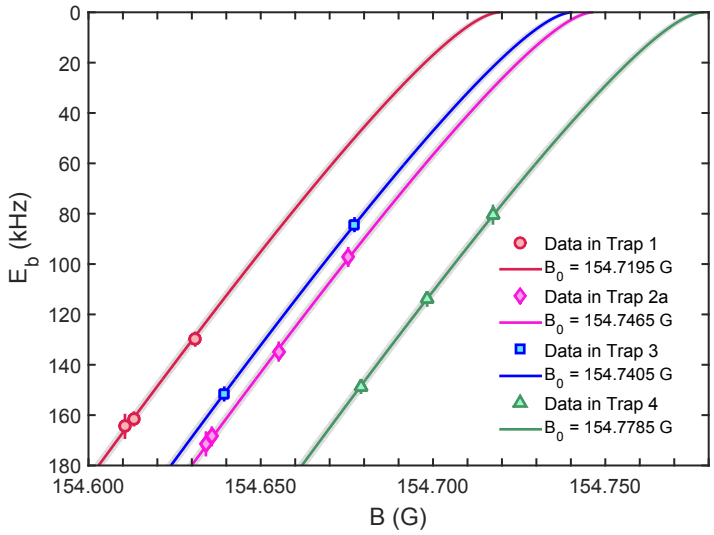

Figure 4.8: Determination of the FR center B_0 by rf association of dimers. The points show the experimentally determined molecular binding energies $E_\mathrm{b}(B)$ for four trap settings. The solid curves are fits of the binding energy according to Eq. (4.3). The gray shaded areas indicate the typical error range of our fit analysis.

The interaction between the formed LiK molecules and the Li atoms leads to an energy shift of the molecular state. We use the mean-field model from [Jag14] to predict the corresponding shift in the onset frequency in the rf association measurements as +2.0(4) kHz. To determine the molecular binding energy in the absence of the Li cloud, we subtract this small offset from the onset frequencies determined above.

We fit the binding energy according to Eq. (4.3) to the data, with B_0 as the only free parameter (see Fig. 4.8). The other parameters are fixed to the values from Section 4.5.2. This procedure allows us to determine the resonance center in each trap setting with an uncertainty of $\pm 1.5\,\mathrm{mG}$. The accuracy of our determination of the resonance position is limited by the uncertainty in the FR parameters in the model for the binding energy. The FR centers determined for our four trap settings of Fig. 4.8 are given in Table 4.1.

To record the data shown in Figs. 3 and 4 of the main text we switch between trap settings 1 and 2b as well as between settings 3 and 4 within less than 200 ns. In our experiments, switching between trap 1 and 2b (3 and 4) changes the interaction parameter $1/\kappa_F a$ by 1.2 (2.1), without changing the harmonic potential in which the atoms are trapped. When we recorded the data for the FR center determination, the data in trap 2a of Fig. 4.8 was recorded with 11% higher trapping-light powers compared to trap 2b, in which measurements of the main text were taken. Therefore, the FR center $B_{0,2}$ is shifted 11% more relative to the center of the FR in the absence of the 1064-nm light. We determine the latter to be at 154.699(1) G by extrapolating the FR centers for various beam intensities to the zero trapping-light intensity. The correct value of the FR center of trap 2b, as used in the experiments of the main text, is therefore given by $154.699\,\mathrm{G} + (B_{0,2} - 154.699\,\mathrm{G})/1.11 = 154.7420(15)\,\mathrm{G}$.

Trap	B_0 (G)	$\nu_{r,\mathrm{K}}$ (Hz)	$\nu_{a,\mathrm{K}}$ (Hz)	$\nu_{r,\mathrm{Li}}$ (Hz)	$\nu_{a,\mathrm{Li}}$ (Hz)	P_S (W)	P_D (W)	P_V (W)
1	154.7195	415	56	650	88	0.175	0.380	0
2b	154.7420	415	56	650	88	0	0.380	4.4
2a	154.7465	-	-	-	-	0	0.425	4.85
3	154.7405	580	80	945	130	0.380	0.815	0
4	154.7785	580	80	945	130	0	0.815	7.6

Table 4.1: Typical trap parameters for the various trap settings. In our experiments, we switch from trap 1 to 2b i.e. from trap 3 to 4 by switching the powers P_S and P_V of the S and V beams within less than 200 ns.

The determination of the relative shifts of the FR centers of two trap settings can be done with an even higher accuracy. As an example: We record association spectra at a magnetic field B_3 (B_4) in trap 3 (4) with the FR center at $B_{0,3}$ ($B_{0,4}$). The magnetic fields are chosen such that the spectra are taken at roughly the same detuning $B_3 - B_{0,3} \approx B_4 - B_{0,4}$. We then compare these spectra from trap 3 and trap 4, and overlap their association onsets by shifting one of them, say the one in trap 4, with respect to the other, trap 3, along the frequency axis by $\delta\nu$. This frequency shift $\delta\nu$ can be translated into a magnetic detuning shift δB_0 by comparing it to the slope of the binding-energy at that detuning dE_b/dB. Then δB_0 can be extracted from $\delta B_0 = h\delta\nu/[dE_\mathrm{b}/dB]$. Finally we can derive the relative shift of the FR centers in trap 3 and trap 4 to be $B_{0,4} - B_{0,3} = B_4 - B_3 - \delta B_0$. We estimate the accuracy of this relative FR center determination to be on the order of ± 0.5 mG.

Table 4.1 shows the typical resonance positions, trap frequencies and laser powers for the traps used in the measurements in the main text. The trap frequencies are determined by observing oscillations of the atomic clouds. We observe variations in the FR centers of less than 1.5 mG and trap frequencies of less than 4% over weeks of measurement time, which we ascribe to variations of the 1064 nm trapping-laser power and drifts of the relative beam positions. We account for these variations in the data analysis.

4.5.4 Determination of the Li atom number

An accurate determination of the number N_Li of Li atoms in our experiment and the corresponding Fermi energy is an important, non-trivial task. Here we present four different methods to determine the number of Li atoms with an error of less than 10%.

Absorption imaging on a nearly closed transition

One method for determining the number of atoms is absorption imaging. In this method, the spatial dependence of the fraction A of the light absorbed by the atomic cloud is recorded

using a camera and used to obtain a measure of the atom number

$$N_I = -\frac{2\pi}{3\lambda^2}\left(\frac{u}{M}\right)^2 \sum_{X,Y} \ln\left[1 - A\left(X,Y\right)\right] \ ,$$

where λ is the light wavelength, M is the magnification of the imaging system, u is the camera pixel size, and $A\left(X,Y\right)$ is the absorbed light fraction as measured by the camera with X and Y the camera pixel indices. If atoms at rest are imaged using a weak light pulse that resonantly excites a closed atomic transition, N_I will be equal to the true atom number. In this section, we will present reference experimental conditions that approximate this situation and use these conditions to obtain a measure $N_I^{\mathrm{high-B}}$ that is close to the Li atom number N_{Li}. We will then discuss the remaining systematic effects and thereby relate $N_I^{\mathrm{high-B}}$ to N_{Li}.

We approximate a closed transition by imaging Li atoms in the second-lowest Zeeman state ($\mathrm{Li}|2\rangle$, $m_J = -1/2$, $m_I = 0$) using σ^- light near $\lambda = 671$ nm that resonantly excites them to the second-lowest Zeeman state of the $^2\mathrm{P}_{3/2}$ manifold ($\mathrm{Li}|2'\rangle$, $m_J = -3/2$, $m_I = 0$) at the magnetic field of 1150 G. The dominant branching from this transition is due to the spontaneous decay of $\mathrm{Li}|2'\rangle$ to the $\mathrm{Li}|4\rangle$ ($m_J = 1/2$, $m_I = -1$) state. We calculate the corresponding branching ratio as 0.12% using the dipole selection rules and the expression of the relevant states in the (m_J, m_I) basis. Under our imaging conditions, the other branching ratios are more than 100 times smaller.

We record the images of the atoms using a back-illuminated CCD camera (Andor DV-434) with a pixel size of $u = 11$ μm. We determine the magnification $M = 2.93\,(5)$ of our imaging system by imaging the interference pattern formed by two 671-nm laser beams intersecting at an angle of 29.0 (4) mrad at the location of the atoms onto our camera.

We check the purity of the polarization of the imaging light by imaging an optically dense Li cloud. We obtain optical depths greater than 3, corresponding to a sum of the intensities of the unabsorbed σ^+ and π light components that is less than 5% of the intensity of the σ^- imaging light. We minimize the effect of the polarization errors by ensuring that the maximal optical depth of the imaged cloud is smaller than 0.4, implying a relative error in the determined atom number of less than 6%.

We minimize saturation effects by using a low light intensity $I \approx 0.05\,I_{\mathrm{s}}$, where $I_{\mathrm{s}} = 2.5$ mW/cm^2 is the saturation intensity of the Li D2 transition.

While mechanical effects exerted by light on atoms form the basis of laser cooling, the effect of these forces on absorption imaging of atoms is usually neglected. However, for light atoms, this effect can be significant. For Li, the scattering of a single photon of the 671-nm imaging light imparts a momentum $\hbar k_{\mathrm{L}} = 2\pi\hbar/\lambda$ to the atom, leading to a Doppler shift of the imaging transition by $\delta_{\mathrm{rec}} = \hbar k_{\mathrm{L}}^2/m_{\mathrm{Li}} = 0.025\,\Gamma_{\mathrm{D2}}$, where $\Gamma_{\mathrm{D2}} = 36.897$ $\mu\mathrm{s}^{-1}$ is the spontaneous emission rate from the Li $^2\mathrm{P}_{3/2}$ state [McA96]. For imaging Li atoms, we choose a reference set of conditions. The imaging pulse duration is set to 18 μs, the light intensity to $I \approx 0.05\,I_{\mathrm{s}}$ and the detuning δ_0 is adjusted to obtain the maximal value of N_I. Under these conditions, we expect the radiation pressure to lead to a mean laser detuning during the

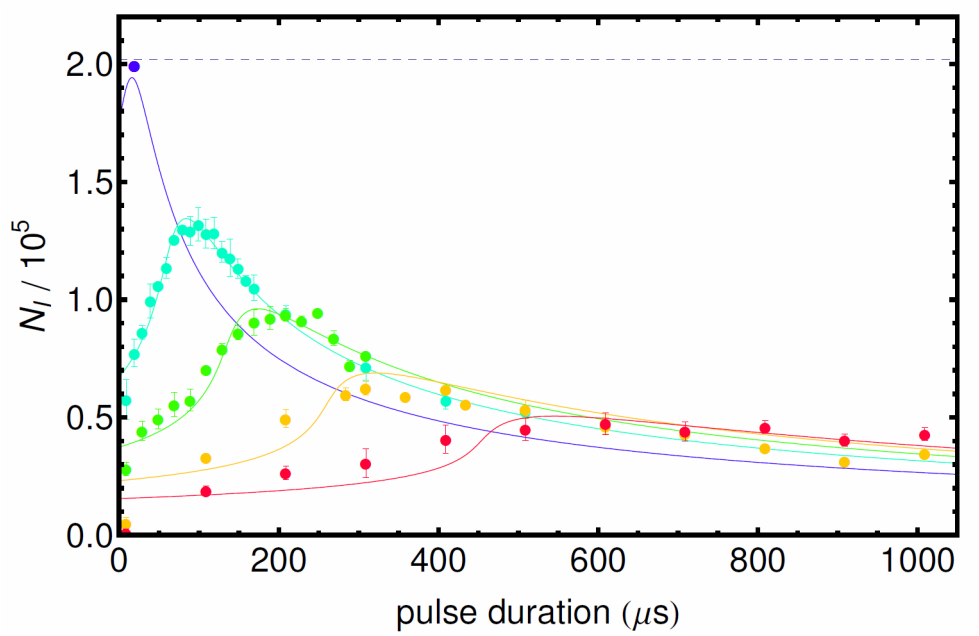

Figure 4.9: Li atom number determined by absorption imaging in the presence of a magnetic field of 1150 G as a function of the duration of the imaging light pulse. The lines show a multivariate fit to the model of Eq. (4.6). The dashed line indicates the Li atom number that would be obtained using a weak resonant light pulse.

imaging pulse that is smaller than $0.1\,\Gamma_{\mathrm{D2}}$, corresponding to a small effect on the measured atomic absorption.

We experimentally investigate the mechanical effects of the light on the atoms by varying the laser detuning δ and the duration of the imaging pulse. Fig. 4.9 shows the number N_I as a function of the duration t of the imaging pulse for different laser detunings. The red, orange, green and cyan points correspond to $(\delta_0 - \delta)/(2\pi) = 9$ MHz, 7 MHz, 5 MHz and 3 MHz, respectively. The single blue point corresponds to the reference imaging conditions.

For pulse durations that are significantly longer than our reference pulse duration, we observe a large effect of the radiation pressure. We model this effect by the following set of differential equations:

$$\begin{aligned} \frac{dN_\gamma}{dt} &= \frac{\Gamma_{\mathrm{D2}}}{2}\frac{s}{1+s+\delta^2/(\Gamma/2)^2}\,\eta\,, \\ \frac{d\eta}{dt} &= -(1-r)\,\frac{dN_\gamma}{dt}\eta\,, \\ \frac{d\delta}{dt} &= \delta_{\mathrm{rec}}\frac{dN_\gamma}{dt}\,, \end{aligned} \tag{4.5}$$

where $s = I/I_{\mathrm{s}}$, the parameter r is the branching ratio to the Li$|2\rangle$ state, and N_γ is the mean number of photons scattered per atom, and η is the fraction of atoms remaining in

the nearly closed two-level system. The time $t = 0$ corresponds to the start of the imaging pulse, with $\eta(0) = 1$.

In the limit of $r = 1$ and small s, these equations can be solved by separation of variables to yield:

$$\begin{aligned} \delta(t) &= \frac{\Gamma_{D2}}{2} g(\delta_{rec} s t) \ , \\ N_\gamma(t) &= [g(\delta_{rec} s t) - g(0)] / \left(\frac{\delta_{rec}}{\Gamma_{D2}/2} \right) \ , \end{aligned}$$

where $g(u)$ satisfies

$$\frac{g(u)^2 - g(0)^2}{2} + \frac{g(u)^4 - g(0)^4}{4} = u$$

with $g(0) = 2\delta(0)/\Gamma$. The number N_I is be proportional to the mean number of photons scattered per unit time N_γ/t. Therefore, we write

$$N_I = N_I^0 [g(\delta_{rec} s t) - g(0)] / (\delta_{rec} s t) \ , \tag{4.6}$$

where N_I^0 is the value of N_I determined in the limit of a weak, resonant light pulse.

We fit the model of Eq. (4.6) to the data from Fig. 4.9 with δ_0, N_I^0 and s as free parameters and obtain $\delta_0 = -2\pi \times 1.2(1)$ MHz, $s = 0.043(2)$, and $N_I^0 = 2.02(4) \times 10^5$. The fitted value of N_I^0 is indicated by the dashed line in the Fig. 4.9.

The above model implies that, under the reference conditions, $\delta_0/2\pi = -1$ MHz and $N_I^{high-B}/N_I^0 = 0.96(1)$, with each atom scattering a mean number of 12 photons during the imaging pulse. Using Eq. (4.5) to include the effects of saturation and branching ratio, we obtain a relation between N_I^{high-B} and the true Li atom number N_{Li} as $N_I^{high-B} = 0.91(2) N_{Li}$. Including the effects of the imperfect light polarization and the uncertainty in the magnification, we obtain $N_I^{high-B} = 0.89(5) N_{Li}$.

Fitting of Li Fermi profiles

Another method to determine the Li atom number is to image a degenerate Li atom cloud after releasing the atoms from a trap. In the zero-temperature limit, the spatial extent of the imaged cloud is determined by the trap frequencies, the time elapsed after release from the trap and the atom number.

To account for the finite temperature of the Li atoms in our experiment, we use a non-degenerate sample of K atoms to measure the temperature of the Li atoms. We prepare a mixed sample of approximately 2.5×10^5 Li$|2\rangle$ atoms and 2×10^4 K$|1\rangle$ atoms at 1150 G in a deep crossed-dipole trap with frequencies $f_r^K = 408(1)$ Hz, $f_r^{Li} = 649(3)$ Hz, $f_z^K = 56.1(4)$ Hz, $f_z^{Li} = 89.1(2)$ Hz. After waiting 0.5 s for the Li and K to thermalize, we release the atoms from the trap. By imaging the non-degenerate K cloud after 5.5 ms time of flight, we determine the temperature of the atoms to be $T = 370(15)$ nK.

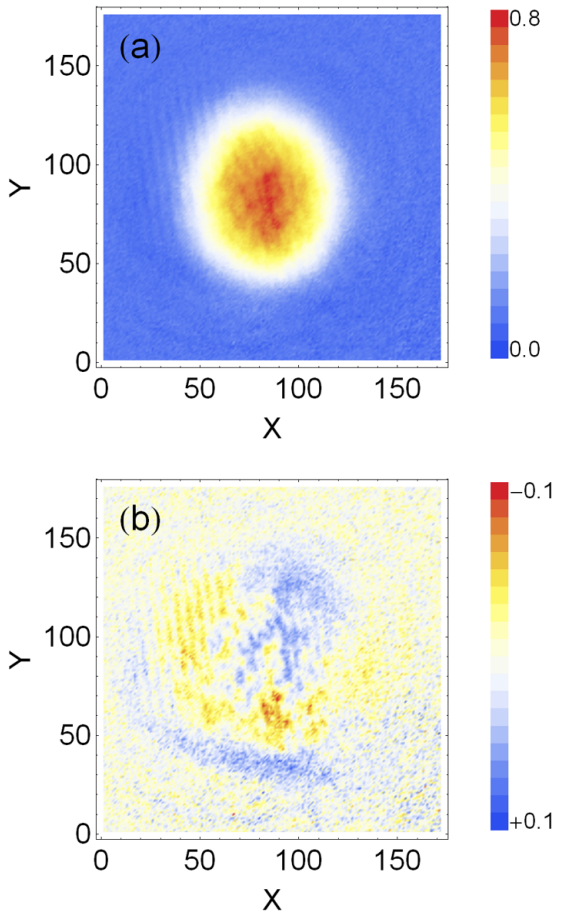

Figure 4.10: Fraction of the imaging light absorbed by a Li atomic cloud after release from an optical trap (a), together with residuals of a fit to the data (b).

We image the Li atoms after t_{TOF}=2.5 ms time of flight using the reference imaging pulse described in Section 4.5.4. By averaging 45 absorption images, we obtain the image shown in Fig. 4.10. We fit the obtained absorption data to a function of the form $A+e^{-\sigma n_{2\mathrm{D}}}$, where

$$n_{2\mathrm{D}} = -\frac{k_{\mathrm{B}}^2 m_{\mathrm{Li}} T^2}{4\pi^2\hbar^3 f_r^{\mathrm{Li}}}\mathrm{Li}_2\left(-q\exp\left(-\frac{m_{\mathrm{Li}}u^2\left(X-X_0\right)^2}{2\chi_r M^2 k_{\mathrm{B}} T}-\frac{m_{\mathrm{Li}}u^2\left(Z-Z_0\right)^2}{2\chi_z M^2 k_{\mathrm{B}} T}\right)\right)$$

is the 2D Fermi atom density profile with Li the polylogarithm function and $\chi_{r,z} = \sqrt{1+\left(2\pi f_{r,z}^{\mathrm{Li}} t_{\mathrm{TOF}}\right)^2}$. The fit parameter A accounts for technical offsets in the absorption data while X_0 and Y_0 fit the location of the cloud center on the camera image. The fit parameters q and σ correspond to the atoms' fugacity and the light absorption cross-section. The fit residual is shown in Fig. 4.10b. Taking into accounts the uncertainties in the magnification, the temperature and the trap frequencies, we obtain $\sigma = 0.82(9)\times 6\pi/k_{\mathrm{L}}^2$, corresponding to $N_I^{\mathrm{high-B}} = 0.82(9)\, N_{\mathrm{Li}}$.

LiK molecule dissociation and K number determination

Another method to determine the Li atom number is to associate LiK Feshbach molecules and to compare the number of K and Li atoms after dissociating the molecules. The advantage of this method is that the K atoms can be imaged on a closed transition and that, being 6.6 times heavier than the Li atoms, the K atoms are much less affected by the radiation pressure of the imaging light.

We associate the Li$|1\rangle$K$|3\rangle$ molecules by a magnetic ramp across the FR and then thoroughly clean our trapped sample from any remaining free Li and K atoms by a combination of radio-frequency and laser light pulses; see [Jag14] for details. The obtained molecule samples are essentially pure, consisting of approximately 1.5×10^4 molecules and less than 300 remaining free Li and K atoms.

We subsequently dissociate the molecules by an inverse ramp across the FR and determine number of the free Li$|1\rangle$ and K$|3\rangle$ atoms via absorption imaging at a magnetic field near 154.7 G. For imaging the Li$|1\rangle$ atoms, we use the parameters from Section 4.5.6. We convert the atom number $N_I^{\mathrm{low-B}}$ determined using these parameters to the number $N_I^{\mathrm{high-B}}$ of Li atoms obtained by absorption imaging at 1150 G using the imaging ratios from Section 4.5.6.

We relate the number of atoms determined by absorption imaging of K$|3\rangle$ atoms near 154.7 G to the true K atom number in two steps. First, we transfer an independent sample of K atoms from the state K$|1\rangle$ to the state K$|3\rangle$ using two consecutive resonant rf pulses. Imaging these atoms before and after the transfer allows us to relate the number of K$|3\rangle$ atoms determined by absorption imaging after molecule dissociation to the number $N_{I,\mathrm{K}}^{\mathrm{low-B}}$ of K$|1\rangle$ atoms that would be measured by absorption imaging near 154.7 G. In the second step, using a similar procedure to the one described in Section 4.5.6, we compare $N_{I,\mathrm{K}}^{\mathrm{low-B}}$ to the number $N_{I,\mathrm{K}}^{\mathrm{high-B}}$ of K$|1\rangle$ atoms determined by absorption imaging at 1150 G using a weak laser-light pulse. We then find for the relative atom number of K and Li determined at 1150 G: $N_I^{\mathrm{high-B}} = 0.92(5)\, N_{I,\mathrm{K}}^{\mathrm{high-B}}$.

Accounting for the saturation of the K imaging light ($s \approx 0.05$) and the errors in the light polarization and the magnification of the K imaging system, we can relate $N_{I,\mathrm{K}}^{\mathrm{high-B}}$ to the true K atom number as $N_{I,\mathrm{K}}^{\mathrm{high-B}} = 0.92\,(5)\ N_{\mathrm{K}}$.

Finally, assuming the real numbers of K and Li atoms after dissociation to be equal, we obtain $N_I^{\mathrm{high-B}} = 0.85(7)\,N_{\mathrm{Li}}$.

Measurement of rf shifts

A different method to determine the Li number is to use rf spectroscopy to measure the interaction energy of the K atoms with the Li cloud. By comparing the measured data to the predictions of a dressed quasiparticle model [Mas12] with accurately determined parameters of the FR, one can determine the mean Fermi energy of Li sampled by the K atoms. From the knowledge of the Li temperature and trap frequencies, one can then determine the Li atom number.

We prepare a sample of about $2.7{\times}10^5$ Li atoms and $2{\times}10^4$ K atoms at the temperature of $T = 290(15)$ nK in a crossed-beam optical dipole trap with trap frequencies $f_r^{\mathrm{K}} = 395(2)$ Hz, $f_r^{\mathrm{Li}} = 632(3)$ Hz, $f_z^{\mathrm{K}} = 50.0(5)$ Hz, $f_z^{\mathrm{Li}} = 80(1)$ Hz. We use a Blackman-shaped rf π-pulse to transfer the K atoms from the K$|2\rangle$ to the K$|3\rangle$ state at various magnetic fields B near the 154.7 G Li$|1\rangle$-K$|3\rangle$ Feshbach resonance. We compare the rf frequency at which we obtain maximal transfer of the K atoms when the Li atoms are in the Li$|1\rangle$ state (f) to the frequency for maximum transfer with the Li atoms in the Li$|2\rangle$ state (f_0).

Fig. 4.11 shows the frequency difference $f - f_0$ as a function of the magnetic field near 154.7 G. We verify that f_0 remains unchanged in the absence of the Li atoms. Therefore, $h(f - f_0)$ corresponds to the difference $E_3 - E_2$ of the mean interaction energies of the K atoms in the K$|3\rangle$ and K$|2\rangle$ states with Li atoms in the Li$|1\rangle$ state.

We assume a uniform distribution of the Li atoms across the K cloud and use the mean Li Fermi energy $\epsilon_F = \hbar^2\kappa_F^2/2m_{\mathrm{Li}}$ sampled by the K atoms as a free parameter. We calculate the interaction energy E_3 between the K$|3\rangle$ atoms and Li$|1\rangle$ atoms from a two-channel polaron model [Mas12] with the resonance parameters determined in Section 4.5.2: $a_{\mathrm{bg}} = 63.0\ a_0$, $r_{\mathrm{eff}} = -5175\ a_0$, $\Delta B = 0.880$ G. Since the interaction between the K$|2\rangle$ atoms and Li$|1\rangle$ atoms is weak, we may approximate E_2 by the mean-field expression $E_2 = 2\pi a_{\mathrm{bg}}\hbar^2\kappa_F^3/\left(6\pi^2\right)$, where $a_{21} = 63\,a_0$ is K$|2\rangle$-Li$|1\rangle$ scattering length [Nai11]. We use the position B_0 of the Feshbach resonance as the second free parameter. By fitting the above model to our data, we find $\epsilon_F = h \times 31.8\,(4)$, $B_0 = 154.715\,(1)$ G.

From the knowledge of the trap frequencies and the Li atom temperature, we can use ϵ_F to determine the Li atom number as $N_{\mathrm{Li}} = 275\,(15) \times 10^3$. Simultaneous with the above measurements, we record the number of Li atoms $N_I^{\mathrm{low-B}}$ determined using absorption imaging near 154.7 G as described in the Section 4.5.6. We use the conversion between $N_I^{\mathrm{low-B}}$ and $N_I^{\mathrm{high-B}}$ described in the same section to find $N_I^{\mathrm{high-B}} = 0.91\,(7)\ N_{\mathrm{Li}}$.

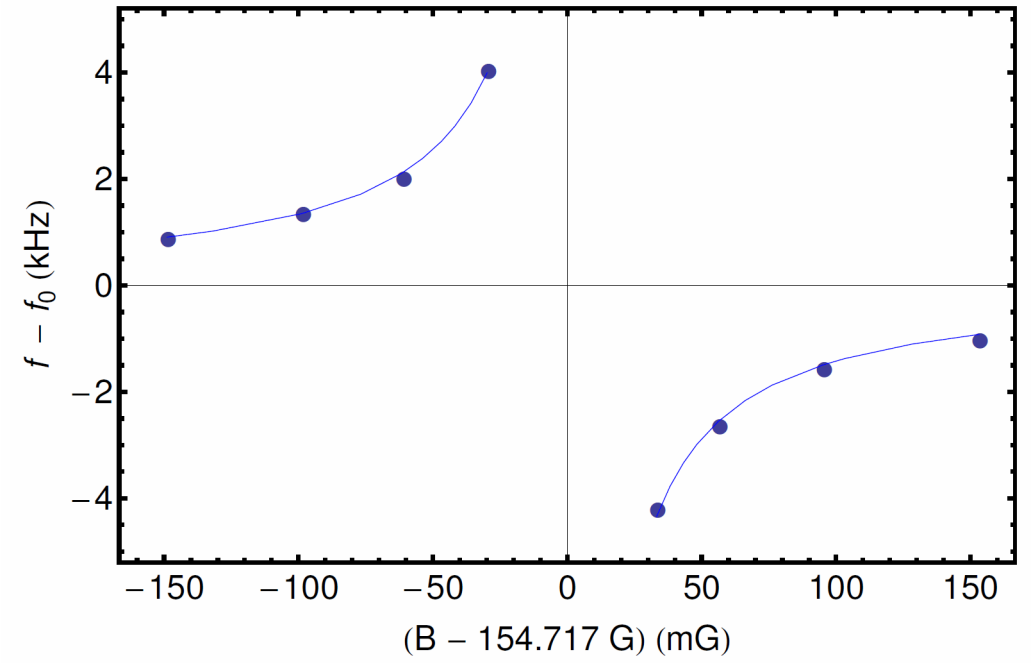

Figure 4.11: The measured shifts of the K$|2\rangle \rightarrow$K$|3\rangle$ rf transition frequency due to the presence of Li$|1\rangle$ atoms as a function of the magnetic field (dots) together with a fit using a quasiparticle model (see text).

4.5.5 Determination of Li atom number: summary

We summarize the results of our measurements of the Li atom number by the obtained ratios $N_I^{\mathrm{low-B}}/N_{\mathrm{Li}}$. These ratios are subject to errors that are largely uncorrelated between the different methods, with the notable exception of the error in the determination of the magnification of the imaging system. To obtain the best estimate for the ratio $N_I^{\mathrm{high-B}}/N_{\mathrm{Li}}$, we fix the magnification to a certain value M_0 and calculate the mean $\mu\,(M_0)$ and variance $V\,(M_0)$ of the four results weighted by their inverse uncorrelated variances. We repeat the same procedure with M_0 sampled from a normal distribution whose mean and variance correspond to our experimental determination of M. We add the variance of μ due to the variation in M_0 to V to obtain:

$$N_I^{\mathrm{low-B}}/N_{\mathrm{Li}} = 0.86\,(5) \quad .$$

In the main text, we use a more conservative error estimate of 16% for the relative uncertainty in the Li atom number determination. This corresponds to a relative uncertainty in the Fermi energy of 6%.

4.5.6 Absorption imaging near 154.7 G

We commonly determine the Li atom number near the Li$|1\rangle$-K$|3\rangle$ FR at 154.7 G. We do this by absorption imaging of Li$|1\rangle$ atoms using σ^- light on the Li$|1\rangle$ ($m_I = 1$, $m_J = -1/2$)$\rightarrow$

Li$|3'\rangle$ ($m_I = 1, m_J = -3/2$) transition. The dominant loss channel for this imaging transition is the spontaneous decay from the Li$|3'\rangle$ state to the Li$|5\rangle$ ($m_I = 0$, $m_J = +1/2$) state. We calculate the corresponding branching ratio as 4% using the method from Section 4.5.4. The other loss processes are at least three orders of magnitude less probable. We use an 8-μs long imaging pulse whose intensity corresponds to $s = 0.26$ and whose frequency is adjusted to obtain the maximal value of N_I.

We calibrate this imaging method relative to the imaging of Li atoms in the $|2\rangle$ state at the magnetic field of 1150 G as follows. We first prepare a Li$|2\rangle$ sample at the field of 1150 G and image it as described above. Then, in a separate experiment, we ramp the magnetic field to 154.7 G, followed by a ramp back to 1150 G. We verify that these ramps lead to the loss of less than 5% of the atoms. In the third experiment, we execute only the first field ramp and then use rapid adiabatic passage to transfer the Li atoms into the Li$|1\rangle$ state with efficiency larger than 98%. We image these atoms as described above to obtain the atom number $N_I^{\mathrm{low-B}}$. We use the relationship between $N_I^{\mathrm{low-B}}$ and the average of the atom numbers recorded at the magnetic field of 1150 G with and without the double field ramp to determine $N_I^{\mathrm{high-B}} = 2.4\,(1)\; N_I^{\mathrm{low-B}}$.

4.5.7 Heating due to molecule formation

As explained in the main text, on the repulsive side of the FR, the K atoms can pair with Li atoms to form molecules. By removing Li atoms from the Fermi sea and releasing energy, this pairing process leads to heating with a corresponding increase in $k_{\mathrm{B}}T/\epsilon_F$.

To estimate the effects of this decay to molecules, we approximate our system by a uniform system with Li and K densities $\bar{n}_{\mathrm{Li}}$ and $\bar{n}_{\mathrm{K}}$, respectively. Before the impurity atoms are transferred into the interacting state, the system is in thermal equilibrium and we may write the number and energy densities of the Li atoms as

$$\bar{n}_{\mathrm{Li}} \;=\; -f_{3/2}\left(-q_0\right)/\lambda_{\mathrm{dB}}^3 \tag{4.7}$$

and

$$u_{\mathrm{Li}} \;=\; -f_{5/2}\left(-q_0\right) \times \frac{3}{2}\frac{k_{\mathrm{B}}T_0}{\lambda_{\mathrm{dB}}^3}\;, \tag{4.8}$$

where q_0 and T_0 are the fugacity and the temperature of the Li atoms before the start of the experiment, $\lambda_{\mathrm{dB}} = \left(2\pi\hbar^2/mk_{\mathrm{B}}T_0\right)^{1/2}$ is the thermal de Broglie wavelength of the Li atoms and $f_{3/2}$ i.e. $f_{5/2}$ are the polylogarithm functions [Hua87]. The Fermi energy ϵ_F of the Li atoms is related to $\bar{n}_{\mathrm{Li}}$ as

$$\epsilon_F = \frac{\hbar^2}{2m_{\mathrm{Li}}}\left(6\pi^2\bar{n}_{\mathrm{Li}}\right)^{2/3} \tag{4.9}$$

and to the fugacity as

$$\frac{k_{\mathrm{B}}T}{\epsilon_F} \;=\; \left[\frac{4}{3\sqrt{\pi}}\frac{-1}{f_{3/2}\left(-q_0\right)}\right]^{2/3}\;. \tag{4.10}$$

The heating due to molecule formation progresses during the interaction time. To estimate the effect of this heating on our measurements of the decoherence rate, we choose a typical interaction time $\tau_{\mathrm{D}} = \gamma_{\mathrm{coh}}^{-1}$. We also assume that each decay event removes a single Li atom from the Fermi sea. We also assume that only 50% of the K atoms participate in the decay since the other 50% are in the non-interacting state during the echo sequence. This implies that the fraction $l = \Gamma\tau_{\mathrm{D}}\bar{n}_{\mathrm{K}}/2\bar{n}_{\mathrm{Li}}$ of the Li atoms will be converted to molecules. As the decay rate Γ, we take the sum of the two-body and three-body decay rates from [Koh12b].

We further assume that each decay to molecules releases energy αE_F equal to the difference between the repulsive polaron energy and the middle of the molecule-hole continuum from [Koh12b]. Since the Li is much lighter than LiK, we assume that the full energy released to the decay is delivered to the Li sea. Finally, we assume that remaining Li atoms thermalize with each other.

Under these conditions, we may express the number density $\bar{n}'_{\mathrm{Li}}$, the energy density u'_{Li} and the Fermi energy ϵ'_F of the Li atoms during the experiment as:

$$\begin{aligned} \bar{n}'_{\mathrm{Li}} &= (1-l)\,\bar{n}_{\mathrm{Li}} \ , \\ u'_{\mathrm{Li}} &= (1-l)\,u_{\mathrm{Li}} + l\alpha n_{\mathrm{Li}}\epsilon_{F,0} \ , \\ \epsilon'_F &= \epsilon_F\,(1-l)^{2/3} \ . \end{aligned}$$

Using Eqns. (4.7-4.10), we obtain

$$\begin{aligned} -f_{3/2}\,(-q_1)\,(T_1/T_0)^{3/2} &= -\,(1-l)\,f_{3/2}\,(-q_0) \ , \\ -f_{5/2}\,(-q_1)\,(T_1/T_0)^{5/2} &= -\,(1-l)\,f_{5/2}\,(-q_0) + l\left[-f_{5/2}\,(-q_0)\right]^{5/3}(\pi/6)^{1/3}\,\alpha \ , \end{aligned}$$

where q_1 and T_1 are the average fugacity and temperature of the Li atoms during the experiment. Using Eq. (4.9), we can then obtain the average degeneracy parameter $k_{\mathrm{B}}T_1/\epsilon'_F$.

Fig. 4.12 shows the predicted typical degeneracy parameter $k_{\mathrm{B}}T_1/\epsilon'_F$ of the Li atoms in the spin-echo measurements as a function of the interaction parameter, for the parameters from Fig. 4.3 of the main text.

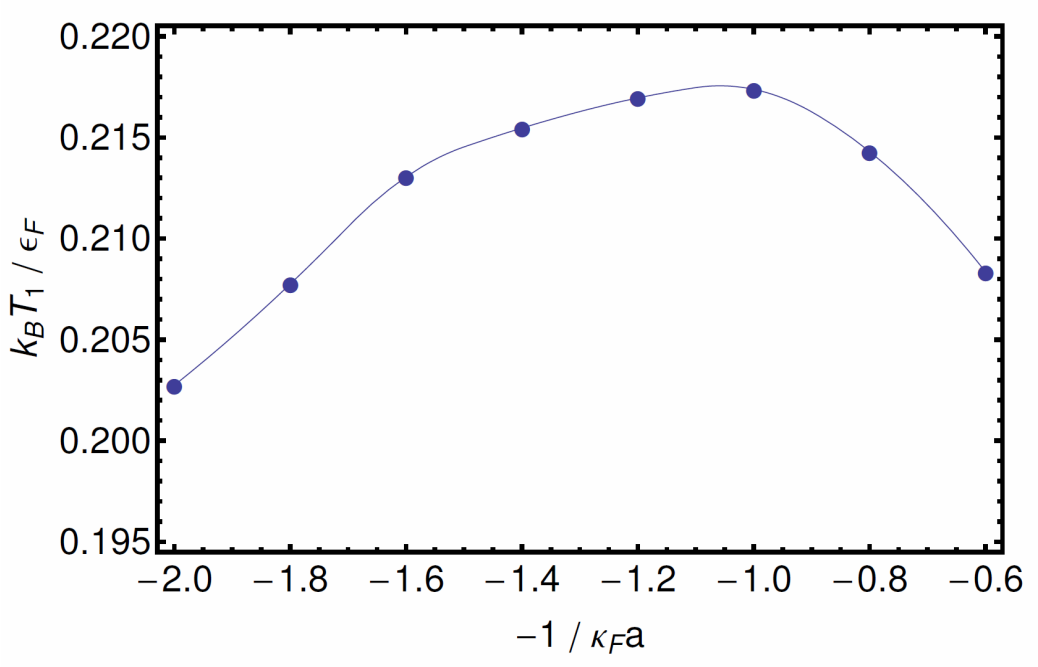

Figure 4.12: The predicted degeneracy parameter of the Li atoms during the echo sequence computed for $k_{\mathrm{B}}T_0/\epsilon_F = 0.16$, $\bar{n}_{\mathrm{K}}/\bar{n}_{\mathrm{Li}} = 0.27$ and the typical interaction time τ_{D}, as a function of the interaction parameter. The line shows a second-order interpolation between the data points.

Chapter 5

Preprint: Ultrafast many-body interferometry of impurities coupled to a Fermi sea[1]

Preprint, arXiv:1604.07423
submitted 19 February 2016

M. Cetina[1,2], M. Jag[1,2], R. S. Lous[1,2], I. Fritsche[1,2], J. T. M. Walraven[1,3], R. Grimm[1,2], J. Levinsen[4], M. M. Parish[4], R. Schmidt[5,6], M. Knap[7], and E. Demler[6]

[1] *Institut für Quantenoptik und Quanteninformation,Österreichische Akademie der Wissenschaften, 6020 Innsbruck, Austria*
[2] *Institut für Experimentalphysik, Universität Innsbruck, 6020 Innsbruck, Austria*
[3] *Van der Waals-Zeeman Institute, Institute of Physics, University of Amsterdam, 1098 XH Amsterdam, The Netherlands*
[4] *School of Physics and Astronomy, Monash University, Victoria 3800, Australia*
[5] *ITAMP, Harvard-Smithsonian Center for Astrophysics, Cambridge, MA 02138, USA*
[6] *Department of Physics, Harvard University, Cambridge, MA 02138, USA*
[7] *Department of Physics, Walter Schottky Institute and Institute for Advanced Study, Technical University of Munich, 85748 Garching, Germany*

[1] The author of the present thesis contributed to developing the experimental procedures together with M.C., performed the measurements, and analyzed the data with M.C., R.S.L. and I.F. under the supervision of R.G. All authors contributed to writing the manuscript.

5.1 Abstract

The fastest possible collective response of a quantum many-body system is related to its excitations at the highest possible energy. In condensed-matter systems, the corresponding timescale is typically set by the Fermi energy. Taking advantage of fast and precise control of interactions between ultracold atoms, we report on the observation of ultrafast dynamics of impurities coupled to an atomic Fermi sea. Our interferometric measurements track the non-perturbative quantum evolution of a fermionic many-body system, revealing in real time the formation dynamics of quasiparticles and the quantum interference between attractive and repulsive states throughout the full depth of the Fermi sea. Ultrafast time-domain methods to manipulate and investigate strongly interacting quantum gases open up new windows on the dynamics of quantum matter under extreme non-equilibrium conditions.

5.2 Introduction

Non-equilibrium dynamics of fermionic systems is at the heart of many problems in science and technology, from the physics of neutron stars and heavy ion collisions to the operation of electronic devices. The wide range of energy scales, spanning the low energies of excitations near the Fermi surface up to high energies of excitations from deep within the Fermi sea, challenges our understanding of the quantum dynamics in such fundamental systems. The Fermi energy E_F sets the shortest response time for the collective response of a fermionic many-body system through the Fermi time $\tau_F = \hbar/E_F$, where $\hbar$ is the reduced Planck constant. In a metal, i.e. a Fermi sea of electrons, E_F is in the range of a few electronvolts, which corresponds to τ_F on the order of 100 attoseconds. Dynamics in condensed matter systems on this timescale can be recorded by attosecond streaking techniques [Kra09] and the initial applications were demonstrated by probing photoelectron emission from a surface [Paz15]. However, despite these spectacular advances, the direct observation of the coherent evolution of a fermionic many-body system on the Fermi timescale has remained beyond reach.

In atomic quantum gases, the fermions are much heavier and the densities far lower, which brings τ_F into the experimentally accessible range of typically a few microseconds. Furthermore, the powerful techniques of atom interferometry [Cro09] now offer the exciting opportunity to probe and manipulate the real-time coherent evolution of a fermionic quantum many-body system. Such techniques have been successfully used, e.g. to measure bosonic Hanbury-Brown-Twiss correlations [Sim11], demonstrate topological bands [Ata13], probe quantum and thermal fluctuations in low-dimensional condensates [Gri12, Had06], and to measure demagnetization dynamics of a fermionic gas [Kos13, Bar14]. Impurities coupled to a quantum gas provide a novel and unique probe of the many-body state. Strikingly, they allow direct access to the system's wave function when the internal states of the impurities are manipulated using a Ramsey atom-interferometric technique [Goo11, Kna12].

We employ dilute ^{40}K atoms in a ^{6}Li Fermi sea to measure the response of the sea to a suddenly introduced impurity. For near-resonant interactions, we observe coherent quantum

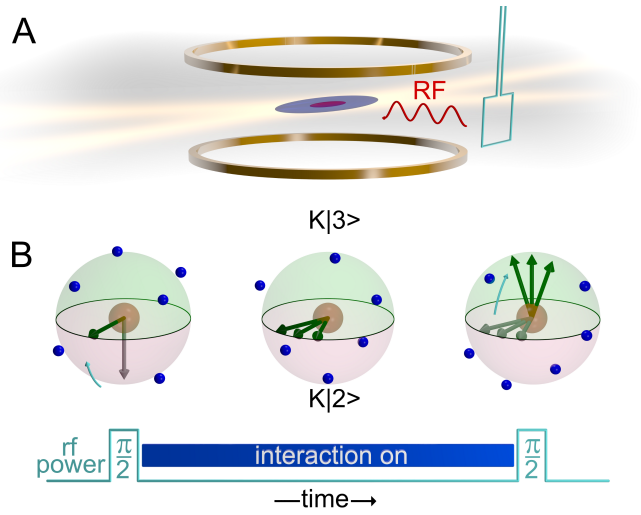

Figure 5.1: Illustration of the experimental setup and procedure. (**A**) Li (blue) and K (red) atoms are held in a crossed-beam optical dipole trap. The magnetic field coils (gold) and the rf coil (blue) are used to manipulate the atoms. (**B**) An rf $\pi/2$ pulse is used to prepare the K atoms in a superposition of internal Zeeman states as shown on a Bloch sphere. A second rf pulse is used to probe the final state.

many-body dynamics involving the entire ^{6}Li Fermi sea. We also observe in real time the formation dynamics of the repulsive and attractive impurity quasiparticles. In the limit of low impurity concentration, our experiments confirm that an elementary Ramsey sequence is equivalent to linear-response frequency-domain spectroscopy. We demonstrate that our time-domain approaches allow us to prepare, control, and measure many-body interacting states.

5.3 Main results

Our system consists of a small sample of typically 1.5×10^4 ^{40}K impurity atoms immersed in a Fermi sea of $3{\times}10^5$ ^{6}Li atoms (Sec. 5.5 and [Cet15]). The mixture is held in an optical dipole trap (Fig. 5.1A) at a temperature of $T = 430\,\mathrm{nK}$ after forced evaporative cooling. Because of the Li Fermi pressure and a more than two times stronger optical potential for K, the K impurities are concentrated in the central region of the large Li cloud. Here they experience a nearly homogeneous environment with an effective Fermi energy of $\epsilon_F = k_B \times 2.6\mu\mathrm{K}$ (Sec. 5.5), where k_B is Boltzmann's constant. The corresponding Fermi time $\tau_F = 2.9\ \mu\mathrm{s}$ sets the natural time scale for our experiments. The degeneracy of the Fermi sea is characterized by $k_BT/\epsilon_F \approx 0.17$. The concentration of K in the Li sea remains low, with $\bar{n}_\mathrm{K}/\bar{n}_{\mathrm{Li}} \approx 0.2$, where $\bar{n}_{\mathrm{Li}}$ ($\bar{n}_\mathrm{K}$) is the average of the Li (K) number density sampled by the K atoms (Sec. 5.5).

The interaction between the impurity atoms in the internal state K$|3\rangle$ (third-to-lowest Zeeman sublevel) and the Li atoms (always kept in the lowest Zeeman sublevel) is controlled

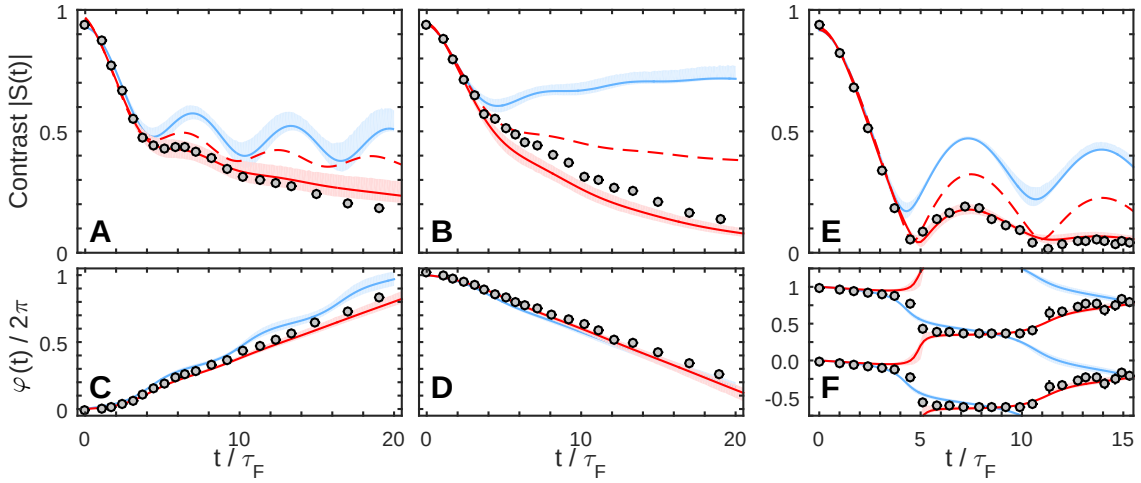

Figure 5.2: Impurity dynamics in the Fermi sea. (**A** and **C**) Contrast $|S(t)|$ and phase $\varphi(t)$ of the interference signal depending on the interaction time t in the repulsive polaron regime for $X = -0.23(6)$, with the rf pulse applied at $X_1 = -3.9$. (**B** and **D**) Same quantities in the attractive polaron regime for $X = 0.86(6)$ and $X_1 = 5.8$. (**E** and **F**) Same quantities for resonant interactions ($X = 0.08(5)$, $X_1 = 4.8$). The solid blue lines show the results of the TBM calculations. The solid (dashed) red lines show the results of the FDA calculations at the measured (at zero) temperature. The shaded regions reflect the combined experimental uncertainties in X, k_BT and ϵ_F. The errors in the experimental data are typically smaller than the symbol size.

using a rather narrow (Sec. 5.5) interspecies Feshbach resonance near a magnetic field of 154.7 G [Nai11, Cet15]. We quantify the interaction with the Fermi sea by the dimensionless parameter $X \equiv -1/\kappa_F a$, where $\kappa_F = \hbar^{-1}\sqrt{2m_{\mathrm{Li}}\epsilon_F}$ is the Li Fermi wavenumber with m_{Li} the Li mass, and a is the s-wave interspecies scattering length. While slow control of X is realized in a standard way by variations of the magnetic field, fast control is achieved using an optical resonance shifting technique [Cet15]. The latter permits sudden changes of X by up to about ± 5 within a time shorter than $\tau_F/15 \approx 200\,\mathrm{ns}$.

Our interferometric probing method is based on a two-pulse Ramsey scheme (Fig. 5.1B), following the suggestions of Refs. [Goo11, Kna12]. The sequence starts with the impurity atoms prepared in the spin state K$|2\rangle$ (second-to-lowest Zeeman sublevel), for which the background interaction with the Fermi sea can be neglected. A first, 10-μs-long, radio-frequency (rf) $\pi/2$-pulse drives the K atoms into a coherent superposition between this non-interacting initial state and the state K$|3\rangle$ under weakly interacting conditions (interaction parameter X_1 with $|X_1| \approx 5$). Using the optical resonance shifting technique [Cet15], the system is then rapidly quenched into the strongly interacting regime ($|X| < 1$). After an evolution time t, the system is quenched back into the regime of weak interactions and a second $\pi/2$-pulse is applied. The population difference $N_3 - N_2$ in the two impurity states is measured as a function of the phase of the rf pulse [Cet15]. The contrast $|S(t)|$ and the phase φ of the resulting sinusoidal signal is finally determined as a function of t. In the limit of low impurity concentration, the complex function $S(t) = |S(t)|e^{-i\varphi(t)}$ can be interpreted as the overlap of the interacting and the non-interacting components of the system's wavefunction [Goo11]. The squared amplitude $|S(t)|^2$ is then equivalent to the common definition of a Loschmidt echo [Los76, Jal01].

We first consider the interaction conditions where polaronic quasiparticles are known to exist [Mas14]. Figures 5.2A-D show the evolution of the contrast and the phase measured in the repulsive and the attractive polaron regimes, where $X = -0.23(6)$ and $X = +0.86(6)$, respectively. For short evolution times of up to about $4\tau_F$, we observe both contrast signals to exhibit a similar initial parabolic transient, which is typical of a Loschmidt echo [Jal01]. For longer times, this connects to an exponential decay of the contrast and a linear evolution of the phase. In Ref. [Cet15], we showed that the long-time decay of the contrast in this regime can be interpreted in terms of quasiparticle scattering. Here, the linear phase evolution corresponds to the energy shift of the quasiparticle state, for which we obtain $+0.29(1)\epsilon_F$ for the repulsive case in Fig. 5.2C and $-0.27(1)\epsilon_F$ for the attractive case in Fig. 5.2D. Remarkably, while the long-time behavior reflects the quasiparticle properties, the observed initial transient reveals the ultrafast real-time dynamics of the quasiparticle formation.

On resonance, for the strongest possible interactions, the quasiparticle picture breaks down. Here our measurements, displayed in Fig. 5.2E and 5.2F for $X = 0.08(5)$, reveal the striking quantum dynamics of a strongly interacting fermionic system forced into an extreme non-equilibrium state. The contrast $|S(t)|$ shows pronounced oscillations reaching zero, while the phase $\varphi(t)$ exhibits plateaus. The revivals of the contrast $|S(t)|$ indicate partially reversible entanglement between the internal state of the impurity and the Fermi sea [Goo11]. This process involves the whole Fermi sea and occurs on the fastest timescale available to the collective dynamics of a fermionic system.

To further interpret our measurements we employ two different theoretical approaches: the truncated basis method (TBM) (Sec. 5.5) and the functional determinant approach (FDA) [Kna12]. The TBM models our full experimental procedure assuming zero temperature and considering only single particle-hole excitations. This approximation, known as the Chevy ansatz [Che06], has been successfully used to predict the properties of quasiparticles in cold gases [Mas14]. The predictions of the TBM are represented by the blue lines in Fig. 5.2. This method accurately describes the initial transient, as well as the period of the oscillations of $S(t)$ on resonance. While the zero-temperature TBM calculation naturally overestimates the contrast in the thermally dominated regime ($t > 6\tau_F$), it accurately reproduces the observed linear phase evolution and thus the quasiparticle energy. The FDA is an exact solution for a fixed impurity at arbitrary temperatures taking into account the non-perturbative creation of infinitely many particle-hole pairs. The FDA calculation is represented by the solid red lines in Fig. 5.2. We see remarkable agreement with our experimental results, which indicates that the effects of impurity motion remain small in our system. This observation can be explained by the fact that our impurity is sufficiently heavy so that the effects of its recoil with energies of about $0.25\,\epsilon_F$ (Sec. 5.5) are masked by thermal fluctuations. To identify the effect of temperature, we performed a corresponding FDA calculation for $T = 0$ and show the results as the dashed lines in Fig. 5.2. Here, we see a slower decay of $|S(t)|$, which follows a power law at long times (Sec. 5.5) under the idealizing assumption of infinitely heavy impurities.

Time-domain and frequency-domain methods are closely related, as is well known in spectroscopy. In the limit of low impurity density, where the interactions between the impurities can be neglected, $S(t)$ is predicted to be proportional to the inverse Fourier transform of the linear excitation spectrum $A(\omega)$ of the impurity [Noz69]. To benchmark our interferometric

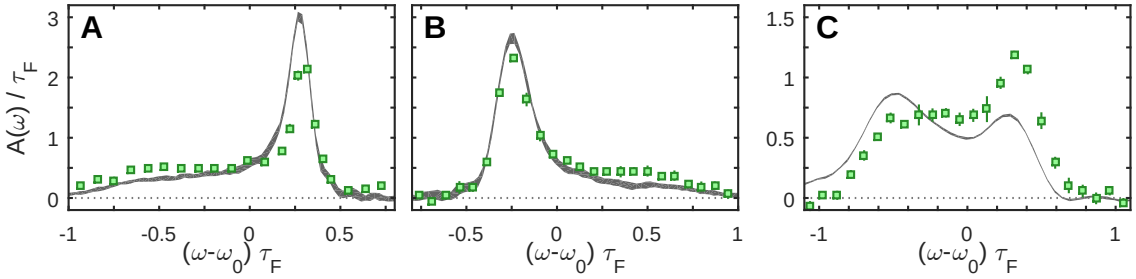

Figure 5.3: Rf spectroscopy of an impurity in the Fermi sea. (**A** and **B**) show the rf spectra for the repulsive ($X = -0.23(6)$) and the attractive ($X = 0.86(6)$) interactions, respectively. (**C**) shows the rf spectrum for resonant interactions ($X = 0.08(5)$). The spectral data are normalized to unit integral. The gray lines correspond to the numerical Fourier transform of the $S(t)$ data from Fig. 5.2. The width of the gray curve reflects the combined experimental errors in the $S(t)$ data.

method, we measure $A(\omega)$ using rf spectroscopy similar to our earlier work [Koh12b], but with great care to ensure linear response (Sec. 5.5). The measured excitation spectra are shown in Fig. 5.3. In the repulsive and attractive polaron regimes, we observe the characteristic structure of a peak on top of a broad pedestal [Mas14]. While the peak determines the long-time evolution of the quasiparticle, the pedestal is associated with the rapid dynamics related to the emergence of many-body correlations. For resonant interactions, the rf response is broad and nearly symmetric about ω_0, implying that the zero crossings of $S(t)$ are accompanied by jumps in its phase by π, as is seen in Fig. 5.2E and 5.2F. Based on the observed spectral response, we interpret the oscillations of $S(t)$ in Figs. 5.2E and 5.2F as arising from simultaneous excitations of the two branches of our many-body system corresponding to the two humps in the rf spectrum.

A detailed comparison of our time- and frequency-domain measurements reveals the powerful capability of our approach to prepare and control many-body states. This is revealed in Fig. 5.2, where we show the Fourier transform of the $S(t)$ data from Fig. 5.2 as the gray curves. We observe that time-domain measurements where the rf pulses are applied in the presence of weakly repulsive interactions (Fig. 5.3A) emphasize the upper branch of the many-body system while in the attractive case (Fig. 5.3B,C), the lower branch is emphasized. We explain this observation by the action of the rf pulses to prepare weakly interacting polaron states (Sec. 5.5). Compared to the non-interacting initial state used in the frequency-domain spectroscopy, these polarons have an increased wavefunction overlap with the corresponding strongly interacting repulsive and attractive branches, leading to the observed shift in the spectral weight. Our measurements demonstrate that the control over the initial state of many particles can be used to precisely manipulate quantum dynamics in the strongly interacting regime. This unique capability of time-domain techniques opens up a wide range of applications, including the study of the dynamical behavior near the phase transition from a polaronic to a molecular system [Mas14] and the creation of specific excitations of a Fermi sea down to individual atoms [Dub13].

Our interpretation of the results in Figs. 5.2 and 5.3 relies on the assumption that our fermionic impurities are sufficiently dilute so that any interactions between them can be neglected. We can extend our experiments into a complex many-body regime where the

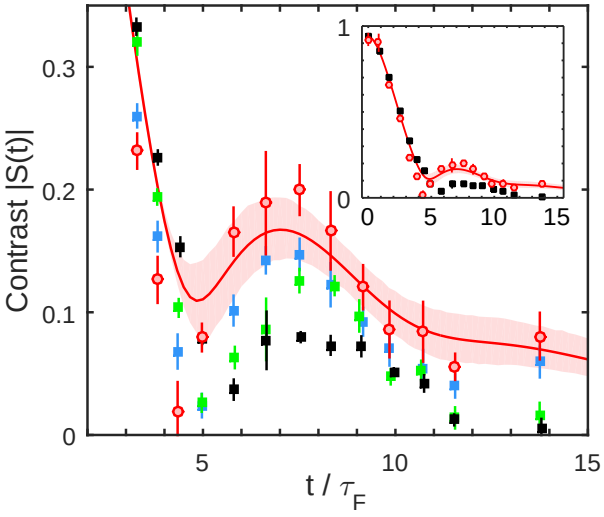

Figure 5.4: Observation of induced impurity-impurity interactions. Resonant dynamics of the contrast is shown for $X = -0.01(5)$, $X_1 = 5.2$, $\epsilon_F = k_B \times 2.1(1)$ μK, $k_BT/\epsilon_F = 0.24(2)$ and different impurity concentrations $\bar{n}_K/\bar{n}_{Li}$. The black, green, and blue squares correspond to $\bar{n}_K/\bar{n}_{Li} = 0.53$, 0.33, and 0.20, respectively. The red circles correspond to the linear extrapolation of the complex $S(t)$ data to the limit of a single impurity, taking into account the errors in the data. The inset reproduces this extrapolation together with the highest-concentration data points. The red line shows the result of the FDA calculation. The shaded region reflects the combined experimental uncertainties in X, k_BT and ϵ_F.

impurities interact both with the Fermi sea and with each other, by increasing the impurity concentration (Sec. 5.5). Figure 5.4 shows the time-dependent contrast measured for $k_BT = 0.24(2)\epsilon_F$ and $\bar{n}_K/\bar{n}_{Li}$ =0.20, 0.33, and 0.53. An extrapolation of the $S(t)$ data to zero concentration (open red circles) lies close to the data points for $\bar{n}_K/\bar{n}_{Li}$ =0.20, which is the typical concentration in our measurements, and agrees with the FDA calculation. This confirms that the physics that we access in the measurements with a small sample of fermionic impurities is close to that of a single impurity, which we posit to be a consequence of the fermionic nature of the impurities. When the impurity concentration is increased, we find that the contrast for $t > 5\tau_F$ is decreased and the period of the revivals of $|S(t)|$ is prolonged. We interpret this as arising from effective interactions between the impurities induced by the Fermi sea [Mor10, Yu10]. Such interactions between fermionic impurities are predicted to lead to novel quantum phases [Zwe12].

5.4 Conclusion

Our results demonstrate the power of many-body interferometry to study ultrafast processes in strongly interacting Fermi gases in real time, including the formation dynamics of quasiparticles and the extreme non-equilibrium dynamics arising from quantum interference between different many-body branches. Of particular interest is the prospect of observing Anderson's orthogonality catastrophe (Sec. 5.5 and [Kna12]) by further cooling the Li Fermi sea [Har15] while pinning the K atoms in a deep species-selective optical lattice [LeB07].

Acknowledgements

We thank M. Baranov, F. Schreck, G. Bruun, N. Davidson and R. Folman for stimulating discussions. We acknowledge support by the Austrian Science Fund FWF within the SFB FoQuS (F40-P04). R. S. was supported by the NSF through a grant for the Institute for Theoretical Atomic, Molecular, and Optical Physics at Harvard University and the Smithsonian Astrophysical Observatory. M. K. acknowledges support from Technical University of Munich - Institute for Advanced Study, funded by the German Excellence Initiative and the European Union FP7 under grant agreement 291763. E. D. acknowledges support from Harvard-MIT CUA, NSF Grant No. DMR-1308435, AFOSR Quantum Simulation MURI, the ARO-MURI on Atomtronics, and support from Dr. Max Rössler, the Walter Haefner Foundation, the ETH Foundation, and the Simons Foundation.

5.5 Supplementary materials

5.5.1 Theoretical description

In this section, we summarize the approaches that we developed to theoretically model the results of our interferometric Ramsey experiments. We first discuss the microscopic model that we use to describe the narrow Feshbach resonance of the Li-K mixture, and then we outline how we calculate the time evolution of the system within two approaches: the Truncated Basis Method (TBM) and the Functional Determinant Approach (FDA). In this section, we assume that a 'perfect quench' is performed, where the impurity is initially non-interacting with the Fermi sea and there are no interactions during the radio-frequency (rf) pulses. A discussion of the role played by interactions during the rf pulses is deferred to Section 5.5.3.

Narrow Feshbach resonance model for Li-K mixtures

In our experiment, the K impurities are concentrated in the central region of the Li Fermi gas where they experience a nearly uniform Li environment (see Section S5.A). Hence we consider in our model K impurities that are immersed in a Li Fermi gas of uniform density. The Li-K mixture is prepared at magnetic fields near a closed-channel dominated Feshbach resonance between the Li$|1\rangle$ and K$|3\rangle$ states that occurs near 155 G. The narrow character of this resonance is a consequence of the limited strength of the coupling of atoms in the open channel to a closed-channel molecular state. To describe this system we use the two-channel Hamiltonian

$$\begin{aligned}\hat{H} = &\sum_{\mathbf{k}} \epsilon_{\mathbf{k},\mathrm{Li}} \hat{c}^\dagger_{\mathbf{k}} \hat{c}_{\mathbf{k}} + \sum_{\mathbf{k}} \epsilon_{\mathbf{k},\mathrm{K}} \hat{d}^\dagger_{\mathbf{k}} \hat{d}_{\mathbf{k}} + \sum_{\mathbf{k}} \left[\epsilon_{\mathbf{k},M} + \epsilon_M(B)\right] \hat{b}^\dagger_{\mathbf{k}} \hat{b}_{\mathbf{k}} \\ &+ \frac{g}{\sqrt{V}} \sum_{\mathbf{k},\mathbf{q}} \chi(\mathbf{k}) \left(\hat{b}^\dagger_{\mathbf{q}} \hat{c}_{\mathbf{q}/2+\mathbf{k}} \hat{d}_{\mathbf{q}/2-\mathbf{k}} + \hat{d}^\dagger_{\mathbf{q}/2-\mathbf{k}} \hat{c}^\dagger_{\mathbf{q}/2+\mathbf{k}} \hat{b}_{\mathbf{q}} \right), \end{aligned} \tag{5.1}$$

where the first line defines the non-interacting Hamiltonian $\hat{H}_0$. Here, V is the total system volume, $\hat{c}^\dagger_{\mathbf{k}}$ ($\hat{c}_{\mathbf{k}}$) creates (annihilates) a Li fermion with momentum $\hbar\mathbf{k}$ and single-particle energy $\epsilon_{\mathbf{k},\mathrm{Li}} = \frac{\hbar^2 k^2}{2m_{\mathrm{Li}}}$, and $\hat{d}^\dagger_{\mathbf{k}}$ ($\hat{d}_{\mathbf{k}}$) creates (annihilates) a K impurity atom in the K$|3\rangle$ state with dispersion $\epsilon_{\mathbf{k},\mathrm{K}} = \frac{\hbar^2 k^2}{2m_{\mathrm{K}}}$, where we define $k \equiv |\mathbf{k}|$. The closed-channel molecule is created (annihilated) by $\hat{b}^\dagger_{\mathbf{k}}$ ($\hat{b}_{\mathbf{k}}$). It has the dispersion $\epsilon_{\mathbf{k},M} = \frac{\hbar^2 k^2}{2(m_{\mathrm{K}}+m_{\mathrm{Li}})}$, and a bare energy relative to the scattering threshold, $\epsilon_M(B) = \delta\mu(B - B_c)$. Here $\delta\mu$ is the differential magnetic moment between the open and closed channels, and B_c denotes the threshold crossing of the bare molecular state [Chi10].

Close to the Feshbach resonance, the scattering length a diverges and the interaction between the K impurities and the Li atoms is predominantly mediated by exchange of the closed-channel molecule. We therefore neglect the background scattering potential in the open channel [Nai11]. The strength of the coupling between the open and closed channels is given by g, and we take a form factor $\chi(\mathbf{k}) = 1/[1 + (r_0 k)^2]$, which accounts for the finite extent r_0 of the closed-channel wave function $\sim e^{-r/r_0}/r$.

The parameters of the model $\delta\mu$, B_c, g, and r_0 are fully determined by known experimental parameters. First, the differential magnetic moment has recently been measured to be $\delta\mu = h\times 2.35(2)$ MHz/G [Cet15]. Second, close to resonance, the scattering length may be parametrized as

$$a = a_{\mathrm{bg}}\left(1 + \frac{\Delta B}{B_0 - B}\right) \approx a_{\mathrm{bg}}\frac{\Delta B}{B_0 - B}, \tag{5.2}$$

where B_0 is the center of the Feshbach resonance with width $\Delta B = 0.880\,\mathrm{G}$ and background scattering length $a_{\mathrm{bg}} = 63.0\,a_0$ [Nai11]. To connect with our model, we consider the on-shell two-body scattering amplitude $f(k)$, which for the Hamiltonian 5.1 is given by [Sch12]

$$f(k) = \frac{\mu_{\mathrm{red}}}{2\pi\hbar^2} g^2 \chi(\mathbf{k})^2 \left[-\frac{\hbar^2 k^2}{2\mu_{\mathrm{red}}} + \epsilon_M(B) - \frac{g^2\mu_{\mathrm{red}}}{4\pi\hbar^2 r_0[1 - ikr_0]^2}\right]^{-1}, \tag{5.3}$$

where $\mu_{\mathrm{red}} = m_{\mathrm{Li}}m_{\mathrm{K}}/(m_{\mathrm{Li}} + m_{\mathrm{K}})$ is the reduced mass and $\mathbf{k}$ is the relative scattering wave vector. Using the low energy expansion $f^{-1}(k) \approx -a^{-1} + \frac{1}{2}r_{\mathrm{eff}}k^2 - ik$, with r_{eff} the effective range, we thus identify

$$a = \frac{1}{\frac{1}{2r_0} + 2R^*\mu_{\mathrm{red}}\delta\mu(B - B_c)/\hbar^2}, \tag{5.4}$$

$$r_{\mathrm{eff}} = -2R^* + 3r_0 - 4r_0^2/a, \tag{5.5}$$

where $R^* \equiv \hbar^4\pi/(\mu_{\mathrm{red}}^2 g^2)$ is the range parameter of the Feshbach resonance [Bru04, Pet04a]. Comparing Eqs. (5.2) and (5.4) yields

$$R^* = \frac{\hbar^2}{2\mu_{\mathrm{red}}a_{\mathrm{bg}}\delta\mu\Delta B}, \tag{5.6}$$

$$B_0 - B_c = \frac{1}{2}\Delta B a_{\mathrm{bg}}/r_0. \tag{5.7}$$

Equation (5.6) relates R^*, and thus the coupling constant g, to the known experimental parameters. The extent of the closed-channel wave function r_0 in turn follows by comparing

Eq. (5.7) to the theoretical prediction from quantum defect theory [Gór04, Szy05], $B_0 - B_c = a_{\rm bg}\Delta B/\bar{a}$, where $\bar{a} = 0.955 l_{\rm vdw}$ and $l_{\rm vdw} = 40.8\, a_0$ is the van der Waals length [Nai11]. Thus we obtain $r_0 = \bar{a}/2$. Finally, B_0 was obtained in Ref. [Cet15], allowing the determination of B_c.

Truncated Basis Method

To model a mobile impurity as in the experiment, we consider an approximate wave function for the zero-momentum impurity that incorporates the scattering of a single particle out of the Fermi sea:

$$|\psi_{\boldsymbol{\alpha}}\rangle = \alpha_0 \hat{d}^\dagger_{\mathbf{0}}|\mathrm{FS}\rangle + \sum_{\mathbf{q}} \alpha_{\mathbf{q}} \hat{b}^\dagger_{\mathbf{q}} \hat{c}_{\mathbf{q}}|\mathrm{FS}\rangle + \sum_{\mathbf{k},\mathbf{q}} \alpha_{\mathbf{k},\mathbf{q}} \hat{d}^\dagger_{\mathbf{q}-\mathbf{k}} \hat{c}^\dagger_{\mathbf{k}} \hat{c}_{\mathbf{q}}|\mathrm{FS}\rangle. \tag{5.8}$$

Here, the first term on the right hand side describes the product state of the impurity K atom at zero momentum and the ground state of the non-interacting Li Fermi sea $|\mathrm{FS}\rangle = \prod_{|\mathbf{k}|<k_F} \hat{c}^\dagger_{\mathbf{k}}|0\rangle$, where k_F is the Fermi momentum, which is related to the Fermi energy by $\epsilon_F = \hbar^2 k_F^2/(2m_{\rm Li})$. The last two terms correspond, respectively, to the impurity binding a Li atom to form a closed-channel molecule, and the impurity exciting a particle out of the Fermi sea, in both cases leaving a hole behind. When using the TBM, we focus on zero temperature in order to capture the purely quantum evolution of the impurity. For convenience, within this model we also take $r_0 \to 0$, which formally requires taking the bare crossing $B_c \to \infty$ to keep a finite. This approximation is justified, as R^* exceeds r_0 by about two orders of magnitude.

Truncated wave functions of the form 5.8 have been used extensively in the study of Fermi polarons in ultracold atomic gases, starting with the work of Chevy [Che06]. While most of the previous work has focused on equilibrium properties, recently it has been proposed that these wave functions may be extended to dynamical problems using a variational approach to obtain the equations of motion [Par13], for instance to calculate the decay rate of excited states.

Here, we adapt the use of truncated wave functions for the Fermi polaron to the calculation of the dynamical response of the impurity to an interaction quench. For a perfect quench and at zero temperature, the quantity measured in experiment corresponds to the overlap between the interacting and non-interacting states of the system, i.e., we have [Goo11, Kna12]

$$S(t) = \langle\psi_0(t)|\psi_{\rm int}(t)\rangle = \langle\psi_0|\, e^{i\hat{H}_0 t/\hbar} e^{-i\hat{H}t/\hbar}\, |\psi_0\rangle\,. \tag{5.9}$$

Here $|\psi_0\rangle \equiv \hat{d}^\dagger_{\mathbf{0}}|\mathrm{FS}\rangle$ is the initial non-interacting state of energy E_0, and $\psi_{int}(t)$ is the state after a quench at time $t = 0$ from zero to finite impurity interactions with the Fermi sea. Formally expanding in a complete set of states for the single impurity problem, the Ramsey signal 5.9 then becomes

$$S(t) = \sum_j |\langle\psi_0|\phi_j\rangle|^2\, e^{-i(E_j - E_0)t/\hbar}, \tag{5.10}$$

where $|\phi_j\rangle$ is an eigenstate of the interacting Hamiltonian with energy E_j. However, this requires one to solve the entire problem which is generally not possible for a mobile impurity. Thus, within the Truncated Basis Method (TBM), we restrict the Hilbert space to wave functions of the form 5.8 and diagonalize the Hamiltonian within this truncated basis. As we shall see, this truncation permits an extremely accurate description of the initial quantum dynamics of the impurity.

For small t, we expand $e^{-i\hat{H}t/\hbar}$ to find

$$S(t) \approx 1 - (t/\tau_F)^2 \frac{(1 + m_{\mathrm{Li}}/m_{\mathrm{K}})^2}{3\pi k_F R^*}, \tag{5.11}$$

with τ_F the Fermi time. This reveals that the short-time dephasing dynamics of $S(t)$ is completely determined by the two-body properties, which are captured exactly by the TBM. As we will see below, the TBM describes the impurity behavior also beyond the two-body timescale since higher order correlations and multiple particle-hole excitations take longer to build up. Indeed, for a mobile impurity and for sufficiently weak attraction where the attractive polaron is the ground state, the TBM correctly describes the long-time behavior $S(t) \to |\alpha_0|^2 e^{-i\varepsilon_p t/\hbar}$. Here, $|\alpha_0|^2$ is the polaron residue (squared overlap with the non-interacting state) and ε_p is the polaron energy, which are both accurately determined using a wave function of the form 5.8 [Vli13].

With the TBM we consider zero temperature in order to isolate the quantum dynamics of the impurity. To better model the experiment, in principle one can extend the TBM to finite temperature by taking the initial state to be a statistical thermal distribution involving multiple impurity momenta. However, a more convenient approach at finite temperature is described in the next section.

Functional Determinant Approach

At times t substantially exceeding τ_F, the full description of the impurity dynamics requires the inclusion of multiple particle-hole pair excitations as well as the effect of finite temperature, both of which present a theoretical challenge. In order to study and describe both effects, we employ the Functional Determinant Approach (FDA) [Lev96, Lev93, Kli03, Kna12].

In the FDA the impurity is treated as an infinitely heavy object. In this limit, the FDA provides an exact solution of the dynamical many-body problem at arbitrary temperatures and times. The justification of the infinite mass approximation, which will be discussed in more detail in Section 5.5.2, is rooted in two observations. First, in our experiment, the mass of the K impurities is much larger than that of the Li atoms (mass ratio $m_{\mathrm{K}}/m_{\mathrm{Li}} \approx 6.7$) which constitute the surrounding Fermi gas. Therefore, the recoil energy gained by the K impurities due to the scattering with a Li atom is small. We estimate the typical recoil momentum k_R by averaging over all possible scattering processes on the Fermi surface, yielding $k_R = 4k_F/3$. From that we obtain an estimate for the typical recoil energy $E_R = \frac{16}{9}\frac{m_{\mathrm{Li}}}{m_{\mathrm{K}}}\epsilon_F \approx 0.25\epsilon_F$, which determines a typical time scale $\tau_R = \hbar/E_R \approx 4\tau_F$, up to which one expects recoil to

have a minimal effect on the many-body quantum dynamics, cf. Section 5.5.2. Second, at times exceeding the thermal time scale $\tau_T = \hbar/(k_B T)$, which in our experiment is given by $\tau_T \approx 6\tau_F$, thermal effects due to the averaging over various statistical realizations become relevant. The resulting thermal fluctuations disrupt the coherent quantum propagation of the impurity, and hence, for times $t > \tau_T$, mask the effect of recoil [Ros99].

To a good approximation, we may thus take the limit of infinite impurity mass, which admits the mapping of Eq. (5.1) onto the bilinear Hamiltonian

$$\hat{H} = \epsilon_M(B)\hat{m}^\dagger\hat{m} + \sum_{\mathbf{k}} \epsilon_{\mathbf{k}}\hat{c}^\dagger_{\mathbf{k}}\hat{c}_{\mathbf{k}} + g\sum_{\mathbf{k}} \chi(\mathbf{k})[\hat{m}^\dagger\hat{c}_{\mathbf{k}} + \hat{m}\hat{c}^\dagger_{\mathbf{k}}]. \tag{5.12}$$

Here, $\hat{m}^\dagger$ is the creation operator of the localized closed channel molecule and the interaction is described by the annihilation of a Li atom converting the empty impurity molecular state into an occupied one. By taking the limit $m_{\mathrm{K}} \to \infty$ we obtain a modified reduced mass $\mu'_{\mathrm{red}} = m_{\mathrm{Li}}$, which differs by a factor of 40/46 from the experimental one. This needs to be taken into account when identifying the microscopic parameters. To ensure, in particular, that the off-diagonal coupling g in Eq. (5.12) remains of the same strength as in the experiment, a reduced resonance parameter $R'^* = (40/46)^2 R^*$ has been used, which we do for all data shown in the main text. Using these identifications, the model Eq. (5.12) also accurately describes the short-time dynamics as given by Eq. (5.11), cf. Fig. 5.2 in the main text.

The calculation of time-resolved, many-body expectation values such as Eq. (5.9) at arbitrary temperature presents a theoretical challenge. However, for the model (5.12), we are able to calculate the time-resolved Ramsey response in an exact way using the FDA [Kli03, Kna12]. This is based on the observation that for bilinear Hamiltonians thermal expectation values in the many-body Fock space can be reduced to determinants in the single-particle space by virtue of the identity

$$\mathrm{Tr}[\hat{\rho}\, e^{\hat{Y}_1} e^{\hat{Y}_2} \ldots] = \det[1 - \hat{n} + \hat{n}\, e^{\hat{y}_1} e^{\hat{y}_2} \ldots]. \tag{5.13}$$

Here $\hat{Y}_1, \hat{Y}_2, \ldots$ are many-body operators, $\hat{y}_1, \hat{y}_2, \ldots$ are their single-particle counterparts, $\hat{\rho}$ is the many-body density matrix describing the state of the system, and $\hat{n} = 1/[e^{\beta(\hat{h}_0 - \mu)} + 1]$ is the occupation operator defined in the single-particle space, with μ the fermion chemical potential. A specific example for Eq. (5.13) is the perfect quench Ramsey response, which at finite temperature is given by [Kna12]

$$S(t) = \mathrm{Tr}[\hat{\rho}\, e^{i\hat{H}_0 t} e^{-i\hat{H}t}] = \det[1 - \hat{n} + \hat{n}\, e^{i\hat{h}_0 t} e^{-i\hat{h}t}]. \tag{5.14}$$

Here, $\hat{H}_0 = \sum_{\mathbf{k}} \epsilon_{\mathbf{k}}\hat{c}^\dagger_{\mathbf{k}}\hat{c}_{\mathbf{k}}$ is the free Hamiltonian of the Li Fermi gas and $\hat{H}$ is the Hamiltonian in the presence of impurity scattering given in Eq. (5.12), while $\hat{h}_0$ and $\hat{h}$ are their single-particle counterparts. A numerical evaluation of Eq. (5.14) then only requires a calculation of the single particle orbitals and energies in order to obtain the single-particle determinant.

5.5.2 Role of physical processes on different time scales

The combination of both our theoretical approaches allows us to accurately model the physics at various time scales in our experiment. Making use of the fact that the FDA and the TBM

differ distinctly in their treatment of multiple particle-hole excitations, the impurity mass, and finite temperature, we can use a comparison of their predictions to determine the role of these processes and effects in the many-body non-equilibrium dynamics of our experiment. To keep the analysis transparent, in this section we still assume that a perfect quench is performed.

Multiple particle-hole excitations

In order to analyze the role of multiple particle-hole excitations, we first consider the limit of a fixed (infinitely heavy) impurity at zero temperature. In this scenario, the FDA yields the exact solution of the impurity problem. Since, in this case, the TBM only differs from the FDA by its neglect of multiple particle-hole excitations, a comparison of the predictions of the two methods allows us to isolate the effect of these excitations.

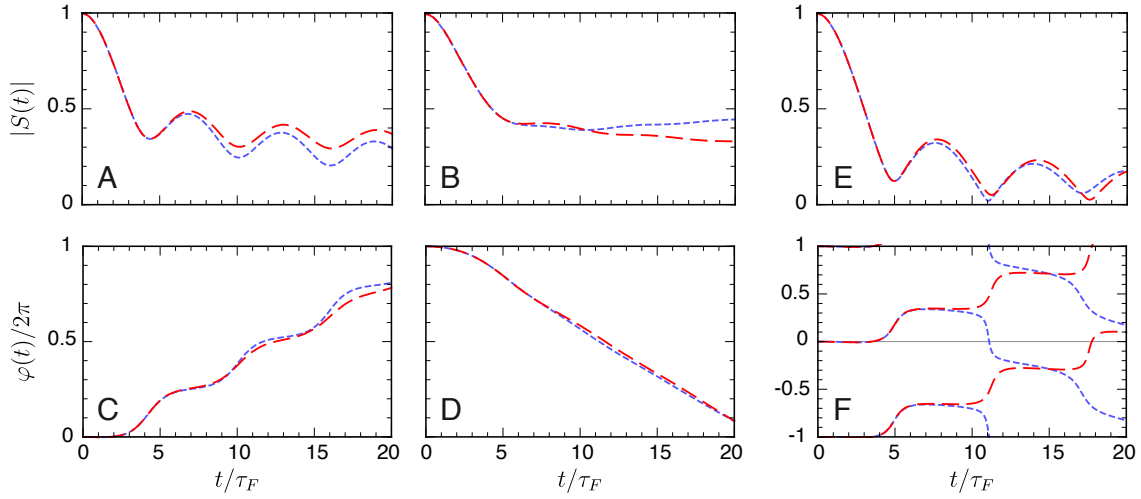

Figure 5.5: Effect of multiple particle-hole fluctuations. Taking the idealizing limit of zero temperature and infinite impurity mass, we compare the Ramsey response for a perfect quench (top: amplitude, bottom: phase) obtained exactly with the FDA (red, long dashed) to the one obtained with TBM (blue, short dashed) for (**A**, **C**) $X = -0.23$, (**B**, **D**) $X = 0.86$, and (**E**, **F**) $X = 0.08$. For this comparison, we take $r_0 = 0$ and $k_F R'^* = 1.1(40/46)^2$.

In Fig. 5.5 we display the predictions for the Ramsey response using the two theoretical approaches. We find that both theoretical predictions agree extremely well at short times. In particular, for both the amplitude and phase of $S(t)$, our results imply that multiple particle-hole excitations start to influence our observables at a time scale of around $6\tau_F$, and only become prominent beyond $10\tau_F$. Thus, at shorter time scales, multiple particle-hole excitations can be neglected when predicting the results of the Ramsey measurements.

We note that the fixed impurity scenario is a worst-case scenario for the TBM: At $T = 0$, the infinitely heavy impurity is subject to the orthogonality catastrophe with an associated power-law decay of the Ramsey contrast at long times [And67]. This decay, which arises due to an infinite number of particle-hole fluctuations and which leads to a vanishing quasiparticle

weight, is exactly incorporated in the FDA. By contrast, in the long-time limit, the TBM predicts the saturation of $|S(t)|$ to a constant value (see Fig. 5.5), corresponding to a spurious finite residue. However, for a *mobile* impurity at zero temperature, recoil becomes relevant. These recoil effects lead to the absence of the orthogonality catastrophe [Ros99], and thus to an increased accuracy of the TBM in the case of finite impurity mass.

Generally, one expects that the relevant time scale for multiple particle-hole excitations is closely related to the Fermi time τ_F. As discussed above, we find that such excitations become relevant for a description of $S(t)$ only at around $6\tau_F$ or beyond. This observation can be understood in a twofold way. First, in the equilibrium case it was found that contact interactions in the Fermi polaron problem lead to an approximate cancellation of terms involving identical fermions, thus suppressing the emergence of multiple particle-hole fluctuations [Com08]. Our observation may hence be interpreted as a generalization of these findings to the non-equilibrium case. Second, the spectrum of the Fermi polaron problem features a dominant contribution involving the excitation of fermions from the bottom of the Fermi sea to the Fermi surface [Kna12]. As discussed in Ref. [Kna12], these excitations manifest themselves as oscillations with period $2\pi\tau_F$ in the Ramsey contrast $|S(t)|$. Such a bottom of the band excitation is also present in the truncated wavefunction 5.8, and indeed the remarkable agreement of the TBM with the exact solution from the FDA up to the time $2\pi\tau_F$ suggests that this effect can be captured by single-particle hole excitations.

Impurity mass

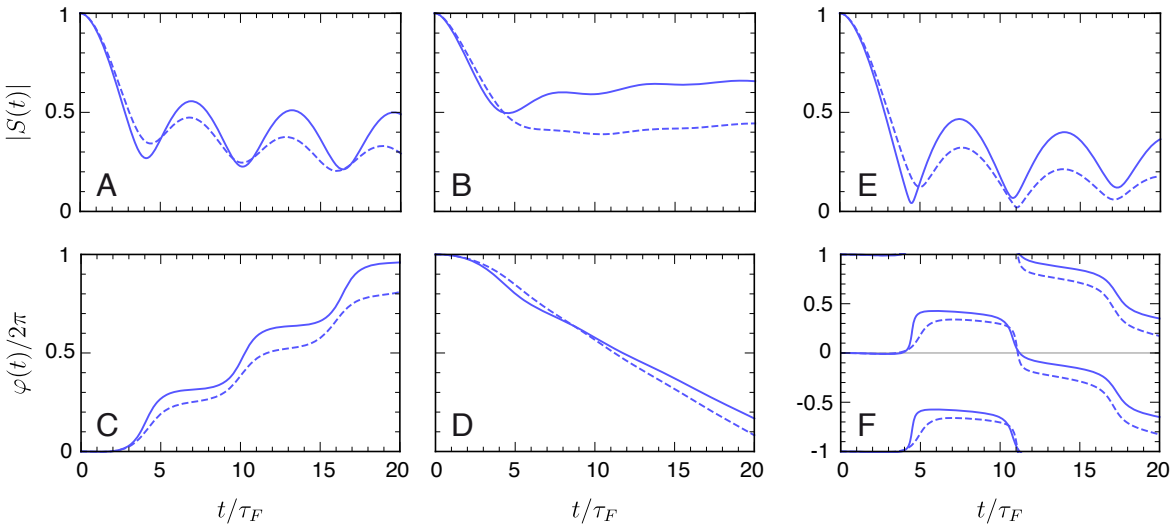

Figure 5.6: Effect of the impurity motion on the short-time dynamics. Amplitude (top) and phase (bottom) of the perfect quench zero temperature Ramsey response $S(t)$ as a function of time for (**A**, **C**) $X = -0.23$, (**B**, **D**) $X = 0.86$, and (**E**, **F**) $X = 0.08$. We compare the results of the TBM obtained for $m_{\mathrm{K}} = (40/6)m_{\mathrm{Li}}$ and $k_F R^* = 1.1$ (solid) with the TBM results for fixed impurities $m_{\mathrm{K}} \to \infty$ and $k_F R'^* = 1.1(40/46)^2$ (dashed).

As discussed in the main text, our experimental findings are well described by the static impurity approximation, although the impurity has finite mass. To quantify the effect of the

finite impurity mass, we study here the case of zero temperature. This allows us to isolate the effect of finite impurity recoil from the influence of thermal fluctuations, which will become dominant beyond times $\tau_T \approx 6\tau_F$, as discussed in the section below. In order to estimate at which time scale recoil becomes important, we make use of the capability of the TBM to describe impurities of arbitrary mass. Furthermore, our analysis in Sec. 5.5.2 shows that the TBM yields highly accurate results for the short-time dynamics of $S(t)$. Accordingly, in Fig. 5.6 we display the Ramsey response for a static impurity and for the experimentally relevant impurity mass, both calculated within the TBM. We see that for both amplitude and phase, the impurity motion only results in a small difference in the Ramsey signal at times $t \lesssim 4\tau_F$. Physically, this time scale corresponds to the effective recoil time τ_R associated with Li collisions on K atoms, which we estimated in Sec. 5.5.1 to be $\tau_R \approx 4\tau_F$, in agreement with our findings here. At times exceeding τ_R, we find that the dynamics is indeed affected by the finite impurity mass. However, at such times, thermal fluctuations dominate the behavior in experiment, as we now discuss.

Temperature

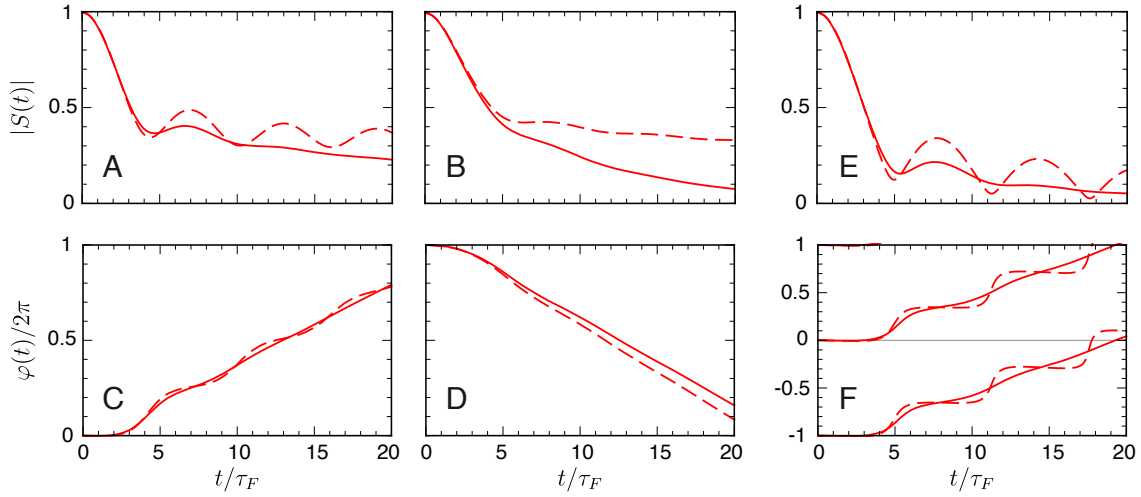

Figure 5.7: Effect of finite temperature on the impurity dynamics. We compare the Ramsey signal (upper panels: amplitude, lower panels: phase) for an infinitely heavy impurity obtained from an exact FDA calculation at zero (long dashed) and finite temperature (solid curves). The ordering of the graphs is as in the main text: (**A**, **C**) $X = -0.23$, $T/T_F = 0.17$, (**B**, **D**) $X = 0.86$, $T/T_F = 0.16$, and (**E**, **F**) $X = 0.08$, $T/T_F = 0.18$. We assume a perfect quench and choose $r_0 = 0$ as well as $k_F R^* = 1.1$, i.e., $k_F R'^* = 1.1(40/46)^2$.

At long times, the time evolution reduces to a simple exponential decoherence of $S(t)$. The time scale at which this crossover to exponential decay takes place is given by the thermal time scale τ_T. In our experiment, where $T/T_F \approx 0.15$, this corresponds to $\tau_T \approx 6\tau_F$ and, hence, we observe both regimes within the dynamical range probed in our experiment.

In this section, we use finite-temperature FDA calculations to gauge the role of temperature in the impurity dynamics. To this end we compare the results for the Ramsey signal at zero

and finite temperature for the experimentally realized parameters. The results are shown in Fig. 5.7. We indeed find that at times $\sim 6\tau_F$ the time evolution at finite temperature starts to deviate from the purely quantum behavior. Finite temperature leads to an exponential decoherence of the Ramsey signal and has the consequence that thermal fluctuations dominate over the impurity motion at times $t \gtrsim 6\tau_F$ [Ros99]. Hence they mask the effect of impurity recoil as discussed in Sec. 5.5.1.

Overall, the conditions in our experiment give rise to three competing time scales. Multiple particle hole excitations become relevant for our measurement of $S(t)$ at around $6\tau_F$, the recoil time is $\tau_R \approx 4\tau_F$, and the thermal scale is set by $\tau_T \approx 6\tau_F$. A comparison of these scales reveals the reason for the remarkable agreement between the FDA and experiment: Recoil is only weakly probed at short times $t < \tau_R$, while its effect is washed out by the thermal fluctuations at long times $t > \tau_T \approx \tau_R$.

5.5.3 Role of interaction during finite-length rf pulses

In this section, we analyze the role of the 'imperfect' interaction quench in our experiments, where residual interactions are present during the rf pulses. Furthermore, we discuss how our findings pave the way towards the use of our experimental techniques to exert control over many-body states in real time.

Idealized versus realized Ramsey scenario

Thus far, we have assumed the idealized scenario of a perfect two-pulse Ramsey scheme. In this case, the initial spin state of the impurity ($\mathrm{K}|2\rangle$ in the experiment) is non-interacting with the Li Fermi sea and there are no interactions during the applied rf $\pi/2$ pulses. Each pulse then yields a perfect rotation on the Bloch sphere, e.g., the initial state $\mathrm{K}|2\rangle$ is transformed into the spin-state superposition $(\mathrm{K}|2\rangle + \mathrm{K}|3\rangle)/\sqrt{2}$. For such a perfect Ramsey sequence, the measured Ramsey signal $S(t)$ gives the overlap between the time-evolved interacting and non-interacting states of the system [Goo11, Kna12], yielding Eqs. (5.9) and (5.14) for zero and finite temperature, respectively. In this idealized scenario, the Fourier transform of $S(t)$ corresponds to the excitation spectrum of the system in linear response [Mah00],

$$A(\omega) = \mathrm{Re} \int_0^\infty \frac{dt}{\pi} e^{i\omega t} S(t), \tag{5.15}$$

where ω is the frequency of the applied field.

In our experiments, however, residual interactions are present during the $\pi/2$ pulses, which take a finite time to be completed. As shown in the illustration of our experimental sequence in Fig. 5.8, the state $\mathrm{K}|3\rangle$ can already interact with the Li cloud during the $\pi/2$ rotation, which potentially affects the observed dynamics of the system. Specifically, this stage of the experiment is performed at a detuning from the Feshbach resonance which corresponds to a weak interaction strength X_1 between the impurities and the Fermi sea (cf. Section 5.5.3 and Fig. 5.8). After preparing the superposition state of the impurity spin, we quench the system

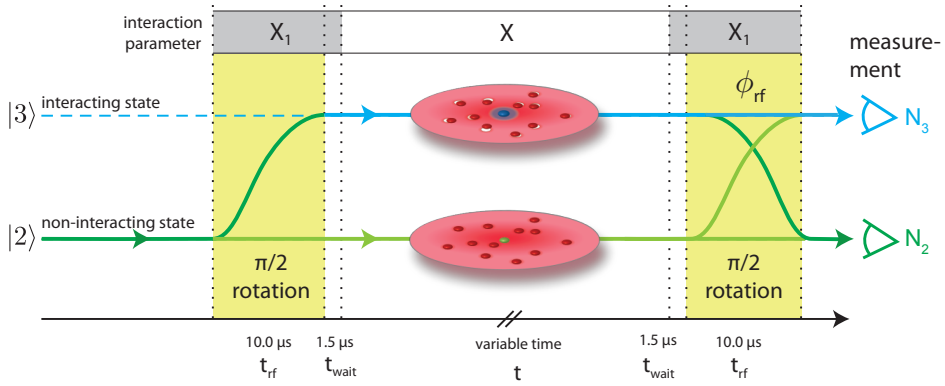

Figure 5.8: Schematic of the experimental Ramsey procedure. The K atoms start out in the hyperfine state K$|2\rangle$, which is effectively non-interacting with the Fermi sea. A 10 μs ($3.4\tau_F$) long square $\pi/2$ pulse is applied in the presence of weak interactions between the K$|3\rangle$ atoms and the Li atoms, quantified by the interaction parameter X_1. We then use optical control of our Feshbach resonance to rapidly (in less than 200 ns (0.08 τ_F)) quench the system into the strongly interacting regime (interaction parameter X). After a variable interaction time t we optically shift the interaction strength back to X_1, and then close the Ramsey sequence by a second $\pi/2$ pulse. We vary the phase of this pulse by shifting the phase of the rf source by $\phi_{\rm rf}$ before the second pulse is applied.

to strong interactions (interaction parameter X) by optically shifting the Feshbach resonance [Cet15]. We previously focussed on the complex non-equilibrium dynamics resulting from the strong interactions X during the time t. In the following, we analyze the effect of the residual interaction X_1 during the finite-duration $\pi/2$ spin rotations. In particular, we investigate the impact of these weak interactions during the rf pulses on the Ramsey response $S(t)$ and the spectrum $A(\omega)$ as obtained from the Fourier transform Eq. (5.15).

Modelling of rf pulses within TBM

In this section, we extend our modelling of the zero-temperature impurity dynamics within the TBM to directly simulate the entire experimental procedure, as illustrated in Fig. 5.8. In order to model the rf pulses, we explicitly include both K$|2\rangle$ and K$|3\rangle$ spin states, as well as the rf field. This modifies the Hamiltonian, Eq. (5.1), to $\hat{\mathcal{H}} = \hat{H} + \hat{H}_{rf}$ with the additional term

$$\hat{H}_{rf} = \frac{\Omega}{2i} \sum_{\mathbf{k}} \left(e^{i\phi_{rf}} \hat{d}^\dagger_{\mathbf{k},2} \hat{d}_{\mathbf{k},3} - e^{-i\phi_{rf}} \hat{d}^\dagger_{\mathbf{k},3} \hat{d}_{\mathbf{k},2} \right) + \sum_{\mathbf{k}} (\epsilon_{\mathbf{k},\mathrm{K}} + \hbar(\omega_{\rm rf} - \omega_0)) \hat{d}^\dagger_{\mathbf{k},2} \hat{d}_{\mathbf{k},2}. \tag{5.16}$$

Here, we have used the rotating wave approximation. Ω corresponds to the strength of the rf field, ϕ_{rf} is the variable phase of the second rf pulse, and $\hat{d}^\dagger_{\mathbf{k},\sigma}$ creates a particle in the state K$|\sigma\rangle$ with momentum $\hbar\mathbf{k}$. Note that $\hat{d}^\dagger_{\mathbf{k}} \equiv \hat{d}^\dagger_{\mathbf{k},3}$ in the original two-channel Hamiltonian 5.1. The interactions during the rf pulses cause a shift in the transition frequency between the K$|2\rangle$ and K$|3\rangle$ states from the bare transition frequency ω_0 to $\omega_0 + \varepsilon_1/\hbar$, where ε_1 is the polaron energy at interaction parameter X_1. As described in Sec. S5.B, we account for this shift by adjusting the frequency of our rf pulses to $\omega_{\rm rf} = \omega_0 + \varepsilon_1/\hbar$.

According to the last term in Eq. (5.16), the shift in the frequency of the rf source from ω_0

to $\omega_{\rm rf}$ causes the observed signal to accumulate an additional phase $(\omega_{\rm rf}-\omega_0)t$ during the interaction time t. To account for this, we introduce the phase $\phi = \phi_{\rm rf} + (\omega_{\rm rf}-\omega_0)t$. We then determine $|S(t)|$ and the phase $\varphi(t)$ by noting that the Ramsey signal $(N_3 - N_2)/(N_3+N_2)$ corresponds to a sine-wave function of ϕ plus an offset, i.e., it takes the form $F(t) + |S(t)|\cos(\phi-\varphi(t))$ with $F(t)$ a real, ϕ-independent function. This mirrors the experimental procedure, where $F(t)$, $|S(t)|$, and $\varphi(t)$ appear as fit-parameters for the Ramsey signal, see Sec. S5.B.

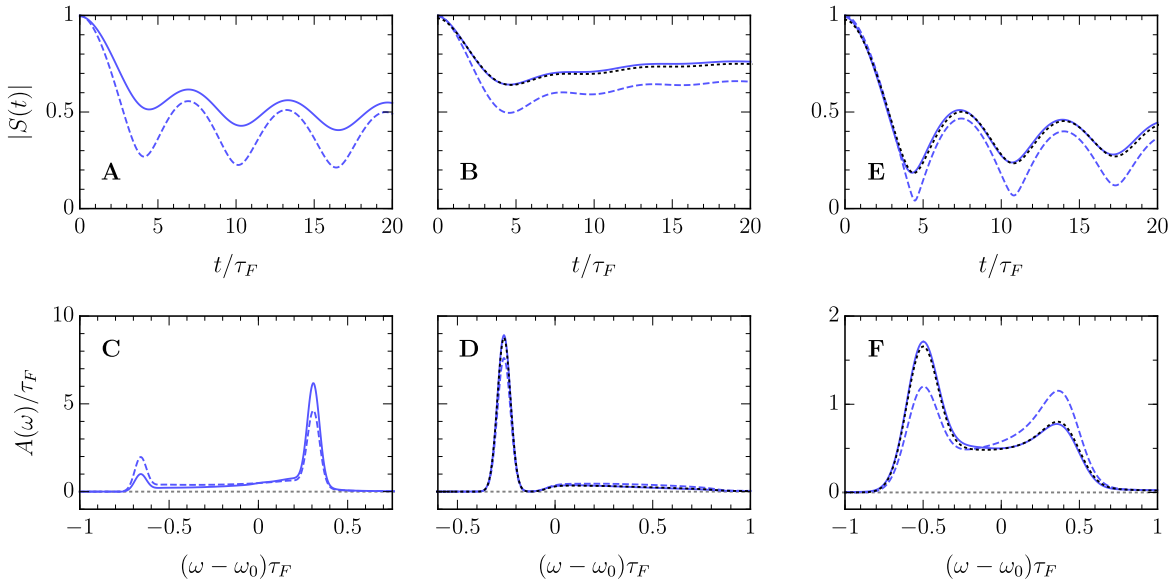

Figure 5.9: Role of the residual interactions within TBM. We present the zero-temperature response $S(t)$ and the corresponding spectrum $A(\omega)$ for the perfect quench (dashed blue) and the actual experimental sequence shown in Fig. 5.8 (solid blue). As in the main text, we take $k_F R^* = 1.1$ and the interaction parameters: (**A**, **C**) $X = -0.23$, $X_1 = -3.9$, (**B**, **D**) $X = 0.86$, $X_1 = 5.8$, and (**E**, **F**) $X = 0.08$, $X_1 = 4.8$. For comparison, in (**B**, **D**, **E**, **F**), we represent by black dotted lines the scenario where the initial state before the quench is approximated as a weakly attractive polaron — see Sec. 5.5.3 for details. The spectra have been convolved with the experimental Fourier-limited rf spectral lineshapes, which are Gaussian-shaped with width σ, where $\sigma\tau_F = 0.03$ for $X = 0.86, -0.23$, and $\sigma\tau_F = 0.1$ for $X = 0.08$.

Within the TBM, we determine the approximate eigenstates and eigenvalues of $\hat{\mathcal{H}}$ within the more general class of truncated wavefunctions:

$$|\psi_{\rm rf}\rangle = \left(\alpha_{0,3}\hat{d}^\dagger_{0,3} + \alpha_{0,2}\hat{d}^\dagger_{0,2}\right)|{\rm FS}\rangle + \sum_{\mathbf{q}} \alpha_{\mathbf{q}}\hat{b}^\dagger_{\mathbf{q}}\hat{c}_{\mathbf{q}}|{\rm FS}\rangle + \sum_{\mathbf{kq}}\left(\alpha_{\mathbf{kq},3}\hat{d}^\dagger_{\mathbf{q}-\mathbf{k}\downarrow}\hat{c}^\dagger_{\mathbf{k}}\hat{c}_{\mathbf{q}} + \alpha_{\mathbf{kq},2}\hat{d}^\dagger_{\mathbf{q}-\mathbf{k},2}\hat{c}^\dagger_{\mathbf{k}}\hat{c}_{\mathbf{q}}\right)|{\rm FS}\rangle. \tag{5.17}$$

To model the experimental quench sequence illustrated in Fig. 5.8, we apply a series of time evolution operators to the initial state consisting of a K$|2\rangle$ atom and the Li Fermi sea. At the end of the sequence we then extract the number of K atoms in states K$|2\rangle$ and K$|3\rangle$, respectively. We include explicitly the rf pulses, the wait times, and the interaction time t during which the system is strongly interacting. The results of this procedure are displayed in Fig. 5.2 of the main text. Here, we account for slight additional experimental decoherence by scaling the prediction for $|S(t)|$ as described in Section S.5C.

In the upper panels of Fig. 5.9 we compare the Ramsey response obtained by simulating the actual experimental sequence (solid line) with that of the perfect quench scenario (dashed line). We see that the residual interactions X_1 in experiment can indeed influence the quantum evolution of the impurity. The difference in the responses can be straightforwardly explained by assuming that the main effect of X_1 is to produce a weakly interacting initial state. Specifically, for weak attractive interactions $X_1 > 0$, the Ramsey response can be approximated as

$$S(t) \simeq Z \langle \psi_{X_1} | \, e^{-i\hat{H}t/\hbar} \, | \psi_{X_1} \rangle \,, \tag{5.18}$$

where $|\psi_{X_1}\rangle$ is the ground state of the Hamiltonian 5.1 at interaction parameter X_1, and Z is the corresponding polaron residue. Note that we cannot formally construct a similar expression for the repulsive case $X_1 < 0$, since the repulsive polaron is a metastable state, involving multiple eigenstates of the Hamiltonian.

Referring to Fig. 5.9, the excellent agreement between the approximation 5.18 and the full Ramsey signal provides strong evidence that the residual interactions X_1 produce a weakly attractive initial state. This is further supported by the spectrum $A(\omega)$ shown in the bottom panels, where we see that the residual interactions enhance the attractive polaron peaks for $X = 0.08$ and 0.86. A similar enhancement of the repulsive polaron peak is observed for $X = -0.23$. Hence we conclude that the explicit modelling of the impurity dynamics using the full Hamiltonian $\hat{\mathcal{H}} = \hat{H} + \hat{H}_{\rm rf}$ is not essential for the description of the dynamics during the initial $\pi/2$ spin rotation and instead one can fully describe the time evolution using the Hamiltonian 5.1.

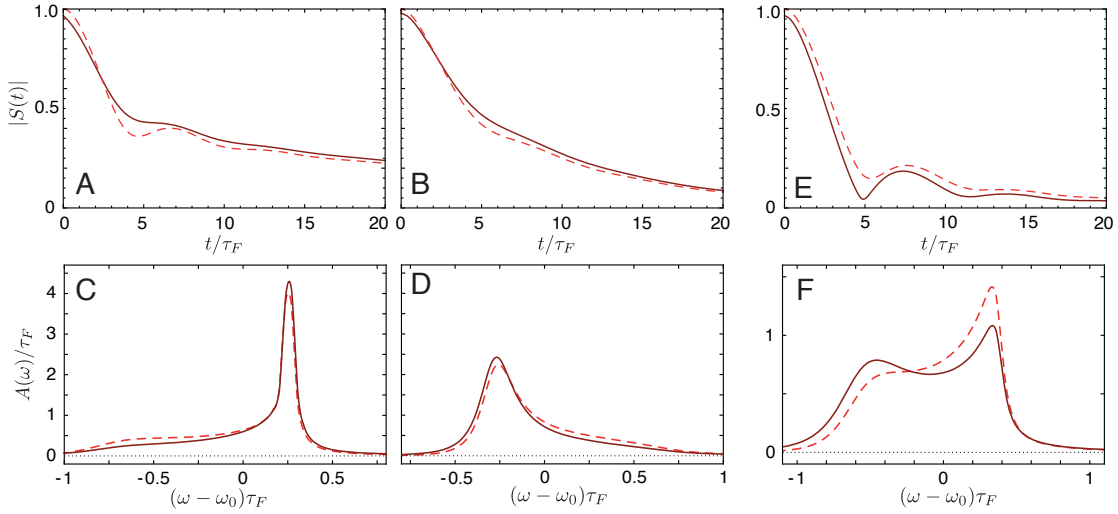

Figure 5.10: Role of the residual interactions in the Ramsey sequence at finite temperature. Upper panels: we compare the perfect quench Ramsey response (dashed) with a simulation of the experimental sequence (solid). Lower panels: we compare the linear-response excitation spectrum (dashed) with the Fourier transform of the signal obtained using the experimental sequence (solid). As in the main text, we take $k_F R^* = 1.1$ and the interaction parameters: (**A**, **C**) $X = -0.23$, $X_1 = -3.9$, (**B**, **D**) $X = 0.86$, $X_1 = 5.8$, and (**E**, **F**) $X = 0.08$, $X_1 = 4.8$. The temperatures are $T/T_F = 0.166$, 0.158, 0.177, respectively.

Modelling of experimental procedure at finite temperature within FDA

The interplay between the residual interactions and finite temperature presents a further theoretical challenge. In the following, we use the FDA to simulate the experimental protocol (Fig. 5.8) at finite temperature. To achieve this, we exploit the finding from Sec. 5.5.3 that the detailed dynamics of the rf-driven oscillations between the K$|2\rangle$ and K$|3\rangle$ states can be ignored when calculating $S(t)$. Thus, we assume that the initial $\pi/2$ rotation effectively produces a spin superposition (K$|2\rangle$ + K$|3\rangle$)$/\sqrt{2}$, independently of the residual interaction X_1 of the impurity in the state K$|3\rangle$ with the Fermi sea. To account for the dynamics due to the weak interaction X_1, we then let the system evolve under this interaction for a hold time $t_\mathrm{h} = t_\mathrm{rf}/2 + t_\mathrm{wait}$, which models the dynamics at weak interaction X_1 as the result of a sudden switch-on of this interaction at the midpoint of the $\pi/2$ pulses. After the hold time t_h, the final quench to the strong interactions X is performed. For the measurement of the Ramsey contrast, this sequence is reversed. Theoretically, this yields the modified time-dependent overlap

$$S(t) = \mathrm{Tr}\left[\hat{\rho}\, e^{i\hat{H}_0(2t_\mathrm{h}+t)} e^{-i\hat{H}_1 t_\mathrm{h}} e^{-i\hat{H}_X t} e^{-i\hat{H}_1 t_\mathrm{h}}\right], \tag{5.19}$$

where $\hat{H}_1$ and $\hat{H}_X$ denote the Hamiltonian 5.1 at interaction strength X_1 and X, respectively. Using the FDA, the expression Eq. (5.19) is evaluated exactly according to Eq. (5.13) at the experimental temperature. As can be inferred from Eq. (5.19), this simplified model of the experimental protocol corresponds to a sequence of interaction quenches.

In the upper panel of Fig. 5.10 we compare the result for $|S(t)|$ at the experimental temperatures obtained for the experimental sequence (solid lines) to the result for an idealized, i.e., perfect quench, Ramsey sequence (dashed lines). Similarly to the case of zero temperature, we see that the time evolution at X_1 has an experimentally observable effect on the dynamics. In particular, it generates an additional decoherence of the Ramsey signal already at $t = 0$, as well as an enhancement of the oscillations in $|S(t)|$ for resonant interactions – see Fig. 5.10E.

For the calculation of the FDA results shown in Fig. 5.2 of the main text we use the same procedure as described above. We account for slight additional experimental decoherence by scaling the prediction for $|S(t)|$ as described in Section S.5C. We also note that the phase $\varphi_\mathrm{FDA}(t)$ of the Ramsey signal $S(t) = |S(t)|e^{-i\varphi_\mathrm{FDA}(t)}$, as determined from Eq. (5.19), differs from the experimentally measured phase $\varphi(t)$ due to the detuning of the rf frequency from ω_0. They are related by $\varphi(t) = \varphi_\mathrm{FDA}(t) - (\omega_\mathrm{rf} - \omega_0)(2t_\mathrm{wait} + t_\mathrm{rf})$. Similar to the previous section and to the experiment, we take $\omega_\mathrm{rf} - \omega_0 = \varepsilon_1/\hbar$.

As outlined in Section 5.5.3, in the idealized Ramsey scenario the Fourier transform $A(\omega)$ of $S(t)$ is equivalent to the rf absorption in linear response, cf. 5.15 [Kna12]. Similarly to our $T = 0$ analysis in Sec. 5.5.3, we now study the effect of the residual interactions X_1 on the spectral decomposition of $S(t)$. To this end we compare the two signals $A(\omega)$ for the perfect quench with the result obtained for the experimental sequence as modelled by Eq. (5.19). We show the comparison of the spectra obtained in the idealized (dashed) and experimentally realized scenario (solid) in the lower panel of Fig. 5.10. As for our $T = 0$ results discussed above, we find only a small difference between the two finite-temperature

spectra. Therefore, in agreement with the experimental observation, cf. Fig. 5.3 in the main paper, under the condition of $|X_1| \approx 5$ we see that the weak interactions during the rf pulses have an observable but small effect on the predicted spectra.

In accordance with the results from the TBM shown in Fig. 5.9, we find from the evaluation of Eq. (5.19) that weak interactions X_1 lead to a small shift of spectral weight into the corresponding dominant polaron branches. This shift of spectral weight is also observed experimentally, see Fig. 5.3 of the main text.

Stronger interactions during rf pulses: illustration of quantum state preparation

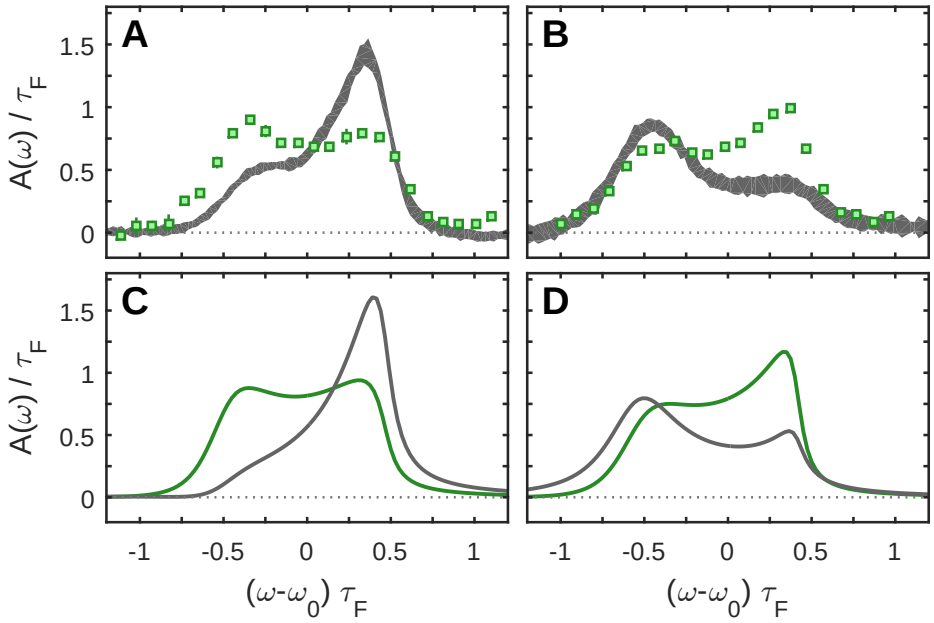

Figure 5.11: Control of the spectral decomposition of many-body quantum states. Upper panel: We compare the experimentally measured rf spectrum at the interaction parameter X (green squares) to the Fourier transform of $S(t)$ obtained using the measurement procedure illustrated in Fig. 5.8 with initial interaction parameter X_1 (gray shading). Lower panel: we compare the theoretical prediction from the FDA for the linear-response excitation spectrum (green) to the Fourier transform of the signal obtained by simulating the experimental sequence according to Eq. (5.19). (**A**, **C**) $X = 0.14$, $X_1 = -2.2$, $k_F R^* = 1.09$, $T/T_F = 0.174$. (**B**, **D**) $X = -0.25$, $X_1 = 1.7$, $k_F R^* = 1.1$, $T/T_F = 0.17$.

The shift of spectral weight towards the attractive or repulsive branches of the spectrum, cf. Figs. 5.9 and 5.10, may be interpreted as follows: The residual interactions present during the initial $\pi/2$ impurity spin rotation serve to produce an interacting many-body quantum state. As such, this procedure can be viewed as an adiabatic preparation of an attractive or repulsive polaron. Compared to the noninteracting state, this polaron has an increased wavefunction overlap with the corresponding branch of the strongly interacting system. When the system is then quenched into the regime of strong interactions, the increased overlap results in the corresponding shift of the spectral weight. An intriguing question is then whether such an approach can provide a novel way to experimentally control the spectral decomposition of quantum states.

To investigate this possibility, we increase the interaction during the $\pi/2$ rotations, corresponding to decreasing $|X_1|$, and determine the effect on $A(\omega)$. In the upper panel of Fig. 5.11 we show the spectra obtained by linear-response rf spectroscopy (green squares). Similar to Fig. 5.3 of the main paper, we compare this result to the Fourier transform of the Ramsey signal $S(t)$ (gray shading), as obtained from the experimental sequence described in Fig. 5.8. We also compare our experimental result to the prediction from the FDA, where the dynamics has been modeled as described by Eq. (5.19). As in the main text, we find excellent agreement between experiment and theory. Indeed, both feature a strong shift of spectral weight to regions of the spectrum that are adiabatically connected to the dominant polaron branches at interaction X_1. Furthermore, when comparing $A(\omega)$ in Fig. 5.11, with the spectrum for $|X_1| \approx 5$ in Figs. 5.9 and 5.10, it is clear that the amount by which the spectrum is shifted can be controlled by the strength of the interaction during the rf pulses. This strongly supports the assertion that the initial interactions can be used to precisely control the many-body dynamics. Our experimental techniques thus allow for a precise, dynamic control of the spectral decomposition of quantum states in future experiments.

The excellent agreement between theory and experiment also demonstrates that our theoretical approaches can be used to explore experimental ramps in combination with interferometric protocols in order to find, for instance, optimized spin and interaction trajectories.

5.5.4 Universal features of impurity dynamics and relation to orthogonality catastrophe

For impurities localized in space, which, for instance, can be achieved by species-selective three dimensional optical lattices, our experimental setup allows one to study universal features exhibited by the Anderson orthogonality catastrophe [And67]. The orthogonality catastrophe was originally studied in the context of x-ray absorption spectra in metals, where high-energy x-ray photons create atomic core holes by photo emission of inner-shell electrons [Mah00]. These core holes produce a scattering potential for the electrons in the conduction band, leading to characteristic power-law edges in the absorption spectra with an exponent that is universally determined by the scattering phase shift at the Fermi surface [And67]. However, impurities, phonons, residual interactions between the electrons, and a lack of knowledge of microscopic parameters makes it difficult to unambiguously determine the universal features of the orthogonality catastrophe in typical solid state materials [Oht90]. In contrast, the Hamiltonian in our experiment is well characterized on all relevant energy scales, and therefore the full dynamic response of the system can be reliably calculated by theory and probed by the ultrafast experimental techniques demonstrated in this work. This enables one to obtain fundamental insights into universal features of the orthogonality catastrophe, which are difficult to access in other systems.

To illustrate how the orthogonality catastrophe would manifest itself in an ultracold atomic gas experiment, the response of infinite mass impurities calculated using the FDA for the perfect quench scenario is shown in Fig. 5.12. First, at short times and for a range parameter of the Feshbach resonance $R^* > 0$, we see that the Ramsey contrast decays quadratically for all scattering parameters and temperatures considered, in accordance with Eq. (5.11). The main universal feature associated with the orthogonality catastrophe is expected in the long-

time dynamics at $T = 0$: Here, the Ramsey response is predicted to exhibit power law tails, which depend only on the scattering phase shift at the Fermi surface [And67, Kna12]. This is explicitly verified in Fig. 5.12A where we fix the scattering phase shift at the Fermi surface but change the scattering parameters. While the response at intermediate times depends on the scattering parameters, we see that the long-time evolution approaches a universal power law that only depends on the phase shift at the Fermi surface. We note that the long-time dynamics is universal: It is the same for a system with a broad resonance where $R^* = 0$ (solid line in Fig. 5.12A), as it is for our system with a finite range parameter (dashed and dotted lines).

When the temperature is non-zero, as in the experiment, thermal fluctuations alter the power law dephasing dynamics at sufficiently long times. Instead, exponential tails due to thermal decoherence appear as another universal feature of the dynamics [Kor50, And67, Yuv70, Kna12]. The exponential tails are illustrated in Fig. 5.12B. The effects of thermal decoherence could be countered by employing the recently developed cooling methods [Har15], opening the door to observing the orthogonality catastrophe in a cold-atom system.

Finally, we note that in our experiment temperature becomes relevant at a time scale similar to those associated with recoil and multiple particle-hole excitations. It is a challenge for theoretical approaches to exactly account for both recoil and higher order particle-hole excitations [Ros99]. However, experiments at lower temperatures which take advantage of the tunability of the impurity mass using optical lattices would be ideally suited to probe the competition between these effects. Such ultracold-atom experiments would hence provide important insight into this long standing theoretical question.

5.5.5 Experimental and data analysis procedures

In this section we discuss the procedures used to record and analyze the data presented in this work. We detail the cooling and preparation of our atomic samples, the details of the rf pulses used in our Ramsey sequences, the methods used to analyze the data and the method that we use to vary the concentration of the K atoms.

Sample preparation

The atomic samples are prepared by forced evaporation of Li atoms from a Li-K mixture held in an optical trap, where the K atoms are sympathetically cooled by the Li environment. This preparation procedure is described in detail in Refs. [Tre11a, Spi10a]. At the end of the forced evaporation, the Li and K atoms are transferred into an optical trap composed of two crossed 1064-nm laser beams, as described in Ref. [Cet15]. The measured radial and axial trap frequencies of the Li atoms are $f_{r,\mathrm{Li}} = 941(5)$ Hz and $f_{z,\mathrm{Li}} = 134(1)$ Hz, respectively. The measured radial and axial trap frequencies of the K atoms are $f_{r,\mathrm{K}} = 585(3)$ Hz and $f_{z,\mathrm{K}} = 81(1)$ Hz, respectively.

At the end of the preparation procedure, the Li and the K atoms are in their lowest Zeeman

states Li$|1\rangle$ and K$|1\rangle$. Before the Ramsey sequence, the K atoms are transferred to the K$|2\rangle$ state using an rf pulse. Following this rf transfer, the Li and K atoms are thermalized by holding them for 750 ms in the crossed-beam optical trap. While the interaction between the Li$|1\rangle$ and K$|2\rangle$ atoms, characterized by the scattering length $a_{12} = 63a_0$ [Nai11], is sufficient to ensure thermalization during this hold time, it can be neglected during the Ramsey experiments. The temperature of the atoms is determined by releasing the atoms from the trap and observing the free expansion of the K cloud.

Due to the Li Fermi pressure and the more than two times stronger optical potential for K, the K cloud is much smaller than the Li cloud [Tre11a], and therefore samples a nearly homogeneous Li environment. Because of the small variation of the Li environment sampled by the K atoms, we introduce the effective Li Fermi energy ϵ_F as

$$\epsilon_F = \frac{1}{N_\mathrm{K}} \int E_F(\mathbf{r}) n_\mathrm{K}(\mathbf{r}) d^3\mathbf{r}\,. \tag{5.20}$$

Here, $n_\mathrm{K}(\mathbf{r})$ is the local K number density at position $\mathbf{r}$ in the trap, and

$$E_F(\mathbf{r}) = \frac{\hbar^2 \left(6\pi^2 n_\mathrm{Li}(\mathbf{r})\right)^{2/3}}{2m_\mathrm{Li}} \tag{5.21}$$

is the local Li Fermi energy as determined by the local Li number density $n_\mathrm{Li}(\mathbf{r})$. We quantify the small inhomogeneity of the Li environment experienced by the K atoms by the standard deviation of the local Li Fermi energy

$$\sigma(E_F) = \left(\frac{1}{N_\mathrm{K}} \int (E_F(\mathbf{r}) - \epsilon_F)^2 n_\mathrm{K}(\mathbf{r}) d^3\mathbf{r} \right)^{1/2}. \tag{5.22}$$

We also introduce the average Li and K number densities $\bar{n}_\mathrm{Li}$ and $\bar{n}_\mathrm{K}$ sampled by the K atoms as

$$\bar{n}_\mathrm{Li,K} = \frac{1}{N_\mathrm{K}} \int n_\mathrm{Li,K}(\mathbf{r}) n_\mathrm{K}(\mathbf{r}) d^3\mathbf{r}\,. \tag{5.23}$$

In contrast to the Li atoms, the K atoms in our measurements remain non-degenerate, with $k_B T / E_F^\mathrm{K}(0) > 1.2$, where $E_F^\mathrm{K}(0)$ is the local potassium Fermi energy in the center of the trap when all K atoms are in the same internal state.

For all measurement presented in this work, Table 5.1 lists the total numbers of the Li and K atoms, their temperatures and trap-averaged densities, as well as the effective Li Fermi energies and their standard deviations. Throughout our measurements, these parameters remain nearly constant, with the exception of the measurements shown in Fig. 5.4. Here, in order to investigate the effect of the K concentration, the total number of the K atoms is increased from about 1×10^4 to 2.5×10^4. The attendant increase in the thermal load during the Li evaporation results in a decrease of the Li atom number and an increase in the temperature of the final atomic sample.

Note that, in contrast to our previous work [Cet15], our present experiments have been optimized for large optically induced interaction shifts ($|X - X_1| \approx 5$). These shifts are

Figure(s)	N_{Li} (10^5)	N_{K} (10^4)	T (nK)	ϵ_F/h (kHz)	$\frac{\sigma(E_F)}{\epsilon_F}$ %	$\bar{n}_{\mathrm{Li}}$ $10^{12}\mathrm{cm}^{-3}$	$\bar{n}_{\mathrm{K}}$ $10^{12}\mathrm{cm}^{-3}$
2A, 2C, 3A	3.5(4)	0.95(10)	435(25)	54.6(2.7)	7.4	8.9(7)	1.8(3)
2B, 2D, 3B	3.3(4)	1.0(1)	410(25)	53.9(2.4)	7.1	8.7(6)	2.0(3)
2E, 2F, 3C	3.5(4)	1.0(1)	460(30)	54.1(2.4)	7.7	8.8(6)	1.7(3)
5.11A	3.1(4)	1.0(1)	430(30)	52.0(2.9)	7.7	8.2(7)	1.8(3)
5.11B	2.9(3)	1.05(10)	425(35)	50.8(2.1)	7.7	8.0(6)	2.0(3)
4	2.35(30)	2.5(1)	520(25)	44.2(2.3)	10.4	6.5(5)	3.4(3)

Table 5.1: The total number of the Li atoms N_{Li}, the total number of the K atoms N_{K}, the sample temperature T, the effective Li Fermi energy ϵ_F, the standard deviation $\sigma(E_F)$ of the local Li Fermi energy across the trap, the trap-averaged Li and K number densities $\bar{n}_{\mathrm{Li}}$ and $\bar{n}_{\mathrm{K}}$ in our measurements.

produced by switching one of the crossed trapping beams from a beam with a low peak intensity and small size to a beam with a large intensity and large size propagating in the same direction. In our previous work [Cet15], as well as in the measurements shown in Fig. 5.11, the waists, positions and intensities of the two beams are adjusted so as to yield mode-matched trapping potentials, preventing excitations of the center-of-mass and breathing collective modes of the atomic clouds. In the measurements presented in Figs. 2, 3 and 4, a larger beam intensity was used in order to produce a larger optical shift, resulting in some excitation of the breathing modes.

The maximal interaction time in our Ramsey measurements of 60 μs is much smaller than the shortest period of a collective oscillation (about 500 μs). We calculate that, during our short interaction time, the oscillations of the breathing modes cause at most a 6% variation of ϵ_F around its initial value specified in Table 5.1, without any significant effect on the measurements presented here.

Rf pulses

We apply rf pulses in the Ramsey procedures by discretely gating a continously running rf source. To record the atomic populations N_3 and N_2 as a function of the phase of the second rf pulse, we change the phase of the rf source by a variable amount ϕ_{rf} before applying this pulse.

The weak interactions between the K atoms in the K$|3\rangle$ state and the Li atoms corresponding to the interaction parameter X_1 cause the transition frequency between the K$|2\rangle$ and the K$|3\rangle$ states to differ from the transition frequency ω_0 in the absence of the Li atoms. We compensate for this effect by adjusting the frequency ω_{rf} of the rf source to be resonant with the K$|2\rangle-$K$|3\rangle$ transition at the time when the rf pulses are applied. For the data in Figs. 2A, 2B, 2C, $(\omega_{\mathrm{rf}}-\omega_0)\tau_F$ is equal to $+0.06$, -0.07, -0.05, respectively. For the data in Fig. 5.11C and 5.11D where the interaction of the K atoms during the rf pulses is stronger, $(\omega_{\mathrm{rf}}-\omega_0)\tau_F$ is equal to $+0.11$ and -0.16.

The shift in the frequency of the rf source from ω_0 to ω_{rf} causes the signal $S(t)$ to accumulate

an additional phase $(\omega_{\rm rf}-\omega_0)t$ during the interaction time t. To account for this added phase, we introduce the phase $\phi = \phi_{\rm rf} + (\omega_{\rm rf} - \omega_0)t$.

Analysis methods

We determine the contrast $|S(t)|$ and the phase $\varphi(t)$ by fitting the Ramsey signal $(N_3 - N_2)/(N_3 + N_2)$ as a function of the phase ϕ to a sine wave with an offset i.e. $F(t) + |S(t)|\cos(\phi - \varphi(t))$. Decoherence during the rf pulses, as well as imperfections of the rf pulses and the atom detection, cause the contrast for $t = 0$ to be slightly smaller than unity. When comparing theoretical results from Figs. 5.9 and 5.10 to the experimental data in Fig. 5.2, we account for this effect by scaling the theoretical predictions for $|S(t)|$ by an overall factor η. For each calculation, this factor is determined by fitting the prediction for $|S(t)|$ to the three data points with the the shortest interaction times. We obtain $0.92 < \eta < 1$, which corresponds to an additional loss of contrast that is of the same order as the decoherence during the rf pulses predicted by the FDA (see Fig. 5.10).

To compute the Fourier transform of the experimental $S(t)$ data, we use piecewise linear interpolations of $\log S(t)$ and $\varphi(t)$ between the individual data points. Outside of the range of the data, we set $S(t) = 0$. To determine the error of the Fourier transform, we sample the values of $S(t)$ and $\varphi(t)$ at each data point from Gaussian distributions whose means and standard deviations correspond to the measured values and errors, respectively. We use the standard deviation of the computed values of the Fourier transform for each value of ω as an estimate of the error indicated by the shaded areas in Figs. 3 and 5.11.

Varying the K concentration

We study the effects of the impurity concentration by varying the number of the strongly interacting K atoms. If this were done by changing the total number of the K atoms in the experiment, the change in the thermal load on the Li atoms during forced evaporation would result in a correlated variation in the number of Li atoms and the sample temperature (compare the settings for Fig. 5.2 and Fig. 5.4 in Table 5.1). To avoid these systematic effects, in the measurements presented in Fig. 5.4, we keep the total number of the K atoms constant and vary the fraction of the K atoms that participate in the Ramsey sequence. We accomplish this by changing the intensity of the rf pulse that transfers the K atoms from the $|1\rangle$ state to the $|2\rangle$ state before the Ramsey procedure. During the subsequent 750 ms preceding the Ramsey sequence, the K atoms collisionally thermalize with the much larger Li cloud, resulting in an incoherent mixture of K$|1\rangle$ and K$|2\rangle$ atoms at a constant temperature. When referring to these measurements, we use $\bar{n}_{\rm K}$ not for the average density of all K atoms, but for the density of those K atoms that participate in the Ramsey sequence.

We minimized the small effects of long-time drifts in the temperature, the atom numbers and the trapping potential by varying the experimental parameters in a specific order. For each K concentration and interaction time, we recorded data for 4 different phases of the second rf pulse in order to obtain $S(t)$. For each interaction time, the data with different K

concentrations were recorded in immediate succession. The data sets for different interaction times were then recorded in a random order.

5.5.6 Linearity of rf response

The response of atoms to an applied rf field is linear if the fraction of the atoms transferred from one state to another is proportional to the intensity of the field. Linearity can be ensured by using a sufficiently weak rf pulse that is also much longer than the inverse width of the relevant spectral features. The narrowest spectral features in the present work are the polaron peaks in Figs. 3A and 3B with rms widths $0.06\,\hbar/\tau_F$ and $0.09\,\hbar/\tau_F$, respectively. To record these polaron spectra, we used Blackman-shaped rf pulses [Kas92] whose duration $t_{\rm rf} = 300\,\mu{\rm s} \approx 100\,\tau_F$ is much longer than the inverse widths of the polaron peaks.

We checked the linearity of the response by varying the intensity $I_{\rm rf}$ of the applied rf field. Fig. 5.13A shows the fraction of the K atoms transferred from the K$|2\rangle$ to the K$|3\rangle$ state in the repulsive polaron regime, under conditions similar to those in the measurements shown in Fig. 5.3A. The frequency of the rf pulse is adjusted so that $(\omega_{\rm rf} - \omega_0)\tau_F = 0.3$, corresponding to peak response and resonant excitation of the repulsive polaron. The rf intensity is measured in units of the intensity I_π that results in a π-pulse for noninteracting K atoms. For intensities up to the intensity $I_{\rm rf} = 0.79\ I_\pi$, which is used in the measurements shown in Figs. 3A and 3B, we observe that the transferred fraction of the K atoms stays essentially proportional to the intensity of the pulse.

In the linear-response regime, the atomic response is predicted to be proportional to the duration of the rf pulse. Fig. 5.13B shows the fraction of the K atoms transferred in the repulsive polaron regime by rf pulses with $I_{\rm rf} = 0.79\ I_\pi$, as a function of the pulse duration. The frequency of the rf pulse is adjusted so that $(\omega_{\rm rf} - \omega_0)\tau_F = 0.3$, in order to obtain the peak response, as in Fig 5.13A. For pulses with duration up to 300 μs (indicated by the dashed line), we observe that the transferred fraction of the K atoms stays essentially proportional to the duration of the pulse.

Note that the maximal transferred fraction exceeds 0.5. We explain this observation by the coupling of the initial non-interacting K state to multiple interacting K states by the rf pulse, which manifest themselves as the polaron peak and the broad pedestal in our spectra.

The spectra for resonant Li-K interactions shown in Figs. 3B, 5.11A, 5.11B were recorded using Blackman-shaped rf pulses with duration of $t_{\rm rf} = 100\,\mu{\rm s}$ (approximately $35\,\tau_F$). The intensity of these pulses was adjusted to 50% of that needed to produce π pulses for non-interacting K atoms. We verified the linearity of the rf response by comparing the spectra recorded using this rf intensity to those recorded using the intensity needed to produce full π pulses for noninteracting K atoms (Fig. 5.14). Our observations are in good agreement with linear response.

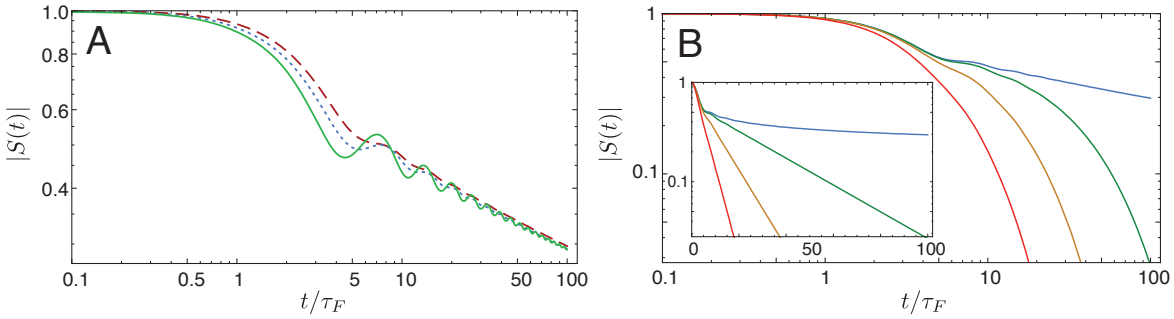

Figure 5.12: Universal features of the dynamical orthogonality catastrophe. We show the Ramsey contrast for an infinitely heavy impurity obtained within the FDA. (**A**) The zero-temperature Ramsey contrast exhibits a power law decay, shown on a double logarithmic scale. We change the Feshbach resonance range $k_F R^*$ and interaction parameter X in such a way that the scattering phase shift at the Fermi surface is constant leading to a constant exponent of the power law tail. The data corresponds to a fixed phase shift $\delta_{k_F} = 1.4$ with the choices $(X, k_F R^*) = (1, 1.12)$ (dashed red), $(X, k_F R^*) = (0.58, 0.56)$ (dotted blue), and $(X, k_F R^*) = (0.15, 0)$ (solid green). (**B**) Ramsey contrast at various temperatures on a double logarithmic scale. We choose temperatures $T/T_F = 0$ (blue), 0.05 (green), 0.15 (orange), 0.4 (red) at fixed values $X = 1$ and $k_F R^* = 1.12$. The inset shows the same data on a logarithmic-linear scale to emphasize the appearance of exponential tails at finite temperature.

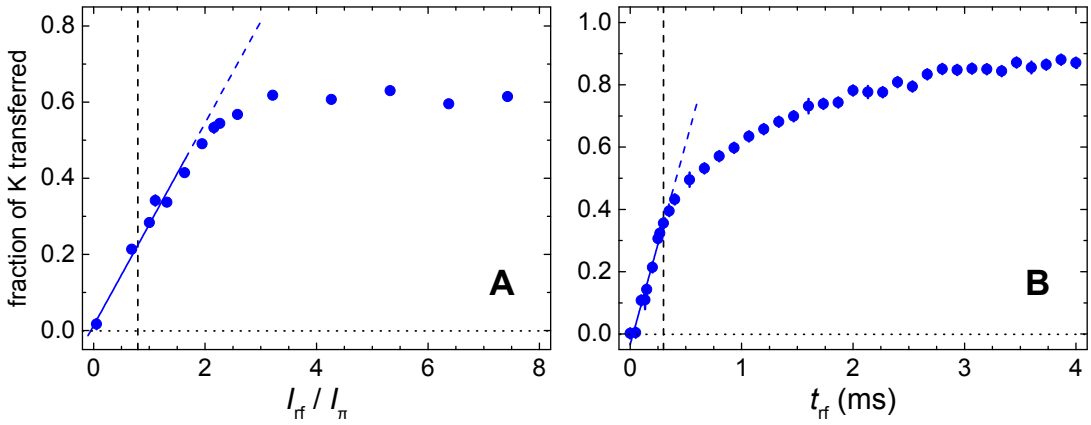

Figure 5.13: Linearity of the rf response in the repulsive polaron regime. (**A**) Fraction of the K atoms transferred from state K$|2\rangle$ to the state K$|3\rangle$ for $X = -0.13(6)$ as a function of the intensity $I_{\rm rf}$ of an rf pulse with duration $t_{\rm rf} = 300\,\mu$s. (**B**) Fraction of the K atoms transferred for $X = -0.23(6)$ as a function of the duration $t_{\rm rf}$ of the rf pulse for the rf pulse intensity $I_{\rm rf} = 0.79\,I_\pi$. Vertical dashed lines correspond to $I_{\rm rf} = 0.79\,I_\pi$ and $t_{\rm rf} = 300\,\mu$s, respectively. The pulse frequencies are adjusted to resonantly excite the repulsive polaron. The blue solid lines indicate linear fits to the data in the ranges indicated by the same lines. The blue dashed lines show extrapolations of these fits.

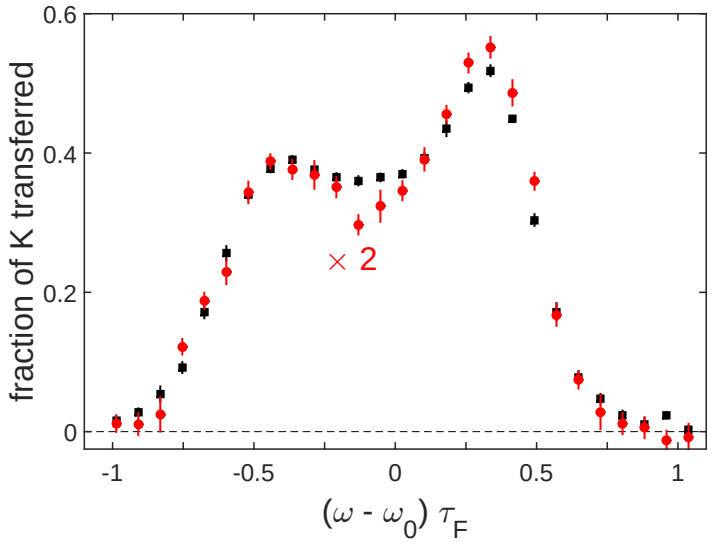

Figure 5.14: Linearity of the rf response for resonant interactions. Fraction of the K atoms transferred from state K$|2\rangle$ to the state K$|3\rangle$ by an rf pulse with duration $t_{\mathrm{rf}} = 100\,\mu$s for $X = +0.02(6)$. For the black data points, the intensity of the rf pulse is adjusted to obtain a π-pulse in the absence of Li atoms. The red data points correspond to a 50% lower intensity of the rf field.

Chapter 6

Publication: Observation of a Strong Atom-Dimer Attraction in a Mass-Imbalanced Fermi-Fermi Mixture[1]

Physical Review Letters **112**, 075302 (2014)
submitted 20 November 2013, published 21 February 2014
DOI: 10.1103/PhysRevLett.112.075302
Editor's suggestion

M. Jag[1,2], M. Zaccanti[1,3], M. Cetina[1], R. S. Lous[1,2], F. Schreck[1], R. Grimm[1,2], D. S. Petrov[4], and J. Levinsen[5,6]

[1] *Institut für Quantenoptik und Quanteninformation (IQOQI), Österreichische Akademie der Wissenschaften*
[2] *Institut für Experimentalphysik, Universität Innsbruck, 6020 Innsbruck, Austria*
[3] *CNR Istituto Nazionale Ottica, 50019 Sesto Fiorentino, Italy*
[4] *Université Paris-Sud, CNRS, LPTMS, UMR8626, Orsay, F-91405, France*
[5] *TCM group, Cavendish Laboratory, JJ Thomson Avenue, Cambridge, CB3 0HE, United Kingdom*
[6] *Aarhus Institute of Advanced Studies, Aarhus University, DK-8000 Aarhus C, Denmark*

[1] The author of the present thesis developed the experimental procedures together with M.Z., performed all measurements together with M.Z. and M.C., and analyzed the data together with M.Z., M.C., and R.S.L. under the supervision of F.S. and R.G. All authors contributed to writing the manuscript.

6.1 Abstract

We investigate a mixture of ultracold fermionic ^{40}K atoms and weakly bound ^{6}Li^{40}K dimers on the repulsive side of a heteronuclear atomic Feshbach resonance. By radio-frequency spectroscopy we demonstrate that the normally repulsive atom-dimer interaction is turned into a strong attraction. The phenomenon can be understood as a three-body effect in which two heavy ^{40}K fermions exchange the light ^{6}Li atom, leading to attraction in odd partial-wave channels (mainly p-wave). Our observations show that mass imbalance in a fermionic system can profoundly change the character of interactions as compared to the well-established mass-balanced case.

6.2 Introduction

Ultracold fermions with tunable interactions provide remarkable possibilities to model the many-body physics of strongly interacting states of quantum matter under well-controllable conditions [Gio08, Blo08]. Fermionic superfluids, realized by combining two different spin states of a fermionic atomic species and controlling their s-wave interaction through a Feshbach resonance [Chi10], have led to spectacular achievements. Beyond these experimentally well-established fermionic systems, mass imbalance offers an additional degree of freedom, with interesting prospects for new many-body phenomena having no counterpart in the mass-balanced case, such as novel quantum phases or superfluid states in various trapping environments [Isk06, Bau09c, Gez09, vK11, Sot12, Cui13, Gub09, Mat11, Qi12, Dai12, Pet07, Bar08, SC91, Ors10, Dal12, Nis08, Nis09b].

Striking effects of mass imbalance in fermionic systems already emerge at the few-body level. A resonantly interacting three-body system of one light ($\downarrow$) and two heavy ($\uparrow$) fermions is known to exhibit bound states depending on the mass ratio $m_\uparrow/m_\downarrow$. While Efimov trimer states require large mass ratios ($m_\uparrow/m_\downarrow > 13.6$), for repulsive interactions, non-Efimovian trimer states can exist in an intermediate regime ($13.6 > m_\uparrow/m_\downarrow > 8.17$) [Kar07]. Below the critical value of 8.17, the last state turns into an atom-dimer scattering resonance in the p-wave channel [Kar07].

The ^{40}K-^{6}Li mixture serves as the prime system for current experiments on tunable mass-imbalanced Fermi-Fermi mixtures [Wil08, Cos10, Tre11a]. The corresponding mass ratio of $m_\uparrow/m_\downarrow \approx 6.64$ lies well in the regime of near-resonant atom-dimer interactions [Lev09, Lev11]: as the most prominent effect, theory predicts a substantial attraction resulting from higher partial waves (mainly p-wave) in a regime where one would naively, based on s waves alone, expect a strong repulsion. This also makes the corresponding many-body problem in a ^{40}K-^{6}Li mixture significantly more complicated and much richer than in the widely investigated mass-balanced case.

In this Letter, we investigate the interaction between ^{40}K atoms and weakly bound ^{6}Li^{40}K dimers near an interspecies Feshbach resonance (FR). We employ radio-frequency (rf) spectroscopy by using two different internal states of ^{40}K, one strongly interacting with the

dimers and the other one practically non-interacting [Koh12b]. We observe line shifts and collisional broadening and interpret these in terms of the real and imaginary part of the forward-scattering amplitude $f(0)$ for atom-dimer collisions, calculated on the basis of the theoretical approach of Ref. [Lev11]. The comparison between theory and experiment shows excellent agreement and, in particular, demonstrates the predicted atom-dimer attraction on the repulsive side of the interspecies FR.

6.3 Main results

The interaction of a heavy atom with a heavy-light dimer can be understood in the Born-Oppenheimer approximation, where the atom-dimer potentials are taken to be the eigenenergies of the light atom for a given separation R between the heavy ones. As in the usual double-well problem with tunneling, the state localized near one heavy atom is mixed with the state localized near the other; the symmetric and antisymmetric superpositions lead to the attractive $U_+(R) < 0$ and repulsive $U_-(R) > 0$ potentials, respectively. Note the analogy to the well-known H_2^+ cation, where the exchange of the electron leads to a symmetric bound state and an antisymmetric unbound state [Pau28]. In our experiment, the heavy particles are identical fermions, making the atom-dimer interaction channel dependent. The symmetric (antisymmetric) state corresponds to odd (even) values of the total angular momentum l [Lev11]. In Fig. 6.1(a) we plot the total effective potentials $U_\pm + U_{cb}$ (solid lines) and the bare centrifugal barriers $U_{cb} = l(l+1)\hbar^2/m_\uparrow R^2$ (dashed lines) for $l = 0$, 1, and 2 (i.e., s-, p-, and d-wave channels) for typical experimental conditions. At distances on the order of typical de Broglie wavelength, $U_\pm$ can be comparable to U_{cb} and we expect significant interaction effects in non-zero partial waves.

The relevant quantity that characterizes the net effect of all partial waves is the atom-dimer forward scattering amplitude [Sob72, Bar58b, Bar58a],

$$f(0) = \sum_{l=0}^{\infty}(2l+1)\left[\frac{\sin 2\delta_l(k_{coll})}{2k_{coll}} + i\frac{\sin^2\delta_l(k_{coll})}{k_{coll}}\right], \tag{6.1}$$

where $k_{coll} = \sqrt{2\mu_3 E_{coll}}/\hbar$ is the wavenumber associated with the relative atom-dimer motion and μ_3 is the reduced atom-dimer mass. The phase shifts δ_l for the three lowest partial waves have been computed in Ref. [Lev11] and here we extend the result to higher ones since they give significant contributions (Supplemental Material). In Fig. 6.1(b) we show the resulting $-\mathrm{Re}\, f(0)$ as a function of the collision energy E_{coll} for the same conditions as in Fig. 6.1(a). In the limit of $E_{coll} \to 0$, the quantity $-\mathrm{Re}\, f(0)$ corresponds to the atom-dimer s-wave scattering length. At $E_{coll} \ll 0.1E_\mathrm{b}$, with E_b being the dimer binding energy, s-wave scattering (dashed line) dominates and the net interaction is repulsive, $-\mathrm{Re}\, f(0) > 0$.

For $E_{coll} \gtrsim 0.1E_\mathrm{b}$, higher partial-wave contributions lead to a sign reversal of $\mathrm{Re}\, f(0)$, changing the character of the interaction from repulsive into attractive. This sign reversal also appears if, at a fixed collision energy, the magnetic detuning from the FR center is varied, see Fig. 6.1(c). In the realistic example of Fig. 6.1(c) the sign reversal takes place at a magnetic detuning of $B - B_0 = -53\,\mathrm{mG}$, where the binding energy is $E_\mathrm{b}/k_\mathrm{B} \approx 3.1\,\mu\mathrm{K}$,

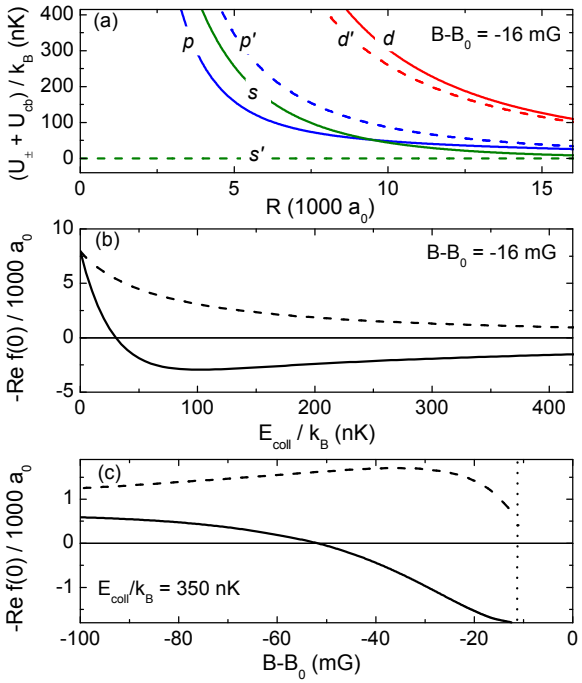

Figure 6.1: Interaction between ^{40}K atoms and ^{6}Li^{40}K dimers near the 155 G interspecies FR. (a) Total interaction potentials as a function of the distance R between the two K atoms for the s, p, and d channels (dashed curves with labels s', p', d' refer to the unmodified centrifugal barriers). Here we have chosen a magnetic detuning of $B - B_0 = -16\,\mathrm{mG}$, corresponding to a s-wave scatering length of $a = 3528\,a_0$ and to a dimer binding energy of $E_\mathrm{b}/k_\mathrm{B} = 600\,\mathrm{nK}$. (b) Real part of the forward-scattering amplitude $f(0)$ as a function of the collision energy E_{coll} (solid line) in comparison with the s-wave contribution (dashed line). (c) Same as in (b), but as a function of the magnetic detuning $B - B_0$ for a fixed collision energy $E_{coll}/k_\mathrm{B} = 350\,\mathrm{nK}$. The dotted line indicates the dimer breakup threshold, $E_{coll} = E_\mathrm{b}$.

corresponding to roughly ten times the collision energy $E_{coll}/k_B = 350\,\mathrm{nK}$. The theory lines in Fig. 6.1(c) stop close to the FR center at the magnetic field detuning where $|E_b| = E_{coll}$ (dotted line), beyond which the inelastic channel of collisional dimer dissociation opens up.

The starting point of our experiments is an optically trapped, near-degenerate Fermi-Fermi mixture of typically 4×10^4 ^{40}K atoms and 1×10^5 ^{6}Li atoms. The preparation procedures are described in our previous work [Spi10a, Tre11a]. We choose a particular FR that occurs between Li atoms in the lowest Zeeman sub-level Li$|1\rangle$ ($f = 1/2, m_f = +1/2$) and K atoms in the third-to-lowest sub-level K$|3\rangle$ ($f = 9/2, m_f = -5/2$) [Nai11]. The s-wave interspecies scattering length a can be magnetically tuned as $a = a_{bg}[1 - \Delta/(B - B_0)]$ with $a_{bg} = 63.0\,a_0$ (a_0 is Bohr's radius) and $\Delta = 880\,\mathrm{mG}$ [Nai11]. The resonance is rather narrow, as characterized by the length parameter $R^* = 2700\,a_0$ [Pet04a]. The position of the FR center near $B \approx 154.7\,\mathrm{G}$ depends on the trap setting, as it includes small shifts induced by the trapping light. For each trap setting we have calibrated the FR center B_0 with $\leq 2\,\mathrm{mG}$ accuracy (Supplemental Material).

We create an atom-dimer mixture by a Feshbach ramp across the resonance and by subsequent purification and spin-manipulation techniques (Supplemental Material). While the dimers are formed in the Li$|1\rangle$-K$|3\rangle$ spin channel, we initially prepare the free atoms in the second-to-lowest spin state K$|2\rangle$ ($f = 9/2, m_f = -7/2$), for which the interaction with the dimers is negligible. The total number of dimers and atoms is 1.5×10^4 and 7×10^3, respectively. The interspecies attraction during the Feshbach ramp results in a collective oscillation of the dimer cloud, which we can take into account by introducing an effective temperature T_{eff} (Supplemental Material). We use three different trap settings, for which $T_{eff} = 165\,\mathrm{nK}$, 232 nK, and 370 nK. This corresponds to mean dimer densities as experienced by the atoms of $\bar{n}_D = 5.2 \times 10^{11}\,\mathrm{cm}^{-3}$, $8.2 \times 10^{11}\,\mathrm{cm}^{-3}$, and $1.4 \times 10^{12}\,\mathrm{cm}^{-3}$, respectively.

To investigate the interaction between the K$|3\rangle$ atoms and the Li$|1\rangle$K$|3\rangle$ dimers, we carry out rf spectroscopy. This can be done in two different ways, either by driving the K atoms from the noninteracting state $|2\rangle$ into the interacting state $|3\rangle$ (method A) or vice versa (method B). With our K atoms initially prepared in the state $|2\rangle$, we carry out method A by applying a 1-ms rf pulse. For method B, we rapidly transfer the full K$|2\rangle$ population into K$|3\rangle$ using a short 90-μs preparation pulse without spectral resolution, and then drive the spectrally resolving transition with a 1-ms pulse. Our signal in both cases is the fraction of transferred atoms as a function of the rf detuning $\nu - \nu_0$ with respect to the unperturbed transition frequency ν_0, the latter being determined by the rf spectroscopy in the absence of dimers.

Sample spectra, at a magnetic detuning of $B - B_0 = -20\,\mathrm{mG}$, are shown in Fig. 6.2. The spectra recorded by methods A and B (circles and diamonds in Fig. 6.2) show both a broadening and a peak shift, as compared to the spectra recorded in the absence of dimers (triangles). Although the spectra very close to the FR center reveal asymmetries in their wings, which depend on the method applied, their peak shifts and broadenings are consistent for both methods. In the range of detunings $B - B_0$ studied in the present work the molecular dissociation signal is always well separated from the atomic line (inset of Fig. 6.2), and thus does not affect the lineshape of the atomic signal.

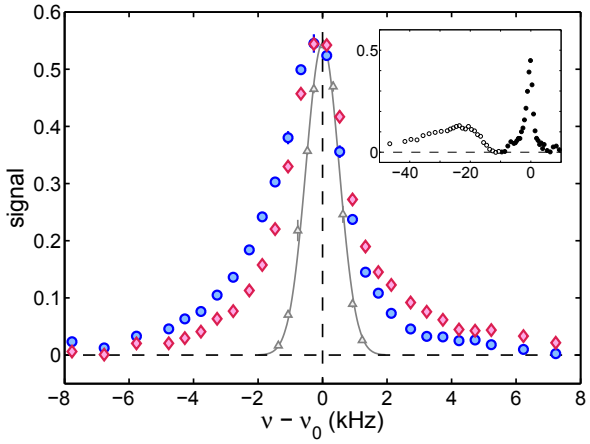

Figure 6.2: Sample rf spectra taken at $B - B_0 = -20\,\mathrm{mG}$ at $T_{eff} = 232\,\mathrm{nK}$. The red diamonds (blue circles) show data recorded using method A (B). For reference, the gray triangles show data recorded in the absence of dimers together with a Gaussian fit (gray line). Inset: Spectrum at $-17\,\mathrm{mG}$ over an extended frequency range. The molecular dissociation signal (open symbols), recorded with $30\times$ increased rf power, is clearly separated from the atomic peak (filled symbols).

Figure 6.3 shows the widths and peak shifts [2] of the rf spectroscopic signal, recorded by method A, as a function of $B - B_0$ for our three values of T_{eff}. When the FR center is approached, the spectrum broadens and its peak shifts from a positive to a negative rf detuning. With increasing temperature, the corresponding zero crossing shows a trend to move towards larger detunings.

We interpret the obtained results in the framework of the impact theory of pressure-induced effects on spectral lines, which assumes the collisions to be effectively instantaneous. This theory predicts Lorentzian profiles centered near the unperturbed frequency ν_0 whose line shifts and broadenings are proportional to the real and imaginary parts of the thermally averaged atom-dimer forward scattering amplitude $f(0)$ [Sob72, Bar58b, Bar58a], respectively. The real part of $f(0)$ shifts the energy of the K atoms, causing an average shift in the frequency of their peak rf response of $\delta\nu = -\hbar\bar{n}_{\mathrm{D}}\mathrm{Re}\langle f(0)\rangle/\mu_3$, where $\langle f(0)\rangle$ denotes the thermal average of $f(0)$ over all atom-dimer collision energies E_{coll}. The red solid lines in Fig. 6.3 show the theoretical results for $\delta\nu$ for the respective molecule densities and collision energies. The optical theorem relates the imaginary part of $f(0)$ to the average elastic scattering rate τ^{-1} as $\tau^{-1} = 4\pi\hbar\bar{n}_{\mathrm{D}}\mathrm{Im}\langle f(0)\rangle/\mu_3$. The resulting finite lifetime τ of the atoms' wavepackets causes Lorentzian broadening with a full-width at half-maximum (FWHM) $1/2\pi\tau$. The blue solid lines in Fig. 6.3 show the predicted FWHM, including additional broadening due to the finite duration of our rf pulse [3].

The collisional broadening yields information on the elastic scattering rate. At typical detunings of $B - B_0 \approx -20\,\mathrm{mG}$, our data show an elastic atom-dimer scattering rate on the order of $1/(100\,\mu\mathrm{s})$. A comparison with the observed dimer decay rate of about $1/(5\,\mathrm{ms})$ gives a lower limit for the ratio of elastic to inelastic atom-dimer collisions of 50. We note that in

[2] To determine the peak shift and the width, we apply a double-Gaussian fit to the spectra. From the fit, we identify the rf detuning of maximum signal and the width.

[3] The finite duration of our rf pulse causes an additional Gaussian broadening of typically 1.2 kHz (FWHM).

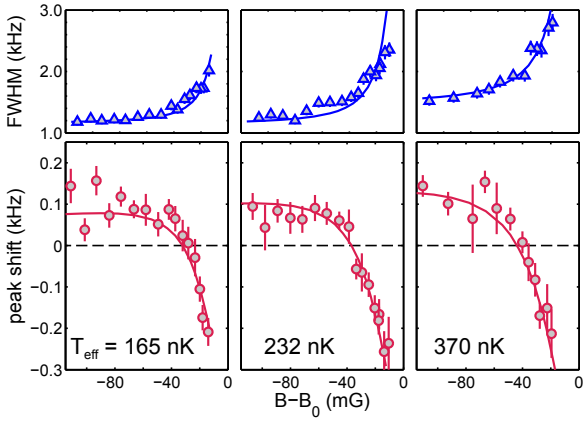

Figure 6.3: Widths (blue triangles) and peak shifts (red circles) extracted from the rf spectra as a function of the magnetic field detuning $B - B_0$ for the three different values of T_{eff}. The lines are the corresponding theoretical predictions. To account for fluctuations in the dimer number of different spectra, the widths and peak shifts are scaled to a dimer number of 15,000, which is typical for all spectra.

our system the dimers spontaneously dissociate on a timescale of about 10 ms [Nai11].

The comparison between the experimentally observed and the theoretically calculated line shifts and broadenings shows remarkable agreement over the whole parameter range investigated. The somewhat asymmetric spectral wings are beyond the impact theory [Szu96] and thus cannot be reproduced. Indeed, a substantial contribution to the wings comes from the photon emission/absorption events for which K atoms find themselves inside the atom-dimer interaction range, i.e. *during atom-dimer collisions*, which are assumed instantaneous in the impact theory. It is then understood that, for example, the left "attractive" wing of the B-spectrum is larger than that of the A-spectrum. Since in the former case potassium atoms are initially attracted by dimers, the probability to find them near dimers is enhanced. Effects that are beyond the impact theory become more pronounced as we approach the FR because of the increased atom-dimer collision time.

We finally discuss the interaction strength in our mixture in terms of $-\mathrm{Re}\langle f(0)\rangle$, which characterizes the interactions in a way that is analogous to a in the s-wave mean-field picture. We use the experimental peak-shift data from Fig. 6.3 to extract $-\mathrm{Re}\langle f(0)\rangle$ and plot it together with the corresponding theoretical results in Fig. 6.4. The sign reversal shows up for values of a being somewhat below $2000\,a_0$, with the expected temperature dependence of the zero crossing. For $a \approx 4000\,a_0$, the attractive interaction already corresponds to about $-2000\,a_0$. For even larger values of a, we would enter the more complicated regime of collisional dimer dissociation, which is beyond the scope of the present investigations. We note, however, that rf spectra acquired more deeply in the strongly interacting regime show strongly asymmetric lineshapes and have peaks shifted to even larger negative detunings.

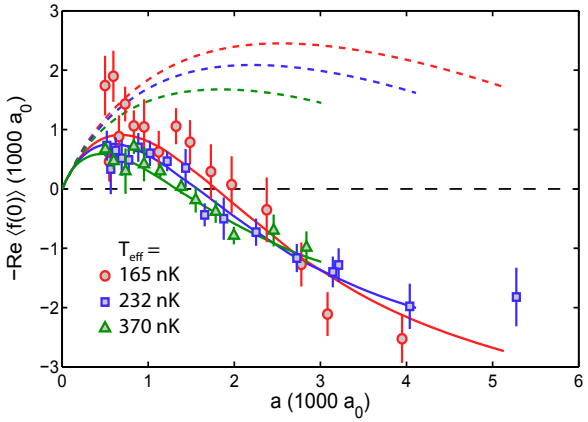

Figure 6.4: Real part of the atom-dimer forward-scattering amplitude as a function of the atom-atom scattering length a for the three different values of T_{eff}. The symbols and the lines show the data and the theoretical predictions from Fig. 6.3. For comparison, the dashed lines indicate the respective s-wave contributions. The theoretical lines stop at $k_{\mathrm{B}}T_{eff} = E_{\mathrm{b}}/2$.

6.4 Conclusion

In conclusion, we have demonstrated a three-body phenomenon in a mixture of heavy and light fermions, which leads to a sign reversal of the atom-dimer interaction near a FR, turning repulsion into a strong attraction. The effect is due to higher partial-wave (mainly p-wave) contributions, which are present even at very low collision energies in the nanokelvin regime. Remarkably, this few-body effect changes the character of the interaction without introducing detrimental losses. In contrast to few-body phenomena of the Efimov type [Fer11], the centrifugal barrier still protects the atoms from approaching each other too closely. The resulting collisional stability is a promising feature for many-body physics in Fermi-Fermi mixtures.

Our work lays the ground for a wealth of future studies on mass-imbalanced fermionic mixtures in the strongly interacting regime. Asymmetric phases with coexisting dimers and heavy atoms are energetically favored in a way not present in mass-balanced systems [Qi12]. Related mechanisms in quantum-degenerate situations may lead to exotic new many-body effects, including the emergence of imbalanced superfluids [Qi12], the condensation into non-zero momentum states [Mat11], and the appearance of p-wave superfluidity of heavy atoms mediated by light atoms [Nis09a]. On the few-body side, a direct prospect for our K-Li system is to confine the K atoms in an optical lattice, which is predicted to lead to the formation of stable trimer states [Pet07, Nis09b, Lev09].

Acknowledgements

We acknowledge funding by the Austrian Science Fund FWF with SFB FoQuS (F40-P04). M.Z. was supported by the FWF within the Lise Meitner program (M1318), D.S.P. by the Institut Francilien de Recherche sur les Atomes Froids (IFRAF), and J.L. acknowledges

support from the Carlsberg Foundation.

6.5 Supplemental material

6.5.1 Light shift of the Feshbach resonance

The Feshbach resonance (FR) that we employ for tuning the interactions in our system occurs between ^{6}Li atoms in their lowest internal state, denoted Li$|1\rangle$ ($f = 1/2, m_f = +1/2$), and ^{40}K atoms in their third-to-lowest state K$|3\rangle$ ($f = 9/2, m_f = -5/2$). This resonance has been investigated in detail in Ref. [Nai11]. The magnetic field dependent Li-K s-wave scattering length is given by

$$a(B) = a_{\mathrm{bg}} \left(1 - \frac{\Delta}{B - B_0}\right) \tag{6.2}$$

where $a_{\mathrm{bg}} = 63.0\, a_0$ is the background scattering length, $\Delta = 0.88\,\mathrm{G}$ is the width, and B_0 is the center of the resonance near 154.7 G.

As we already pointed out in Ref. [Koh12b], the optical trap induces a differential light shift between the atom pair state and the molecular state. This leads to a light-induced shift of the FR center. For the experiments presented in the main text, we use a near-infrared laser with a wavelength of 1064 nm (single-mode operation) in three different trap settings. Therefore, the center of the FR needs to be determined for each trap setting.

To determine B_0 we perform radio-frequency (rf) spectroscopy of the Feshbach molecules. For each trap setting, this is done in the following way: We prepare a nonresonant mixture of Li atoms in state Li$|1\rangle$ and K atoms in their second-to-lowest state K$|2\rangle$ several tens of mG below the approximate position of the resonance center. Here, we apply a strong 500-μs rf pulse at a variable frequency ν, several kHz below the unperturbed K$|2\rangle \rightarrow$K$|3\rangle$ transition frequency ν_0. This pulse drives Li$|1\rangle$-K$|2\rangle$ atom pairs into the Li$|1\rangle$K$|3\rangle$ dimer state. To determine the number of dimers associated, we subsequently dissociate the dimers into a Li$|1\rangle$ and a K$|3\rangle$ atom by a 300-μs magnetic field ramp to 154.8 G. By recording absorption images we then determine the populations N_2 and N_3 of the K spin states K$|2\rangle$ and K$|3\rangle$, respectively.

By plotting the signal, given by $N_3/(N_3 + N_2)$, against the rf detuning $\nu - \nu_0$, we resolve the molecule association spectrum; see Fig. 6.5. The unperturbed transition frequency ν_0, corresponding to the Zeeman splitting of the two states, is determined by rf spectroscopy in the absence of Li$|1\rangle$ (red points). We determine the binding energy of the molecules from the onset frequency of the molecular association spectra. As the onset frequency, we use

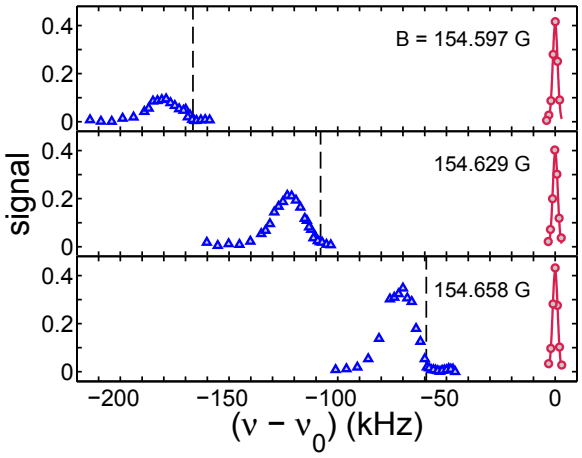

Figure 6.5: Data from the molecular rf association spectroscopy in trap 2. Red circles were taken with a rf power set to the value to match the π-pulse condition in the absence of interactions (no Li$|1\rangle$ present) and is scaled by 0.5. Blue points were taken with a 30$\times$ larger rf power. The dashed lines indicate the binding energy $E_\mathrm{b}(B)$.

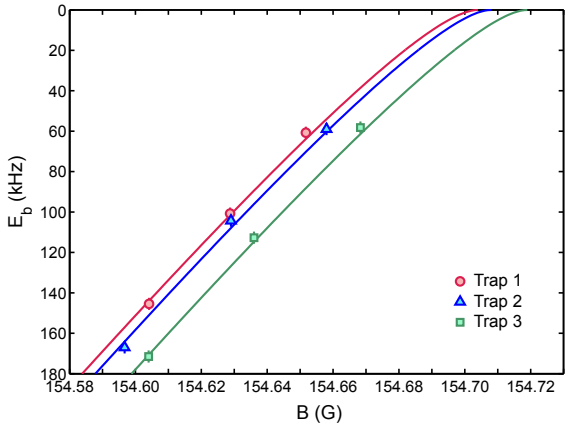

Figure 6.6: Determination of the FR center B_0 by rf association of dimers. The points show the experimentally determined molecular binding energies $E_\mathrm{b}(B)$ for the three trap settings. The solid curves are fits of a theoretical model (see text) to the experimental data.

the upper rf frequency at which the fraction of atoms transferred is roughly 10% of its peak height. We have checked that, within the errors of our measurements, this criterion agrees with the result obtained by fitting the line-shape model [Chi05] to the spectra, as was done in Ref. [Koh12b]. This procedure is repeated for each trap power at various magnetic fields.

We then fit a model [Koh12b] for the molecular binding energy near our FR to the data with B_0 as the only free parameter; see Fig. 6.6. This procedure allows us to determine the resonance center in each trap setting with an uncertainty of $\pm 2\,\mathrm{mG}$. The accuracy of our determination of the resonance position is limited by the uncertainty in the FR parameters [Nai11] used in the model for the binding energy. We determine the center of the FR of trap 1, 2, and 3 to be at the magnetic field of 154.704 G, 154.708 G, and 154.719 G, respectively.

6.5.2 Preparation of the atom-dimer mixture

To cool our atomic sample, we evaporate a Li$|1\rangle$-Li$|2\rangle$ spin mixture at a magnetic field near 1150 G on the attractive side of the 834-G Li$|1\rangle$-Li$|2\rangle$ Feshbach resonance in a single-beam optical dipole trap [Spi10a]. During evaporation, a few 10^4 K atoms are sympathetically cooled by the Li environment. The endpoint of evaporation is always set to the same final value. After evaporation, we follow the scheme described in Ref. [Spi10a] to transfer the atoms into a crossed-beam optical dipole trap and reach a magnetic field of 154.8 G with typically 10^6 Li atoms in state Li$|1\rangle$ and 4×10^4 K atoms in state K$|1\rangle$. We finally vary the temperature of our sample by increasing the power of our crossed beams to adiabatically recompress the trapped sample. This scheme allows us to maintain a similar population imbalance and degeneracy for the three trap settings used.

To prepare for dimer association, we first create a weakly interacting Li$|1\rangle$-K$|3\rangle$ mixture at $B_0 + 180\,\mathrm{mG}$. A first rf pulse transfers ∼80% of the K$|1\rangle$ population into state K$|2\rangle$ and a second rf pulse then transfers the total K$|2\rangle$ population into the interacting state K$|3\rangle$. The ∼7 000 K atoms, which remain in the K$|1\rangle$ state, later serve for the spectroscopy.

We associate dimers using a two-step magnetic field ramp. In a first 20-ms step we ramp the magnetic field from $B_0 + 180\,\mathrm{mG}$ to $B_0 + 5\,\mathrm{mG}$. This ramp is sufficiently slow for the Li atoms to be attracted into the regions of high K density, increasing the density overlap between the two clouds. We then associate the Li$|1\rangle$K$|3\rangle$ dimers via a 0.5-ms Feshbach ramp to $B_0 - 17\,\mathrm{mG}$. We note that, during these magnetic field ramps, two-body inelastic losses [Nai11] are negligible.

To obtain a pure sample of about 15 000 Li$|1\rangle$K$|3\rangle$ dimers, we remove all unbound atoms from the states Li$|1\rangle$ and K$|3\rangle$. The Li$|1\rangle$ atoms are removed by a sequence of rf and laser pulses. This procedure consists of a first 250-μs rf pulse resonant with the free Li$|1\rangle \rightarrow$Li$|2\rangle$ transition, followed by a 10-μs resonant light pulse, which selectively removes the Li$|2\rangle$ atoms from the trap. This scheme removes about 95% of the excess Li atoms without causing any observable loss of KLi dimers. A second 250-μs rf pulse transfers the leftover 5% of Li$|1\rangle$ atoms into the noninteracting Li$|2\rangle$ state, where they remain without further affecting the experiment.

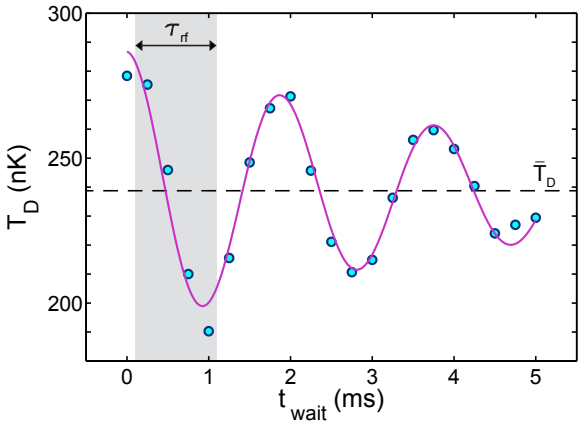

Figure 6.7: Radial oscillation of the dimer cloud after the magnetic field ramp and the removal of the Li atoms. We plot the dimer temperature T_D versus the wait time t_{wait} after the first rf cleaning pulse to release from the trap. The filled circles are the experimental data, the solid line is a fit of a damped harmonic oscillation to the data. The shaded area indicates the time at which the spectroscopy rf pulses are applied and the dashed line marks the experimentally relevant averaged dimer temperature $\bar{T}_D$.

Simultaneously with this "double-cleaning" of the unbound Li atoms, we remove the unbound K$|3\rangle$ atoms in a similar way. Using a 90-μs rf pulse resonant with the K$|3\rangle\rightarrow$K$|2\rangle$ transition, followed by a second 145-μs rf pulse resonant with the K$|3\rangle\rightarrow$K$|4\rangle$ transition, we empty the K$|3\rangle$ state with $>$99 % efficiency. The pulse lengths are chosen such that they are short, i.e. spectroscopically wide, compared to the frequency shifts due to atom-dimer and atom-atom interactions but long, i.e spectroscopically narrow, compared to the binding energy $E_\mathrm{b} = h \times 17\,\mathrm{kHz}$ (h is Planck's constant) of the dimers, avoiding the dissociation of dimers.

In a final step, the $\sim$7 000 K atoms which resided in state K$|1\rangle$ during the entire dimer association process, are transferred in the K$|2\rangle$ state and thus prepared for the rf spectroscopy. This is accomplished by a rf pulse which flips the K$|1\rangle$ and K$|2\rangle$ populations. We note that these K atoms remain unaffected by the dimer association since their interactions with the other components are negligible over the timescales of the experiment.

From here, we reach the specific magnetic field detunings $B - B_0$, at which the spectroscopy is performed, by a 200-μs magnetic field ramp.

6.5.3 Determination of the temperatures and the densities

Here, we describe how we determine the temperatures and the densities of the atom cloud and the dimer cloud. The resulting experimental parameters are summarized in Table 6.1.

Atom and dimer temperatures – The temperatures of our atom and dimer clouds are obtained by Gaussian fits to absorption images of the clouds after a long time-of-flight of $t_{tof} = 6\,\mathrm{m}s$.

Table 6.1: Parameters characterizing the three exploited trap settings. The table shows the effectice atom-dimer temperature T_{eff}, the temperature of the K atoms, T_{K}, and the average dimer temperature, $\bar{T}_{\mathrm{D}}$. From the radial (axial) trap frequencies of K and Li, $\nu_{r(a),\mathrm{K}}$ and $\nu_{r(a),\mathrm{Li}}$, we determine the trap frequencies $\nu_{r(a),\mathrm{D}}$ of the dimers. We also show the axial and radial in-situ Gaussian widths of dimers (K atoms), $\sigma_{a,\mathrm{D}(K)}$ and $\sigma_{r,\mathrm{D}(K)}$, respectively.

Trap	T_{eff} (nK)	T_{K} (nK)	$\bar{T}_{\mathrm{D}}$ (nK)	$\nu_{r,\mathrm{K}}$ (Hz)	$\nu_{a,\mathrm{K}}$ (Hz)	$\nu_{r,\mathrm{Li}}$ (Hz)	$\nu_{a,\mathrm{Li}}$ (Hz)
1	165(15)	138(5)	195(15)	197(5)	25.5(10)	314(5)	34.0(10)
2	232(15)	225(5)	240(15)	284(5)	36.4(10)	446(5)	54.6(10)
3	370(15)	345(5)	398(15)	415(5)	54.0(10)	671(5)	85.0(10)

Trap	$\nu_{r,\mathrm{D}}$ (Hz)	$\nu_{a,\mathrm{D}}$ (Hz)	$\sigma_{r,\mathrm{K}}$ (μm)	$\sigma_{a,\mathrm{K}}$ (μm)	$\bar{\sigma}_{r,\mathrm{D}}$ (μm)	$\sigma_{a,\mathrm{D}}$ (μm)
1	216(5)	27.0(10)	4.3(1)	33(2)	4.4(1)	36(2)
2	310(5)	39.3(10)	3.8(1)	30(2)	3.4(1)	33(2)
3	457(5)	59.0(10)	3.2(1)	25(2)	2.9(1)	26(2)

With the measured radial Gaussian width $\sigma_{tof,K(D)}$ the atom (dimer) temperature $T_{\mathrm{K}(D)}$ is given by

$$k_{\mathrm{B}}T_{\mathrm{K}(D)} = m_{\mathrm{K}(D)}\left(\sigma_{tof,K(D)}/t_{tof}\right)^2, \tag{6.3}$$

where $m_{\mathrm{K}(D)}$ is the mass of the atom (dimer).

The magnetic field ramps and the removal of the surrounding Li shell, described in the previous section, excite collective oscillations of the dimer cloud. We trace these oscillations in momentum space as a function of a wait time t_{wait} after the cleaning procedure to release from the trap. An example of such an oscillation is shown in Fig. 6.7. In order to characterize the temperature at the time of the experiment, i.e. during the application of the 1-ms rf pulse (shaded area), we introduce the average temperature

$$\bar{T}_{\mathrm{D}} = \frac{1}{\tau_{rf}}\int_{rf} T_{\mathrm{D}}dt. \tag{6.4}$$

Axial and radial sizes – To determine the densities of the atom (K) cloud and the dimer (D) cloud, we measure their Gaussian radial (r) and axial (a) widths $\sigma_{r,\mathrm{K}(D)}$ and $\sigma_{a,\mathrm{K}(D)}$, respectively. The axial widths are measured from a Gaussian fit to the axial profiles of in-situ absorption images. Since the radial widths are on the order of our imaging resolution, they can not be determined from in-situ images. We instead determine the radial widths of the K atom cloud as

$$\sigma_{r,\mathrm{K}} = \sqrt{\frac{k_{\mathrm{B}}T_{\mathrm{K}}}{m_{\mathrm{K}}(2\pi\nu_{r,\mathrm{K}})^2}}, \tag{6.5}$$

where T_{K} and $\nu_{r,\mathrm{K}}$ denote the temperature and the radial trap frequency of the K atoms, respectively. Accordingly we determine the average radial in-situ width of the dimers,

$$\bar{\sigma}_{r,\mathrm{D}} = \sqrt{\frac{k_{\mathrm{B}}\bar{T}_{\mathrm{D}}}{m_{\mathrm{D}}(2\pi\nu_{r,\mathrm{D}})^2}}, \tag{6.6}$$

using the averaged dimer temperature $\bar{T}_{\mathrm{D}}$, and the radial dimer trap frequency $\nu_{r,\mathrm{D}}$.

Trap frequencies of the dimers – We use the measured trap frequencies of the K and Li atoms to determine the trap frequencies $\nu_{r(a),\mathrm{D}}$of the LiK-dimers. Since the dimers are weakly bound over the magnetic field range investigated, their polarizabilities are approximately given by the sum of the polarizabilities of the Li and the K atoms. We want to point out that the differential light shift, shifting the FR center (see section 6.5.1), gives only a $< 10\%$ correction to the trap potential and is neglected. Therefore, to a good aproximation, the dimer trap frequencies are given by

$$\nu_{a(r),\mathrm{D}} = \sqrt{(m_{\mathrm{K}}\nu^2_{a(r),\mathrm{K}} + m_{\mathrm{L}i}\nu^2_{a(r),\mathrm{L}i})/m_{\mathrm{D}}}, \tag{6.7}$$

with $m_{\mathrm{L}i}$ being the mass of a Li atom.

Mean Dimer Density – For a given dimer number, N_{D}, the mean dimer density experienced by the K atoms $\bar{n}_{\mathrm{D}}$ is given by

$$\bar{n}_{\mathrm{D}} = \frac{N_{\mathrm{D}}}{(2\pi)^{3/2}(\sigma^2_{r,\mathrm{K}} + \bar{\sigma}^2_{r,\mathrm{D}})\sqrt{\sigma^2_{a,\mathrm{K}} + \sigma^2_{a,\mathrm{D}}}}, \tag{6.8}$$

where we have assumed Gaussian-shaped atom and dimer clouds.

Effective temperature – Due to heating and oscillations caused by our preparation procedure, the dimer temperature T_{D} in our system is different from the temperature of the non-interacting K$|2\rangle$ atoms that we use for rf spectroscopy. However, since our dimer and atom clouds are both non-degenerate, the energies of the atom-dimer collisions still assume a Boltzmann distribution. Averaging this distribution over the oscillations of the dimer cloud results in an effective atom-dimer collision temperature

$$T_{eff} = \mu_3(T_{\mathrm{K}}/m_{\mathrm{K}} + \bar{T}_{\mathrm{D}}/m_{\mathrm{D}}), \tag{6.9}$$

where $\mu_3 = m_{\mathrm{K}}m_{\mathrm{D}}/(m_{\mathrm{K}} + m_{\mathrm{D}})$ is the atom-dimer reduced mass.

6.5.4 Importance of higher partial wave scattering and comparison to the equal-mass case

In this Section, we justify several important statements made in the main text. First, we have argued that the range of the atom-dimer interaction is comparable with the typical de Broglie wavelength and, therefore, quite a few partial waves are necessary to quantitatively characterize the line shift. In Fig. 6.8, we display $-\mathrm{Re}\, f(0)$, the quantity which is thermally averaged in the main text to obtain the line shifts. The method of calculating the scattering amplitude is described in Ref. [Lev09]. Remarkably, the real part of the forward-scattering amplitude is seen to change sign at a collision energy much smaller than the binding energy, even for a relatively large detuning of 21 mG. The second change of sign of $-\mathrm{Re}\, f(0)$ seen in Fig. 6.8(a) is attributed to the fact that δ_p exceeds $\pi/2$ above $E_{\mathrm{coll}} \approx 0.1E_{\mathrm{b}}$, the point of the p-wave resonance. The p-wave contribution at larger collision energies then becomes positive (repulsive) [see Eq. (6.1) of the main text]. However, this peculiar phenomenon

takes place only in a very close vicinity of the wide resonance limit as the p-wave phase shift drops rather abruptly with R^*/a [Lev09]. We also note how, as the collision energy is increased, more and more partial wave channels are needed to accurately describe the forward-scattering amplitude. The calculation presented here includes the first 16 partial waves, which is sufficient to obtain an essentially converged scattering amplitude at the dimer breakup threshold.

As far as the equal mass case is concerned, the competition between the attraction in odd partial waves and repulsion in even partial waves is also quite significant, yet much less pronounced compared to the K-Li case. In Fig. 6.9 we display $-\mathrm{Re}\, f(0)$ as a function of E_{coll} for equal masses. Here the broad resonance case in Fig. 6.9(a) is relevant since it is readily available in current experiments and since there the effect of higher partial waves is most noticeable. We see that the forward-scattering amplitude does change sign in this case. However, in contrast to the K-Li case, this happens at a high collision energy close to the dimer breakup threshold and, in fact, already for $R^*/a \gtrsim 0.03$ the crossing is no longer on the scale. Thus, in the narrow resonance case illustrated in Fig. 6.9(b) and (c) the interaction is found to be repulsive below the dimer breakup threshold. In all cases the thermally averaged quantity $-\mathrm{Re}\,\langle f(0)\rangle$ is positive.

Finally, let us also make a remark concerning the thermal averaging of the scattering amplitude which we use in the main text. In principle, the averaging procedure requires the knowledge of the phase shifts above the atom-dimer breakup threshold. However, we always restrict ourselves to temperatures $k_{\mathrm{B}}T \lesssim E_{\mathrm{b}}/2$ and we check that in this case the integration result is insensitive to the exact extrapolation scheme. In practice we extrapolate the phase shift $\delta_l(k)$ using the log function, which works very well when we calculate the phase shifts above the breakup threshold in the Born-Oppenheimer approximation [Lev11].

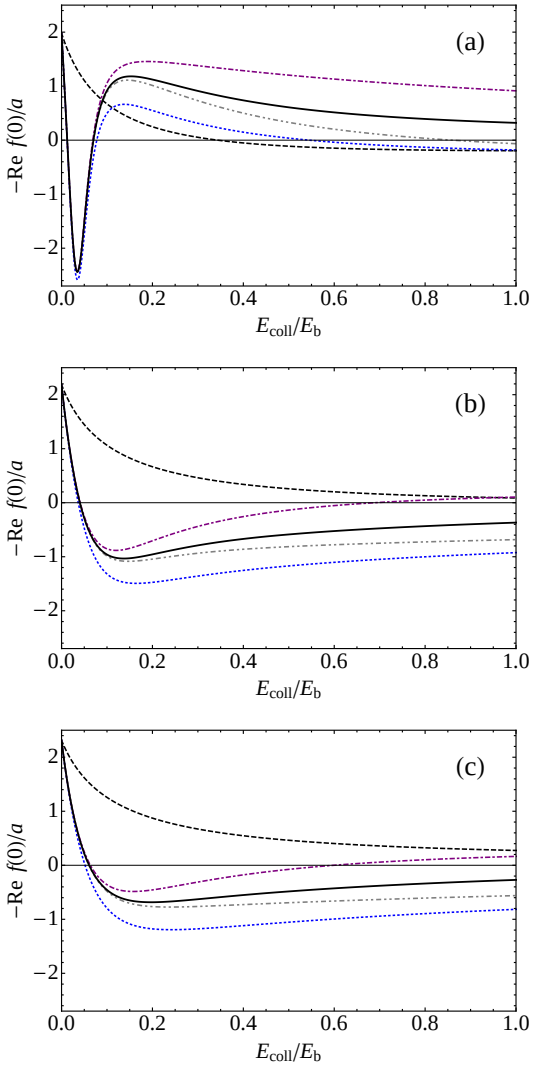

Figure 6.8: Scattering of a ^{40}K atom with a ^{6}Li^{40}K dimer. The quantitiy $-\mathrm{Re}\, f(0)$ is plotted as a function of atom-dimer collision energy for (a) $R^*/a = 0$ [$B - B_0 = 0$], (b) $R^*/a = 1/2$ [$B - B_0 = -10\,\mathrm{mG}$], and (c) $R^*/a = 1$ [$B - B_0 = -21\,\mathrm{mG}$]. The lines are including s-wave scattering only (black, dashed), including up to p-wave (blue, dotted), up to d-wave (purple, dot-dashed), and up to f-wave (gray, double dot-dashed). The solid black line is $-\mathrm{Re}\, f(0)$ including the first 16 partial waves.

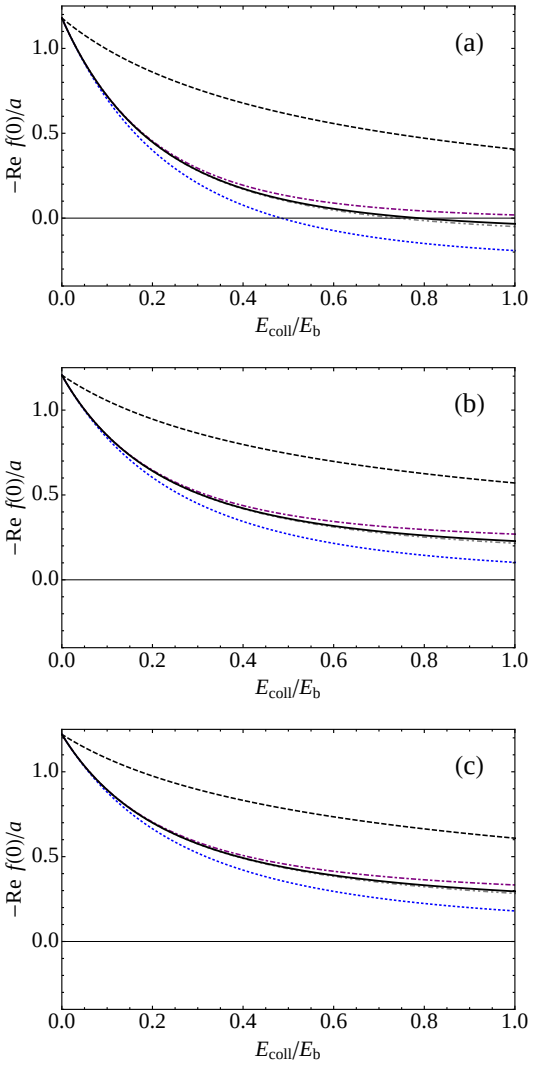

Figure 6.9: Equal-mass case of atom-dimer scattering. We plot $-\mathrm{Re}\, f(0)$ as a function of collision energy for the homonuclear case, $m_\uparrow = m_\downarrow$. The conventions used for the lines as well as the detunings in (a) to (c) are the same as in Fig. 6.8. The solid black line includes the first 9 partial waves.

Chapter 7

Lifetime of ^{6}Li-^{40}K Dimers near a Feshbach Resonance[1]

The present chapter contains the experimental part of a manuscript in preparation, authored by M. Jag[1,2], M. Cetina[1,2], R. S. Lous[1,2], R. Grimm[1,2], J. Levinsen[3], and D. Petrov[4].

[1] *Institut für Quantenoptik und Quanteninformation,Österreichische Akademie der Wissenschaften, 6020 Innsbruck, Austria*
[2] *Institut für Experimentalphysik, Universität Innsbruck, 6020 Innsbruck, Austria*
[3] *School of Physics and Astronomy, Monash University, Victoria 3800, Australia*
[4] *LPTMS, CNRS, Université Paris Sud, Université Paris-Saclay, 91405 Orsay, France*

7.1 Introduction

At ultra-low collision energies, radiative losses in collisions between ground-state neutral atoms are suppressed and losses in collisions of pairs of such atoms chiefly occur by spontaneous relaxation into lower-lying atomic Zeeman states. This suppression of losses has played a decisive role in achieving Bose-Einstein condensation in cold atomic gasses.

In the presence of strong interactions between atoms, such as those achievable using atomic Feshbach resonances [Chi10], three-body losses play a significant role. Due to Pauli's exclusion principle, three-body losses in fermionic gases can be strongly suppressed, resulting in lifetimes of strongly interacting fermionic gases that are measured in seconds [Cub03, Joc03a]. This remarkable property of tunable fermionic gases has led to spectacular achievements, including the realization of a BEC of molecules [Joc03b, Gre03] and the study of the BEC-BCS crossover [Bar04b, Reg04b].

Feshbach resonances (FR) arise from the coupling of molecular bound states of pairs of atoms to unbound scattering states. For weak atom-molecule couplings corresponding to narrow

[1] The author of the present thesis developed the experimental procedures, performed the measurements together with M.C. and R.S.L, and analyzed the data together with M.C. under the supervision R.G.

Feshbach resonances, close to the FR, the molecular state can be significantly populated. Since the molecular bound states are distinguishable from free fermionic atoms, fermionic suppression is predicted to be less effective in this case. Indeed, measurements of losses in collisions involving Feshbach molecules near the narrow ^{6}Li Feshbach resonance at 543 G are consistent with the absence of fermionic suppression [Wan13]. In the intermediate regime of a moderately narrow FR, the lifetimes of inter-species Feshbach molecules were investigated in the ^{6}Li-^{40}K Fermi-Fermi mixture by [Voi09]. The lifetime of these dimers was observed to increase near the FR, consistent with fermionic suppression.

In the following, we present detailed measurements of the lifetime of ^{6}Li^{40}K dimers near two different inter-species FR. Improving on the earlier work by [Voi09], we distinguish between spontaneous and collisional decay processes in our system and determine the loss-rate coefficient of a trapped dimer sample as well as an atom-dimer mixture. Near the Feshbach resonances, we find the atom-dimer and dimer-dimer collisional decay to be suppressed by more than a factor of five and three, respectively. We compare our observations to theoretical predictions by Levinsen and Petrov [Lev11] and find very good agreement.

7.2 Experimental procedures

7.2.1 Feshbach resonances

We study the lifetime of Li-K dimers near two different interspecies Feshbach resonances. The first resonance has been widely used in our previous work on Fermi-Fermi mixtures, including the observation of the hydrodynamic expansion of a strongly interacting mixture [Tre11a], the investigation of polarons (*Chapters* 3 and 4), and the study of LiK-K atom-dimer interactions [Jag14]. The resonance is found near 155 G in the combination of lithium in its lowest Zeeman sub-level Li$|1\rangle$ ($f = 1/2$, $m_f = +1/2$) and potassium in its third-lowest sub-level K$|3\rangle$ ($f = 9/2$, $m_f = -5/2$). The other resonance is found near 158 G in the lowest spin-state combination of Li$|1\rangle$ and K$|1\rangle$ ($f = 9/2$, $m_f = -9/2$). We use this narrower resonance for comparison as it has the advantage of an absence of any Li-K two-body losses.

The dependence of the Li-K s-wave scattering length a on the magnetic field B near a FR can be described by the standard expression $a(B) = a_{\mathrm{bg}}\,[1 - \Delta/(B - B_0)]$ [Chi10] with the relevant background scattering length a_{bg}, width Δ, and the resonance center B_0. In Table 7.1 we summarize the values of these parameters for both resonances. To fully characterize the FRs, we also present the differential magnetic moments $\delta\mu$ between the relevant open and closed channels. From these parameters, we derive the length parameter $R^* = \hbar^2/(2m_{\mathrm{r}}\Delta a_{\mathrm{bg}}\delta\mu)$ [Pet04a], characterizing the coupling strength between the open and the closed channels. Here m_{r} represents the Li-K reduced mass. The values for a_{bg} and Δ have been obtained from a coupled-channels calculation [Nai11]. The values for $\delta\mu$ as well as B_0 for the Li$|1\rangle$-K$|3\rangle$ FR were experimentally determined, with a very high accuracy, as described in *Chapter* 4. For $\delta\mu$ near the Li$|1\rangle$-K$|1\rangle$ FR we use the data obtained from a coupled-channels calculation

Channel	B_0 (G)	a_{bg} (a_0)	Δ (G)	$\delta\mu/h$ (MHz/G)	R^* (a_0)
Li$\|1\rangle$K$\|3\rangle$	154.708(2)	63.0	0.88	2.35	2 650
Li$\|1\rangle$K$\|1\rangle$	157.530(3)	65.0	0.14	2.3	16 500

Table 7.1: Parameters characterizing the two Feshbach resonances. We summarize the values from *Chapter* 4, Ref. [Nai11] and the footnote[2] for the position B_0, background scattering length a_{bg}, and width Δ as well as the differential magnetic moment $\delta\mu$. The values given for B_0 include a small shift (9 mG) induced by the trapping-laser light (see *Chapter* 4).

[Nai11] and for B_0 we use the value of an independent experimental determination[2].

7.2.2 Sample preparation

Our procedure to prepare Li$|1\rangle$K$|3\rangle$-dimer samples is nearly identical to the one described in Ref. [Jag14]. To produce Li$|1\rangle$K$|1\rangle$ dimer samples, we slightly adapt this procedure to account for the narrower character of the FR. In both cases, the starting point for our experiments is an optically trapped and thermally equilibrated mixture of typically 10^5 Li atoms and approximately 3×10^4 K atoms at a temperature of ~ 370 nK and at a magnetic field of 156.4 G. We reach these conditions by a preparation procedure described in detail in Ref. [Spi10a]. The cigar-shaped optical confinement of the atom mixture, realized by two 1064-nm laser-light beams intersecting at an angle of about 16°, is characterized by the radial and axial trap frequencies $\nu_{\mathrm{r,K}} = 420(10)$ Hz and $\nu_{\mathrm{a,K}} = 55(2)$ Hz for the K and $\nu_{\mathrm{r,Li}} = 600(10)$ Hz and $\nu_{\mathrm{a,Li}} = 90(3)$ Hz for the Li atoms. At this stage, all Li atoms are in their lowest Zeeman sub-level Li$|1\rangle$ and all K atoms are in their second-lowest sub-level K$|2\rangle$ ($f = 9/2$, $m_f = -7/2$).

From here on, the preparation steps differ depending on the Li-K spin-state combination from which the dimers are created. Preparing for the creation of Li$|1\rangle$K$|3\rangle$ (Li$|1\rangle$K$|1\rangle$) dimers from these mixtures, we slowly ramp the magnetic field within 2 s to a value of 154.89 G (157.565 G), approximately 180 mG (35 mG) above the center of the FR. Here, we transfer all K atoms into the K$|3\rangle$ (K$|1\rangle$) state by a radio-frequency rapid adiabatic passage.

We then associate approximately 10^4 LiK dimers by a Feshbach ramp [KÖ6, Chi10]. To associate dimers from the Li$|1\rangle$-K$|3\rangle$ mixture, we do this in two steps, as illustrated in Fig. 7.1. In a first step we ramp the magnetic field to $B_0 + 5$ mG in 20 ms, which is sufficiently slow for the Li atoms to be attracted into the regions of high K density, increasing the density overlap between the two clouds. This is followed by the second step, in which we quickly ramp the magnetic field to $B_0 - 20$ mG in 0.5 ms. In contrast, for the Li$|1\rangle$-K$|1\rangle$ mixture, we associate the dimers by a single 2-ms Feshbach ramp to a magnetic field $B = B_0 - 16$ mG. Due to the more elaborate, two-step magnetic-field ramping, typical dimer numbers of Li$|1\rangle$K$|3\rangle$ samples are roughly 20% larger than typical dimer numbers of Li$|1\rangle$K$|1\rangle$ samples.

[2] We determined B_0 by measuring the energy shift of K atoms in a Li cloud and comparing it to the predictions of a dressed quasiparticle model [Mas12]

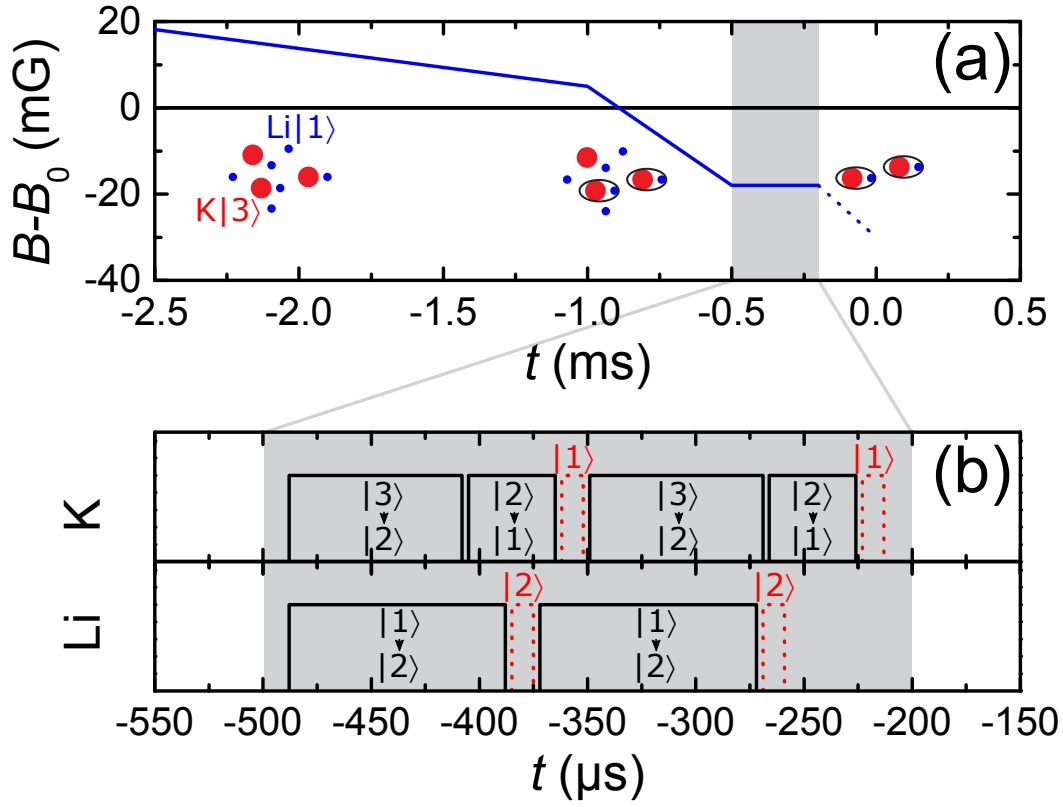

Figure 7.1: (Color online) Scheme of the preparation of a pure Li$|1\rangle$K$|3\rangle$ dimer sample. (a) Starting from a magnetic field $B = B_0+180\,\mathrm{mG}$ we approach the resonance by a first 20-ms ramp to $B_0+5\,\mathrm{mG}$. Then, we associate dimers by a quick (0.5 ms) ramp across the FR to a magnetic field $B_0 - 20\,\mathrm{mG}$. Here, we remove unbound K and Li atoms from the sample. After this cleaning procedure we reach the final magnetic field B, at which we perform the lifetime measurement, by a 200-μs ramp (dotted line). (b) The cleaning procedure for both Li and K consists of radio-frequency pulses (solid black), selectively transferring unbound atoms into another spin state, and successive removal of these atoms from the trap by a resonant laser-light pulse (dotted red). This cleaning procedure is once repeated to increase the purity of the dimer sample.

To obtain pure dimer samples we apply cleaning sequences to remove unbound atoms. In both cases, for Li$|1\rangle$K$|3\rangle$ and for Li$|1\rangle$K$|1\rangle$ samples, this sequence consists of a combination of radio-frequency (rf) and laser-light pulses. A roughly 100 μs-long rf π pulse selectively transfers the free Li atoms from state Li$|1\rangle$ into state Li$|2\rangle$. A subsequent 10-μs laser-light pulse selectively removes the Li$|2\rangle$ atoms from the trap. Simultaneously to this Li cleaning procedure, we remove the unbound K atoms in a similar way. Applying two rf π pulses of about 80 μs and 40 μs duration, we transfer the free K atoms from the initial to the second nearest neighboring state, and successively remove them from the trap by applying a resonant laser-light pulse. As these cleaning procedures remove about 95% of the free Li and K atoms, they are repeated one time to clean the respective states more thoroughly, see Fig. 7.1. We then quickly, within 200 μs, ramp the magnetic field to its variable final value, at which we then perform the measurements.

7.2.3 Dimer detection and dimer temperature determination

We determine the dimer numbers from absorption images of Li and K atoms after dissociation of the LiK dimers into Li-K pairs by a reverse Feshbach ramp [KÖ6, Chi10]. For both resonances we ramp the magnetic field B up to a value $\geq B_0 + 50\,\mathrm{mG}$ within 10 μs. After an additional wait time of a few 10 μs, we simultaneously take absorption images of the Li and the K clouds, from which we determine the numbers of Li and K atoms. In some measurements, which were carried out at an earlier stage of the experiments, we detected only the number of Li atoms resulting after the reverse Feshbach ramp.

The temperature of the dimers is determined from Gaussian fits to absorption images of the clouds after a time-of-flight expansion period of $t_{\mathrm{TOF}} = 4\,\mathrm{ms}$. The procedure is discussed in detail in Ref. [Jag14]. From the measured radial width σ_{r}, we obtain the dimer temperature T_{D} from $k_{\mathrm{B}}T_{\mathrm{D}} = m_{\mathrm{D}}(\sigma_{\mathrm{r}}/t_{\mathrm{TOF}})^2$, where $m_{\mathrm{D}} = m_{\mathrm{Li}} + m_{\mathrm{K}}$ is the mass of a Li-K dimer. Typically, the temperatures of our dimer samples are about $T_{\mathrm{D}} = 550\,\mathrm{nK}$. This corresponds to peak phase-space densities of about 0.1 for typical dimer number densities in our samples. We explain the increased temperature of our dimer cloud compared to the temperature prior to the dimer association (370 nK) by heating and oscillations caused by our preparation procedure [Jag14].

7.3 Measurements of dimer decay

Our dimers created from atom pairs in an excited Zeeman state are subject to spontaneous decay. In a sample of dimers, a dimer can furthermore decay in collisions with another dimer. When such a sample is mixed with an atomic cloud there will be additional dimer decay arising from atom-dimer collisions. We perform several series of experiments on dilute, expanded as well as dense, trapped dimer samples both pure and mixed with an atomic cloud. The combination of the results of these measurements allows us to extract accurate rates at which the spontaneous and collisional processes occur.

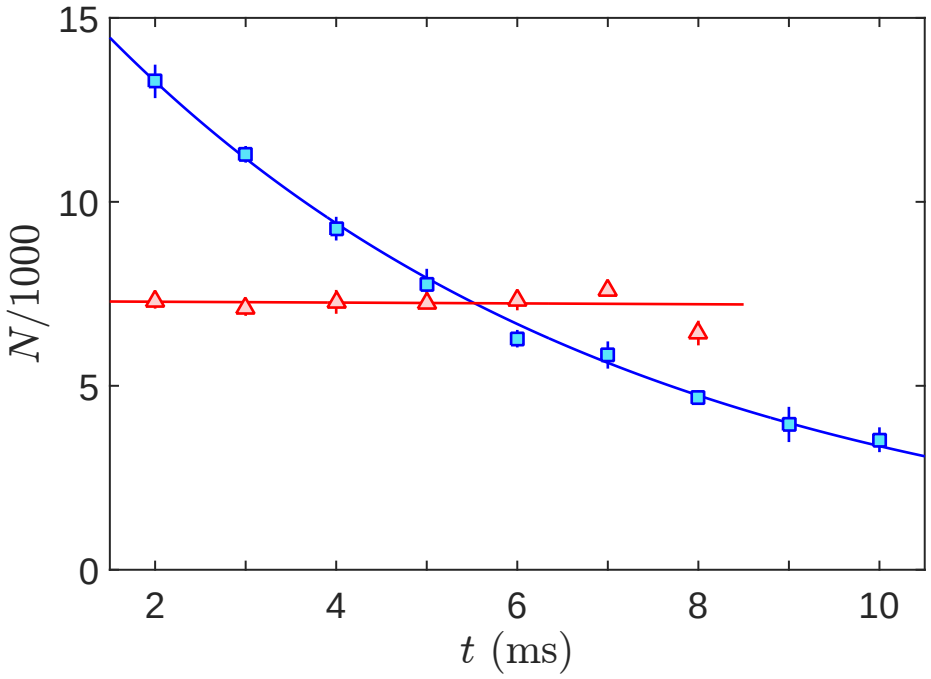

Figure 7.2: (Color online) Comparison of the dimer number evolution near the Li$|1\rangle$-K$|3\rangle$ and the Li$|1\rangle$-K$|1\rangle$ FR. The blue squares show a typical decay curve of a Li$|1\rangle$K$|3\rangle$-dimer sample at $B = B_0 - 296\,\mathrm{mG}$. Fitting an exponential decay to the data yields the 1/e-lifetime $\tau = 5.8(4)\,\mathrm{ms}$. The fit is represented by the blue solid line. The results from similar measurements with a Li$|1\rangle$K$|1\rangle$-dimer sample at a magnetic detuning of $-75\,\mathrm{mG}$ from the respective resonance center, are shown as the red triangles. Here, we observe the dimer number to remain essentially constant. A fit of an exponential decay to the data (red solid line) is consistent with infinite lifetime. The error bars represent 1σ uncertainties; in some cases they are smaller than the symbol size.

7.3.1 Spontaneous dissociation of Li$|1\rangle$K$|3\rangle$ dimers

A dimer created from atom pairs with at least one component in an excited Zeeman state can spontaneously decay via processes involving coupling between the two spins [Chi10]. Such decay has previously been studied theoretically and experimentally for the case of $^{85}Rb_2$ molecules [KÖ5, Tho05]. The spontaneous decay of Li$|1\rangle$K$|3\rangle$ dimers has been theoretically investigated in detail in Ref. [Nai11]. There, predictions for the lifetime of the dimers were obtained from coupled-channels calculations, and we show these predictions in Fig. 7.3 as the black solid line. While for magnetic detunings $B - B_0$ of around a few hundred mG the lifetime is around 6 ms, it is predicted to substantially increase near the resonance. This increase can be attributed to the increasing halo character of the dimer wave function as the FR is approached. This is accompanied by a decreased probability to find a pair of Li and K atoms within the short range where the spin coupling occurs [Nai11].

We investigate the lifetime of Li$|1\rangle$K$|3\rangle$ against spontaneous decay using dimer samples

with a very low number density, such that density-dependent collisional losses do not play a significant role. We realize such dilute dimer samples by allowing the optically trapped dimer cloud to expand after switching off the trap. After a variable expansion time t, we determine the molecule number in the sample. Note that the 1064-nm light induces a shift of the FR center B_0, as described in *Chapter* 4. When the optical trap is off, the FR center B_0 of the Li$|1\rangle$-K$|3\rangle$ resonance is found at 154.699 G, i.e. 9 mG lower than in the trap (Table 7.1). For the Li$|1\rangle$-K$|1\rangle$ channel we assume the same small shift.

In Fig. 7.2 we show a typical decay curve of a Li$|1\rangle$K$|3\rangle$-dimer sample, recorded at a magnetic detuning $B-B_0 = -296$ mG (blue squares). For our analysis, we only consider data obtained for $t \geq 1.5$ ms, where the mean dimer number density in the sample is below $5 \times 10^{10}/\mathrm{cm}^3$. To these data we fit a simple exponential decay, $N_0 \exp(-t/\tau)$, with the initial dimer number N_0 and the lifetime τ as free parameters. For the specific example of Fig. 7.2, this procedure yields $\tau = 5.8(4)$ ms and the fit result is shown as the blue solid line.

For comparison, we also show the evolution of the number of Li$|1\rangle$K$|1\rangle$ dimers recorded 75 mG below the center of the Li$|1\rangle$-K$|1\rangle$ resonance (red triangles). Here, the spontaneous decay mechanism is absent. Indeed, we observe an essentially constant number of Li$|1\rangle$K$|1\rangle$ dimers, with the fit yielding the decay rate $1/\tau = 0.008(7)\,\mathrm{s}^{-1}$. This result is essentially consistent with an infinite lifetime and, at a 95% confidence level, provides a lower bound of 50 ms.

In Fig. 7.3, the blue circles show the experimentally determined lifetimes of the dimers against spontaneous decay over a wide range of magnetic detunings. Our experimental results are in excellent agreement with the theoretical prediction from Ref. [Nai11] over the whole magnetic field range investigated. The lifetimes of the dimers we determine are generally longer than 5 ms. In particular, we observe the onset of the halo-dimer regime close to the FR, with dimer lifetimes surpassing 8 ms. Our results on the lifetime of the Li$|1\rangle$K$|3\rangle$ dimers in dilute samples can be fully understood in terms of spontaneous dissociation.

7.3.2 Dimer-dimer collisions

In a second series of experiments, we investigate the collisional decay of a trapped dimer cloud. In collisions with other dimers our shallowly bound dimers can relax into more deeply bound states. The released binding energy is much larger than the depth of the trapping potential, and thus the relaxation products are always lost from the trap. This two-body decay occurs at a rate $\beta_\mathrm{D} n$, which results as the product of the dimer-dimer two-body loss-rate coefficient β_D and the dimer number density n.

To experimentally determine the rate coefficient β_D for these collisional decay processes, we investigate the decay of a trapped sample of dimers. The initial number of typically $N_0 = 1.3 \times 10^4$ dimers corresponds to an initial number density N_0/V_eff of about $1 \times 10^{12}/\mathrm{cm}^3$, where $V_\mathrm{eff} = [(4\pi k_\mathrm{B} T_\mathrm{D})/(m_\mathrm{D} \bar{\omega}_\mathrm{D}^2)]^{3/2}$ is the effective volume of a thermalized sample, and $\bar{\omega}_\mathrm{D} = 2\pi(\nu_{\mathrm{r,D}}^2 \nu_{\mathrm{a,D}})^{1/3} = 2\pi \times 222\,\mathrm{Hz}$ is the mean dimer trapping frequency. After a hold time t at a magnetic field B we measure the number of dimers, $N(t)$, remaining in the

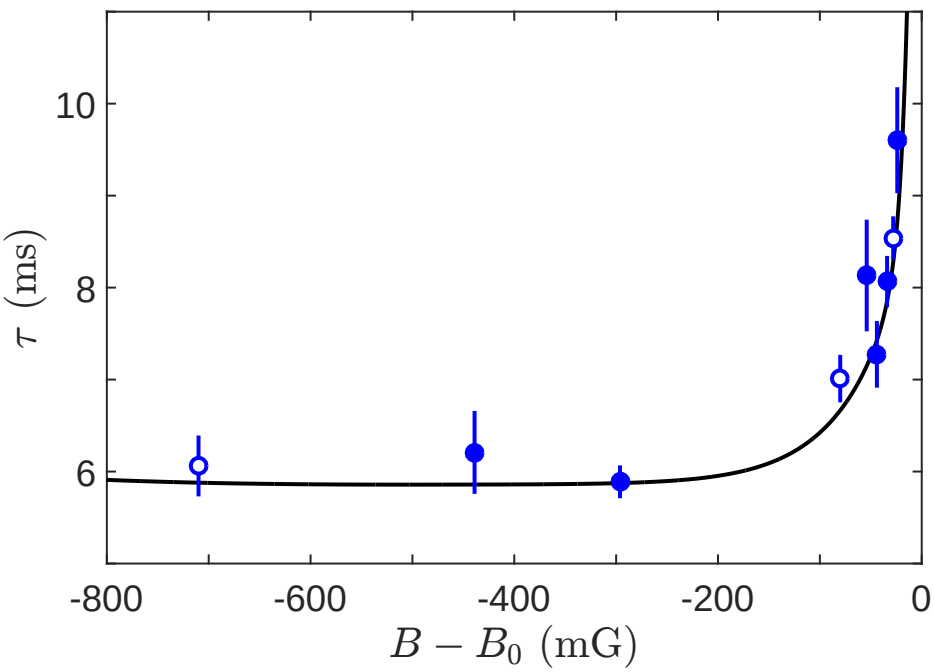

Figure 7.3: (Color online) Lifetime of dimers against spontaneous decay near the Li$|1\rangle$-K$|3\rangle$ FR. The data points show the experimental results and the black solid line represents the theoretical prediction from Ref. [Nai11]. While the filled symbols result from decay curves, where both the Li and the K component have been imaged after dissociation, the open symbols are based on detecting K alone. The error bars represent the 1σ fit uncertainties.

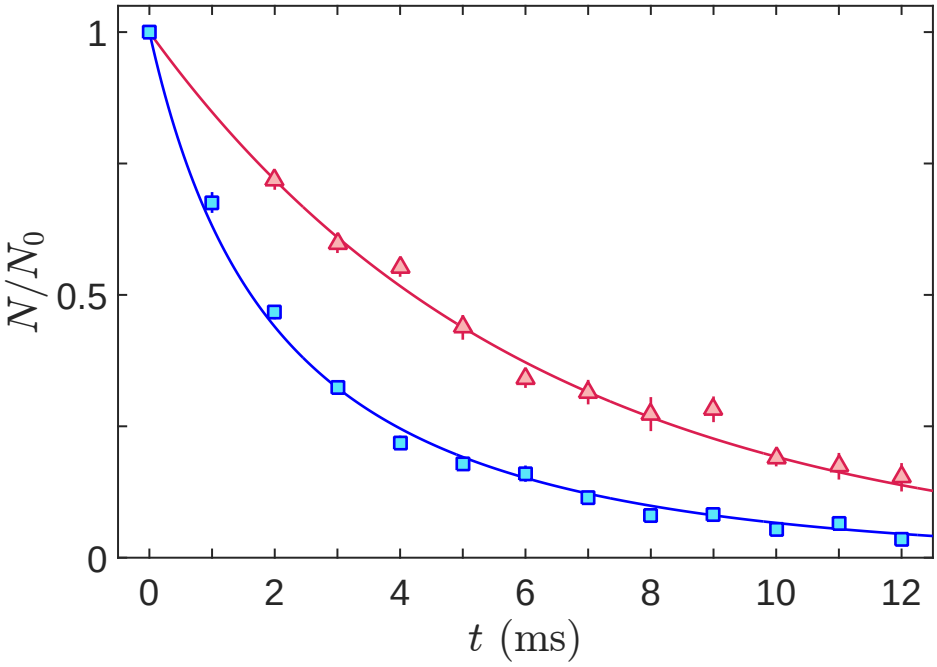

Figure 7.4: (Color online) Comparison of the decay of a trapped and an expanding dimer sample. The blue squares show the measured dimer number in a trapped sample versus hold time t in the trap. The red triangles show the dimer number determined in a dilute, expanding sample, 1.5 ms after release from the trap. The blue and red lines correspond to the fit of our model to the data without and with two-body decay (see text). For a direct comparison, the experimental data are normalized to the initial dimer number $N_0 = 13000$ (15300) obtained from the fit to the data acquired from the trapped (expanding) sample. The error bars represent 1σ uncertainties; in some cases they are smaller than the symbol size.

sample. In Fig. 7.4 we show an example for a decay curve obtained at a magnetic detuning of −710 mG from the Li|1⟩-K|3⟩ FR (blue squares).

We model the decay with the common loss-rate equation

$$\dot{N}/N = -1/\tau - (\beta_{\mathrm{D}}/V_{\mathrm{eff}})N. \tag{7.1}$$

Under the assumption that the sample remains in thermal equilibrium at the initial temperature T_{D}, the differential equation has the solution

$$N(t) = \frac{V_{\mathrm{eff}}/\tau}{\left(\beta_{\mathrm{D}} + \frac{V_{\mathrm{eff}}}{N_0\tau}\right)\exp(t/\tau) - \beta_{\mathrm{D}}}. \tag{7.2}$$

We fit Eq. (7.2) to the data to experimentally determine the loss rate coefficient β_{D}. For the fit, we fix τ to the corresponding theoretical value, as verified in the independent measurements presented before. Assuming a constant temperature of the sample, we neglect anti-evaporation heating [Web03]. We have checked that including the latter into our analysis, leads to slightly higher values for β_{D}. We found the correction to stay well below 15%. Furthermore, our determination of the loss coefficient is affected by a systematic error of the dimer number density. We estimate a combined systematic error of about 40%, arising from largely uncorrelated estimated uncertainties of 25%, 7%, and 20% in the dimer number, the dimer trapping frequencies, and the dimer temperature, respectively. For the data of Fig. 7.4, the fit result is shown as the blue solid line. For comparison, we also show the decay curve of a dilute dimer sample, where collisional loss is absent (red triangles), together with the result of a fit of an simple exponential decay to this data (red line). This shows that, under typical experimental conditions, both collisional relaxation and spontaneous dissociation give similar contributions to the total decay of the trapped dimer sample.

We take corresponding measurements at various magnetic detunings. Our experimental results for β_{D}, obtained with Li|1⟩K|3⟩ (Li|1⟩K|1⟩) dimer samples, are shown in Fig. 7.5 as the blue circles (red squares). For the Li|1⟩K|1⟩ dimer sample we obtain values for the loss rate coefficient β_{D} of roughly $3\times10^{-10}\mathrm{cm}^3/\mathrm{s}$ without significant dependence on the magnetic detuning. For the Li|1⟩K|3⟩ dimer sample we obtain roughly the same value for detunings $B - B_0 \lesssim -400$ mG. The Feshbach molecules, at these large magnetic detunings, have a very small admixtures of the entrance channel and are thus strongly closed-channel dominated [Chin2010fri]. The decay of such molecules is largely independent of the exact state they are in [cite].

When approaching the Li|1⟩-K|3⟩ resonance, our experimental results (with the exception of one clear outlier [3]) show an increasing reduction of collisional losses. For our data points closest to resonance (about −30 mG detuning), this suppression effect amounts to more than a factor of three. Note that we cannot measure closer to resonance because of an onset of collisional dissociation [Joc03a].

We attribute this suppression of losses to the change of quantum statistics these dimers follow as the FR is being approached. Closer to the resonance, the dimers have an in-

[3] The data point at −142 mG clearly lies beyond the trend of the other data. Thoroughly re-checking the settings of our experimental setup for this measurement yielded no hint for what could have caused the discrepancy.

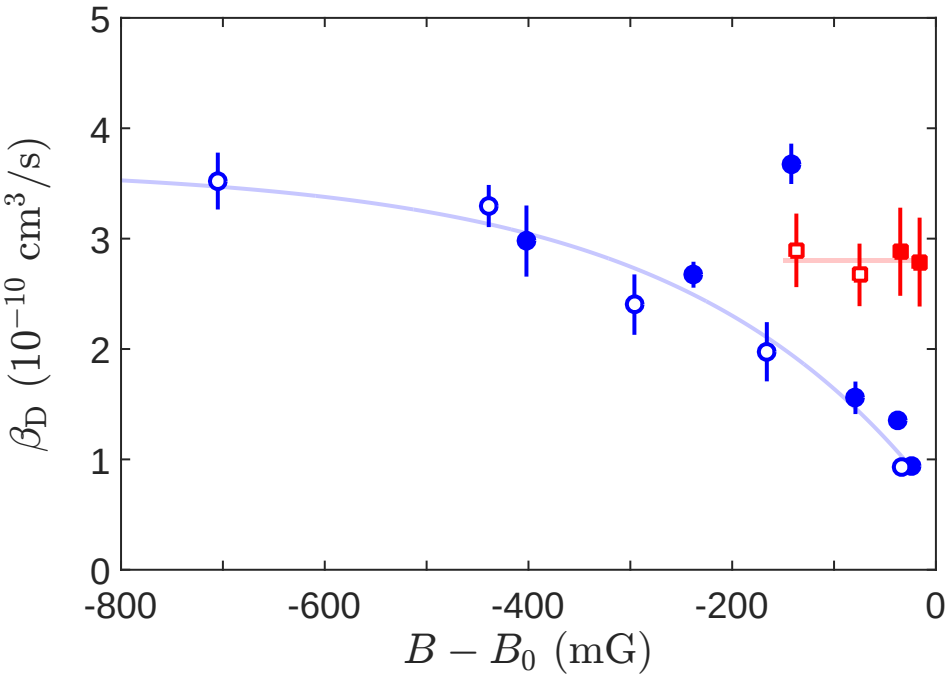

Figure 7.5: (Color online) Measured loss rate coefficient for inelastic dimer-dimer collisions as a function of magnetic detuning. The blue circles (red squares) correspond to the experimental results obtained with samples of Li|1⟩K|3⟩ (Li|1⟩K|1⟩) dimers. The filled symbols correspond to results we obtained when determining the molecule number from both Li and K absorption images. Open circles (squares) represent fit results based on analyzing Li (K) images alone. The error bars represent the 1σ fit uncertainties; in some cases they are smaller than the symbol size. We show the light blue and a light red line as guides to the eye.

creasing open-channel character and the fermionic nature of the dimer constituents becomes apparent in a collision. As it takes at least three particles, out of which two necessarily are identical fermions, to come close for the dimer to decay into a deeper-bound state, collisional decay of open-channel dimers will be Pauli blocked. This fermionic suppression of collisional relaxation of Fermi-Fermi molecules has previously been observed in experiments with homonuclear Li_2 [Cub03, Joc03a] and K_2 [Reg04a].

7.3.3 Atom-dimer collisions

In another set of experiments, we study the decay of dimers arising from their collisions with Li atoms in a mixture of LiK dimers and Li atoms. Such decay occurs at a rate $\beta_{\mathrm{LiD}} n_{\mathrm{Li}}$, which results as the product of the Li atom dimer loss coefficient β_{LiD} and the Li density n_{Li}. The measurement of atom-dimer collisions is challenging because the corresponding decay has to be discriminated against the background from spontaneous decay and dimer-dimer collisional decay.

We realize Li atom dimer mixtures by adapting our preparation scheme presented in Sec. 7.2.2. Here we start with the lithium component in a nearly balanced spin mixture of Li$|1\rangle$ and Li$|2\rangle$. The Feshbach ramp then produces a mixture of Li-K dimers, some remaining Li$|1\rangle$ atoms, and the unaffected Li$|2\rangle$ atoms. Then, at $B = B_0 - 20\,\mathrm{mG}$, we apply only one radio-frequency π pulse flipping the populations of the Li$|1\rangle$ and Li$|2\rangle$ states. We subsequently remove the Li$|2\rangle$ atoms from the trap with a laser-light pulse. All other preparation steps, in particular the K spin state cleaning, remain as described in Sec. 7.2.2. Applying this procedure, the number density distribution of the Li atoms in the trap, n_{Li}, can be well approximated from the initial Li temperature and the Li trap frequencies using the well known expressions for the density distribution of a trapped Fermi gas. Typically, we obtain samples of $\gtrsim 9\times10^3$ dimers and $\gtrsim 6\times10^4$ Li atoms, corresponding to a mean dimer density of about $6\times10^{11}/\mathrm{cm}^3$ and a Li density averaged over the dimer distribution, $\langle n_{\mathrm{Li}}\rangle$ (*Chapter* 5), of about $1.5\times10^{12}/\mathrm{cm}^3$. These conditions correspond to a thermal sample of dimers immersed into a weakly degenerate Fermi sea, characterized by $k_{\mathrm{B}}T/\epsilon_F \approx 0.55$, where ϵ_F is the average Fermi energy sampled by the dimers (*Chapter* 5).

To experimentally determine the rate coefficient β_{LiD}, we again investigate the decay of dimers from our sample. We ramp the magnetic field to a desired value B and, after a variable hold time t, we measure the number of dimers, N, remaining in the sample. For each decay curve in the atom-dimer mixture we record a corresponding reference curve in a pure dimer sample. The reference measurements, which independently provide the dimer-dimer loss coefficient β_{D}, have already been presented in the preceding section. To minimize systematic errors by long-term drifts of the experiment the measurements in the atom-dimer mixtures and the pure dimer samples are carried out in an alternating way.

We model the decay of dimers with a simple extension of the decay model from the previous section. Our Li sample is much larger than the dimer sample, such that losses from the Li sample can be neglected. In this case, the Li sample represents a constant bath and the loss of dimers arising from Li atom dimer collisions appears as a one-body loss, which we include into our model by adding $-\beta_{\mathrm{LiD}}\langle n_{\mathrm{Li}}\rangle$ to the right-hand side of Eq. (7.1). Hence, the solution of our model is given by substituting τ^{-1} with $\beta_{\mathrm{LiD}}\langle n_{\mathrm{Li}}\rangle + \tau^{-1}$ in Eq. (7.2). We fit this solution to our experimental data to determine the Li atom dimer loss coefficient β_{LiD}. For the fit, we fix τ to the corresponding theoretical value and the decay coefficient β_{D} to the value we determined in the corresponding reference measurement on a pure dimer sample.

In Fig. 7.6, we show our results for the Li atom dimer loss coefficient β_{LiD} at various magnetic detunings. The blue circles (red squares) correspond to data acquired with a Li$|1\rangle$K$|3\rangle$ (Li$|1\rangle$K$|1\rangle$) dimer sample. The error bars reflect the 1σ fit uncertainty of β_{LiD} as well as the contribution arising from the uncertainty in our determination of β_{D}. We obtain atom-dimer loss-rate coefficients of roughly $1.5\times10^{-10}\mathrm{cm}^3/\mathrm{s}$ near the Li$|1\rangle$K$|1\rangle$ FR, where the molecules have closed-channel character. The data obtained with Li$|1\rangle$K$|3\rangle$ dimers show a suppression of atom-dimer collisional losses, which gets stronger as we approach the FR and the open-channel fraction of the dimers increases. The data point at a magnetic detuning of about $-40\,\mathrm{mG}$ already shows a suppression by a factor of roughly five. From our measurements closest to the FR, we determine a negative loss coefficient. We speculate, that this unphysical result is due to the repulsive mean-field interaction between the dimers and the Li atoms, effectively increasing the cloud sizes and therefore decreasing the mean densities of the dimers

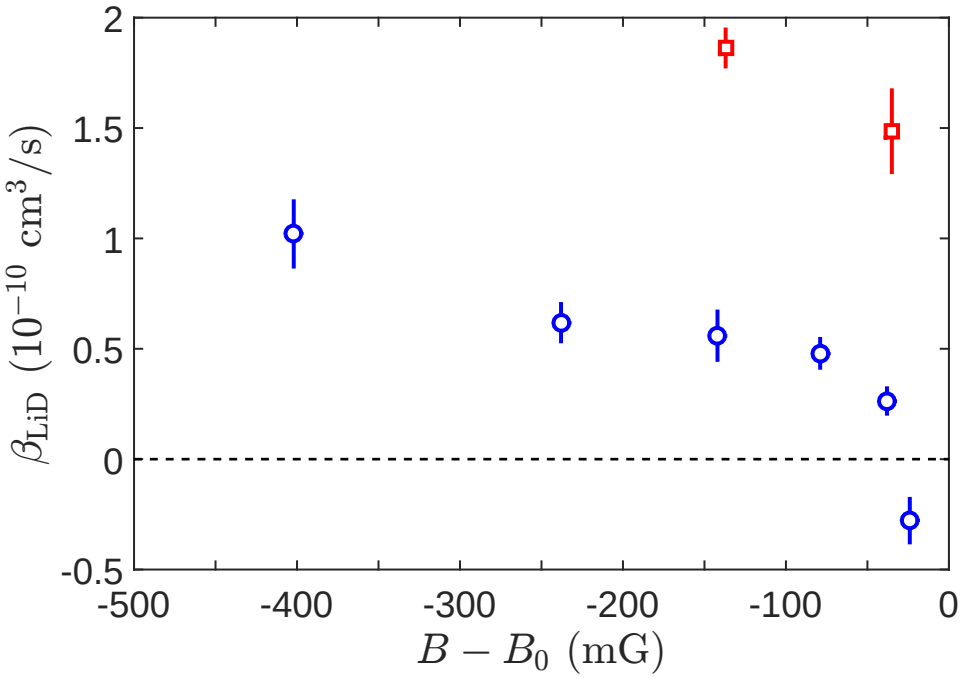

Figure 7.6: (Color online) Measured loss rate coefficient for inelastic Li atom dimer collisions as a function of the magnetic detuning. The blue circles (red squares) correspond to the experimental results obtained with samples of Li$|1\rangle$K$|3\rangle$ (Li$|1\rangle$K$|1\rangle$) dimers co-trapped with Li$|1\rangle$ atoms. In these experiments, the dimer number was determined from the K absorption images only. The error bars include the combined fit uncertainties (see text).

and the Li atoms. Such an effect is beyond the assumptions of the model underlying our data analysis and can therefore produce unphysical results. We estimate that all other values, taken at larger detunings, do not suffer from such interaction effects.

We ascribe the observed suppression of atom-dimer collisional losses, similar to the suppression of dimer-dimer collisional losses presented before, to the increased fermionic character of the dimers, as the FR is being approached.

7.4 Conclusion and outlook

We have experimentally determined the lifetime of dimers against spontaneous and collisional decay. Our measurements of the spontaneous decay confirm the theoretical prediction from Ref. [Nai11]. Furthermore, we showed that, approaching the resonance, the dimer decay in atom-dimer and dimer-dimer collisions is being suppressed by a factor of five and three, respectively. The observed suppression qualitatively agrees well with the results from a few-body theory [Lev11], which relates the collisional decay rate to the probability of finding the colliding atoms within a short range.

We will, in close cooperation with Dima Petrov and Jesper Levinsen, the authors of Ref. [Lev11], work on quantifying the agreement of their theory and our measurements. Preliminary results show good agreement and encourage to apply the theory to Fermi-Fermi mixtures of other species. The obtained theoretical prediction would then allow to analyze the prospect of such Fermi-Fermi mixtures for creating a BEC of dimers, which typically is a first step towards the investigation of the BEC-BCS crossover or the realization of exotic quantum phases.

Chapter 8

Outlook

Here we shortly discuss a few research topics, which can be tackled using the FeLiKx machine. These are immediate extensions of measurements done within this thesis work, which require only small add-ons to the existing setup.

Many-body physics with FeLiKx - bosonic vs. fermionic impurities
For the experiments with the fermionic impurities, described in Chapters 3, 4, and 5, typically $\sim 5 \times 10^3$ K impurities were immersed into the Fermi sea consisting of $\sim 3 \times 10^5$ Li atoms. We could show, that with this system, we are very close to the regime of a single impurity in a Fermi sea, c.f. Fig. 4 in *Chapter* 5. This is due to the fact that the impurities were identical fermions, ^{40}K, and therefore did not directly interact with each other.

Recently, we extended the K laser setup by a few optical components to also allow for the generation of laser light needed for laser cooling and imaging of the bosonic isotope ^{41}K. Bose-Einstein condensates as pure as $\sim 80\%$, mixed with a highly degenerate Fermi sea of ^{6}Li, were realized so far. The ^{6}Li-^{41}K Fermi-Bose mixture, with both species prepared in their lowest Zeeman state, exhibits a Feshbach resonance at a magnetic field around 335.3 G. This resonance, with a width of 0.93 G and sitting on a background scattering length of $+62\,a_0$, is very similar to the resonance of the ^{6}Li-^{40}K Fermi-Fermi mixture at a magnetic field around 154.8 G [1]. As a first step, the stability of a mixture of a dilute boson cloud immersed into a degenerate Fermi sea will be investigated across an inter-species Feshbach resonance, which is already a highly interesting research topic by itself [Yu11].

The major research block will be devoted to polarons, formed by bosons dressed by a fermionic cloud, which are investigated using our well understood radio-frequency spectroscopy approaches in the time and frequency domain presented within this thesis. Using bosonic ^{41}K instead of the fermionic ^{40}K as the impurities, where there is no Pauli blocking preventing them to collide with each other, we expect strong effects arising from impurity-impurity interactions already for the low concentrations mentioned above. Further increasing the impurity concentration, it will be interesting to see if the condensation of such polarons can be observed [Yu11, Wu11]. The fortunate fact, that near the proposed Feshbach resonances interaction tuning can be achieved in such a similar manner, will facilitate the

[1] The ^{6}Li-^{40}K resonance appears between Li prepared in the lowest and K in the third-to-lowest state. Its width and background scattering length are given by 0.88 G and $+63\,a_0$, respectively.

investigation of the effect of quantum statistics on the impurity physics.

Few-body physics with FeLiKx - ^{40}K-^{40}K^{6}Li coupling to a trimer state
In Chapter 6, we discussed the attractive interaction between ^{6}Li^{40}K dimers and ^{40}K atoms in a regime of repulsive Li-K interactions. This attraction is due to the presence of a p-wave atom-dimer scattering resonance in our mass-imbalanced mixture ($m_{\mathrm{K}}/m_{\mathrm{Li}} \approx 6.6$), which originates from coupling to a virtual trimer state at positive energy [Lev09, Lev11]. For a mass ratio above a critical value of 8.2 this state becomes a bound trimer state [Kar07].

We can increase our mass imbalance $m_{\mathrm{K}}/m_{\mathrm{Li}} \approx 6.6$ above the critical value by adding a (e.g. one-dimensional) optical lattice to the existing experimental setup (see e.g. Ref. [Zwe03]). Due to the more than two times deeper optical potential, which 1064-nm light creates for the K atoms compared to the Li atoms, the K-Li effective-mass ratio can be tuned by varying the intensity of the laser beam forming the optical lattice. The needed laser light can right away be deduced from the source used for our current optical traps (Innolight Mephisto 42NE MOPA).

In such a (quasi-)two-dimensional geometry, a trimer state is predicted to exist in the immediate vicinity of the Feshbach resonance [Lev09]. Here, the trimer binding energy will only be a few percent larger than the dimer binding energy [Lev13] and, at typical temperatures in our experiments, already thermal excitations allow these trimers to dissociate into an atom and a dimer. If a proof of the experimental realization of this three-body state in our system will be provided using radio-frequency spectroscopy is questionable. However, signatures of coupling to this trimer state can be obtained by applying a method measuring few-body correlations, such as Bragg spectroscopy [Vee08, Vee09].

Bibliography

[Aik14] K. Aikawa, A. Frisch, M. Mark, S. Baier, R. Grimm, and F. Ferlaino, *Reaching Fermi Degeneracy via Universal Dipolar Scattering*, Phys. Rev. Lett. **112**, 010404 (2014).

[And67] P. W. Anderson, *Infrared Catastrophe in Fermi Gases with Local Scattering Potentials*, Phys. Rev. Lett. **18**, 1049 (1967).

[And95] M. H. Anderson, J. R. Ensher, M. R. Matthews, C. E. Wieman, and E. A. Cornell, *Observation of Bose-Einstein Condensation in a Dilute Atomic Vapor*, Science **269**, 198 (1995).

[Ata13] M. Atala, M. Aidelsburger, J. T. Barreiro, D. Abanin, T. Kitagawa, E. Demmler, and I. Bloch, *Direct measurement of the Zak phase in topological Bloch bands*, Nature Physics **9**, 795 (2013).

[Bar58a] M. Baranger, *General Impact Theory of Pressure Broadening*, Phys. Rev. **112**, 855 (1958).

[Bar58b] M. Baranger, *Simplified Quantum-Mechanical Theory of Pressure Broadening*, Phys. Rev. **111**, 481 (1958).

[Bar04a] M. Bartenstein, A. Altmeyer, S. Riedl, S. Jochim, C. Chin, J. Hecker Denschlag, and R. Grimm, *Collective Excitations of a Degenerate Gas at the BEC-BCS Crossover*, Phys. Rev. Lett. **92**, 203201 (2004).

[Bar04b] M. Bartenstein, A. Altmeyer, S. Riedl, S. Jochim, C. Chin, J. Hecker Denschlag, and R. Grimm, *Crossover from a Molecular Bose-Einstein Condensate to a Degenerate Fermi Gas*, Phys. Rev. Lett. **92**, 120401 (2004).

[Bar08] M. A. Baranov, C. Lobo, and G. V. Shlyapnikov, *Superfluid pairing between fermions with unequal masses*, Phys. Rev. A **78**, 033620 (2008).

[Bar14] A. B. Bardon, S. Beattie, C. Luciuk, W. Cairncross, D. Fine, N. S. Cheng, G. J. A. Edge, E. Taylor, S. Zhang, S. Trotzky, and J. H. Thywissen, *Transverse Demagnetization Dynamics of a Unitary Fermi Gas*, Science **344**, 722 (2014).

[Bau09a] D. M. Bauer, M. Lettner, C. Vo, G. Rempe, and S. Dürr, *Combination of a magnetic Feshbach resonance and an optical bound-to-bound transition*, Phys. Rev. A **79**, 062713 (2009).

[Bau09b] D. M. Bauer, M. Lettner, C. Vo, G. Rempe, and S. Dürr, *Control of a magnetic Feshbach resonance with laser light*, Nature Phys. **5**, 339 (2009).

[Bau09c] I. Bausmerth, A. Recati, and S. Stringari, *Chandrasekhar-Clogston limit and phase separation in Fermi mixtures at unitarity*, Phys. Rev. A **79**, 043622 (2009).

[Bay04] G. Baym and C. Pethick, *Landau Fermi Liquid Theory: Concepts and Applications*, Wiley-VCH, 2004.

[Ben14] K.-H. Bennemann and J. B. Ketterson, *Novel Superfluids: Volume 2*, Oxford University Press, Oxford, 2014.

[Ber95] Y. Berk, A. Kamenev, A. Palevski, L. N. Pfeiffer, and K. W. West, *Resonance magnetoresistance of coupled quantum wells*, Phys. Rev. B **51**, 2604 (1995).

[Blo08] I. Bloch, J. Dalibard, and W. Zwerger, *Many-body physics with ultracold gases*, Rev. Mod. Phys. **80**, 885 (2008).

[Blo12] I. Bloch, J. Dalibard, and S. Nascimbene, *Quantum simulations with ultracold quantum gases*, Nature Phys. **8**, 267 (2012).

[Blu12] D. Blume, *Universal Four-Body States in Heavy-Light Mixtures with a Positive Scattering Length*, Phys. Rev. Lett. **109**, 230404 (2012).

[Bou03] T. Bourdel, J. Cubizolles, L. Khaykovich, K. M. F. Magalhães, S. J. J. M. F. Kokkelmans, G. V. Shlyapnikov, and C. Salomon, *Measurement of the Interaction Energy near a Feshbach Resonance in a* ^{6}Li *Fermi Gas*, Phys. Rev. Lett. **91**, 020402 (2003).

[Bou04] T. Bourdel, L. Khaykovich, J. Cubizolles, J. Zhang, F. Chevy, M. Teichmann, L. Tarruell, S. J. J. M. F. Kokkelmans, and C. Salomon, *Experimental Study of the BEC-BCS Crossover Region in Lithium 6*, Phys. Rev. Lett. **93**, 050401 (2004).

[Bre31] G. Breit and I. I. Rabi, *Measurement of Nuclear Spin*, Phys. Rev. **38**, 2082 (1931).

[Bru04] G. M. Bruun and C. J. Pethick, *Effective Theory of Feshbach Resonances and Many-Body Properties of Fermi Gases*, Phys. Rev. Lett. **92**, 140404 (2004).

[Bru05a] G. M. Bruun, A. D. Jackson, and E. E. Kolomeitsev, *Multichannel scattering and Feshbach resonances: Effective theory, phenomenology, and many-body effects*, Phys. Rev. A **71**, 052713 (2005).

[Bru05b] G. M. Bruun and H. Smith, *Viscosity and thermal relaxation for a resonantly interacting Fermi gas*, Phys. Rev. A **72**, 043605 (2005).

[Bru10] G. M. Bruun and P. Massignan, *Decay of Polarons and Molecules in a Strongly Polarized Fermi Gas*, Phys. Rev. Lett. **105**, 020403 (2010).

[Bru12] D. A. Brue and J. M. Hutson, *Magnetically Tunable Feshbach Resonances in Ultracold Li-Yb Mixtures*, Phys. Rev. Lett. **108**, 043201 (2012).

[Cet15] M. Cetina, M. Jag, R. S. Lous, J. T. M. Walraven, R. Grimm, R. S. Christensen, and G. M. Bruun, *Decoherence of Impurities in a Fermi Sea of Ultracold Atoms*, Phys. Rev. Lett. **115**, 135302 (2015).

[Cha11] S.-Y. Chang, M. Randeria, and N. Trivedi, *Ferromagnetism in the upper branch of the Feshbach resonance and the hard-sphere Fermi gas*, PNAS **108**, 51 (2011).

[Che06] F. Chevy, *Universal phase diagram of a strongly interacting Fermi gas with unbalanced spin populations*, Phys. Rev. A **74**, 063628 (2006).

[Che10] F. Chevy and C. Mora, *Ultra-cold polarized Fermi gases*, Rep. Prog. Phys. **73**, 112401 (2010).

[Chi04] C. Chin, M. Bartenstein, A. Altmeyer, S. Riedl, S. Jochim, J. Hecker Denschlag, and R. Grimm, *Observation of the Pairing Gap in a Strongly Interacting Fermi Gas*, Science **305**, 1128 (2004).

[Chi05] C. Chin and P. S. Julienne, *Radio-frequency transitions on weakly bound ultracold molecules*, Phys. Rev. A **71**, 012713 (2005).

[Chi10] C. Chin, R. Grimm, P. Julienne, and E. Tiesinga, *Feshbach resonances in ultracold gases*, Rev. Mod. Phys. **82**, 1225 (2010).

[Chr15] R. S. Christensen and G. M. Bruun, *Quasiparticle scattering rate in a strongly polarized Fermi mixture*, Phys. Rev. A **91**, 042702 (2015), for the relevant parameter r_{eff}, see [Pet04a].

[Cla15] L. W. Clark, L.-C. Ha, C.-Y. Xu, and C. Chin, *Quantum Dynamics with Spatiotemporal Control of Interactions in a Stable Bose-Einstein Condensate*, Phys. Rev. Lett. **115**, 155301 (2015).

[Com07] R. Combescot, A. Recati, C. Lobo, and F. Chevy, *Normal state of highly polarized Fermi gases: Simple many-body approaches*, Phys. Rev. Lett. **98**, 180402 (2007).

[Com08] R. Combescot and S. Giraud, *Normal state of highly polarized Fermi gases: Full many-body treatment*, Phys. Rev. Lett. **101**, 050404 (2008).

[Com09] R. Combescot, S. Giraud, and X. Leyronas, *Analytical theory of the dressed bound state in highly polarized Fermi gases*, Europhys. Lett. **88**, 60007 (2009).

[Con09] G. J. Conduit, A. G. Green, and B. D. Simons, *Inhomogeneous Phase Formation on the Border of Itinerant Ferromagnetism*, Phys. Rev. Lett. **103**, 207201 (2009).

[Cos10] L. Costa, J. Brachmann, A.-C. Voigt, C. Hahn, M. Taglieber, T. W. Hänsch, and K. Dieckmann, *s-Wave Interaction in a Two-Species Fermi-Fermi Mixture at a Narrow Feshbach Resonance*, Phys. Rev. Lett. **105**, 123201 (2010).

[Cro09] A. D. Cronin, J. Schmiedmayer, and D. E. Pritchard, *Optics and interferometry with atoms and molecules*, Rev. Mod. Phys. **81**, 1051 (2009).

[Cub03] J. Cubizolles, T. Bourdel, S. J. J. M. F. Kokkelmans, G. V. Shlyapnikov, and C. Salomon, *Production of Long-Lived Ultracold* Li_2 *Molecules from a Fermi Gas*, Phys. Rev. Lett. **91**, 240401 (2003).

[Cui13] X. Cui and T.-L. Ho, *Phase Separation in Mixtures of Repulsive Fermi Gases Driven by Mass Difference*, Phys. Rev. Lett. **110**, 165302 (2013).

[Dai12] K. M. Daily and D. Blume, *Thermodynamics of the two-component Fermi gas with unequal masses at unitarity*, Phys. Rev. A **85**, 013609 (2012).

[Dal98] J. Dalibard, *Collisional dynamics of ultra-cold atomic gases*, Proceedings of the International School of Physics Enrico Fermi (M. Inguscio, S. Stringari, and C. Wieman, eds.), 1998.

[Dal12] M. Dalmonte, K. Dieckmann, T. Roscilde, C. Hartl, A. E. Feiguin, U. Schollwöck, and F. Heidrich-Meisner, *Dimer, trimer, and Fulde-Ferrell-Larkin-Ovchinnikov liquids in mass- and spin-imbalanced trapped binary mixtures in one dimension*, Phys. Rev. A **85**, 063608 (2012).

[Dav95] K. B. Davis, M. O. Mewes, M. R. Andrews, N. J. van Druten, D. S. Durfee, D. M. Kurn, and W. Ketterle, *Bose-Einstein Condensation in a Gas of Sodium Atoms*, Phys. Rev. Lett. **75**, 3969 (1995).

[DeM99] B. DeMarco and D. S. Jin, *Onset of Fermi Degeneracy in a Trapped Atomic Gas*, Science **285**, 1703 (1999).

[DeS10] B. J. DeSalvo, M. Yan, P. G. Mickelson, Y. N. Martinez de Escobar, and T. C. Killian, *Degenerate Fermi Gas of* ^{87}Sr, Phys. Rev. Lett. **105**, 030402 (2010).

[Din01] H. Ding, J. R. Engelbrecht, Z. Wang, J. C. Campuzano, S.-C. Wang, H.-B. Yang, R. Rogan, T. Takahashi, K. Kadowaki, and D. G. Hinks, *Coherent Quasiparticle Weight and Its Connection to High-* T_c *Superconductivity from Angle-Resolved Photoemission*, Phys. Rev. Lett. **87**, 227001 (2001).

[Dub13] J. Dubois, T. Jullien, F. Portier, P. Roche, A. Cavanna, Y. Jin, W. Wegscheider, P. Roulleau, and D. C. Glattli, *Minimal-excitation states for electron quantum optics using levitons*, Nature (London) **502**, 659 (2013).

[Dui05] R. A. Duine and A. H. MacDonald, *Itinerant Ferromagnetism in an Ultracold Atom Fermi Gas*, Phys. Rev. Lett. **95**, 230403 (2005).

[Efi70] V. Efimov, *Energy levels arising from resonant two-body forces in a three-body system*, Phys. Lett. B **33**, 563 (1970).

[Ens12] T. Enss, *Quantum critical transport in the unitary Fermi gas*, Phys. Rev. A **86**, 013616 (2012).

[Fan61] U. Fano, *Effects of Configuration Interaction on Intensities and Phase Shifts*, Phys. Rev. **124**, 1866 (1961).

[Fer11] F. Ferlaino, A. Zenesini, M. Berninger, B. Huang, H. C. Nägerl, and R. Grimm, *Efimov Resonances in Ultracold Quantum Gases*, Few-Body Syst. **51**, 113 (2011).

[Fes58] H. Feshbach, *Unified theory of nuclear reactions*, Ann. Phys. (NY) **5**, 357 (1958).

[Fes62] H. Feshbach, *A unified theory of nuclear reactions. II*, Ann. Phys. (NY) **19**, 287 (1962).

[For05] M. M. Forbes, E. Gubankova, W. V. Liu, and F. Wilczek, *Stability Criteria for Breached-Pair Superfluidity*, Phys. Rev. Lett. **94**, 017001 (2005).

[Fuk07a] T. Fukuhara, Y. Takasu, S. Sugawa, and Y. Takahashi, *Quantum Degenerate Fermi Gases of Ytterbium Atoms*, J. Low Temp. Phys. **148**, 441 (2007).

[Fuk07b] T. Fukuhara, Y. Takasu, M. Kumakura, and Y. Takahashi, *Degenerate Fermi Gases of Ytterbium*, Phys. Rev. Lett. **98**, 030401 (2007).

[Ful64] P. Fulde and R. A. Ferrell, *Superconductivity in a Strong Spin-Exchange Field*, Phys. Rev. **135**, A550 (1964).

[Gez09] A. Gezerlis, S. Gandolfi, K. E. Schmidt, and J. Carlson, *Heavy-Light Fermion Mixtures at Unitarity*, Phys. Rev. Lett. **103**, 060403 (2009).

[Gio08] S. Giorgini, L. P. Pitaevskii, and S. Stringari, *Theory of ultracold atomic Fermi gases*, Rev. Mod. Phys. **80**, 1215 (2008).

[Goo11] J. Goold, T. Fogarty, N. Lo Gullo, M. Paternostro, and T. Busch, *Orthogonality catastrophe as a consequence of qubit embedding in an ultracold Fermi gas*, Phys. Rev. A **84**, 063632 (2011).

[Gór04] K. Góral, T. Köhler, S. A. Gardiner, E. Tiesinga, and P. S. Julienne, *Adiabatic association of ultracold molecules via magnetic-field tunable interactions*, J. Phys. B **37**, 3457 (2004).

[Gra02] S. R. Granade, M. E. Gehm, K. M. O'Hara, and J. E. Thomas, *All-Optical Production of a Degenerate Fermi Gas*, Phys. Rev. Lett. **88**, 120405 (2002).

[Gre03] M. Greiner, C. A. Regal, and D. S. Jin, *Emergence of a molecular Bose–Einstein condensate from a Fermi gas*, Nature (London) **426**, 537 (2003).

[Gri12] M. Gring, M. Kuhnert, T. Langen, T. Kitagawa, B. Rauer, M. Schreitl, I. Mazets, D. A. Smith, E. Demler, and J. Schmiedmayer, *Relaxation and Prethermalization in an Isolated Quantum System*, Science **337**, 1318 (2012).

[Gub03] E. Gubankova, W. V. Liu, and F. Wilczek, *Breached Pairing Superfluidity: Possible Realization in QCD*, Phys. Rev. Lett. **91**, 032001 (2003).

[Gub09] K. B. Gubbels, J. E. Baarsma, and H. T. C. Stoof, *Lifshitz Point in the Phase Diagram of Resonantly Interacting* ^{6}Li-^{40}K *Mixtures*, Phys. Rev. Lett. **103**, 195301 (2009).

[Had02] Z. Hadzibabic, C. A. Stan, K. Dieckmann, S. Gupta, M. W. Zwierlein, A. Görlitz, and W. Ketterle, *Two-Species Mixture of Quantum Degenerate Bose and Fermi Gases*, Phys. Rev. Lett. **88**, 160401 (2002).

[Had06] Z. Hadzibabic, P. Krüger, M. Cheneau, B. Battelier, and J. Dalibard, *Berezinskii–Kosterlitz–Thouless crossover in a trapped atomic gas*, Nature (London) **441**, 1118 (2006).

[Han13] A. H. Hansen, A. Y. Khramov, W. H. Dowd, A. O. Jamison, B. Plotkin-Swing, R. J. Roy, and S. Gupta, *Production of quantum-degenerate mixtures of ytterbium and lithium with controllable interspecies overlap*, Phys. Rev. A **87**, 013615 (2013).

[Har11] H. Hara, Y. Takasu, Y. Yamaoka, J. M. Doyle, and Y. Takahashi, *Quantum Degenerate Mixtures of Alkali and Alkaline-Earth-Like Atoms*, Phys. Rev. Lett. **106**, 205304 (2011).

[Har15] R. A. Hart, P. M. Duarte, T.-L. Yang, X. Liu, T. Paiva, E. Khatami, R. T. Scalettar, N. Trivedi, D. A. Huse, and R. G. Hulet, *Observation of antiferromagnetic correlations in the Hubbard model with ultracold atoms*, Nature (London) **519**, 211 (2015).

[Hec02] E. Hecht, *Optics*, vol. 4, Addison Wesley, 2002.

[Ho12] T.-L. Ho, X. Cui, and W. Li, *Alternative Route to Strong Interaction: Narrow Feshbach Resonance*, Phys. Rev. Lett. **108**, 250401 (2012).

[Hua87] K. Huang, *Statistical Mechanics*, John Wiley & Sons, Inc., Hoboken, USA, 1987.

[Isk06] M. Iskin and C. A. R. Sá de Melo, *Two-Species Fermion Mixtures with Population Imbalance*, Phys. Rev. Lett. **97**, 100404 (2006).

[Jac99] J. D. Jackson, *Classical Electrodynamics*, Wiley, 1999.

[Jag14] M. Jag, M. Zaccanti, M. Cetina, R. S. Lous, F. Schreck, R. Grimm, D. S. Petrov, and J. Levinsen, *Observation of a Strong Atom-Dimer Attraction in a Mass-Imbalanced Fermi-Fermi Mixture*, Phys. Rev. Lett. **112**, 075302 (2014).

[Jal01] R. A. Jalabert and H. M. Pastawski, *The Semiclassical Tool in Complex Physical Systems: Mesoscopics and Decoherence*, Adv. Solid State Phys. **41**, 483 (2001).

[Jo09] G.-B. Jo, Y.-R. Lee, J.-H. Choi, C. A. Christensen, T. H. Kim, J. H. Thywissen, D. E. Pritchard, and W. Ketterle, *Itinerant Ferromagnetism in a Fermi Gas of Ultracold Atoms*, Science **325**, 1521 (2009).

[Joc03a] S. Jochim, M. Bartenstein, A. Altmeyer, G. Hendl, C. Chin, J. Hecker Denschlag, and R. Grimm, *Pure Gas of Optically Trapped Molecules Created from Fermionic Atoms*, Phys. Rev. Lett. **91**, 240402 (2003).

[Joc03b] S. Jochim, M. Bartenstein, A. Altmeyer, G. Hendl, S. Riedl, C. Chin, J. Hecker Denschlag, and R. Grimm, *Bose-Einstein Condensation of Molecules*, Science **302**, 2101 (2003).

[KÖ5] T. Köhler, E. Tiesinga, and P. S. Julienne, *Spontaneous Dissociation of Long-Range Feshbach Molecules*, Phys. Rev. Lett. **94**, 020402 (2005).

[KÖ6] T. Köhler, K. Góral, and P. S. Julienne, *Production of cold molecules via magnetically tunable Feshbach resonances*, Rev. Mod. Phys. **78**, 1311 (2006).

[Kar07] O. I. Kartavtsev and A. V. Malykh, *Low-energy three-body dynamics in binary quantum gases*, J. Phys. B **40**, 1429 (2007).

[Kas92] M. Kasevich and S. Chu, *Laser cooling below a photon recoil with three-level atoms*, Phys. Rev. Lett. **69**, 1741 (1992).

[Kin04] J. Kinast, S. L. Hemmer, M. E. Gehm, A. Turlapov, and J. E. Thomas, *Evidence for Superfluidity in a Resonantly Interacting Fermi Gas*, Phys. Rev. Lett. **92**, 150402 (2004).

[Kin05] J. Kinast, A. Turlapov, J. E. Thomas, Q. Chen, J. Stajic, and K. Levin, *Heat Capacity of a Strongly Interacting Fermi Gas*, Science **307**, 1296–1299 (2005).

[Kli03] I. Klich, *Full Counting Statistics: An elementary derivation of Levitov's formula*, Quantum Noise in Mesoscopic Systems (Y. V. Nazarov, ed.), Kluwer, Dordrecht, 2003, p. 397.

[Kna12] M. Knap, A. Shashi, Y. Nishida, A. Imambekov, D. A. Abanin, and E. Demler, *Time-Dependent Impurity in Ultracold Fermions: Orthogonality Catastrophe and Beyond*, Phys. Rev. X **2**, 041020 (2012).

[Koh12a] C. Kohstall, *Resonantly Interacting Fermi Gases: Coherence, Collective Dynamics, and Polarons*, Ph.D. thesis, University of Innsbruck (2012).

[Koh12b] C. Kohstall, M. Zaccanti, M. Jag, A. Trenkwalder, P. Massignan, G. M. Bruun, F. Schreck, and R. Grimm, *Metastability and coherence of repulsive polarons in a strongly interacting Fermi mixture*, Nature (London) **485**, 615 (2012).

[Kor50] J. Korringa, *Nuclear magnetic relaxation and resonnance line shift in metals*, Physica **16**, 601 (1950).

[Kos12] M. Koschorreck, D. Pertot, E. Vogt, B. Frölich, M. Feld, and M. Köhl, *Attractive and repulsive Fermi polarons in two dimensions*, Nature (London) **485**, 619 (2012).

[Kos13] M. Koschorreck, D. Pertot, E. Vogt, and M. Köhl, *Universal spin dynamics in two-dimensional Fermi gases*, Nat. Phys. **9**, 405 (2013).

[Kra09] F. Krausz and M. Ivanov, *Attosecond physics*, Rev. Mod. Phys. **81**, 163 (2009).

[Lan56] L. D. Landau, *The Theory of a Fermi Liquid*, Sov. Phys. JETP **3**, 920 (1956).

[Lan57] L. D. Landau, *Oscillations in a Fermi-liquid*, Sov. Phys. JETP **5**, 101 (1957).

[Lan81] L. D. Landau and E. M. Lifshitz, *Quantum mechanics: non-relativistic theory*, vol. 3, Butterworth Heinemann, 1981.

[Lan09] A. D. Lange, K. Pilch, A. Prantner, F. Ferlaino, B. Engeser, H.-C. Nägerl, R. Grimm, and C. Chin, *Determination of atomic scattering lengths from measurements of molecular binding energies near Feshbach resonances*, Phys. Rev. A **79**, 013622 (2009).

[Lar65] A. I. Larkin and I. U. N. Ovchinnikov, *Inhomogeneous state of superconductors*, Sov. Phys. JETP **20**, 762 (1965).

[LeB07] L. J. LeBlanc and J. H. Thywissen, *Species-specific optical lattices*, Phys. Rev. A **75**, 053612 (2007).

[LeB09] L. J. LeBlanc, J. H. Thywissen, A. A. Burkov, and A. Paramekanti, *Repulsive Fermi gas in a harmonic trap: Ferromagnetism and spin textures*, Phys. Rev. A **80**, 013607 (2009).

[Lev93] L. Levitov and G. Lesovik, *Charge distribution in quantum shot noise*, JETP Lett. **58**, 230 (1993).

[Lev96] L. S. Levitov, H. Lee, and G. B. Lesovik, *Electron counting statistics and coherent states of electric current*, J. Math. Phys. **37**, 4845 (1996).

[Lev09] J. Levinsen, T. G. Tiecke, J. T. M. Walraven, and D. S. Petrov, *Atom-Dimer Scattering and Long-Lived Trimers in Fermionic Mixtures*, Phys. Rev. Lett. **103**, 153202 (2009).

[Lev11] J. Levinsen and D. Petrov, *Atom-dimer and dimer-dimer scattering in fermionic mixtures near a narrow Feshbach resonance*, Eur. Phys. J. D **65**, 67 (2011).

[Lev13] J. Levinsen and M. M. Parish, *Bound States in a Quasi-Two-Dimensional Fermi Gas*, Phys. Rev. Lett. **110**, 055304 (2013).

[Lob06] C. Lobo, A. Recati, S. Giorgini, and S. Stringari, *Normal State of a Polarized Fermi Gas at Unitarity*, Phys. Rev. Lett. **97**, 200403 (2006).

[Los76] J. Loschmidt, *Über den Zustand des Wärmegleichgewichts eines Systems von Körpern mit Rücksicht auf die Schwerkraft*, Sitzungsberichte der Akademie der Wissenschaften, Wien **73**, 128 (1876).

[Lu12] M. Lu, N. Q. Burdick, and B. L. Lev, *Quantum Degenerate Dipolar Fermi Gas*, Phys. Rev. Lett. **108**, 215301 (2012).

[Mah00] G. D. Mahan, *Many-Particle Physics, 3rd edition*, Physics of solids and liquids, Kluwer Academic/Plenum Publishers, New York, 2000.

[Mas08a] P. Massignan, G. M. Bruun, and H. T. C. Stoof, *Twin peaks in rf spectra of Fermi gases at unitarity*, Phys. Rev. A **77**, 031601 (2008).

[Mas08b] P. Massignan and H. T. C. Stoof, *Efimov states near a Feshbach resonance*, Phys. Rev. A **78**, 030701 (2008).

[Mas11] P. Massignan and G. Bruun, *Repulsive polarons and itinerant ferromagnetism in strongly polarized Fermi gases*, Eur. Phys. J. D **65**, 83 (2011).

[Mas12] P. Massignan, *Polarons and dressed molecules near narrow Feshbach resonances*, Europhys. Lett. **98**, 10012 (2012).

[Mas14] P. Massignan, M. Zaccanti, and G. M. Bruun, *Polarons, dressed molecules and itinerant ferromagnetism in ultracold Fermi gases*, Rep. Prog. Phys. **77**, 034401 (2014).

[Mat11] C. J. M. Mathy, M. M. Parish, and D. A. Huse, *Trimers, Molecules, and Polarons in Mass-Imbalanced Atomic Fermi Gases*, Phys. Rev. Lett. **106**, 166404 (2011).

[McA96] W. I. McAlexander, E. R. I. Abraham, and R. G. Hulet, *Radiative lifetime of the 2P state of lithium*, Phys. Rev. A **54**, R5 (1996).

[McN06] J. M. McNamara, T. Jeltes, A. S. Tychkov, W. Hogervorst, and W. Vassen, *Degenerate Bose-Fermi Mixture of Metastable Atoms*, Phys. Rev. Lett. **97**, 080404 (2006).

[Mil07] D. E. Miller, J. K. Chin, C. A. Stan, Y. Liu, W. Setiawan, C. Sanner, and W. Ketterle, *Critical Velocity for Superfluid Flow across the BEC-BCS Crossover*, Phys. Rev. Lett. **99**, 070402 (2007).

[Moe95] A. J. Moerdijk, B. J. Verhaar, and A. Axelsson, *Resonances in ultracold collisions of* ^{6}Li, ^{7}Li, *and* ^{23}Na, Phys. Rev. A **51**, 4852 (1995).

[Mor09] C. Mora and F. Chevy, *Ground state of a tightly bound composite dimer immersed in a Fermi sea*, Phys. Rev. A **80**, 033607 (2009).

[Mor10] C. Mora and F. Chevy, *Normal Phase of an Imbalanced Fermi Gas*, Phys. Rev. Lett. **104**, 230402 (2010).

[Mur95] S. Q. Murphy, J. P. Eisenstein, L. N. Pfeiffer, and K. W. West, *Lifetime of two-dimensional electrons measured by tunneling spectroscopy*, Phys. Rev. B **52**, 14825 (1995).

[Nai11] D. Naik, A. Trenkwalder, C. Kohstall, F. Spiegelhalder, M. Zaccanti, G. Hendl, F. Schreck, R. Grimm, T. Hanna, and P. Julienne, *Feshbach resonances in the 6Li-40K Fermi-Fermi mixture: elastic versus inelastic interactions*, Eur. Phys. J. D **65**, 55 (2011).

[Nas09] S. Nascimbène, N. Navon, K. J. Jiang, L. Tarruell, M. Teichmann, J. McKeever, F. Chevy, and C. Salomon, *Collective Oscillations of an Imbalanced Fermi Gas: Axial Compression Modes and Polaron Effective Mass*, Phys. Rev. Lett. **103**, 170402 (2009).

[Nas10] S. Nascimbene, N. Navon, K. Jiang, F. Chevy, and C. Salomon, *Exploring the thermodynamics of a universal Fermi gas*, Nature (London) **463**, 1057 (2010).

[Nas11] S. Nascimbène, N. Navon, S. Pilati, F. Chevy, S. Giorgini, A. Georges, and C. Salomon, *Fermi-Liquid Behavior of the Normal Phase of a Strongly Interacting Gas of Cold Atoms*, Phys. Rev. Lett. **106**, 215303 (2011).

[Nav10] N. Navon, S. Nascimbène, F. Chevy, and C. Salomon, *The Equation of State of a Low-Temperature Fermi Gas with Tunable Interactions*, Science **328**, 729 (2010).

[Nay15] B. Naylor, A. Reigue, E. Maréchal, O. Gorceix, B. Laburthe-Tolra, and L. Vernac, *Chromium dipolar Fermi sea*, Phys. Rev. A **91**, 011603 (2015).

[Nis08] Y. Nishida and S. Tan, *Universal Fermi Gases in Mixed Dimensions*, Phys. Rev. Lett. **101**, 170401 (2008).

[Nis09a] Y. Nishida, *Casimir interaction among heavy fermions in the BCS-BEC crossover*, Phys. Rev. A **79**, 013629 (2009).

[Nis09b] Y. Nishida and S. Tan, *Confinement-induced Efimov resonances in Fermi-Fermi mixtures*, Phys. Rev. A **79**, 060701 (2009).

[Noz69] P. Nozières and C. T. de Dominicis, *Singularities in the X-Ray Absorption and Emission of Metals. III. One-Body Theory Exact Solution*, Phys. Rev. **178**, 1097 (1969).

[O'H02] K. M. O'Hara, S. L. Hemmer, M. E. Gehm, S. R. Granade, and J. E. Thomas, *Observation of a Strongly Interacting Degenerate Fermi Gas of Atoms*, Science **298**, 2179 (2002).

[Oht90] K. Ohtaka and Y. Tanabe, *Theory of the soft-x-ray edge problem in simple metals: historical survey and recent developments*, Rev. Mod. Phys. **62**, 929 (1990).

[Ors10] G. Orso, E. Burovski, and T. Jolicoeur, *Luttinger Liquid of Trimers in Fermi Gases with Unequal Masses*, Phys. Rev. Lett. **104**, 065301 (2010).

[Par06] G. B. Partridge, W. Li, R. I. Kamar, Y.-a. Liao, and R. G. Hulet, *Pairing and Phase Separation in a Polarized Fermi Gas*, Science **311**, 503 (2006).

[Par07] M. M. Parish, F. M. Marchetti, A. Lamacraft, and B. D. Simons, *Polarized Fermi Condensates with Unequal Masses: Tuning the Tricritical Point*, Phys. Rev. Lett. **98**, 160402 (2007).

[Par13] M. M. Parish and J. Levinsen, *Highly polarized Fermi gases in two dimensions*, Phys. Rev. A **87**, 033616 (2013).

[Pau28] L. Pauling, *The Application of the Quantum Mechanics to the Structure of the Hydrogen Molecule and Hydrogen Molecule-Ion and to Related Problems*, Chem. Rev. **5**, 173 (1928).

[Paz15] R. Pazourek, S. Nagele, and J. Burgdörfer, *Attosecond chronoscopy of photoemission*, Rev. Mod. Phys. **87**, 765 (2015).

[Pek11] D. Pekker, M. Babadi, R. Sensarma, N. Zinner, L. Pollet, M. W. Zwierlein, and E. Demler, *Competition between Pairing and Ferromagnetic Instabilities in Ultracold Fermi Gases near Feshbach Resonances*, Phys. Rev. Lett. **106**, 050402 (2011).

[Pet03] D. S. Petrov, *Three-body problem in Fermi gases with short-range interparticle interaction*, Phys. Rev. A **67**, 010703 (2003).

[Pet04a] D. S. Petrov, *Three-Boson Problem near a Narrow Feshbach Resonance*, Phys. Rev. Lett. **93**, 143201 (2004).

[Pet04b] D. S. Petrov, C. Salomon, and G. V. Shlyapnikov, *Weakly Bound Dimers of Fermionic Atoms*, Phys. Rev. Lett. **93**, 090404 (2004).

[Pet05] D. S. Petrov, C. Salomon, and G. V. Shlyapnikov, *Diatomic molecules in ultracold Fermi gases—novel composite bosons*, J. Phys. B **38**, S645 (2005).

[Pet07] D. S. Petrov, G. E. Astrakharchik, D. J. Papoular, C. Salomon, and G. V. Shlyapnikov, *Crystalline Phase of Strongly Interacting Fermi Mixtures*, Phys. Rev. Lett. **99**, 130407 (2007).

[Pet13] D. S. Petrov, *Few-atom problem*, Proceedings of the Les Houches Summer Schools (C. Salomon, G. Shlyapnikov, and L. Cugliandolo, eds.), 94, Oxford University Press, 2013.

[Pil10] S. Pilati, G. Bertaina, S. Giorgini, and M. Troyer, *Itinerant Ferromagnetism of a Repulsive Atomic Fermi Gas: A Quantum Monte Carlo Study*, Phys. Rev. Lett. **105**, 030405 (2010).

[Pro08] N. Prokof'ev and B. Svistunov, *Fermi-polaron problem: Diagrammatic Monte Carlo method for divergent sign-alternating series*, Phys. Rev. B **77**, 020408 (2008).

[Pun09] M. Punk, P. T. Dumitrescu, and W. Zwerger, *Polaron-to-molecule transition in a strongly imbalanced Fermi gas*, Phys. Rev. A **80**, 053605 (2009).

[Qi12] R. Qi and H. Zhai, *Highly polarized Fermi gases across a narrow Feshbach resonance*, Phys. Rev. A **85**, 041603(R) (2012).

[Rad10] L. Radzihovsky and D. E. Sheehy, *Imbalanced Feshbach-resonant Fermi gases*, Rep. Prog. Phys. **73**, 076501 (2010).

[Reg03] C. A. Regal, C. Ticknor, J. L. Bohn, and D. S. Jin, *Creation of ultracold molecules from a Fermi gas of atoms*, Nature (London) **424**, 47 (2003).

[Reg04a] C. A. Regal, M. Greiner, and D. S. Jin, *Lifetime of Molecule-Atom Mixtures near a Feshbach Resonance in* ^{40}K, Phys. Rev. Lett. **92**, 083201 (2004).

[Reg04b] C. A. Regal, M. Greiner, and D. S. Jin, *Observation of Resonance Condensation of Fermionic Atom Pairs*, Phys. Rev. Lett. **92**, 040403 (2004).

[Rie11] S. Riedl, E. R. S. Guajardo, C. Kohstall, J. H. Denschlag, and R. Grimm, *Superfluid quenching of the moment of inertia in a strongly interacting Fermi gas*, New J. Phys. **13**, 035003 (2011).

[Roa02] G. Roati, F. Riboli, G. Modugno, and M. Inguscio, *Fermi-Bose Quantum Degenerate ^{40}K-^{87}Rb Mixture with Attractive Interaction*, Phys. Rev. Lett. **89**, 150403 (2002).

[Ros99] A. Rosch, *Quantum-coherent transport of a heavy particle in a fermionic bath*, Adv. Phys. **48**, 295 (1999).

[Ruf04] A. B. Ruffin, *Stimulated Brillouin Scattering: An Overview of Measurement, System Improvements and Applications*, NIST Symposium on Optical Fiber Measurements, 23 (2004).

[Sad11] K. Sadeghzadeh, G. M. Bruun, C. Lobo, P. Massignan, and A. Recati, *Metastability in spin-polarized Fermi gases and quasiparticle decays*, New J. Phys. **13**, 055011 (2011).

[Sag15] Y. Sagi, T. E. Drake, R. Paudel, R. Chapurin, and D. S. Jin, *Breakdown of the Fermi Liquid Description for Strongly Interacting Fermions*, Phys. Rev. Lett. **114**, 075301 (2015).

[San12] C. Sanner, E. J. Su, W. Huang, A. Keshet, J. Gillen, and W. Ketterle, *Correlations and Pair Formation in a Repulsively Interacting Fermi Gas*, Phys. Rev. Lett. **108**, 240404 (2012).

[Sar63] G. Sarma, *On the influence of a uniform exchange field acting on the spins of the conduction electrons in a superconductor*, J. Phys. Chem. Solids **24**, 1029 (1963).

[SC91] C. Sanchez-Castro and K. S. Bedell, *Two-component Fermi liquids and the induced-interaction model*, Phys. Rev. B **43**, 12874 (1991).

[Sce13] R. Scelle, T. Rentrop, A. Trautmann, T. Schuster, and M. K. Oberthaler, *Motional Coherence of Fermions Immersed in a Bose Gas*, Phys. Rev. Lett. **111**, 070401 (2013).

[Sch01] F. Schreck, L. Khaykovich, K. L. Corwin, G. Ferrari, T. Bourdel, J. Cubizolles, and C. Salomon, *Quasipure Bose-Einstein Condensate Immersed in a Fermi Sea*, Phys. Rev. Lett. **87**, 080403 (2001).

[Sch09] A. Schirotzek, C.-H. Wu, A. Sommer, and M. W. Zwierlein, *Observation of Fermi Polarons in a Tunable Fermi Liquid of Ultracold Atoms*, Phys. Rev. Lett. **102**, 230402 (2009).

[Sch11] R. Schmidt and T. Enss, *Excitation spectra and rf response near the polaron-to-molecule transition from the functional renormalization group*, Phys. Rev. A **83**, 063620 (2011).

[Sch12] R. Schmidt, S. Rath, and W. Zwerger, *Efimov physics beyond universality*, Eur. Phys. J. B **85**, 1 (2012).

[Shi06] Y.-i. Shin, M. W. Zwierlein, C. H. Schunck, A. Schirotzek, and W. Ketterle, *Observation of Phase Separation in a Strongly Interacting Imbalanced Fermi Gas*, Phys. Rev. Lett. **97**, 030401 (2006).

[Shi07] Y.-i. Shin, C. H. Schunck, A. Schirotzek, and W. Ketterle, *Tomographic rf Spectroscopy of a Trapped Fermi Gas at Unitarity*, Phys. Rev. Lett. **99**, 090403 (2007).

[Shi08] Y.-i. Shin, C. H. Schunck, A. Schirotzek, and W. Ketterle, *Phase diagram of a two-component Fermi gas with resonant interactions*, Nature (London) **451**, 689 (2008).

[Sid13] L. A. Sidorenkov, M. K. Tey, R. Grimm, Y.-H. Hou, L. Pitaevskii, and S. Stringari, *Second sound and the superfluid fraction in a Fermi gas with resonant interactions*, Nature (London) **498**, 78 (2013).

[Sie15] F. Sievers, N. Kretzschmar, D. R. Fernandes, D. Suchet, M. Rabinovic, S. Wu, C. V. Parker, L. Khaykovich, C. Salomon, and F. Chevy, *Simultaneous sub-Doppler laser cooling of fermionic* ^{6}Li *and* ^{40}K *on the* D_1 *line: Theory and experiment*, Phys. Rev. A **91**, 023426 (2015).

[Sim11] J. Simon, W. S. Bakr, R. Ma, M. E. Tai, P. M. Preiss, and M. Greiner, *Quantum simulation of antiferromagnetic spin chains in an optical lattice*, Nature (London) **472**, 307 (2011).

[Slu96] M. Slutzky, O. Entin-Wohlman, Y. Berk, A. Palevski, and H. Shtrikman, *Electron-electron scattering in coupled quantum wells*, Phys. Rev. B **53**, 4065 (1996).

[SN13] A. Safavi-Naini, S. T. Rittenhouse, D. Blume, and H. R. Sadeghpour, *Nonuniversal bound states of two identical heavy fermions and one light particle*, Phys. Rev. A **87**, 032713 (2013).

[Sob72] I. I. Sobelman, *An introduction to the theory of atomic spectra*, Pergamon Press, Oxford, 1972.

[Sot12] A. Sotnikov, D. Cocks, and W. Hofstetter, *Advantages of Mass-Imbalanced Ultracold Fermionic Mixtures for Approaching Quantum Magnetism in Optical Lattices*, Phys. Rev. Lett. **109**, 065301 (2012).

[Spi09] F. M. Spiegelhalder, A. Trenkwalder, D. Naik, G. Hendl, F. Schreck, and R. Grimm, *Collisional Stability of* ^{40}**K** *Immersed in a Strongly Interacting Fermi Gas of* ^{6}Li, Phys. Rev. Lett. **103**, 223203 (2009).

[Spi10a] F. M. Spiegelhalder, A. Trenkwalder, D. Naik, G. Kerner, E. Wille, G. Hendl, F. Schreck, and R. Grimm, *All-optical production of a degenerate mixture of* ^{6}*Li and* ^{40}*K and creation of heteronuclear molecules*, Phys. Rev. A **81**, 043637 (2010).

[Spi10b] F. M. Spiegelhalder, *Ultracold Fermi-Fermi Mixtures of Lithium and Potassium*, Ph.D. thesis, University of Innsbruck (2010).

[Ste08] J. Stewart, J. Gaebler, and D. Jin, *Using photoemission spectroscopy to probe a strongly interacting Fermi gas*, Nature (London) **454**, 744 (2008).

[Str03] K. E. Strecker, G. B. Partridge, and R. G. Hulet, *Conversion of an Atomic Fermi Gas to a Long-Lived Molecular Bose Gas*, Phys. Rev. Lett. **91**, 080406 (2003).

[Szu96] J. Szudy and W. E. Baylis, *Profiles of line wings and rainbow satellites associated with optical and radiative collisions*, Phys. Rep. **266**, 127 (1996).

[Szy05] M. H. Szymańska, K. Góral, T. Köhler, and K. Burnett, *Conventional character of the BCS-BEC crossover in ultracold gases of* ^{40}K, Phys. Rev. A **72**, 013610 (2005).

[Tag08] M. Taglieber, A.-C. Voigt, T. Aoki, T. W. Hänsch, and K. Dieckmann, *Quantum Degenerate Two-Species Fermi-Fermi Mixture Coexisting with a Bose-Einstein Condensate*, Phys. Rev. Lett. **100**, 010401 (2008).

[Tey10] M. K. Tey, S. Stellmer, R. Grimm, and F. Schreck, *Double-degenerate Bose-Fermi mixture of strontium*, Phys. Rev. A **82**, 011608 (2010).

[Tho05] S. T. Thompson, E. Hodby, and C. E. Wieman, *Spontaneous Dissociation of* ^{85}Rb *Feshbach Molecules*, Phys. Rev. Lett. **94**, 020401 (2005).

[Tie10] T. G. Tiecke, M. R. Goosen, A. Ludewig, S. D. Gensemer, S. Kraft, S. J. J. M. F. Kokkelmans, and J. T. M. Walraven, *Broad Feshbach Resonance in the* ^{6}*Li-*^{40}*K Mixture*, Phys. Rev. Lett. **104**, 053202 (2010).

[Tre11a] A. Trenkwalder, C. Kohstall, M. Zaccanti, D. Naik, A. I. Sidorov, F. Schreck, and R. Grimm, *Hydrodynamic Expansion of a Strongly Interacting Fermi-Fermi Mixture*, Phys. Rev. Lett. **106**, 115304 (2011).

[Tre11b] A. Trenkwalder, *Creation of a Strongly Interacting Fermi-Fermi Mixture of* ^{6}*Li and* ^{40}*K*, Ph.D. thesis, University of Innsbruck (2011).

[Tru01] A. G. Truscott, K. E. Strecker, W. I. McAlexander, G. B. Partridge, and R. G. Hulet, *Observation of Fermi Pressure in a Gas of Trapped Atoms*, Science **291**, 2570 (2001).

[Vee08] G. Veeravalli, E. Kuhnle, P. Dyke, and C. J. Vale, *Bragg Spectroscopy of a Strongly Interacting Fermi Gas*, Phys. Rev. Lett. **101**, 250403 (2008).

[Vee09] G. Veeravalli, *Bragg Spectroscopy of a Strongly Interacting Fermi Gas*, Ph.D. thesis, Swinburne University of Technology Melbourne, Australia (2009).

[vK11] C. W. von Keyserlingk and G. J. Conduit, *Itinerant ferromagnetism in an interacting Fermi gas with mass imbalance*, Phys. Rev. A **83**, 053625 (2011).

[Vli13] J. Vlietinck, J. Ryckebusch, and K. Van Houcke, *Quasiparticle properties of an impurity in a Fermi gas*, Phys. Rev. B **87**, 115133 (2013).

[Voi09] A.-C. Voigt, M. Taglieber, L. Costa, T. Aoki, W. Wieser, T. W. Hänsch, and K. Dieckmann, *Ultracold Heteronuclear Fermi-Fermi Molecules*, Phys. Rev. Lett. **102**, 020405 (2009).

[Wal10] J. T. M. Walraven, *Elements of Quantum Gases: Thermodynamic and Collisional Properties of Trapped Atomic Gases*, University of Amsterdam, 2010.

[Wan13] T. T. Wang, M.-S. Heo, T. M. Rvachov, D. A. Cotta, and W. Ketterle, *Deviation from Universality in Collisions of Ultracold $^6Li_2$ Molecules*, Phys. Rev. Lett. **110**, 173203 (2013).

[Web03] T. Weber, J. Herbig, M. Mark, H.-C. Nägerl, and R. Grimm, *Three-Body Recombination at Large Scattering Lengths in an Ultracold Atomic Gas*, Phys. Rev. Lett. **91**, 123201 (2003).

[Wil08] E. Wille, F. M. Spiegelhalder, G. Kerner, D. Naik, A. Trenkwalder, G. Hendl, F. Schreck, R. Grimm, T. G. Tiecke, J. T. M. Walraven, S. J. J. M. F. Kokkelmans, E. Tiesinga, and P. S. Julienne, *Exploring an Ultracold Fermi-Fermi Mixture: Interspecies Feshbach Resonances and Scattering Properties of ^6Li and ^{40}K*, Phys. Rev. Lett. **100**, 053201 (2008).

[Wil09] E. Wille, *Preparation of an Optically Trapped Fermi-Fermi Mixture of ^6Li and ^{40}K Atoms and Characterization of the Interspecies Interactions by Feshbach Spectroscopy*, Ph.D. thesis, University of Innsbruck (2009).

[Wu11] C.-H. Wu, I. Santiago, J. W. Park, P. Ahmadi, and M. W. Zwierlein, *Strongly interacting isotopic Bose-Fermi mixture immersed in a Fermi sea*, Phys. Rev. A **84**, 011601 (2011).

[Yu10] Z. Yu, S. Zöllner, and C. J. Pethick, *Comment on "Normal Phase of an Imbalanced Fermi Gas"*, Phys. Rev. Lett. **105**, 188901 (2010).

[Yu11] Z.-Q. Yu, S. Zhang, and H. Zhai, *Stability condition of a strongly interacting boson-fermion mixture across an interspecies Feshbach resonance*, Phys. Rev. A **83**, 041603 (2011).

[Yuv70] G. Yuval and P. Anderson, *Exact results for the Kondo problem: One-body theory and extension to finite temperature*, Phys. Rev. B **1**, 1522 (1970).

[Zür13] G. Zürn, T. Lompe, A. N. Wenz, S. Jochim, P. S. Julienne, and J. M. Hutson, *Precise Characterization of ^{6}Li Feshbach Resonances Using Trap-Sideband-Resolved RF Spectroscopy of Weakly Bound Molecules*, Phys. Rev. Lett. **110**, 135301 (2013).

[Zwe03] W. Zwerger, *Mott–Hubbard transition of cold atoms in optical lattices*, J. Opt. B **5**, S9 (2003).

[Zwe12] W. Zwerger (ed.), *The BCS-BEC Crossover and the Unitary Fermi Gas*, Springer, Berlin, 2012.

[Zwi03] M. W. Zwierlein, C. A. Stan, C. H. Schunck, S. M. F. Raupach, S. Gupta, Z. Hadzibabic, and W. Ketterle, *Observation of Bose-Einstein Condensation of Molecules*, Phys. Rev. Lett. **91**, 250401 (2003).

[Zwi05] M. W. Zwierlein, J. R. Abo-Shaeer, A. Schirotzek, C. H. Schunck, and W. Ketterle, *Vortices and superfluidity in a strongly interacting Fermi gas*, Nature (London) **435**, 1047 (2005).

[Zwi06] M. W. Zwierlein, A. Schirotzek, C. H. Schunck, and W. Ketterle, *Fermionic Superfluidity with Imbalanced Spin Populations*, Science **311**, 492 (2006).

[Zwi15] M. W. Zwierlein, *Superfluidity in Ultracold Atomic Fermi Gases, Chapter 18 in "Novel Superfluids, Volume 2", edited by K.-H. Bennemann and J.B. Ketterson*, Oxford University Press, Oxford, 2015.

Acknowledgements

I want to thank the people who made my PhD time in Innsbruck possible and so enjoyable.

My supervisor Rudi Grimm, thank you for allowing me to be part of the great research environment we have at the institutes. I am grateful for learning about your intuition and your view on the physics in the many meetings we had. In particular, I will treasure our Maria Waldrast conclaves - though the beer could have been better. I am especially grateful for your obliging support that made it possible to complete my PhD while still meeting my family obligations.

The former Co-PI and architect of the FeLiKx experiment Florian Schreck, I thank you for having built this brilliant machine with the team, supervising my initial activities in the lab and having a good practical advice to absolutely everything that happened or was supposed to happen in the lab.

Matteo Zaccanti, thanks for the first 20 months in and around the lab. Besides making me fluent in Italian swearing, you really aroused my (and the others') curiosity and were the driving force for the results from the lab. Thank you for that, boss.

I thank my predecessors in the lab: Andreas Trenkwalder for his inexhaustible patience during the process of passing the lab over to me and Christoph Kohstall for many discussions and for exchanging the views on new experimental insights. It really was a great pleasure to work with you!

I thank Marko Cetina for the four years we spent together in the lab. I absolutely admire your eagerness to convey knowledge you gained in the lab and I am grateful for learning from you in numerous discussions. Jook Walraven I thank for the months he stayed with us in Innsbruck. I value his input to the on-going experiments, the lectures he gave, and the plenty of discussions we had. I also absolutely enjoyed working with the new team in the lab: Isabella Fritsche, Bo Huang, and Rianne Lous, I very much appreciate the time we spent together. I thank you for this time and I wish you a lot of success and nice results with FeLiBoKx. Additionally, I thank Isabella Fritsche for making life in the office so bearable.

I also thank all the other members of the ultracold group at the IQOQI and at the university for their advices, for their assistance, and for the discussions with them.

I thank the colleagues in the workshops, Gerhard Hendl, Andreas Strasser, Stefan Haslwanter and Bernhard Öttl, for the support and for extremely fast delivered solutions! I thank the colleagues in the offices around Christine Götsch, Herr Knabl, Elisabeth Huck, Doris Corona,

Valentin Staubmann, and David Jordan for their assistance with bureaucracy and IT matters of any kind.

For proof reading of my thesis I thank Simon Stellmer, Leonid Sidorenkov and Bo Huang and I thank Katharina for *Jeden Tag mit Michael Jag*!